THE TECTONICS AND THREE-DIMENSIONAL STRUCTURE OF SPREADING CENTERS: MICROEARTHQUAKE STUDIES AND TOMOGRAPHIC INVERSIONS

by

Douglas Ray Toomey

B.S., Pennsylvania State University
(1981)

SUBMITTED IN PARTIAL FULFILLMENT
OF THE REQUIREMENTS FOR THE DEGREE OF
DOCTOR OF PHILOSOPHY

at the

MASSACHUSETTS INSTITUTE OF TECHNOLOGY

and the

WOODS HOLE OCEANOGRAPHIC INSTITUTION

September, 1987

Signature of Author _____
Joint Program in Oceanography, Massachusetts Institute of Technology and Woods Hole Oceanographic Institution, and the Department of Earth, Atmospheric, and Planetary Sciences, Massachusetts Institute of Technology, July 1, 1987

Certified by _____
Thesis Co-supervisor

Certified by _____
Thesis Co-supervisor

Accepted by _____
Chair, Joint Committee for Geology and Geophysics, Massachusetts Institute of Technology/Woods Hole Oceanographic Institution

THE TECTONICS AND THREE-DIMENSIONAL STRUCTURE OF SPREADING CENTERS: MICROEARTHQUAKE STUDIES AND TOMOGRAPHIC INVERSIONS

by

Douglas Ray Toomey

Submitted to the Department of Earth, Atmospheric, and Planetary Sciences
Massachusetts Institute of Technology
and
the Department of Geology and Geophysics
Woods Hole Oceanographic Institution
on July 1, 1987
in partial fulfillment of the requirements
for the degree of Doctor of Philosophy

ABSTRACT

Two-thirds of the Earth's surface has been formed along a global system of spreading centers that are presently manifested in several different structural forms, including the classic rift valley of the Mid-Atlantic Ridge, the more morphologically subdued East Pacific Rise, and the pronounced *en echelon* structure of the Reykjanes Peninsula within southwestern Iceland. In this thesis, each of these different spreading centers is investigated with microearthquake studies or tomographic inversion of travel times. Results of these studies are used to constrain the spatial variability of physical properties and processes beneath the axis of spreading and, together with other observations, the temporal characteristics of crustal accretion and rifting.

In Chapter 2 the theoretical basis of seismic body-wave travel-time tomography and techniques for the simultaneous inversion for hypocentral parameters and velocity structure are reviewed. A functional analysis approach assures that the theoretical results are independent of model parameterization. An important aspect of this review is the demonstration that travel time anomalies due to path and source effects are nearly independent. The discussion of the simultaneous inverse technique examines theoretically the dependence of tomographic images on the parameterization of the velocity model. In particular, the effects of

parameterization on model resolution are examined, and it is shown that an optimum set of parameters averages velocity over localized volumes. Chapter 2 ends with the presentation of the results of tomographic inversions of synthetic data generated for a model of the axial magma chamber postulated to exist beneath the East Pacific Rise. These inversions demonstrate the power of the tomographic method for imaging three-dimensional structure on a scale appropriate to heterogeneity along a spreading ridge axis.

Chapter 3 is the first of two chapters that present the results of a microearthquake experiment carried out within the median valley of the Mid-Atlantic Ridge near 23^{o} N during a three week period in early 1982. In this chapter, the experiment site, the seismic network, the relocation of instruments by acoustic ranging, the hypocenter location method, and the treatment of arrival time data are described. Moreover, hypocentral parameters of the 26 largest microearthquakes are reported; 18 of these events have epicenters and focal depths which are resolvable to within ±1 km formal error at the 95% confidence level. Microearthquakes occur beneath the inner floor of the median valley and have focal depths generally between 5 and 8 km beneath the seafloor. Composite fault plane solutions for two spatially related groups of microearthquakes beneath the inner floor indicate normal faulting along fault planes that dip at angles of 30^{o} or more. Microearthquakes also occur beneath the steep eastern inner rift mountains. The rift mountain earthquakes have nominal focal depths of 5-7 km and epicenters as distant as 10-15 km from the center of the median valley. The depth distribution and source mechanisms of these microearthquakes are interpreted to indicate that this segment of ridge axis is undergoing brittle failure under extension to a depth of at least 7-8 km.

In Chapter 4, the population of earthquakes considered in Chapter 3 is doubled and is used to define seismicity trends, to improve source mechanisms, and to estimate seismic moment and source dimensions of selected events. From a total of 53 microearthquakes, 23 are located beneath the inner floor and the epicenters of 20 of these occur within approximately 1 km of a line which strikes $N25^{o}E$; this seismicity trend is over 17 km in length. For 12 events located along the seismicity trend, the composite fault plane solutions clearly indicate normal faulting along planes that dip near 45^{o}. The seismic moments of inner floor microearthquakes are in the range 10^{17}-10^{20} dyn cm, and a B value of 0.8±0.2 is determined for events with moments greater than 10^{18}dyn cm. Epicenters of rift mountain

earthquakes do not appear to define linear trends; however, over a 24 hour period a high concentration of activity within a small area was observed. The seismic moments of events beneath the inner rift mountains vary between 10^{18} and 10^{20} dyn cm and define a B value of 0.5±0.1.

Also in Chapter 4, a tomographic inversion of travel times from earthquakes and local shots indicates a region of relatively lower velocities at 1-5 km depth beneath the central portion of the median valley inner floor, presumably the site of most recent crustal accretion. Results of microearthquake analysis and tomographic inversion are synthesized with local bathymetry and the record of larger earthquakes in the region to suggest that this section of the median valley has been undergoing continued horizontal extension and modest block rotation without crustal-level magma injection for at least the last 10^4 yr.

In Chapter 5, the simultaneous inverse technique is applied to a microearthquake data set collected at the Hengill central volcano and geothermal complex in southwestern Iceland. Arrival time data from 153 well-located microearthquakes and 2 shots, as recorded by 20 vertical component seismometers, are used to image velocity heterogeneity within a 14 x 15 x 6 km^3 volume that underlies the high-temperature Hengill geothermal field. The dense distribution of sources and receivers within the volume to be imaged permits structure to be resolved to within ±1 and ±2 km in the vertical and horizontal directions, respectively. The final model of stuctural heterogeneity is characterized by distinct bodies of anomously high velocities: two of these bodies are continuous from the surface to a depth of about 3 km, and each is associated with a site of past volcanic eruption; the third body of high velocity lies beneath the center of the active geothermal field at depths of 3-4 km.

The results of this thesis demonstrate that microearthquake surveying and seismic tomography are powerful tools for investigating the spatial variability of the dynamic processes that accompany the generation and early evolution of oceanic lithosphere.

ACKNOWLEDGEMENTS

Without the guidance, encouragement, and often-needed criticism of my advisors, Mike Purdy and Sean Solomon, this thesis would not have been completed. In matters both objective and abstract, their advice and everyday example has been crucial to my growth as a scientist and a person.

Several people made singular contributions to the eclectic topics included in this thesis. I thank Cliff Thurber for generously providing important elements of the software used in this dissertation and for enlightening discussions related to simultaneous inversion. Pall Einarsson provided helpful suggestions that led to the cooperative work between Gill Foulger and myself. I am grateful to Gill Foulger for the opportunity to work together on the inversion of the Hengill microearthquake data.

The WHOI Education Office deserves special thanks for providing funding that permitted me to attend the IUGG assembly in Iceland and that assisted Gill Foulger while she was a visiting investigator at WHOI. In addition to material munificence, Jake Peirson, Abbie Jackson, and, more recently, Jane Smith managed to keep me from winning, despite zealous attempts at negligence on my part, the coveted Golden Sneaker Award.

I owe sincere thanks to Chuck Denham and Hans Schouten. From the beginning, their contagious enthusiasm and offbeat creativity has been inspirational. The absence of Chuck from WHOI within the past years is not only my misfortune, but that of all students in search of guidance and representation.

Several other staff members and students merit recognition for generously sharing either ideas or scientific philosophies that have directly influenced this research. I extend thanks, in particular, to Eric Bergman, Paul Huang, Jeff Karson, Pat Lohmann, Mark Murray, Peter Shaw, Loren Shure, Anne Trehu, and the J.P. students.

Noteworthy among those deserving of both thanks and praise are the members of the WHOI seismology group. The comraderie and combined expertise within this group has contributed significantly to a rewarding experience. Dickie Allison

and Dave Dubois have graciously helped me with the inumerable and often arcane requests that accompany data reduction and completing a thesis. Don Koelsch and Butch Grant have repeatedly demonstrated, through their work with the ocean-bottom instruments, the meaning of quality craftsmanship. Moreover, when the instruments were safely, albeit disappointedly stored away in Bigelow for interminable periods, Butch showed me the finer aspects of lobstering and sailing within New England waters. Leon 'life is a virtual Friday' Gove deserves special thanks for computer-related advice and program development, particularly the nascent programs used for A to D conversion. Also, I feel honored that he and Debby Hutchinson trusted me with the sanctified triumvirate of their house, their boat, and their dog, in increasing order of cannonization. The summer weeks that I spent living on *Tautog* in Great Harbor will always be an especially fond memory. Finally, within our cabal, I extend my deep felt thanks to my fellow student and friend, John A. Collins, for the many and varied experiences we have survived together.

Inevitably, in the course of completing an almost mythical personal goal one acquires vital support from persons and events that exist on a rarefied plane above almost all other things. In the worst of times, when graduate school attempted to devalue my own self-perspective and self-worth, I was unbelievebly fortunate to have friends of such closeness and such selfless strength, that this could never happen. To Phil Stevens, Ray Howard and, undoubtedly, most of all Ginger Fry, I owe infinite gratitude.

This research was supported by the National Science Foundation, under grants EAR-8416192 and EAR-8617967, and by the Office of Naval Research, under contract N00014-86-K-0325.

The labor put into this thesis was devoted to my mother and father, and the town where our memories live.

The more distant you are from it, the more the implications of what you grew up with start to emerge. You can't escape, that's the whole thing, you can't. You finally find yourself in a situation where. . . that's the way it is -- you can't get out of it. But there's always that impulse toward another kind of world.

Sam Shepard
Introduction to Fool for Love and Other Plays

TABLE OF CONTENTS

ABSTRACT 2

ACKNOWLEDGEMENTS 5

CHAPTER 1. INTRODUCTION 11
References 17

CHAPTER 2. BODY WAVE TRAVEL TIME INVERSION: THEORY, METHOD, AND EXAMPLE 19

Principles of Seismic Tomography 20

The Differential Ray Equation 21

The Seismic Body Wave Tomography Equation: Path Effects 24

Hypocentral Partial Derivatives: Source Effects 27

Path and Source Effects Combined 28

Simultaneous Inversion and Parameter Separation 29

A Parameterized Formulation: Review of Thurber's Method 33

Velocity Model Parameterization and Model Partial Derivatives 33

Solution Method 37

Optimum Parameterization and Interpretation of Resolution 47

A Synthetic Experiment in Seismic Tomography 52

Postulated Magma Chamber Structure and Its Effect on Travel Time and Ray Path 53

Experimental Design and Results of Synthetic Inversions 58

Specific Objectives of a Tomogaphy Experiment 60

References 63

Figures 67

CHAPTER 3. MICROEARTHQUAKES BENEATH THE MEDIAN VALLEY OF THE MID-ATLANTIC RIDGE NEAR 23°N: HYPOCENTERS AND FOCAL MECHANISMS 80

Introduction 81

Experiment Site 82

The Seismic Network 83

Instrument Location 83

Hypocenter Location Method 85

Arrival Time Data 86

Velocity Model 87

Hypocenter Locations 87

Body Wave Particle Motion 90

Focal Mechanisms 91

Discussion 92

Conclusions 94

Appendix: Error Analysis for Instrument Location 95

References 95

CHAPTER 4. MICROEARTHQUAKES BENEATH THE MEDIAN VALLEY OF THE MID-ATLANTIC RIDGE NEAR 23°N: TOMOGRAPHY AND TECTONICS 97

Introduction 97

Microearthquake Data 99

Hypocenter Locations 100

Focal Mechanisms 105

Seismic Moments and Source Dimensions 106

	Tomographic Analysis of Travel Time Data	110
	Effects of Velocity Heterogeneity on Hypocenter Locations	120
	Tectonic Synthesis	126
	Discussion	132
	Conclusions	136
	References	140
	Tables	145
	Figures	148
CHAPTER 5.	A TOMOGRAPHIC INVERSION OF LOCAL EARTHQUAKE DATA: HENGILL-GRENSDALUR CENTRAL VOLCANO, ICELAND	172
	Introduction	172
	Experiment Site	173
	Arrival Time Data	174
	Simultaneous Inversion Method, Optimum Parameterization, and Resolution	176
	Application of Simultaneous Inversion	182
	Conclusions	190
	References	192
	Figures	195

CHAPTER 1. INTRODUCTION

Oceanic spreading centers are responsible for the formation of two-thirds of the Earth's surface. Within a spreading center, the thermal and mechanical structure of the lithosphere and the geology and morphology of the seafloor are controlled by the complex interplay of magmatic, tectonic, and hydrothermal processes. These are all dynamic processes that exhibit strong spatial and temporal dependencies. Moreover, while an individual process may manifest itself on the seafloor -- possibly as a volcano, an uplifted mountain range, or a hydrothermal vent field -- the majority of the dynamic activity invariably occurs at some depth. Any attempt to understand the mechanics of oceanic spreading centers necessarily requires knowledge of the dynamic processes operating directly beneath the axis of accretion.

In recent years, working models of oceanic spreading centers have evolved from two-dimensional, steady state idealizations to more realistic, three-dimensional, and time dependent systems. The new dimension added to the working models is the pervasive along-strike variability of mid-ocean ridge processes. Initially, this longitudinal variability was inferred from the along-strike discontinuities in seafloor magnetic anomalies [*Schouten and White,* 1980, *Schouten and Klitgord,* 1982, 1983]. These magnetic discontinuities can be observed off-axis, where the crust is many millions of years old, and are typically spaced at intervals of 50-80 km [*Schouten and Klitgord,* 1982, 1983]. On the basis of these data, it was proposed that a maximum in axial magmatism occurs midway between the axial loci of observed magnetic discontinuities, which are manifested either as large-offset or 'zero-offset' fracture zones [*Schouten and White,* 1980]. Theoretical studies of viscous flow provided a physical mechanism for local maxima in the axial magmatic budget [*Whitehead et al.,* 1984; *Crane,*

1985; *Schouten et al.,* 1985]. The hypothetical structural unit, consisting of a local maximum of magmatism bounded by along-axis minima (i.e., magnetic discontinuities), became known as a spreading center segment or cell.

This simple model of cellular segmentation provides an improved, but controversial, working hypothesis for mid-ocean ridge studies. One consequence of the segmentation hypothesis is that the quantity of magma emplaced within the crust varies systematically along axis and within a single cellular unit. However, while many observations collected near fracture zones are apparently consistent with along-axis variations in magmatic volume [e.g., *Detrick and Purdy,* 1980; *Cormier et al.,* 1984; *Mutter and Detrick,* 1984; *Fox and Gallo,* 1984; *Langmuir and Bender,* 1984], other causative mechanisms for the variation are equally plausible. For example, *Fox and Gallo* [1984] argue that the presence of old and thick lithosphere near a ridge-transform intersection constitutes a cold thermal boundary that effectively reduces partial melting within the nearby upper mantle; geochemical studies support this scenario [*Bender et al.,* 1984]. Away from fracture zones, recent geochemical data collected at closely spaced intervals on the East Pacific Rise have demonstrated that petrologically distinct magmatic units occur within a single ridge segment that is tectonically defined by fracture zones or overlapping spreading centers [*Langmuir et al.,* 1986]. The existence of distinct magmatic units within a spreading cell is not predicted by the simple segmentation hypothesis. As yet, the original magnetic data [*Schouten and White,* 1980; *Schouten and Klitgord,* 1982, 1983] and axial morphology [*Whitehead et al.,* 1985; *Crane,* 1985; *Schouten et al.,* 1985] remain the best supporting evidence for a segmented ocean ridge system.

Current three-dimensional and time-dependent descriptions of oceanic spreading centers can be rigorously tested by collecting data that are sensitive to the spatial variability of physical properties and processes. By conducting several

experiments on ridge axes in different stages of evolution and different rates of spreading it should also be possible to infer the temporal evolution of magmatic and tectonic activity at a given segment. Because the fundamental axial processes of magmatism, tectonism, and hydrothermal circulation predominantly evolve at depth, it is necessary to collect data that directly sample the crust and lithosphere beneath the axis of accretion.

Two geophysical methods, microearthquake surveying and seismic tomography, are excellent tools for mapping physical processes and properties that vary in time and in three dimensions. Microearthquake observations provide direct evidence of physical processes occurring kilometers beneath the seafloor. The cause of a dynamic event at depth can be distinguished by observing the spatial and temporal distribution of seismicity and microearthquake source characteristics. For example, tectonic stresses initiate seismogenic shear faulting, magma migration can be accompanied by seismic harmonic tremor, and hydrothermal cooling of a hot rock mass creates thermal contraction stresses and possibly seismogenic tensile failure. The documentation of along-axis variations in microearthquake characteristics is thus a straightforward means of testing further both the segmentation hypothesis and the details of intracellular processes.

Seismic tomography, the three-dimensional mapping of seismic velocity structure, is an important new tool that promises to revolutionize studies of oceanic spreading centers. The appeal of seismic tomography is its potential for imaging three-dimensional physical properties over a wide spectrum of length scales, including, for example, cross-borehole images of the upper crust near regions of hydrothermal venting, reconstruction of velocity anomalies characterizing axial magma chambers, and maps of physical properties within the upwelling mantle beneath seafloor spreading centers. Several fundamental improvements in the

descriptive and theoretical models of oceanic ridges await the detailed three-dimensional mapping of velocity structure. For example, a long-standing fundamental question is the size and shape of axial magma chambers along oceanic ridge segements [*Macdonald,* 1982].

In this thesis, microearthquake studies and tomographic inversions are used to investigate the spatial variability of physical processes deep within spreading centers. In addition, the observed spatial variability of spreading center properties are used in conjunction with the results of other studies to infer, when possible, temporal characteristics of magmatism, tectonism, or hydrothermal circulation. Divergent plate boundaries display several different structural forms, including the classic rift valley of the Mid-Atlantic Ridge, the more morphologically subdued East Pacific Rise, or the pronounced *en echelon* structure of the Reykjanes Peninsula within southwest Iceland. Each of these different spreading centers is the topic of a microearthquake or tomographic study in this thesis. These diverse investigations are unified by a common theme: furthering our knowledge of the nature of dynamic physical processes at ridge axes and relating these observations to working hypotheses of the mechanics of divergent lithospheric plate boundaries.

In Chapter 2, the theoretical basis of seismic body-wave travel-time tomography and techniques for simultaneous inversion for hypocentral parameters and heterogeneous velocity structure are reviewed. As part of this review the fundamental relationships governing the forward problem are derived from functional analysis; such derivations can be found in the literature, but in widely scattered references. In comparison with expansion series derivations that rely on parameterization of the velocity field [*e.g., Aki and Lee,* 1976], functional analysis provides an improved understanding of the near-independence of travel time anomalies due to path and source effects. A particular method of

simultaneous inversion, due to *Thurber* [1981, 1983], is discussed in detail. The presentation of Thurber's method for simultaneous inversion incorporates a discussion of parameterization and interpretation of model resolution; in particular, the effects of parameter densification are explored in the context of the damped-least squares operator. Thurber's method is then applied to synthetic data generated for a 'typical' East Pacific Rise axial magma chamber. These inversions of synthetic data are designed to evaluate the efficacy of the tomographic technique, using realistic configurations of sources and receivers, for imaging axial magma chambers beneath the fast-spreading East Pacific Rise. These results demonstrate that current tomographic methods can successfully image the size and shape of axial magma chambers.

In chapters 3 and 4, the results of a microearthquake experiment in the median valley of the Mid-Atlantic Ridge south of the Kane Fracture Zone are reported. This experiment was jointly conducted by the Massachusetts Institute of Technology and Woods Hole Oceanographic Institution from the R/V Knorr during February and March 1982. Chapter 3 reports, in addition to the basic techniques of data analysis, the hypocentral locations of 26 well-recorded events and composite focal mechanism solutions of selected earthquakes beneath the median valley inner floor. A fundamental result of this chapter is that observed microearthquake activity is concentrated 5-8 km beneath the central median valley floor and that these earthquakes occur predominantly by slip on normal faults dipping in excess of 30^{o}.

In Chapter 4, the population of earthquakes considered in Chapter 3 is doubled and is used to define seismicity trends and improved source mechanisms. In addition, seismic moments and source dimensions are presented for selected events. Travel time residual data from microearthquakes and local shots are then inverted to image tomographically the lateral heterogeneity in

crustal seismic velocity. The earthquake and velocity results are integrated with the findings of other geological and geophysical studies conducted south of the Kane Fracture Zone in order to derive a simple model of the recent tectonic extension and block-faulting of the median valley inner floor.

Chapter 5 reports results of an application of the simultaneous inversion technique of *Thurber* [1981, 1983] to a microearthquake data set collected in the vicinity of the Hengill geothermal area located on the Reykjanes Peninsula within southwest Iceland [*Foulger,* 1984]. The Hengill geothermal area has an areal extent of 70 km^2 and is Iceland's principal source of geothermal energy. During the summer of 1982, an area of approximately roughly 20x20 km^2 encompassing the geothermal field was the site of a temporary microearthquake network [*Foulger,* 1984]. Over a four month period, the 23-station network recorded approximately 2000 locatable microearthquakes [*Foulger,* 1984], and from this extensive catalogue of seismicity 153 of the best-located and -recorded events were chosen as input to a tomographic inversion. Results of the inversions provide a detailed image of velocity heterogeneities within a 14x15x6 km^3 volume. These heterogeneities are the consequence of a number of different processes, including magmatic intrusion, gradual cooling of igneous rock masses, and compositional variations within individual intrusions.

The results of this thesis support the potential of microearthquake and tomographic studies for exploring oceanic spreading centers. The tomographic studies of seismic velocity structure beneath local segments of the East Pacific Rise (Chapter 2), the Mid-Atlantic Ridge (Chapters 3 and 4), and the Icelandic rift (Chapter 5) represent a new approach to the seismological study of divergent lithospheric plate boundaries. Several future experiments designed to image the three-dimensional nature of physical properties at mid-ocean ridges are suggested on the basis of these results.

REFERENCES

Aki, K., and W.H.K. Lee, Determination of three-dimensional velocity anomalies under a seismic array using first P arrival times from local earthquakes, 1, A homogeneous initial model, *J. Geophys. Res., 81,* 4381-4399, 1976.

Bender, J.F., C.H. Langmuir, and G.N. Hanson, Petrogenesis of basalt glasses from the Tamayo region, East Pacific Rise, *J. Petrol., 25,* 213-254, 1984.

Cormier, M.H., R.S. Detrick, and G.M. Purdy, Anomalously thin crust in oceanic fracture zones: New constraints from the Kane Fracture Zone, *J. Geophys. Res., 89,* 10249-10266, 1984.

Crane, K., The spacing of rift axis highs: Dependence upon diapiric processes in the underlying asthenosphere?, *Earth Planet. Sci. Lett., 72,* 405-414, 1985.

Detrick, R.S., and G.M. Purdy, The crustal structure of the Kane Fracture Zone from seismic refraction studies, *J. Geophys. Res., 85,* 3759-3777.

Foulger, G.R., Seismological studies at the Hengill geothermal area, SW Iceland, Ph.D. Thesis, Univ. of Durham, England, 313 pp.,1984.

Fox, P.J., and D.G. Gallo, A tectonic model for ridge-transform-ridge plate boundaries: Implications for the structure of oceanic lithosphere, *Tectonophysics, 104,* 205-242, 1984.

Langmuir, C.H., and J.F. Bender, The geochemistry of oceanic basalts in the vicinity of transform faults: Observations and implications, *Earth Planet. Sci. Lett., 69,* 107-127, 1984.

Langmuir, C.H., J.F. Bender, and R. Batiza, Petrological and tectonic segmentation of the East Pacific Rise, $5^{o}30'$-$14^{o}30'$ N, *Nature, 322,* 422-429, 1986.

Macdonald, K.C., Mid-ocean ridges: fine scale tectonic, volcanic, and hydrothermal precesses within the plate boundary zone, *Ann. Rev. Earth Planet. Sci., 10,* 155-190, 1982.

Mutter, J.C., R.S. Detrick, and North Atlantic Study Group, Multichannel seismic evidence for anomalously thin crust at the Blake Spur Fracture Zone, *Geology, 12,* 534-537,1984.

Schouten, H., and K.D. Klitgord, The memory of the accreting plate boundary and the coninutuity of fracture zones, *Earth Planet. Sci. Lett., 59,* 255-266, 1982.

Schouten, H., and K.D. Klitgord, Overlapping spreading centers on the East Pacific Rise, Comment, *Nature, 503,* 549-550, 1983.

Schouten, H., and R.S. White, Zero-offset fracture zones, *Geology, 8*, 175-179, 1980.

Schouten, H., K.D. Klitgord, and J.A. Whitehead, Segmentation of mid-ocean ridges, *Nature, 317,* 225-229, 1985.

Thurber, C.H., Earth structure and earthquake locations in the Coyete Lake area, central California, Ph.D. Thesis, Mass. Inst. of Technol., Cambridge, 332 pp., 1981.

Thurber, C.H., Earthquake locations and three-dimensional crustal structure in the Coyote Lake area, central California, *J. Geophys. Res., 88,* 8226-8236, 1983.

Whitehead, J.A., H.J.B. Dick, and H. Schouten, A mechanism for magmatic accretion under spreading centres, *Nature, 312,* 146-148, 1984.

CHAPTER 2

BODY WAVE TRAVEL TIME INVERSION: THEORY, METHOD, AND EXAMPLE

The inversion of seismic body wave travel time data for heterogeneous Earth structure is known as seismic tomography. The principle of the tomographic technique is the reconstruction of a physical property from the values of its integrals evaluated along a large number of different paths. Discrete or continuous geophysical inverse theory is usually employed for this reconstruction. In this chapter, the theory of seismic tomography for body wave travel time data and a method of inversion, due to Thurber [1981, 1983], are reviewed. In addition, results of a tomographic inversion of synthetic data, generated from a hypothetical model of the East Pacific Rise, are presented.

The emphasis in this chapter is on the theoretical analysis of questions that have arisen in the course of applying tomographic techniques to real data. In the next section the principles of seismic tomography are reviewed and, in particular, the near-independence of travel time anomalies due to hypocentral mislocation and those due to velocity perturbations is established. Later, in Chapter 4, this result is used to justify assumptions that permit a tomographic inversion of travel time anomalies from microearthquakes on the Mid-Atlantic Ridge. In the subsequent section a tomographic inversion method, due to Thurber [1981, 1983], is described; emphasis is placed on the effects of velocity model parameterization on the resolution of the final model. This analysis of model parameterization and resolution includes ideas that are applied later, in Chapter 5, to the Icelandic data set.

PRINCIPLES OF SEISMIC TOMOGRAPHY

All of the tomographic inversions presented in this thesis use observations of microearthquakes or shots that have been recorded by a local seismic network whose aperture is on the order of tens of kilometers. The review of seismic tomography theory is thus limited to the inversion of body wave travel time data generated by sources that are located within or very near the volume to be imaged. A more general review is presented by Thurber and Aki [1987]. The derivations presented in this section are independent of velocity model parameterization or numerical methods. This general approach assures that assumptions and results discussed here are intrinsic to the theory. An important aspect of this review is the demonstration that, in the limit of small perturbations to either the hypocentral parameters or velocity structure, the travel time anomalies due to path and source effects is simply a linear combination of independent terms.

Throughout this section Fermat's principle is used to investigate the seismic body wave travel time functional

$$T = \int v(\underline{r})^{-1} ds \qquad (2.1)$$

where ds is an elemental arc length along the ray path and $v(\underline{r})$ is an inhomogeneous, isotropic velocity field that depends only on the spatial coordinates $\underline{r}=(x,y,z)$. The limits of integration are unspecified in (2.1) since they depend on the application. For example, by choosing the integration limits in (2.1) to be two fixed points p_i and p_j, and specifying a velocity model $v_o(\underline{r})$, Fermat's principle can be utilized to derive the well-known differential seismic ray equation [e.g., Aki and Richards, 1980; Lee and Stewart, 1981]. The differential seismic ray equation, or simply the ray equation, can then be utilized to calculate a

stationary travel path P_{ij} connecting the source and receiver endpoints p_i and p_j, respectively, for the medium $v_o(\underline{r})$. Alternatively, choosing the limits of integration in (2.1) to be the line or path P_{ij} (calculated for $v_o(\underline{r})$), Fermat's principle can be utilized to develop an approximate, linear relationship for the travel time variation caused by perturbations of the velocity medium $v_o(\underline{r})$ [Backus and Gilbert, 1969]. This first-order perturbational relationship is the seismic tomography equation for body wave travel times. Finally, by permitting the endpoint p_j of the path P_{ij} to vary, relationships for the partial derivatives of travel time with respect to hypocentral parameters can be obtained. In the following three sections, we examine each of the above three variations of (2.1).

The Differential Ray Equation

A fundamental application of Fermat's principle is the derivation of the differential seismic ray equation for a general velocity medium $v(\underline{r})$. This particular approach is well-known and the derivation presented here follows that of Lee and Stewart [1981]. The assumptions are that the velocity model and its first partial derivatives are continuous functions of the spatial coordinates and that the seismic wavelength is much shorter than the length scale of seismic velocity inhomogeneity.

The travel time T between two points p_1 and p_2 is expressed by the functional

$$T = \int_{p_1}^{p_2} v(\underline{r})^{-1} ds \qquad (2.2)$$

where ds is the elemental arc length along a path. Fermat's principle requires that the travel time functional be stationary (i.e., $\delta T=0$) for a

physically plausible seismic ray path. This constraint provides a means for deriving the equations that govern the geometry of seismic ray paths.

First, introduce a new parameter q which describes a single position along the ray path for each value of q

$$x=x(q),\ y=y(q),\ \text{and}\ z=z(q) \tag{2.3}$$

An infinitesimal ray path element may be expressed as

$$ds=(x'^2+y'^2+z'^2)^{1/2}dq \tag{2.4}$$

where a prime indicates a derivative with respect to q. Substituting (2.4) into (2.2) yields

$$T = \int_{q_1}^{q_2} w\ dq \tag{2.5}$$

where q_1 and q_2 are the values associated with p_1 and p_2, respectively, and

$$w \equiv (x'^2+y'^2+z'^2)^{1/2}/v(\underline{r}) \tag{2.6}$$

Note that the integrand of (2.5) is a function of x,y,z,x',y', and z'.

The variation of the travel time functional is expressed as

$$\begin{aligned}\delta T &= \int_{q_1}^{q_2} \delta w\ dq \\ &= \int_{q_1}^{q_2} \left(\frac{\partial w}{\partial x}\delta x + \frac{\partial w}{\partial y}\delta y + \frac{\partial w}{\partial z}\delta z\right. \\ &\quad \left. + \frac{\partial w}{\partial x'}\delta x' + \frac{\partial w}{\partial y'}\delta y' + \frac{\partial w}{\partial z'}\delta z'\right)dq\end{aligned} \tag{2.7}$$

Integration by parts of the last three terms in (2.7) yields

$$\delta T = \left[\frac{\partial w}{\partial x'}\,\delta x + \frac{\partial w}{\partial y'}\,\delta y + \frac{\partial w}{\partial z'}\,\delta z\right]\Big|_{q_1}^{q_2}$$

$$-\int_{q_1}^{q_2}\left(\frac{d}{dq}\frac{\partial w}{\partial x'} - \frac{\partial w}{\partial x}\right)\delta x\,dq$$

$$-\int_{q_1}^{q_2}\left(\frac{d}{dq}\frac{\partial w}{\partial y'} - \frac{\partial w}{\partial y}\right)\delta y\,dq \qquad (2.8)$$

$$-\int_{q_1}^{q_2}\left(\frac{d}{dq}\frac{\partial w}{\partial z'} - \frac{\partial w}{\partial z}\right)\delta z\,dq$$

Now assume that a seismic ray path P_{12} exists which connects the endpoints q_1 and q_2. Since the variations δx, δy, and δz evaluated at the fixed endpoints q_1 and q_2 are zero, the first term on the right hand side of (2.8) vanishes. Fermat's principle states that the travel time functional is a local minimum with respect to nearby ray paths; this requires that $\delta T=0$ for the path P_{12}. For a true ray path, (2.8) and $\delta T=0$ reduce to the following conditions

$$\frac{d}{dq}\frac{\partial w}{\partial x'} - \frac{\partial w}{\partial x} = 0$$

$$\frac{d}{dq}\frac{\partial w}{\partial y'} - \frac{\partial w}{\partial y} = 0 \qquad (2.9)$$

$$\frac{d}{dq}\frac{\partial w}{\partial z'} - \frac{\partial w}{\partial z} = 0$$

These equations are recognised as Euler's equations [Hildebrand, 1965].

A change of variables in (2.9) yields the more familiar form of the differential seismic ray equations. Substituting the definition of w in

(2.6) into (2.9) and assuming that q=s and $(x'^2+y'^2+x'^2)^{1/2}=1$ reduce (2.9) to

$$\begin{aligned} \frac{d}{ds}\left(\frac{1}{v}\frac{dx}{ds}\right) - \frac{\partial}{\partial x}\left(\frac{1}{v}\right) &= 0 \\ \frac{d}{ds}\left(\frac{1}{v}\frac{dy}{ds}\right) - \frac{\partial}{\partial y}\left(\frac{1}{v}\right) &= 0 \\ \frac{d}{ds}\left(\frac{1}{v}\frac{dz}{ds}\right) - \frac{\partial}{\partial z}\left(\frac{1}{v}\right) &= 0 \end{aligned} \qquad (2.10)$$

Equations (2.10) are recognized as the differential seismic ray equations [Lee and Stewart, 1981].

The above derivation shows that, for high frequency waves, an application of Fermat's principle to the travel time functional (2.2) yields conditions that can be used to calculate seismic ray paths (2.10) through an inhomogeneous, isotropic medium. For tomographic applications, we require a method to solve (2.10). In practice, the determination of a true ray path between two points can be a computational challenge. A review of numerical methods is presented in Lee and Stewart [1981], and detailed presentations of individual techniques are found in Julian and Gubbins [1977] and Pereyra et al. [1980].

The Seismic Body Wave Tomography Equation: Path Effects

In the last section, equations were derived that determine the ray path between two fixed points for a given velocity model. Here, we assume that stationary seismic ray paths have been determined for an initial model $v(\underline{r})$, and we derive an approximate linear relationship between small velocity perturbations of the initial model $\delta v(\underline{r})$ and travel time variations [Backus and Gilbert, 1969; Chou and Booker, 1979]. The general results presented here are independent of our choice of velocity model representation.

The travel time functional for a specified path is

$$T_{ij} = \int_{P_{ij}} u(\underline{r})ds \tag{2.11}$$

where i is a station index, j is a source index, P_{ij} is the seismic ray path between the j^{th} source and i^{th} station, and $u(\underline{r})$ is the slowness field. The path P_{ij} satisfies (2.10) for the initial model $u(\underline{r})$. Equation (2.11) is nonlinear in u because of the dependence of P_{ij} on $u(\underline{r})$. For example, consider the effects on (2.11) of a small perturbation $\delta u(\underline{r})$ to the slowness field. In this case, (2.11) becomes

$$T_{ij}(u+\delta u) = \int_{P_{ij}(u+\delta u)} (u+\delta u)ds \tag{2.12}$$

where $P_{ij}(u+\delta u)$ specifies the nonlinear dependence of the travel time functional on the integration limits. If the slowness perturbations are small, however, we can assert from Fermat's principle that changes in the travel time functional with respect to small changes in the integration path are zero to first order. This assertion simplifies (2.12) to

$$T_{ij}(u+\delta u) = \int_{P_{ij}(u)} (u+\delta u)ds + \Theta(\delta u^2) \tag{2.13}$$

where the integration path is now $P_{ij}(u)$. Dropping the higher-order terms and utilizing (2.11) results in the following:

$$\delta T_{ij} \equiv T_{ij}(u+\delta u) - T_{ij}(u) = \int_{P_{ij}} \delta u \, ds \tag{2.14}$$

Substitution of $v(\underline{r})=u(\underline{r})^{-1}$ and evaluation of the variational yields

$$\begin{aligned} \delta T_{ij} &= \int_{P_{ij}} \delta(v^{-1}) \, ds \\ &= -\int_{P_{ij}} \frac{ds}{v} \frac{\delta v}{v} \end{aligned} \tag{2.15}$$

Equation (2.15) is a general statement of the forward problem of seismic tomography. It is a linear equation, correct to first-order, and it describes the travel time variations caused by perturbations to the initial velocity

model $v(\underline{r})$. Note that $ds/v(\underline{r})$ is simply the incremental time along the infinitesimal arc length, and $\delta v(\underline{r})/v(\underline{r})$ may be regarded as a fractional deviation from the original model. Thus the variation of the travel time functional due to model perturbations is approximated by an integral of travel time deviations along incremental arc lengths. To date, only a few studies have investigated the limitations of (2.15) due to nonlinearity [Thurber, 1981; Gubbins, 1981; Pavlis and Booker, 1983; Koch, 1985].

Since a majority of the numerical methods available are based on a parameterizion of the velocity field, it is worth showing a general parametric form of (2.15) [Thurber, 1981]. If it is assumed that the velocity model depends on a finite set of parameters α_m, then

$$v(\underline{r}) = v(\underline{r};\alpha_1,\ldots,\alpha_m) \tag{2.16}$$

The parameters α_m in turn may depend on the spatial coordinates in the following manner

$$\alpha_i = \alpha_i\delta(\underline{r}_i-\underline{r}) \tag{2.17}$$

where $\delta(\underline{r}_o-\underline{r})$ is the Kronecker delta. In this case, the variation of $v(\underline{r})$ is given as

$$\delta v(\underline{r}) = \sum_{i=1}^{m} \frac{\partial v}{\partial \alpha_i}\,\delta\alpha_i \simeq \sum_{i=1}^{m} \frac{\partial v}{\partial \alpha_i}\,\Delta\alpha_i \tag{2.18}$$

where $\Delta\alpha$ represents a discrete change in the value of a velocity parameter. For a general parametric velocity model, equation (2.15) is written as follows

$$\delta T_{ij} = -\int_{P_{ij}} \frac{1}{v(\underline{r};\alpha_1,\ldots,\alpha_m)^2} \sum_{k=1}^{m} \frac{\partial v}{\partial \alpha_k}\,\Delta\alpha_k \, ds \tag{2.19}$$

In a later section we will define a particular parameterization and evaluate the partial derivative terms of (2.19).

Hypocentral Partial Derivatives: Source Effects

The seismic body wave tomography equation (2.15) presented in the previous section assumes that the ray end points are known. However, earthquake sources are often used to image heterogeneous structure, requiring that (2.15) be generalized to include the effects of unknown source time and location. In this section, equations relating travel time variations to changes in the location of the source are derived following Lee and Stewart [1981]. An important result of this derivation is that small source mislocations give rise to travel time variations which are independent of changes in the ray path.

Consider the travel time variation that arises from movement of the source endpoint from point A to a point B near A. Define Γ_A and Γ_B as the stationary seismic ray paths connecting points A and B, respectively, to the receiver endpoint C. Also, specify the variation of the endpoint of the integration path at the source as $\delta(\underline{r})|_A = (\delta x_A, \delta y_A, \delta z_A)$. Equation (2.8) states that the travel time variation incurred by small changes of the source endpoint is

$$\delta T = \left[\frac{\partial w}{\partial x'}\,\delta x + \frac{\partial w}{\partial y'}\,\delta y + \frac{\partial w}{\partial z'}\,\delta z\right]\Bigg|_A^C$$

$$= -\frac{\partial w}{\partial x'}\Big|_A \delta x_A - \frac{\partial w}{\partial y'}\Big|_A \delta y_A - \frac{\partial w}{\partial z'}\Big|_A \delta z_A \qquad (2.20)$$

Note that in this case the three integrals in (2.8) vanish since both paths, Γ_A and Γ_B, satisfy Euler's equations. Substituting the definition of w in (2.6) into (2.20) yields

$$\delta T = -\frac{dx}{ds}\,\frac{1}{v}\Big|_A \delta x_A - \frac{dy}{ds}\,\frac{1}{v}\Big|_A \delta y_A - \frac{dz}{ds}\,\frac{1}{v}\Big|_A \delta z_A \qquad (2.21)$$

For a given velocity field $v(\underline{r})$, the travel time functional is dependent on

the six coordinates of the endpoints, and this implies the following:

$$\delta T = \frac{\partial T}{\partial x_A}\delta x_A + \frac{\partial T}{\partial y_A}\delta y_A + \frac{\partial T}{\partial z_A}\delta z_A + \frac{\partial T}{\partial x_C}\delta x_C + \frac{\partial T}{\partial y_C}\delta y_C + \frac{\partial T}{\partial z_C}\delta z_C \tag{2.22}$$

Since the receiver endpoint C is fixed the last three terms in (2.22) vanish, and comparison of (2.22) with (2.21) yields the relations

$$\frac{\partial T}{\partial x_A} = -\frac{dx}{ds}\frac{1}{v}\Big|_A \qquad \frac{\partial T}{\partial y_A} = -\frac{dy}{ds}\frac{1}{v}\Big|_A \qquad \frac{\partial T}{\partial z_A} = -\frac{dz}{ds}\frac{1}{v}\Big|_A \tag{2.23}$$

The above equations state that travel time partial derivatives with respect to hypocenter location are related to the slowness at the source by the directional cosines of the emerging ray. An important implication of (2.23) is that hypocentral partial derivatives are independent of changes in the path of integration that are caused by source mislocation.

Previously, we have been discussing variations of travel time. However, since the origin time of an earthquake is unknown, the data recorded by a seismometer are arrival times. A change in origin time obviously affects all arrival times identically; the partial derivative with respect to origin time is unity.

Path and Source Effects Combined

We have demonstrated above that travel time anomalies due to path and source effects are independent of small changes in the seismic ray path. In addition, we have shown that path and source effects are coupled only by the slowness at the earthquake focus (see (2.15) and (2.23)). These results imply

that a perturbation of the velocity field, away from the source, will not affect hypocentral partial derivatives. Likewise, a mislocation of the source by a small amount will not influence the travel time variation caused by velocity perturbations along the seismic ray path. Since hypocentral partial derivatives are proportional to the slowness $u(\underline{r})$, they are affected only marginally by small slowness perturbations $\delta u(\underline{r})$ near the source. Thus, in the limit of small slowness anomalies relative to an assumed model, we can assert that travel time anomalies due to path and source effects are a linear combination of independent terms [e.g., Pavlis and Booker, 1980]. A general statement of the forward problem is

$$\delta T_{ij} = -\int_{P_{ij}} \frac{ds}{v(\underline{r})v(\underline{r})} \delta v(\underline{r}) + \sum_{k=1}^{4} \frac{\partial T_{ij}}{\partial x_k} \delta x_k \qquad (2.24)$$

where δT_{ij} is the arrival time variation, $v(\underline{r})$ is the assumed velocity model, the hypocentral parameters are symbolized by x_k where k=4 denotes origin time, and the ray path P_{ij} and the hypocentral partial derivatives are calculated from $v(\underline{r})$. It is clear from the derivation of (2.24) that the sources of arrival time variations are, to first order, independent.

Simultaneous Inversion and Parameter Separation

The interest in this thesis is in the inverse solution of (2.24). Given a set of body wave arrival time observations, the objective is to utilize (2.24) to refine an *a priori* model consisting of the velocity structure and the hypocentral parameters of a set of earthquakes. An inverse solution of (2.24) is referred to as a simultaneous inversion. While inverse problems are common to geophysics, the simultaneous inversion is unusual in that it brings together, in a single inversion, a continuous function and discrete parameters. Hence, simultaneous inversion is one form of a 'mixed

discrete-continuous inverse problem' [Pavlis and Booker, 1980]. Many inverse problems are unmixed, and separate solution methods are available for each extreme. Inversions for discrete parameters can be solved, for example, by the methods of Franklin [1970], Wiggins [1972], or Jackson [1972] while inversions for continuous functions can be obtained using the methods of Backus and Gilbert [1967, 1968, 1970]. In this section, we review a technique, developed by Pavlis and Booker [1980], that separates mixed discrete-continuous inverse problems into an equivalent set of equations that are unmixed. This technique is termed parameter separation.

The linear, perturbational relationship (2.24) is more compactly written as

$$\underline{b} = \underline{\underline{H}}\,\underline{h} + \langle \underline{\underline{M}} | \underline{m} \rangle \qquad (2.25)$$

where, for a single earthquake, $\underline{b}$ is a d x 1 vector of arrival time residuals, d is the number of arrival times per event, H is a 4 x 4 matrix of hypocentral partial derivatives, $\underline{h}$ is a 4 x 1 vector of hypocentral parameter perturbations, and the term in triangular brackets is an inner product of velocity model perturbations $\underline{m}$ with the kernel M. The residual vector of arrival times $\underline{b}$ is defined as

$$\underline{b} \equiv \underline{T}_o - \underline{T}_c|_{\underline{h}, v(\underline{r})} \qquad (2.26)$$

where $\underline{T}_o$ is the vector of observed arrival time data and $\underline{T}_c$ is a vector of calculated arrival times for an initial model consisting of hypocentral parameters $\underline{h}$ and velocity structure $v(\underline{r})$.

The parameter separation technique of Pavlis and Booker [1980] uses a projection operator to separate a mixed discrete-continuous linear inverse problem. We can understand the principle of the parameter separation technique by examining the mixed discrete-continuous linear equations for a

single earthquake that is well constrained by d arrival time observations, where d >> 4. In this case, it is implicit that the d x 4 matrix H is well-determined or full rank. A singular-value decomposition [Lanczos, 1961] of H is written as

$$\underset{=}{H} = \underset{===}{U\Lambda V^T} \tag{2.27}$$

where U is a d x d orthogonal matrix whose columns are data space eigenvectors, V is a 4 x 4 orthogonal matrix whose columns are parameter space eigenvectors, Λ is a d x 4 matrix with only four non-zero entries that are located along the principal diagonal, and the superscript T denotes transpose. The matrices U and V are coupled only by the four non-zero entries, or eigenvalues, of Λ. This suggests a partition of U as follows:

$$\underset{=}{U} = [\underset{=}{U_p}\underset{=}{U_o}] \tag{2.28}$$

where U_p is d x 4 and composed of the data space eigenvectors coupled to parameter space eigenvectors by the non-zero eigenvalues. The matrix U_o is d x (d-4) in this case and possesses the useful characteristic that it annihilates H as follows:

$$\underset{=}{U_o^T}\underset{=}{H} = 0 \tag{2.29}$$

Equation (2.29) states that the matrix H has no projection onto the data space sector spanned by the eigenvectors, with trivial eigenvalues, comprising the subspace U_o. This is a well-known result [e.g., Aki and Richards, 1980], and it is verified by the following expansion

$$\underset{=}{U_o^T}\underset{=}{H} = \underset{===}{U_o^T U\Lambda V^T} = \underset{=}{U_o^T}[\underset{=}{U_p}\underset{=}{U_o}]\underset{==}{\Lambda V^T} \tag{2.30}$$

Since $U_o^T U_p = 0$ and the bottom (d-4) rows of Λ are zero, it is clear that U_o^T annihilates H.

Operating $\underline{\underline{U}}_o^T$ on equation (2.25) yields

$$\underline{\underline{U}}_o^T \underline{b} = \underline{\underline{U}}_o^T \langle \underline{\underline{M}} | \underline{m} \rangle = \underline{b}' \qquad (2.31)$$

where $\underline{b}'$ is a (d-4) x 1 vector of 'annulled' data [Pavlis and Booker, 1980]. The annulled data can be thought of as a lower dimensional projection of $\underline{b}$ onto the data subspace spanned by the eigenvectors of U_o. Pavlis and Booker [1980] have demonstrated that the residual vector $\underline{b}'$, which is a linear combination of the original data vector $\underline{b}$, is unbiased by initial hypocenter locations; a similar conclusion was obtained by different reasoning in the last section. Thus, $\underline{b}'$ may be used, with a suitable numerical method (e.g., Backus and Gilbert [1967, 1968, 1970], Franklin [1970], Wiggins [1972] or, Jackson [1972]), to estimate model perturbations that are locally independent of hypocenter locations. Though the above example of parameter separation was demonstrated for a single event, extension of this result for a suite of earthquakes is straightforward [Pavlis and Booker, 1980].

Utilization of the parameter separation technique usually involves the following steps: First, hypocentral parameters are estimated, assuming an initial velocity model, by some nonlinear parameter estimation technique. Second, a residual vector $\underline{b}$ is constructed and subsequently operated on by the data space annihilator to obtain the annulled data. Last, velocity model perturbations are calculated, and the entire process is repeated until convergence is achieved.

Spencer and Gubbins [1980] also developed a technique to simultaneously estimate hypocentral parameters and heterogeneous structure for a parameterized velocity model. Their development was motivated by the computational demands of an unseparated simultaneous inversion. Clearly, an unseparated numerical solution of a parameterized model comprised of 4 x n_e

+ n_α parameters (n_e and n_α are the total number of earthquakes and velocity model parameters, respectively), where both n_e and n_α may be in the hundreds, is computationally inefficient . Use of parameter separation reduces the rank of the largest matrix requiring inversion to n_α x n_α. The technique of Spencer and Gubbins [1980] yields results similar to those of Pavlis and Booker [1980]. The parameter separation technique for an unmixed, parameterized problem is not discussed further here.

A PARAMETERIZED FORMULATION: REVIEW OF THURBER'S METHOD

In this section, the general principles of seismic tomography developed above are applied to the velocity model parameterization of Thurber [1981, 1983]. Given a parametric velocity model, an inversion for velocity structure becomes the familiar problem of parameter estimation. Topics to be discussed are the damped least-squares solution to parameterized problems [Franklin, 1970; Wiggins, 1972; Jackson, 1972], the effects of damping on resolution and covariance of model parameters, and the effects of parameter densification on resolution of the final model. Ideas developed in this section, particularily those relating to model resolution, are applied to the Icelandic data set in Chapter 5.

Velocity Model Parameterization and Model Partial Derivatives

The distinguishing characteristic among the various approaches to the seismic tomography problem is often the way in which the velocity model is represented. Heterogeneous earth structure has been parameterized by constant velocity layers [Crosson, 1976a, b], constant velocity blocks [Aki and Lee, 1976], plane layers constructed of laterally varying blocks with vertically constant velocity [Benz and Smith, 1984], analytical functions specified by a

small number of parameters [Spencer and Gubbins, 1980], arbitrarily shaped averaging volumes [Chou and Booker, 1979], continuous valued functions with a priori probability density distribution functions [Tarantola and Nercessian, 1984], and interpolatary functions defined by values specified at nodal points within a three-dimensional grid [Thurber, 1983]. Throughout this thesis the interpolative method of Thurber will be utilized, for the following reasons: (1) it is capable of reproducing three-dimensional bodies with characteristic dimensions on the order of a few kilometers, (2) the representation is general and does not assume a specific geometry of velocity heterogeneity [e.g., Spencer and Gubbins, 1980] and (3) the parameterized model can generate a continuous velocity field as opposed to discrete block strucures with discontinuous values of velocity across cell boundaries.

In the interpolation method of Thurber [1981, 1983] a continuous velocity field is defined by linear interpolation between values defined at a three-dimensional matrix of m nodes. Nodal locations are fixed prior to an inversion, and the distribution of nodes throughout the study volume can be irregular. At a point within the study volume a subset of eight parametric nodes are utilized to determine a velocity value. These eight nodes lie at the corners of a box which surrounds the point of interest. Velocity values at any given point are calculated from the expression [Thurber, 1983]

$$v(\underline{r};\alpha_1,\ldots,\alpha_m) = \sum_{i=1}^{2}\sum_{j=1}^{2}\sum_{k=1}^{2} \alpha(x_i,y_j,z_k)\cdot \left|\left(1-\left|\frac{x - x_i}{x_2 - x_1}\right|\right)\left(1-\left|\frac{y - y_i}{y_2 - y_1}\right|\right)\left(1-\left|\frac{z - z_k}{z_2 - z_1}\right|\right)\right| \equiv \sum_{n=1}^{8} w_n\alpha_n \tag{2.32}$$

where α_n designates the velocity at a parametric node, $\underline{r}=(x,y,z)$ is the

position vector, and the limits of summation are restricted to the eight nodes that define the box enclosing the point $\underline{r}$. The interpolation of velocity is linear in all three coordinate directions, and the resulting field is a continuous function. First partial derivatives of the velocity field with respect to the spatial coordinates, however, are discontinuous.

Given the above parameterization, a specific form of the seismic body wave tomography equations (2.15 and 2.19) can be derived. In particular, an explicit form of the velocity variation at a point $\delta v(\underline{r})$ due to perturbations of parametric nodes can be stated. Recalling equation (2.18), and using equation (2.32), one can now write the following

$$\left.\frac{\partial v(\underline{r})}{\partial \alpha_i}\right|_{r_i} = \frac{\partial}{\partial \alpha_i}\left(\sum_{n=1}^{8} w_n \alpha_n\right) = w_i \tag{2.33}$$

Equation (2.18) then reduces to

$$\delta v(\underline{r}) = \sum_{i=1}^{8} w_i \Delta \alpha_i \tag{2.33}$$

where the summation is limited to the eight nodes defining the box that encloses $\underline{r}$. Substituting (2.33) into (2.19) yields

$$\delta T_{ij} = -\int_{P_{ij}} \frac{1}{v(\underline{r};\alpha_1,\ldots,\alpha_m)^2} \sum_{k=1}^{8} w_k \Delta \alpha_k \; ds \tag{2.35}$$

where it is implied that the summation is evaluated along each incremental arc of the ray path, and the eight weights and parametric values, respectively w_k and $\Delta\alpha_k$, vary with $\underline{r}$. Equation (2.35) is an expression of the observed travel time variation due to model perturbations in the vicinity of the path P_{ij}. Note that an observed travel time anomaly is the result of integrated variations in the velocity field. Because of this, (2.35) is not useful in its present form for estimating individual velocity parameter perturbations.

A relation between travel time variations and individual model parameter perturbations can be obtained in the following manner. For a given path P_{ij} the travel time variation is a function of the nodal parameters only. Thus we can write

$$\delta T_{ij}(\alpha_1,\ldots,\alpha_m) = \sum_{k=1}^{m} \frac{\partial T_{ij}}{\partial \alpha_k} \Delta\alpha_k \tag{2.36}$$

Comparison of (2.36) and (2.35) results in the expression

$$\sum_{k=1}^{m} \frac{\partial T_{ij}}{\partial \alpha_k} \Delta\alpha_k = -\int_{P_{ij}} \frac{1}{v(\underline{r};\alpha_1,\ldots,\alpha_m)^2} \sum_{k=1}^{s} w_k \Delta\alpha_k \; ds \tag{2.37}$$

Multiplying each side by the Kronecker delta δ_{nk} yields [Thurber, 1983]

$$\frac{\partial T_{ij}}{\partial \alpha_n} = -\int_{P_{ij}} \frac{1}{v(\underline{r};\alpha_1,\ldots,\alpha_m)^2} \; w_n(\underline{r}) \; ds \tag{2.38}$$

Equation (2.38) is a very useful expression that describes the travel time partial derivative with respect to an individual velocity parameter perturbation.

For a parameterized velocity model, the matrix equation (2.25) for a simultaneous inversion becomes

$$\underline{b} = \underline{\underline{H}}\,\underline{h} + \underline{\underline{M}}\underline{\Delta m} \tag{2.39}$$

where both vectors $\underline{h}$ and $\underline{\Delta m}$ are finite dimensional. Equation (2.39) is similar to (2.25) except that the inner product term in (2.25) is replaced by the parameterized analog; the vector of velocity model perturbations $\underline{\Delta m}$ contains m elements. The matrix M is contains the partial derivatives of travel time with respect to model parameters; these partial derivatives are calculated from (2.38).

Parameter separation, when applied to (2.39), yields

$$\underline{b}' = \underline{\underline{U}}_o^T \underline{b} = \underline{\underline{U}}_o^T \underline{\underline{M}} \underline{\Delta m} \tag{2.40}$$

In the next section a method is discussed for the inversion of equation (2.40).

Solution Method

In this section we discuss the solution method employed in the simultaneous inversion technique of Thurber [1981, 1983]. Following a brief review of the inverse methods applied to simultaneous inversion, general definitions are presented of the linear parameter estimation problem and the resolution, information density, and parameter covariance matrices [Wiggins, 1972; Jackson, 1972]. Both the generalized inverse [e.g., Aki and Richards, 1980] and the damped least squares (DLS) operator are defined, and it is shown why the DLS operator is superior for under-determined problems. Specific forms of the resolution, information density, and parameter covariance matrices are given for the DLS operator, and the effects of damping on these matrices are discussed.

Seismic tomography is a rapidly evolving method. Coincident with the development of different velocity model representations -- parameterized, functional, or statistical descriptions -- has been the application to seismic tomography of many geophysical inverse techniques. The variety of inverse methods is described, for example, by Backus and Gilbert [1967, 1968, 1970], Franklin [1970], Wiggins [1972], Jackson [1972, 1979], Parker [1975], Sabatier [1977], and more recently Tarantola and Valette [1982]. Importantly, the full power of these methods has not been used in tomographic applications that incorporate real data. Nearly all parameterized approaches to seismic tomography [e.g., Aki and Lee, 1976; Crosson, 1976a, b; Thurber, 1981, 1983; Benz and Smith, 1984] have implemented the Levenburg-Marquardt damped-least squares procedure [Wiggins, 1972; Jackson, 1972, 1979]. In the case of functional model representations, the Backus-Gilbert formalism has been adapted to seismic tomography by Chou and Booker [1979] but to date has not been utilized in a simultaneous inversion of real data for three-dimensional

structure. More recently, the stochastic inverse, as developed by Franklin [1970], discussed by Jordan and Franklin [1971] and Jackson [1979], and generalized to include nonlinear problems by Tarantola and Vallete [1982], was applied to seismic tomography by Tarantola and Nercessian [1984] and Nercessian et al. [1984]. However, the generalized nonlinear stochastic approach of Tarantola and Nercessian [1984] has also not been applied to simultaneous inversions. This brief review shows that available algorithms for simultaneous inversion universally use an iterative Levenburg-Marquardt damped least squares method to optimize parameters of the linear, seismic tomography perturbation equations. Doubtless, future improvements of the simultaneous inversion method will include 'second generation' solution techniques that utilize the full power of geophysical inverse theory.

Consider a linear matrix equation similar to (2.40), but written in the following form:

$$\underline{y} = \underline{\underline{A}}\underline{x} + \underline{e} \tag{2.41}$$

where $\underline{y}$ is a vector of known n data, $\underline{x}$ is a vector of m unknown parameters, A is an n x m matrix, and $\underline{e}$ is a vector that describes n error contributions. The errors in $\underline{e}$ are presumed to have zero mean and covariances known *a priori*. In the event of a non-isotropic covariance matrix it is assumed that a rotation of the data space coordinate axes has been performed to achieve statistically independent random errors [e.g., Wiggins, 1972; Jackson, 1972]. This rotation is always possible if the *a priori* covariance matrix is positive definite. For the body wave tomography problem $\underline{y}$ naturally becomes a vector of annulled travel time residuals, $\underline{x}$ is a vector of model perturbations and A is the matrix of medium partial derivatives. The error vector $\underline{e}$ is a linear sum of random errors (e.g., timing errors) and, possibly, non-random errors; a

source of non-random error is discussed below. We impose the following restrictions on (2.41): (1) the number of data n is always greater than the number of parameters m, causing (2.41) to be overconstrained, and (2) the number of parameters m is chosen to be greater than the rank of A, or the number of linearly independent data, implying that (2.41) is underdetermined. In the case of seismic tomography it is always possible to choose an adequate number of velocity parameters in order to render (2.41) underdetermined. Solutions of overconstrained-underdetermined, parameterized linear systems have been well studied [e.g., Franklin, 1970; Wiggins, 1972; Jackson, 1972, 1979].

We seek solutions to (2.41) in the following form [Wiggins, 1972; Jackson, 1972, 1979]

$$\underline{x}^* = \underline{\underline{H}}\,\underline{y} \tag{2.42}$$

where $\underline{x}^*$ is the vector of estimated parameters and H is a m x n linear matrix operator. Prior to stating the form of H, we can define three additional matrix operators that are useful as measures of the quality of a solution. Substituting (2.41) into (2.42) yields

$$\underline{x}^* = \underline{\underline{H}}\underline{\underline{A}}\,\underline{x} + \underline{\underline{H}}\,\underline{e} \tag{2.43}$$

The solution vector $\underline{x}^*$ expressed in this form is a linear combination, or filter, of the true vector $\underline{x}$ plus a component summarizing the contributions of error, including both random and non-random error [Jackson, 1979]. Wiggins [1972] and Jackson [1972, 1979] define the resolution matrix of parameters as

$$\underline{\underline{R}} = \underline{\underline{H}}\underline{\underline{A}} \tag{2.44}$$

The resolution matrix can be interpreted as the filter through which we observe the true model $\underline{x}$ in the absence of significant error contributions. For well posed problems R=I, where I is the identity matrix, and all

parameters are perfectly resolved by the data. When R does not equal I the estimated parameters are expressed as linear combinations, or averages, of the true parameters. For the seismic tomography problem, if R is compact as defined by Wiggins [1972], it yields an estimate of the volume averaged value of velocity for a given location within the model. The importance of volume-averaged estimates is discussed in a later section.

The estimated parameter vector $\underline{x}^*$ can be used to predict the data as follows

$$\underline{y}^* = \underline{\underline{A}}\underline{x}^* = \underline{\underline{A}}(\underline{\underline{H}}\underline{\underline{A}}\underline{x} + \underline{\underline{H}}\underline{e}) = \underline{\underline{A}}\underline{\underline{H}}\underline{y} \qquad (2.45)$$

$$\underline{y}^* = \underline{\underline{S}}\underline{y}$$

where S=AH is the information distribution matrix [Wiggins, 1972]. The predicted data vector $\underline{y}^*$ is related to the observational data $\underline{y}$ by the n x n linear operator S. The elements, or the weights, of S provide a measure of the linear independence of observed data. For example, if S=I all data are linearly independent and provide unique information.

The third useful matrix operator is an m x m matrix C that defines the covariance matrix of estimated model parameters. C is defined as

$$\begin{aligned} \underline{\underline{C}} &= E\{\underline{x}^*\underline{x}^{*T}\} = E\{\underline{\underline{H}}\underline{y}(\underline{\underline{H}}\underline{y})^T\} \\ &= \underline{\underline{H}}\, E\{\underline{y}\underline{y}^T\}\, \underline{\underline{H}}^T \end{aligned} \qquad (2.46)$$

where E{ } is the expectation operator. Since the observational errors are uncorrelated random variables with zero mean and unit variance

$$\underline{\underline{C}} = \underline{\underline{H}}\underline{\underline{H}}^T \qquad (2.47)$$

Wiggins [1972] and Jackson [1972] discuss the utility of the resolution, information density, and covariance operators for optimizing solutions of (2.41). An optimal inverse solution maximizes the resolution, and minimizes

the a posteriori covariance of model parameters. Jackson [1979] has demonstrated that the simultaneous optimization of resolution and covariance is conceptually similar to the solution methods proposed by Backus and Gilbert [1968, 1970]. Irrespective of the solution method, underdetermined problems are fundamentally characterized by the well-known resolution-covariance trade-off [e.g., Jackson, 1979]. An acceptable form of the inverse operator must simultaneously optimize some combined measure of resolution and covariance.

One possible form of the inverse operator H is the Moore-Penrose or generalized inverse [e.g., Wiggins, 1972; Jackson, 1972; Aki and Richards, 1980]. As the following discussion shows, for ill-conditioned inverse problems the generalized inverse does not minimize model covariance; this behavior is in contrast to the method of damped least squares. The generalized inverse is found by applying the fundamental matrix decomposition theorem of Lanczos [1961] to the matrix A, to obtain

$$\underline{\underline{A}} = \underline{\underline{U}}_p \underline{\underline{\Lambda}}_p \underline{\underline{V}}_p^T \qquad (2.48)$$

where U_p is a n x p matrix of data space eigenvectors, V_p is a m x p matrix of parameter space eigenvectors, and Λ_p is a p x p diagonal matrix of non-zero eigenvalues. For our applications $p < m < n$, i.e., the inverse problem is underdetermined and overconstrained. The non-zero eigenvalues of Λ_p couple data space and parameter space. The inverse of A is

$$\underline{\underline{H}}^+ = \underline{\underline{V}}_p \underline{\underline{\Lambda}}_p^{-1} \underline{\underline{U}}_p^T \qquad (2.50)$$

where H^+ denotes the generalized inverse. (The generalized inverse is equivalent to a least-squares operator when p=m and p<n; a thorough discussion of the properties of the generalized inverse is presented by Aki and Richards [1980].) For the generalized inverse, the explicit form of the covariance

matrix of model parameters is written as

$$\underline{\underline{C}} = \underline{\underline{H}}^{+}\underline{\underline{H}}^{+T} = \underline{\underline{V}}_p\underline{\underline{\Lambda}}_p^{-1}\underline{\underline{U}}_p^T\underline{\underline{U}}_p\underline{\underline{\Lambda}}_p^{-1}\underline{\underline{V}}_p^T$$

$$= \underline{\underline{V}}_p\underline{\underline{\Lambda}}_p^{-2}\underline{\underline{V}}_p^T \qquad (2.51)$$

Equation (2.51) states that parameter covariance is inversely proportional to the square of the eigenvalues. Very small or near-zero eigenvalues are common to ill-conditioned inverse problems for at least two reasons: numerical inaccuracy or, more fundamentally, inadequate data constraints. Clearly, the generalized inverse does not optimize the a posteriori covariance of model parameters that are associated with near-zero eigenvalues. Examination of (2.50) and (2.42) further suggests that small eigenvalues lead to large model perturbations. The generalized inverse is thus characterized, in the case of ill-conditioned problems, as an operator which encourages large perturbations of poorly constrained model parameters.

A second form of the inverse operator H, and the one utilized by Thurber [1983], is the DLS operator. The specific form of the DLS operator for linear problems can be derived by different methods. The most common derivation is motivated by the indequacies of the generalized inverse, in particular, large model perturbations associated with small eigenvalues. Recall that the generalized inverse is solely a least-squares operator, implying that only observational residuals are minimized. The DLS inverse, however, is the result of minimizing a weighted sum of observational residuals and Euclidean model length:

$$\varepsilon^2 = (\underline{y}-\underline{\underline{A}}\underline{x}^*)^T(\underline{y}-\underline{\underline{A}}\underline{x}^*) + \lambda^2(\underline{x}^*)^T(x^*) \qquad (2.52)$$

where λ is an arbitrary weighting factor. Given a non-zero value of λ, an inverse operator that minimizes ε^2 will damp the contributions of small

eigenvalues, and their associated eigenvectors, to the solution vector $\underline{x}^*$. If this were not the case, the second term of (2.52) describing Euclidean model length would grow unacceptably large. The DLS operator fits the data by preferentially adjusting well-constrained model parameters (parameters associated with large eigenvalues) while damping or reducing the contributions of poorly constrained parameters [Wiggins, 1972: Jackson, 1972].

For a non-linear inversion that requires many linearized iterations the advantage of the DLS method over the generalized inverse may be lessened, since the cumulative effect of iteration may be a substantial perturbation to the initial model that is only weakly constrained by the data. In such a case, the a posteriori covariance, which is calculated for the final iteration only and not from the cumulative model perturbation, yields an underestimate of the uncertainty in the poorly constrained model parameters. Inspection of the solutions at each iteration and a rapid convergence to the final solution can reduce the likelihood of undesirably large perturbations to poorly constrained parameters with the DLS method.

A second approach to the derivation of the DLS inverse is to examine an end-member of the stochastic inverse [Franklin, 1970] when the a priori model parameter covariance matrix is isotropic and the diagonal elements are equal [e.g., Wiggins, 1972; Jackson, 1972, 1979]. (An isotropic covariance matrix implies independent uncorrelated statistics of model parameters.) In this case, the stochastic inverse is also obtained as an operator which minimizes ε^2. The value of λ for a stochastic inverse is not strictly arbitrary since the stochastic inverse assumes that some statistical knowledge of the unknown function is known a priori. This statistical knowledge could be in the form of physical relationships which specify the covariance of model parameters. However, in the case of non-linear problems that require

iteration, the use of the stochastic inverse, as defined by Franklin [1970], is incorrect [Tarantola and Vallete, 1982]. Tarantola and Vallete [1982] have recently generalized the stochastic inverse, defined originally for linear problems, to include non-linear problems. However, their method has not yet been applied to simultaneous inversion. The use of DLS in this thesis is motivated by a need to limit the size of model pertrubations; no statistical significance is implied by the value of λ.

The DLS inverse operator that minimizes ε^2, for a specific value of λ, is

$$\underline{\underline{H}} = (\underline{\underline{A}}^T\underline{\underline{A}} + \lambda^2\underline{\underline{I}})^{-1}\underline{\underline{A}}^T \tag{2.53}$$

or, upon substition of the fundamental decomposition of A,

$$\underline{\underline{H}} = \underline{\underline{V}}_p\{(\underline{\underline{\Lambda}}_p^2 + \lambda^2\underline{\underline{I}})^{-1}\underline{\underline{\Lambda}}_p\}\underline{\underline{U}}_p^T \tag{2.54}$$

The term in brackets is a p x p diagonal matrix. Equation (2.54) shows that the underlying principle of the DLS inverse operator is the modification of the diagonal matrix of eigenvalues by the addition of the term λ^2 to each squared eigenvalue. Inspection of the matrix within brackets shows that if λ^2 is sufficiently large, the adjustments associated with small eigenvalues are minimized. On the other hand, for well constrained sectors of parameter space associated with large eigenvalues, the term λ^2 should assert little influence. The damping term λ^2 alters the spectrum of eigenvalues, decreasing the contributions of poorly constrained eigenvectors; this property is similar to the eigenvalue-cutoff scheme of Wiggins [1972], but, it does not require a computationally cumbersome singular-value decomposition. Importantly, a non-zero value of λ^2 decreases the potential number of degrees of freedom for the inverse operator H, since fewer eigenvalues are effectively non-zero [Wiggins, 1972; Aki and Richards, 1980].

Instructive forms of the resolution, covariance, and information density matrices are obtained for the DLS operator by using the fundamental decomposition theorem and the orthogonal properties of data space and parameter space eigenvectors. The three matrix forms are:

$$\underline{\underline{R}} = \underline{\underline{H}}\underline{\underline{A}} = \underline{\underline{V}}_p\{(\underline{\underline{\Lambda}}_p^2 + \lambda^2\underline{\underline{I}})^{-1}\underline{\underline{\Lambda}}_p^2\}\underline{\underline{V}}_p^T \tag{2.55}$$

$$\underline{\underline{C}} = \underline{\underline{H}}\underline{\underline{H}}^T = \underline{\underline{V}}_p\{(\underline{\underline{\Lambda}}_p^2 + \lambda^2\underline{\underline{I}})^{-1}\underline{\underline{\Lambda}}_p\}^2\underline{\underline{V}}_p^T \tag{2.56}$$

$$\underline{\underline{S}} = \underline{\underline{A}}\underline{\underline{H}} = \underline{\underline{U}}_p\{(\underline{\underline{\Lambda}}_p^2 + \lambda^2\underline{\underline{I}})^{-1}\underline{\underline{\Lambda}}_p^2\}\underline{\underline{U}}_p^T \tag{2.57}$$

Properties of the above three matrices, including guidelines for their interpretation, have been discussed by Wiggins [1972] and Jackson [1972, 1979].

A qualitative examination of the model covariance and resolution matrices demonstrates how the value of λ controls the well-known trade-off between error and resolution. Resolution and covariance matrices, equations (2.55) and (2.56), respectively, are similar to the extent that the last two terms of each equation represent a rescaling of parameter space eigenvectors. The amount of rescaling is a function of the diagonal matrix within brackets, and for a given matrix A, depends on the value of λ. The effect of λ on the diagonal matrices is easily understood by examining typical diagonal elements:

$$r_i = \frac{\Lambda_i^2}{\Lambda_i^2+\lambda^2} \tag{2.58a}$$

$$c_i = \frac{\Lambda_i^2}{(\Lambda_i^2+\lambda^2)^2} \tag{2.58b}$$

where r_i and c_i are the non-zero elements of the diagonal matrices within the brackets of (2.55) and (2.56), respectively. The magnitudes of r_i and c_i control the contribution of parameter space eigenvectors to the resolution and covariance matrices, respectively. Consider the case of a small eigenvalue, such that $\Lambda_i \ll \lambda$. In this case, both r_i and c_i

approach zero and, in turn, diminish the contributions of associated parameter space eigenvectors to the resolution and covariance matrices. Removal of small eigenvalue contributions from the covariance matrix is clearly advantageous since an upper limit on model error is imposed [Wiggins, 1972]. However, this diminishes the number of degrees of freedom of the original data. The number of degrees of freedom (DOF) is given by the trace of the resolution matrix [Wiggins, 1972; Aki and Richards, 1980]:

$$DOF = tr(R) = \sum_{i}^{p} \frac{\Lambda_i^2}{\Lambda_i^2+\lambda^2} \qquad (2.59)$$

Non-zero values of λ decrease the potential number of degrees of freedom. A reduction in the number of degrees of freedom of the data, of course, reduces the number of averages of model parameters that are independently resolvable [Wiggins, 1972; Jackson, 1972]. A non-zero value of λ simultaneously improves model variance and degrades resolution.

Choosing a value of λ for non-linear DLS is an arbitrary decision. In making a decision one attempts, by trial and error, to choose a value of λ that stabilizes a solution without severely diminishing resolution. Wiggins [1972] discusses for a linear problem some guidelines for choosing the correct number of eigenvectors to include in an inversion. Although Wiggins recommends a sharp eigenvalue cutoff instead of eigenvalue damping to limit model variance, his guidelines are still useful for damped linear least squares. Quantitative approaches to choosing λ, however, are of limited usefulness in non-linear inverse problems. Throughout this thesis, λ will be chosen by trial and error to be the smallest value for which the errors in the model parameters, i.e., the diagonal elements of the covariance matrix, are significantly less than the largest velocity perturbations without a substantial sacrifice in spatial resolution.

Optimum Parameterization and Interpretation of Resolution

The velocity model parameterization of Thurber [1983] requires a subjective choice for the distribution of nodal locations. The factors influencing such a choice and guidelines for an optimum parameterization are discussed here. For a given data set the resolution of individual model parameters is affected by the spatial density of nodes. This dependence of parameter resolution on nodal spacing suggests that the value of resolution for an individual parameter may not be the best indicator of model resolution. We make use of a spread function [Backus and Gilbert, 1970; Menke, 1984] to provide a quantitative measure of the complete resolution matrix. In Chapter 5, the spread function is shown to be an improved measure of model resolution compared with the resolution values for individual parameters.

For tomographic applications, solutions of (2.41) are dependent on the dimensions of the parameter vector $\underline{x}$. This dependence arises because of the difficulties of representing a continuous velocity field by a few discrete parameters. Underparameterization of a continuous field can give rise to non-random basis function error [Jackson; 1979], loss of information due to poor model fidelity or poor rendering capabilities, and, as described below, poor utilization of the data. Jackson [1979] has rigorously shown that inadequate parameterization of a continuous function contaminates the error vector $\underline{e}$ in (2.41) with non-random or biasing contributions; the effects of non-random errors on a non-linear problem are unpredictable. The amount of non-random error introduced by parameterization is determined by the inability of the basis functions, or parameters, to describe the true fluctuations of the unknown function [Jackson, 1979]. For tomographic applications, this

suggests that increasing the spatial density of nodes will give rise to decreased effects of non-random error.

In practice, an upper limit on the spatial density of nodes may be imposed by the distribution of seismic ray paths. For example, over-densification of velocity model parameters without specifying a priori constraints (e.g., model smoothness [Parker, 1975] or model autocovariance constraints [Franklin, 1970]) will result in a large number of velocity parameters that are not influenced by observations. Moreover, unsampled or undersampled velocity nodes are unperturbed in a DLS inversion since model parameters are assumed to be independent and uncorrelated; this follows since a DLS inversion is simply a stochastic inversion for an isotropic model covariance matrix [Franklin, 1970; Jackson, 1979]. Thus, a combination of excessively dense model parameters with a DLS inversion will produce solutions that are characterized by artificial patches of unperturbed velocity. In the case of a DLS inversion, an optimum middle ground between too few or too many parameters can be found through trial and error as described below.

Given a distribution of seismic rays throughout a study volume, it is a straightfoward task to add or subtract nodal locations and monitor the progressive change in velocity parameter coverage. The optimum nodal distribution maximizes the parameter density and minimizes undersampled velocity nodes. A useful measure for evaluating velocity parameter coverage is the distribution of the derivative weight sum (DWS) [C.H. Thurber, personal communication, 1986]. The DWS provides a relative measure of the density of seismic rays near a given velocity node. The DWS of the n^{th} velocity parameter α_n is defined as

$$DWS(\alpha_n) = \sum_i \sum_j \left\{ \int_{P_{ij}} w_n(\underline{r})\, ds \right\} \tag{2.60}$$

where i and j are the event and station indices, and the term in brackets is defined as before (see (2.38)). The value of the DWS depends on the size of the incremental arc length ds utilized in the numerical evaluation of (2.60); smaller step lengths yield larger DWS values. Thus we are interested only in the relative size of the DWS from one parameter to another. In general, an acceptable distribution of nodal locations should yield values of DWS that vary slowly between closely spaced nodes; examples of DWS for an optimum nodal distribution are found in Chapter 5.

The above discussion suggests guidelines for choosing a nodal distribution. The attention here is on the dependence of the resolution of model parameters on the spatial density of nodal locations. A fundamental property of a finite data set is its limited number, say p, of linearly independent observations; sometimes p is referred to as the potential number of degrees of freedom [e.g., Wiggins, 1972]. In the absence of a priori constraints [e.g., Franklin, 1970; Jackson, 1979], the value of p is fixed for a given data set. Moreover, when the unknown model is a continuous function, such as velocity, a DLS inversion is limited to estimating a maximum of p linear averages of the unknown continuous function [e.g., Wiggins, 1972; Jackson, 1972]. For a finite number of m parameters, where $m > p$, the trace of the m x m resolution matrix R provides an estimate of the potential number of degrees of freedom ((2.59), or Wiggins [1972]); the trace of R is simply the sum of the values of resolution for the m parameters. If the spatial density of model parameters is increased, m increases while p remains fixed. Since the trace of R is always less than or equal to p (see (2.59)), increasing the density of nodal locations effectively reduces the resolution of model parameters.

A reduction in the value of resolution for individual parameters, when due to an increase in the spatial density of nodes, can be a desirable result. For example, consider the case of approximating a inhomogeneous velocity field by a finite set of parameters that are uniquely resolved by a given data set, i.e., R=I. In this case, the resolution matrix R is m x m such that $m \leq p$ and $tr(R) = m \leq p$. In practice, it is highly improbable that m parameters can be chosen such that m=p. Thus, a fundamental consequence of uniquely resolving $m < p$ model parameters is poor utilization of the total information intrinsic to the data set. In other words, high resolution of individual model parameters is obtained at the expense of not exploiting the potential number of degrees of freedom. Increasing the spatial density of nodes may decrease the resolution of individual model parameters but assures that the full information content of the data is utilized.

The apparent problem of low values of resolution along the principal diagonal of R is, in part, misleading. A principal characteristic of underdetermined inverse problems is a resolution matrix with non-zero off-diagonal elements [Wiggins, 1972]. Simply examining the principal diagonal of R is insufficient for underdetermined inversions. Conceptually, the resolution matrix is a linear filter that prescribes the manner in which true model parameters are to be linearly averaged in order to obtain the estimated values of model parameters (see (2.43) and (2.44)). Each row of the resolution matrix is a 'resolving kernel' [Backus and Gilbert, 1970] or 'averaging vector' [Menke, 1984] for a single model parameter. For a given parameter, its linear dependence on the values of all other model parameters is defined by the averaging vector. Since model parameters occupy a volume in the case of seismic tomography, the linear averaging is also evaluated over a volume. Thus, for seismic tomography, we can consider the estimates of model parameters to be volume averaged estimates.

The question of what is implied by 'good' resolution is easily answered when the estimates of model parameters are considered averages over a volume. Wiggins [1972] considered an ideal resolution matrix to be 'compact' if the averaging vectors were non-zero only near the principal diagonal. The notion of a compact matrix can be given physical significance in the case of seismic tomography. There is a natural ordering of the elements of an averaging vector, and this ordering is simply defined by the spatial location of nodes within the study volume. One definition of compact is that for a given parameter, the elements of its averaging vector are zero except for elements that correspond to nodes located near the parameter of interest. Such a definition can be stated quantitatively by defining a spread function [Backus and Gilbert, 1967, 1968; Menke, 1984]. For the present problem, we define the spread function for a single averaging vector, following Menke [1984], as the scalar function

$$S(\underline{r}_p) = (\|\underline{r}_p\|)^{-1} \sum_{q=1}^{m} \Omega(p,q)\, R_{pq}^2 \qquad (2.61)$$

where $\underline{r}_p$ is the averaging vector of the p^{th} parameter, R_{pq} is an element of the resolution matrix, $\Omega(p,q)$ is a weighting function defined as the distance between the nodal locations of the p^{th} and q^{th} parameter, and m is the number of parameters. For a compact averaging vector, the spread function should be close to zero.

A spread function provides a simple means of quantifying m-dimensional averaging vectors with a single number. In practice, however, an acceptable upper limit to $S(\underline{r}_p)$ must be chosen subjectively. In Chapter 5, it is shown for the Icelandic data set that an examination of individual averaging vectors for a range of values of $S(\underline{r}_p)$ provides constraints on an acceptable upper limit. Once an upper limit is established, it is a straightforward task to

evaluate regions of the model where $S(\underline{r}_p)$ is less than this limit and thus define the volumes that are well-resolved (see Chapter 5).

The above discussion of model parameterization and resolution, particularly the use of a spread function to assess model resolution, differs conceptually from previous studies [e.g, Aki and Lee, 1976; Thurber, 1983; Benz and Smith, 1984]. For example, Aki and Lee [1976] suggested that a tomographic image was well-resolved only if the majority of the diagonal elements of the resolution matrix were close to unity; most studies since Aki and Lee [1976] have followed this criterion. However, as discussed above, such a scenario implies underutilization of the data. In contrast with the underparameterized approach of Aki and Lee [1976], a model parameterization that follows the guidelines presented in this section will result in diagonal elements of the resolution matrix that are significantly less than unity. We argue that the tomographic image is well-resolved despite these smaller values and, further, that the information content of the data is put to full use with this approach. Moreover, a resolution matrix with non-zero off-diagonal elements can be given a physical interpretation that expresses quantitatively the volume over which velocity is averaged. These concepts are developed further in Chapter 5.

A SYNTHETIC EXPERIMENT IN SEISMIC TOMOGRAPHY

In order to demonstrate that the tomographic method discussed in the previous sections is capable of resolving the three dimensional variation of velocity on a scale appropriate to a spreading ridge axis, we present in this section the results of several synthetic tomography experiments on a possible structure along the East Pacific Rise. Scientific understanding of the dynamics of spreading centers, including such processes as the formation of

oceanic crust and its thermal and lithologic evolution, the generation and maintenance of hydrothermal systems, and the emplacement and evolution of magma chambers and associated ridge-axis morphology all await the quantitative determination of the size, shape and location of axial magma chambers. The synthetic experiments presented here represent an initial step toward the undertaking of a marine experiment specifically designed to image the three-dimensional seismic velocity structure of the accretion zone.

Two crucial aspects of a East Pacific Rise tomographic experiment are the network design and the geometry of sources. Natural seismicity associated with the East Pacific Rise is infrequent and confined to shallow depth [Riedesel et al., 1982]. The synthetic experiments are thus designed around the exclusive use of artificial sources. In this section we show that an East Pacific Rise magma chamber can cause significant travel time variations relative to a laterally homogeneous crustal model. Specific structures provide a basis for determining the source-receiver paths that are most useful for imaging tomographically a mid-crustal magma chamber. From the results of forward modeling, an experiment design is proposed. Tomographic inversions of synthetic data, generated for the suggested experimental design and velocity model, clearly show that three-dimensional structure within spreading centers can be imaged with current marine seismological methods. This chapter ends with a discussion of some of the scientific questions which may be addressed with a marine seismic tomography study of the East Pacific Rise.

Postulated Magma Chamber Structure and its Effect on Travel Times and Ray Paths

The tomographic method is best suited for imaging distinct bodies of anomalously high- or low-velocity that cause significant and systematic anomalies in the observed travel time. We begin with a model of seismic

velocity near an axial magma chamber; the model is hypothetical but it is abstracted from the interpretation of a number of seismic experiments undertaken along the East Pacific Rise. The velocity model is combined with three-dimensional ray tracing methods to estimate the effects of an axial magma chamber on the travel times and ray paths of P waves from artificial sources in the water column.

Many seismic refraction experiments using both sonobuoy and ocean bottom receivers have been carried out over the crest of the East Pacific Rise during the past ten years. Several experiments have been interpreted to indicate the presence of a shallow crustal low-velocity zone that has been presumed to correspond to a magma chamber. Orcutt et al. [1976] used synthetic seismogram modelling to infer the presence of a shallow crustal low-velocity zone 2 km beneath the rise axis seafloor at 9°N. Similar findings have since been reported by McClain and Lewis [1980] at 23°N, Reid et al. [1977] at 21°N, McClain et al. [1985] at 13°N, Lewis and Garmany [1982] at 12°N, and Rosendahl et al. [1976] at 9°N. Bratt and Solomon [1984] used observations of cross-axis shear wave propagation to argue against the presence of a substantial magma body beneath the East Pacific Rise axis at 12°N. Bibee [1979] inferred an axial low-velocity zone at 3°S, but the top of the zone is subcrustal rather than 1-2 km beneath the sea floor.

The axial velocity structure determined from travel time inversion and synthetic seismogram modelling by Orcutt et al. [1976] and Reid et al. [1977] and that determined by two-dimensional ray tracing by McClain et al. [1985] are shown in Figure 1. All three models show well-developed low velocity zones. These one-dimensional representations of the structure are suggestive of the presence of zones of melt or partial melt, but they do not provide information on the extent of these zones either along or perpendicular to the

rise axis. Figure 2 shows three cross-sections of the rise axis structure inferred from two-dimensional ray tracing [Lewis and Garmany, 1982; McClain et al. 1985] or from closely spaced axis-parallel refraction lines [Rosendahl et al., 1976]. While pronounced differences are apparent in the shape of the inferred axial magma body, it is impossible to assess the significance of these differences for at least two reasons. First, no formal determination of uncertainty is possible for models of this type. Second, because these are simply slices through a three-dimensional body, the differences may be a consequence only of the somewhat different along-axis location of the cross-sections relative to transforms, axial highs, overlapping spreading centers, or episodic spreading processes [Macdonald et al., 1984]. A seismic tomography experiment will overcome both these shortcomings because the derived structure is genuinely three-dimensional in nature and the results will be interpreted using a formal inversion method in which the resolution of the solution is defined quantitatively.

An important recent development is the application of the common-depth-point multichannel seismic reflection method to studies of oceanic crustal structure [e.g., Talwani et al., 1982]. The denser coverage provided by this continuous mapping technique and the resulting spatial resolution has revolutionized our understanding of the extent and distribution of intracrustal reflectors, including the prominent reflector thought to mark the top of the axial magma chamber along the East Pacific Rise. On the axis of the East Pacific Rise near 9°N, a clear reflector is observed at 0.6 to 0.8s beneath the seafloor having a lateral extent (across axis) of 2-7 km [Herron et al., 1978, 1980; Stoffa et al., 1980; Hale et al., 1982]. One of the most thorough analyses of one of these crossings of the axial region is that of Hale et al. [1982], who document an asymmetry in the reflection relative to the rise axis.

Most recently Detrick et al. [1987] carried out an extensive single-ship and two-ship multichannel survey along the East Pacific Rise between 9° and 13°N. The most fundamental result from their study is the observation that a continuous axial reflector is present over more than 60% of the imaged length of the rise axis. The reflector is absent primarily where offsets in the rise associated with overlapping spreading centers and transforms occur.

On the basis of the refraction and reflection results discussed above, a hypothetical three-dimensional model of P-wave velocity for an East Pacific Rise axial magma chamber may be constructed. Figures 3a and b show two cross sections, one perpendicular and one parallel to the rise axis, of one such model which is utilized for the synthetic tomography experiments described below. The low-velocity volume is approximately ellipsoidal, with an along-axis half length of 3 km, a half thickness of about 1 km, and a half width of about 2 km. The velocity versus depth through the center of the low-velocity body is similar to the models of Orcutt et al. [1976] and Hale et al. [1982] derived from seismic refraction and reflection studies near 9°N on the East Pacific Rise (Figure 1). The model in Figure 3 has a velocity anomaly contrast and vertical extent which are significantly smaller than in the model of McClain et al. [1985] for the East Pacific Rise near 13°N (Figure 2). The top of the low velocity body in Figure 3b is not continuous for more than 6 km along-axis, in contrast with the findings of Detrick et al. [1987]. Thus, the model in Figure 3 probably underestimates the maximum dimensions and volume of possible low-velocity magma chambers. Synthetic studies of such a model should yield conservative tests of the resolving power of the seismic tomography method.

The objective of the first synthetic experiment was to determine the general effects of a mid-crustal low-velocity zone on the travel times and ray

paths of P waves using a forward modeling approach. For simplicity, a two-dimensional model of a mid-crustal low-velocity zone was assumed for these calculations: the model is uniform along axis; transverse to the axis the structure is given by Figure 3a. Travel times of P waves calculated for this heterogeneous structure and a laterally homogeneous model were compared for numerous source-receiver configurations; the laterally homogeneous model is given by the off-axis structure in Figure 3a and the sources and receivers are taken to be on a flat seafloor. For both structures, travel times and ray paths were calculated using a three-dimensional ray tracing routine [Lee and Stewart, 1981]. Figure 4 shows an example of the difference between travel times calculated for the heterogeneous and homogeneous models. In this figure, the mid-crustal low-velocity zone is parallel to the y-axis and centered on x=10 km, the receiver location is at x=5km, y=0, and the travel time differences are plotted at the appropriate source locations within the plane of the figure. For a source located at x=5 and y=10 km, for instance, the travel times for the heterogeneous model are delayed by about 0.3 s compared with the homogeneous model. The travel time residual map in Figure 4 can be divided into three regions of distinct anomalies that lie approximately parallel to the rise axis: regions where $x < 12$ km are characterized by small travel time residuals, for $12 < x < 18$ km the travel time residual is greater than 0.2 s, and for $x > 18$ km the travel time residual averages 0.1 s. While these three broad regions are well defined, much of the detail of the travel-time residual map is suspect, because of errors introduced by mixing first and secondary arrivals. Such errors are difficult to remove with a forward modelling approach; in Figure 4 they are likely to be most pronounced for $12 < x < 20$ km. From the contour map of Figure 4 it can be inferred that a tomographic experiment must employ source-receiver separations in excess of

5-10 km in order to be sensitive to mid-crustal low-velocity zones.

A more substantive inference regarding experiment design can be made if the ray paths calculated for the heterogeneous model are examined. Figure 5 depicts such ray paths superimposed on the velocity contours of Figure 3a; in this figure the source is at x=5 km. All rays shown in this figure traveled in a vertical plane perpendicular to the rise axis. Figure 5 clearly shows how the mid-crustal low-velocity zone distorts the ray paths of the P waves, and it also suggests that a 'shadow zone' may exist 10-12 km off-axis (x=20-22 km) for this source location. At small source-receiver separations ($x < 12$-14 km, Figure 5) the ray paths of P waves are unaffected by the low-velocity zone since their turning point is within the shallow crust. For $12 < x < 20$ km, the first arriving ray paths have turning points about 3-4 km deep; these paths are noticeably distorted by the low-velocity zone. Also, these ray paths traverse the low-velocity zone on both their downgoing and upgoing segments, thus accumulating a sizeable travel time anomaly (Figure 4). At larger ranges ($x > 22$ km), the first arriving P waves pass through the low-velocity zone only once, thus incurring a significant but more modest travel time delay (Figure 4). Ray paths at these larger ranges have a simpler, more nearly circular geometry than those that exit the seafloor at about $x = 14$ km.

Experimental Design and Results of Synthetic Inversions

Given the above results, a synthetic marine tomographic experiment was designed, with two following constraints: (1) a seismic network consisting of 15 ocean-bottom instruments was available for deployment, and (2) roughly 300-400 shots were available for insonifying the study area. The seismic network (Figure 6) has two principal components: (1) stations within 0-10 km

of the rise axis provide control of upper crustal velocities beneath the rise axis, and (2) stations greater than 20 km from the axis record data to resolve deep crustal structure (Figure 5). By avoiding station locations that are between approximately 10 and 20 km of the axis or that connect ray paths from shots which travel sub-parallel to the rise axis at depths greater than 2-3 km beneath the sea-floor, ray paths with complex geometries (Figure 5) and possible shadow zones are avoided.

Synthetic travel times for the model in Figure 3 and the station-shot configuration in Figure 6 were calculated by an approximate ray tracing method [Thurber, 1983] and subsequently inverted to test the resolving power of the seismic tomography method. Figure 7 shows the results of one inversion for noise-free travel times and a starting model which was laterally homogeneous and given by the off-axis structure shown in Figure 3a. Comparison of Figures 7 and 3 demonstrates that seismic imaging is capable of defining the location and dimensions of anomalous velocity bodies. Also, the velocity contrast is recovered to a large degree, except for the fine detail of velocity structure within the center of the low velocity zone. These results indicate that the inverse method being used can resolve three-dimensional structure.

Of course, a rigorous test of the imaging method should incorporate the effects of timing errors intrinsic to real observations. This was investigated by adding random, Gaussian-distributed deviations having zero mean and a standard deviation of 0.05s, to the synthetic travel times (Figure 8c) and repeating the inversion. Figure 8 shows the results of imaging the low velocity body in Figure 3 with travel time data that incorporate realistic timing errors [Bratt and Purdy, 1984]. Again the location and dimensions of the low velocity body were successfully recovered. Note that the starting model was a simple laterally homogeneous structure. This may explain the

partial degradation of the inversion solution compared with the assumed model (Figure 3). A laterally heterogeneous initial model that incorporates a priori information, such as the depth to the top of a low-velocity zone, may improve the inversion results. This point is deserving of further study.

These simple synthetic inversions clearly demonstrate that the seismic tomography technique can resolve the postulated structure of an East Pacific Rise magma chamber. Further synthetic studies are required, however, both to test both the potential of the method to discriminate among competing models for the size and shape of the axial magma body (e.g., Figure 2) and to determine the preferred array design for imaging crustal magma chambers. Such analysis should include variations of the shot-receiver geometry in tandem with evaluation of the information density matrix [Wiggins, 1972], possible use of a priori statistical constraints in the inverse problem [Franklin, 1970; Tarantola and Valette, 1982], and development of a methodology to account for sea floor topography and its effects upon travel times.

Specific Objectives of a Tomography Experiment

The determination of the three-dimensional velocity structure of a substantial segment of the East Pacific Rise will allow us to address a number of specific and fundamental problems concerned with magma chamber processes:

a) First of all, what is the size of the magma chamber? What is the total volume of melt? This is crucial to understanding the thermal evolution of the crust and to learning about hydrothermal processes. All models of water circulation in young crust are critically dependent upon a knowledge of the thermal driving force [e.g., Lister, 1974; Strens and Cann, 1982, 1986].

b) To what depth do magma bodies extend, i.e., how are both layer 3 and the Moho formed? Does a substantial body of melt exist to the base of the crustal column, as inferred by Pallister and Hopson [1981]? Or is the shallow axial reflector simply the top of a thin layer of melt only a few hundred meters thick [Dewey and Kidd, 1977; Sleep, 1978]?

c) What is the cross-section of the magma chamber? Is it simply a wide dike, an 'onion' shape, or a broad based triangle? This knowledge is essential to models of magma dynamics, the generation and maintenance of hydrothermal systems, as well as mechanisms of dike injection.

d) Is there internal structure in the magma chamber? Is it a uniform body of melt, do prominent zonations exist, or is it a region of pervasive melt-filled cracks?

e) What is the along-axis geometry of the magma body? Does a discrete 'blob' exist beneath the center of each ridge segment that feeds magma through extensive along-axis fissures? Such a scenario has been suggested to explain the thin crust beneath fracture zones [e.g., Sinha and Louden, 1983; White et al., 1984] as well as along-axis ridge morphology [Francheteau and Ballard, 1983]. The axial reflector is apparently continuous right up to overlapping spreading centers and transforms [Detrick et al., 1987], but it is unlikely that the shape of the magma body remains unchanged in the vicinity of these thermal anomalies.

A seismic tomography experiment will provide well-constrained answers to these critical questions and advance our understanding of how oceanic crust is created, how magma chambers and hydrothermal systems operate, and how the principal features of mid-ocean ridge morphology are generated.

References

Aki, K., and W.H.K. Lee, 1976. Determination of three-dimensional velocity anomalies under a seismic array using first P arrival times from local earthquakes, 1, a homogeneous initial model, J. Geophys. Res., 81, 4381-4399.

Aki, K., and P. Richards, 1980. Quantitative Seismology: Theory and Methods. San Francisco: Freeman. 932 pp.

Backus, G. E., and J. F. Gilbert, 1967. Numerical application of a formalism for geophysical inverse problems, Geophys. J. R. Astron. Soc., 13, 247-276.

Backus, G. E., and F. Gilbert, 1968. The resolving power of gross earth data, Geophys. J. R. Astron. Soc., 16, 169-205.

Backus, G. E., and F. Gilbert, 1969. Constructing P-velocity models to fit restricted sets of travel time data, Bull. Seismol. Soc. Amer., 59, 1407-1414.

Backus, G. E., and F. Gilbert, 1970. Uniqueness in the inversion of inaccurate gross earth data, Philos. Trans. R. Soc. London, 266, 123-192.

Benz, H.M., and R.B. Smith, 1984. Simultaneous inversion for lateral velocity variations and hypocenters in the Yellowstone region using earthquake and refraction data. J. Geophys. Res., 89, 1208-1220.

Bibee, L.D., 1979. Crustal structure in areas of active crustal accretion, Ph.D. dissertation, 155 pp., U. of California, San Diego.

Bratt, S.R., and G.M. Purdy, 1984. Structure and variability of oceanic crust on the flanks of the east Pacific Rise between 11° and 13°N, J. Geophys. Res., 89, 6111-6125.

Bratt, S.R., and S.C. Solomon, 1984. Compressional and shear wave structure of the East Pacific Rise at 11°20'N: Constraints from three-component ocean-bottom seismometer data, J. Geophys. Res., 89, 6095-6110.

Chou, C.W., and J.R. Booker, 1979. A Backus-Gilbert approach to inversion of travel-time data for three-dimensional velocity structure, Geophys. J.R. Astron. Soc., 59, 325-344.

Crosson, R.D., 1976a. Crustal structure modeling of earthquake data, 1, simultaneous least squares estmation of hypocenter and velocity parameters, J. Geophys. Res., 81, 3036-3046.

Crosson, R.D., 1976b. Crustal structure modeling of earthquake data, 2, velocity structure of Puget Sound region, Washington, J. Geophys. Res., 81, 3047-3054.

Detrick, R.S., P. Buhl, J. Mutter, J. Orcutt, J. Madsen and T. Brocher, 1987. Multi-channel seismic imaging of a crustal magma chamber along the East Pacific Rise, Nature, 326, 35-41.

Dewey, J.F., and W.S.F. Kidd, 1977. Geometry of plate accretion, Geol. Soc. Am. Bull., 88, 960-968.

Francheteau, J., and R.D. Ballard, 1983. The East Pacific Rise near 21°N, 13°N and 20°S: inferences for along strike variability of axial processes at mid ocean ridges, Earth Planet. Sci. Lett., 64, 93-116.

Franklin, J.N., 1970. Well posed stochastic extension of ill posed linear problems, J. Math. Anal. Applic., 31, 682-716.

Hale, L.D., C.J. Morton and N.H. Sleep, 1982. Reinterpretation of seismic reflection data over the East Pacific Rise, J. Geophys. Res., 87, 7707-7718.

Herron, T.J., P.L. Stoffa and P. Buhl, 1980. Magma chamber and mantle reflection - East Pacific Rise, Geophys. Res. Lett., 75, 989-992.

Herron, T.J., Ludwig, W.J., Stoffa, P.L., Kan, T.K., and P. Buhl, 1978. Structure of the East Pacific Rise crest from multichannel seismic reflection data, J. Geophys. Res., 83, 798-804.

Hildebrand, F.B., 1965. Methods of Applied Mathematics, Englewood, N.J.: Prentice-Hall, 362 pp.

Jackson, D.D., 1972. Interpretation of inaccurate, insufficient and inconsistent data, Geophys. J. R. Astron. Soc., 28, 97-110.

Jackson, D.D., 1979. The use of a priori data to resolve non-uniqueness in linear inversion, Geophys. J. R. Astron. Soc., 57, 137-157.

Jordan, T.H., and J.N. Franklin, 1971. Optimal solutions to a linear inverse problem in geophysics, Proc. National Acad. Sci, 68, 291-293.

Julian, B.R., and D. Gubbins, 1977, Three dimensional seismic ray tracing, J. Geophys., 43, 95-113.

Koch, M., 1985. A numerical study on the determination of the 3-D structure of the lithosphere by linear and non-linear inversion of teleseismic travel times, Geophys. J. R. Astron. Soc., 80, 73-93.

Lanczos, D., 1961. Linear Differential Operators, New York: Van Nostrand Reinhold, 564 pp.

Lee, W.H.K., and S.W. Stewart, 1981. Principles and Applications of Microearthquake Networks, New York: Academic Press, 293 pp.

Lewis, B.T.R., and J.D. Garmany, 1982. Constraints on the structure of the East Pacific Rise from seismic refraction data, J. Geophys. Res., 87, 8417-8425, 1982.

Lister, C.R.B., 1974. On the penetration of water into hot rock, Geophys. J.R. Astron. Soc., 39, 465-509.

McClain, J.S., and B.T.R. Lewis, 1980. A seismic experiment at the axis of the East Pacific Rise, Mar. Geol., 35, 147-169, 1980.

McClain, J.S., J.A. Orcutt and M. Burnett, 1985. The East Pacific Rise in cross section: a seismic model, J. Geophys. Res., 90, 8627-8639.

Menke, W., 1984. Geophysical Data Analysis: Discrete Inverse Theory, New York: Academic Press, 260 pp.

Nercessian, A., A. Hirn, and A. Tarantola, 1984. Three-dimensional seismic transmission prospecting of the Mont Dore volcano, France, Geophys. J. R. Astron. Soc., 76, 307-315.

Orcutt, J.A., Kennett, B.L.N. and L.M. Dorman, 1976. Structure of the East Pacific Rise from an ocean bottom seismometer survey, Geophys. J.R. Astron. Soc., 45, 305-320.

Parker, R.L., 1975. The theory of ideal bodies for gravity interpretation, Geophys. J. R. Astron. Soc., 42, 315-334.

Pallister, J.S., and C.A. Hopson, 1981. Samail ophiolite plutonic suite: field relations, phase variation, cryptic variation and layering, and a model of a spreading ridge magma chamber, J. Geophys. Res., 86, 2593-2644.

Pavlis, G.L., and J.R. Booker, 1980. The mixed discrete-continuous inverse problem: application to the simultaneous determination of earthquake hypocenters and velocity structure, J. Geophys. Res., 85, 4801-4810.

Pereyra, V., W.H.K. Lee, and H.B. Keller, 1980. Solving two-point seismic ray tracing problems in a heterogeneous medium, Part 1, A general adaptive finite difference method, Bull. Seism. Soc. Am., 70, 79-99.

Reid, I., J.A. Orcutt, W.A. Prothero, 1977. Seismic evidence for a narrow zone of partial melt underlying the East Pacific Rise at 21°N, Geol. Soc. Am. Bull, 88, 678-682.

Riedisel, M., J.A. Orcutt, K.C. Macdonald, and J.S. McClain, Microearthquakes in the black smoker hydrothermal field, East Pacific Rise at 21°N, J. Geophys. Res., 87, 10613-10623, 1982.

Rosendahl, B.R., R.W. Raitt, L.M. Dorman, L.D. Bibee, D.M. Hussong and G.H. Sutton, 1976. Evolution of oceanic crust, 1, A physical model of the East Pacific Rise crest derived from seismic refraction data, J. Geophys. Res., 81, 5294-5304.

Sabatier, P.C., 1977. On geophysical inverse problems and constraints, J. Geophys., 43, 115-137.

Sinha, M.C., and Louden, K.E., 1983. The Oceanographer Fracture Zone, 1, crustal structure from seismic refraction studies, Geophys. J. R. astr. Soc., 75, 713-736.

Sleep, N.H., 1978. Thermal structure and kinematics of mid-ocean ridge axes: some implications to basaltic volcanism, Geophys. Res. Lett., 5, 426-428.

Spencer, C., and D. Gubbins, 1980. Travel time inversion for simultaneous earthquake location and velocity structure determination in laterally varying media, Geophys. J.R. Astron. Soc., 63, 95-116.

Stoffa, P.L., P. Buhl, T.J. Herron, T.K. Kan and W.J. Ludwig, 1980. Mantle reflections beneath the crestal zone of the East Pacific Rise from multichannel seismic data, Marine Geology, 35, 83-97.

Strens, M.R., and J.R Cann, 1982. A model of hydrothermal circulation in fault zones at mid-ocean ridge crests, Geophys. J.R. Astron. Soc., 71, 225-240.

Strens, M.R., and J.R Cann, 1986. A fracture-loop thermal balance model of black smoker circulation, Tectonophysics, 122, 307-324.

Talwani, M., P. Stoffa, P. Buhl, C. Windisch and J.B. Diebold, 1982. Seismic multichannel towed arrays in the exploration of the oceanic crust, Tectonophysics, 81, 273-300.

Tarantola, A., and A. Nercessian, 1984. Three-dimensional inversion without blocks, Geophys. J. R. Astron. Soc., 76, 299-306.

Tarantola, A., and B. Valette, 1982. Inverse problems = quest for information, J. Geophys., 50, 159-170.

Thurber, C.H., 1981. Earth structure and earthquake locations in the Coyote Lake area, central California, Ph.D. Thesis, Mass. Inst. of Technol., Cambridge.

Thurber, C.H., 1983. Earthquake locations and three-dimensional crustal structure in the Coyote Lake area, central California, J. Geophys. Res., 88, 8226-8236.

Thurber, C.H., and K. Aki, 1987. Three-dimensional seismic imaging, Annual Rev. Earth Planet. Sci., 15, 115-139.

White, R.S., R.S. Detrick, M.C. Sinha and M.H. Cormier, 1984. Anomalous seismic crustal structure of oceanic fracture zones, Geophys. J.R. astr. Soc., 79, 779-798.

Wiggins, R.A., 1972. The general linear inverse problem: implication of surface waves and free oscillations for earth structure, Rev. Geophys. Space Phys., 10, 251-285.

Figures

Figure 1 P-wave velocity versus depth for the axis of the East Pacific Rise as determined by McClain et al. [1985] (solid line), Reid et al. [1977] (dotted line) and Orcutt et al. [1976] (dashed line).

Figure 2 Cross sections of the P-wave velocity structure of the East Pacific Rise. (a) Model of McClain et al. [1985] for 13°N. (b) Model of Lewis and Garmany [1982] for 12°N. (c) Model of Rosendahl et al. [1976] for 9°N.

Figure 3 Model of the P-wave velocity structure of the East Pacific Rise used to compute the travel times for the tomographic inversion shown in Figures 7 and 8. Velocity contours are at 0.5 km/s intervals. (a) Cross section perpendicular to the rise axis. (b) Cross section along the rise axis.

Figure 4 Contour map of travel time residuals, in s, for a two-dimensional model with a cross section given by Figure 3a. The residuals are relative to the travel times for a laterally homogeneous model given by the structure at large x in Figure 3a. The axis of the low velocity zone is at x=10 km, the receiver is at the lower left-hand corner, and the travel times are plotted at the corresponding source locations. The contours are based on several hundred travel time differences obtained for a well distributed set of source locations.

Figure 5 Selected in-plane ray paths for the velocity structure of Figure 3a. The rise axis is at x=10 km. Note the suggestion of a shadow zone near x = 20 km.

Figure 6 A synthetic three-dimensional rise-axis tomography experiment. Solid dots are instruments and the ruled box shows the areal extent of a dense (1 km x 1 km) grid of shots. The synthetic data set consisted of travel times from the dense shooting grid to the receivers shown. The rise axis is shaded.

Figure 7 Results of the inversion of noise-free travel times for the structure of Figure 3 and the source-receiver arrangement shown in Figure 6. (a) Cross section perpendicular to the rise axis; contours in km/s. (b) Cross section parallel to the rise axis.

Figure 8 Results of the inversion of travel times with random errors that have zero mean and a standard deviation of 0.05 sec. (a) Cross section perpendicular to the rise axis. (b) Cross section parallel to the rise axis. (c) Sample of Gaussian deviations added to the travel times.

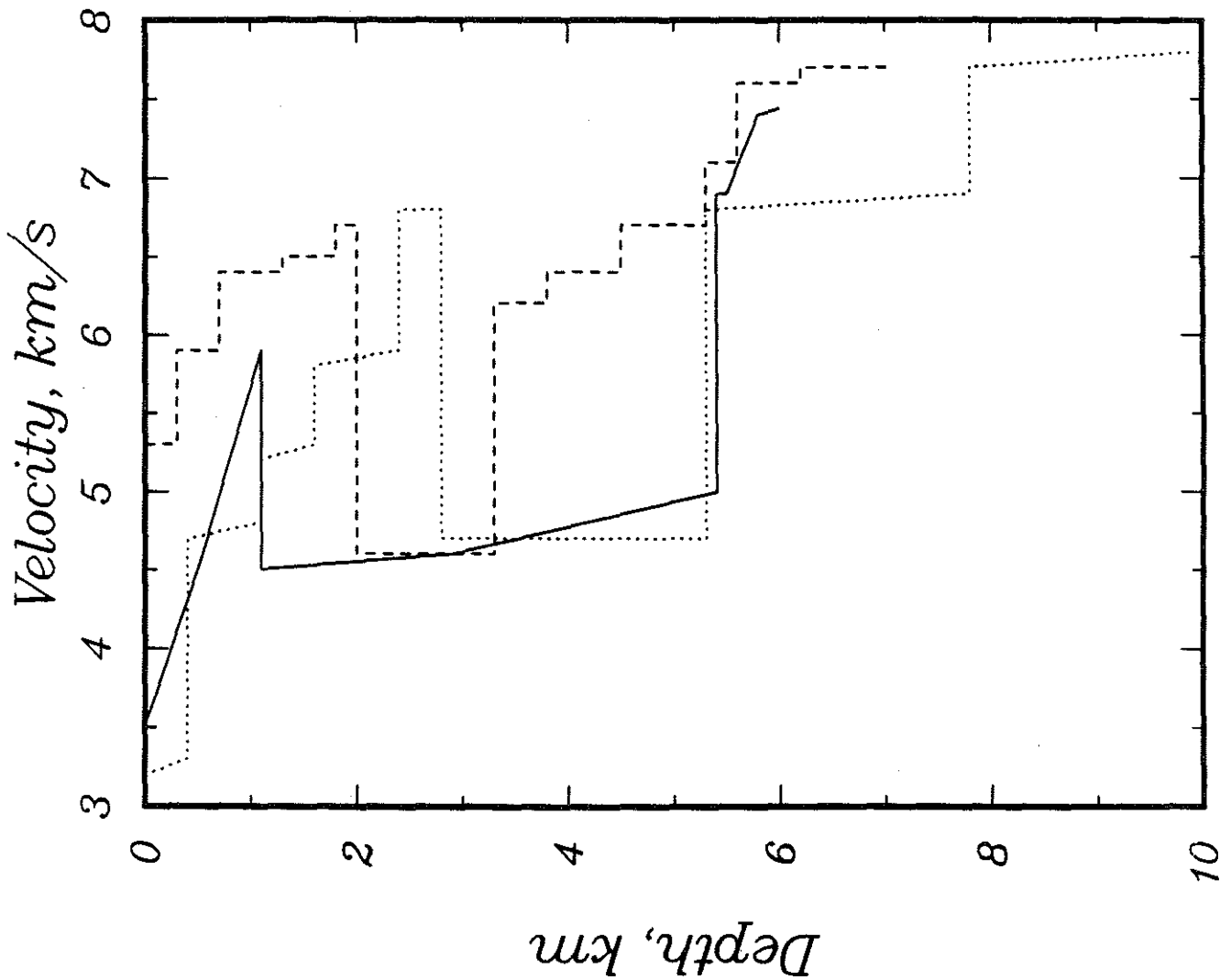

Figure 1

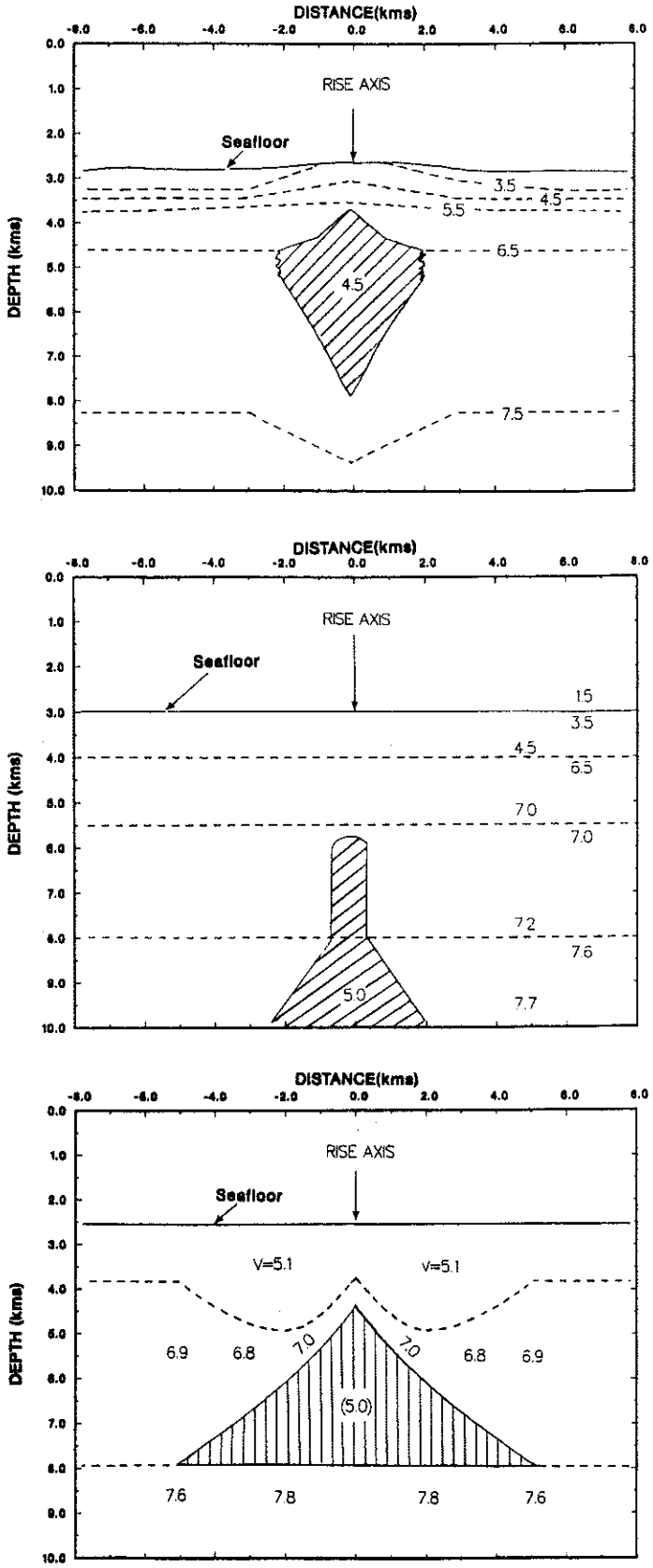
DISTANCE(kms)
-8.0 -6.0 -4.0 -2.0 0.0 2.0 4.0 6.0 8.0
DEPTH (kms)
0.0 1.0 2.0 3.0 4.0 5.0 6.0 7.0 8.0 9.0 10.0
RISE AXIS
Seafloor
3.5
4.5
5.5
6.5
4.5
7.5
DISTANCE(kms)
-8.0 -6.0 -4.0 -2.0 0.0 2.0 4.0 6.0 8.0
DEPTH (kms)
0.0 1.0 2.0 3.0 4.0 5.0 6.0 7.0 8.0 9.0 10.0
RISE AXIS
Seafloor
1.5
3.5
4.5
6.5
7.0
7.0
7.2
7.6
5.0
7.7
DISTANCE(kms)
-8.0 -6.0 -4.0 -2.0 0.0 2.0 4.0 6.0 8.0
DEPTH (kms)
0.0 1.0 2.0 3.0 4.0 5.0 6.0 7.0 8.0 9.0 10.0
RISE AXIS
Seafloor
V=5.1
V=5.1
6.9
6.8
7.0
7.0
6.8
6.9
(5.0)
7.6
7.8
7.8
7.6

Figure 2

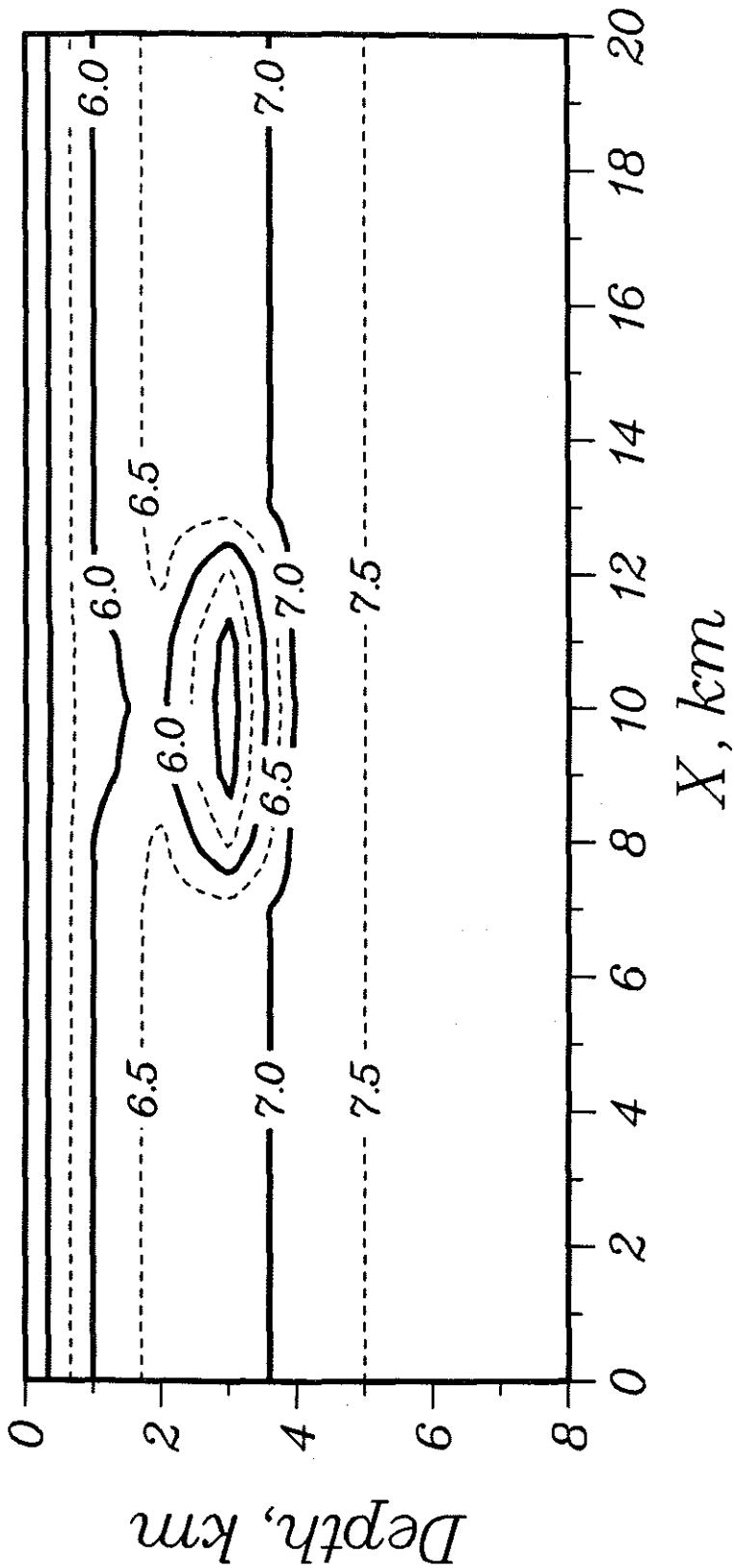

Figure 3a

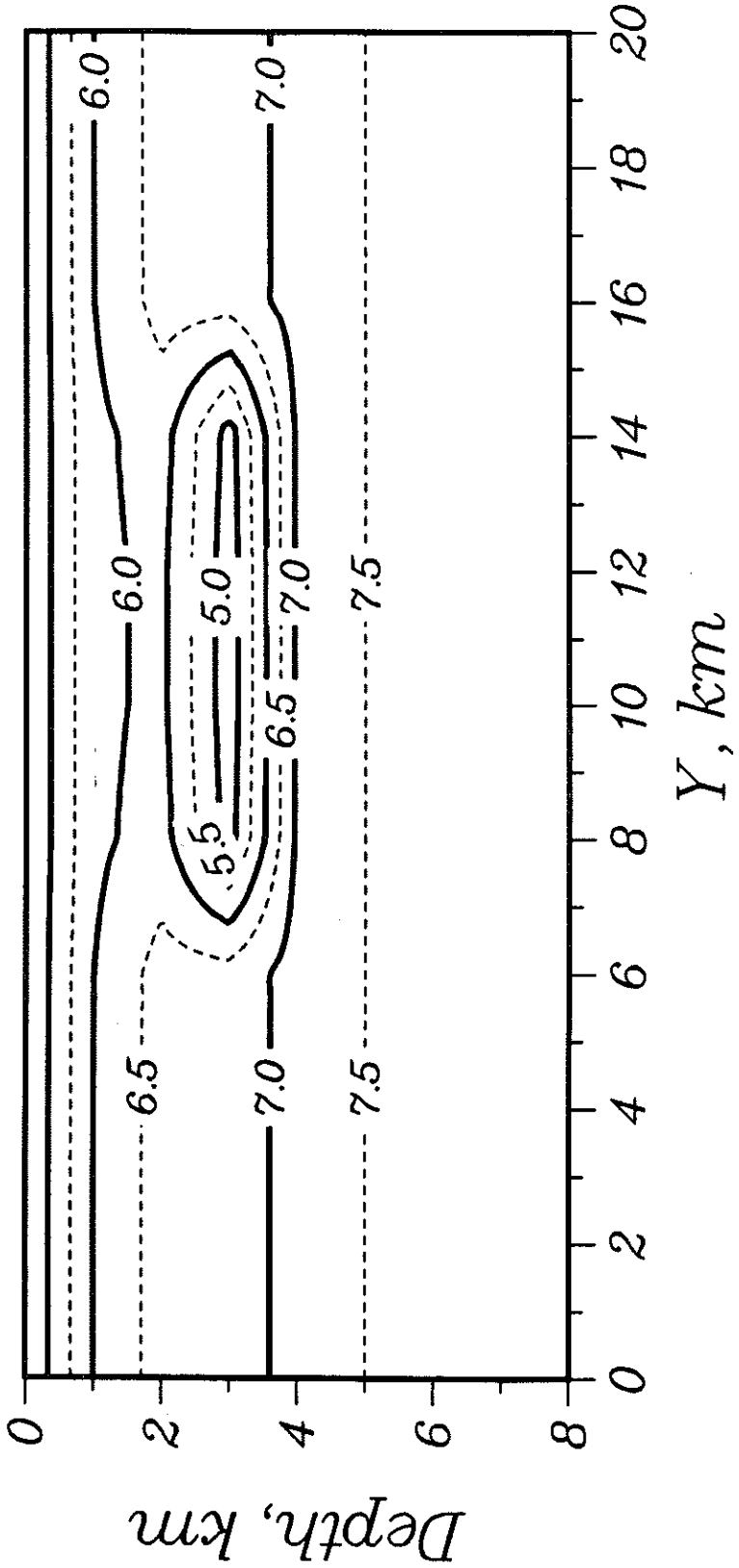
Depth, km
0
2
4
6
8
Y, km
0
2
4
6
8
10
12
14
16
18
20
6.0
6.0
6.5
7.0
5.0
5.5
6.5
7.0
7.0
7.5
7.5

Figure 3b

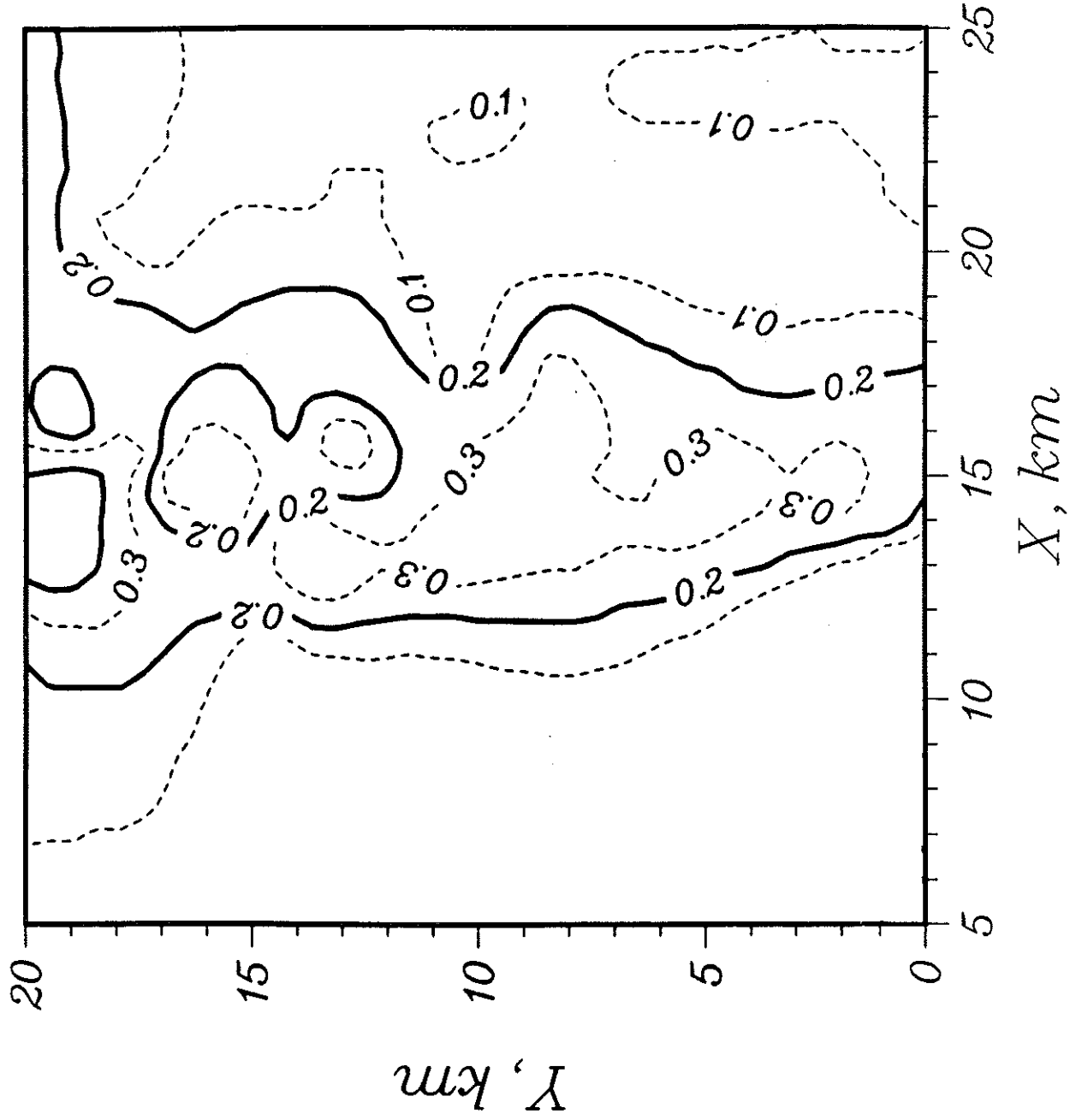

Figure 4

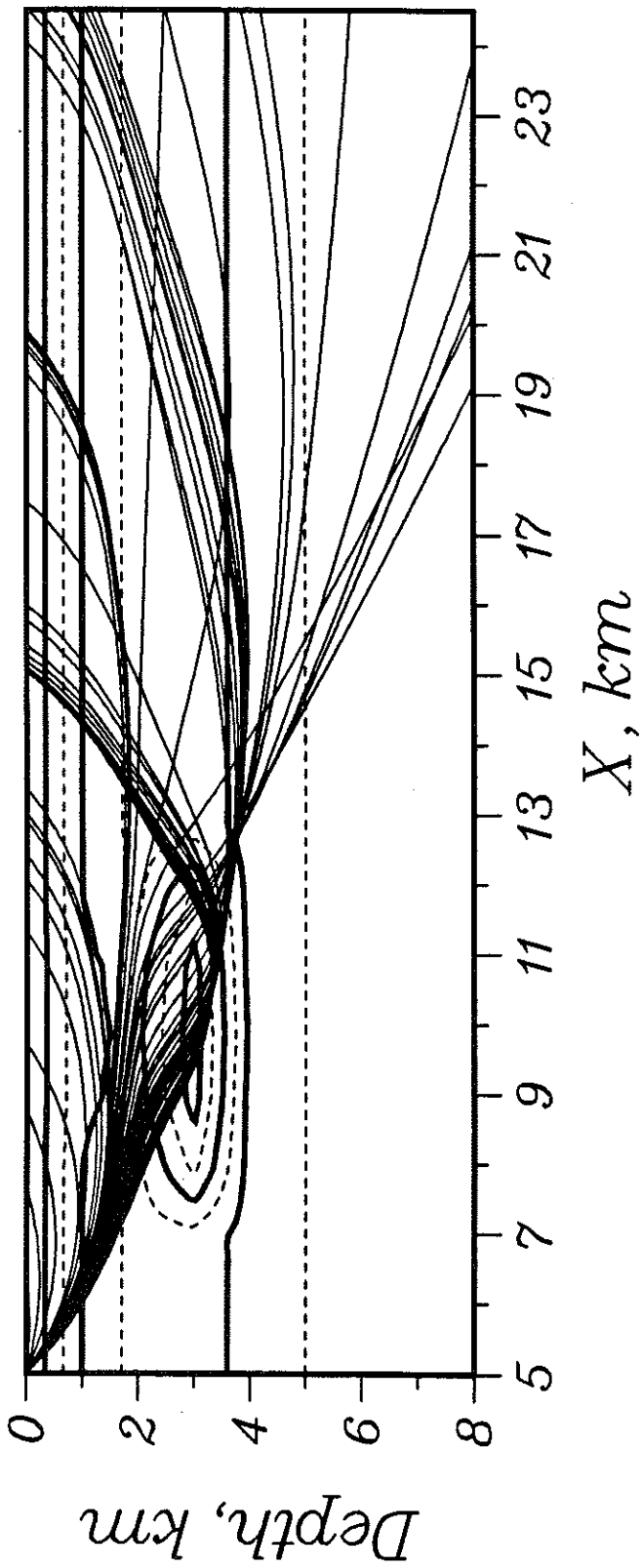

Figure 5

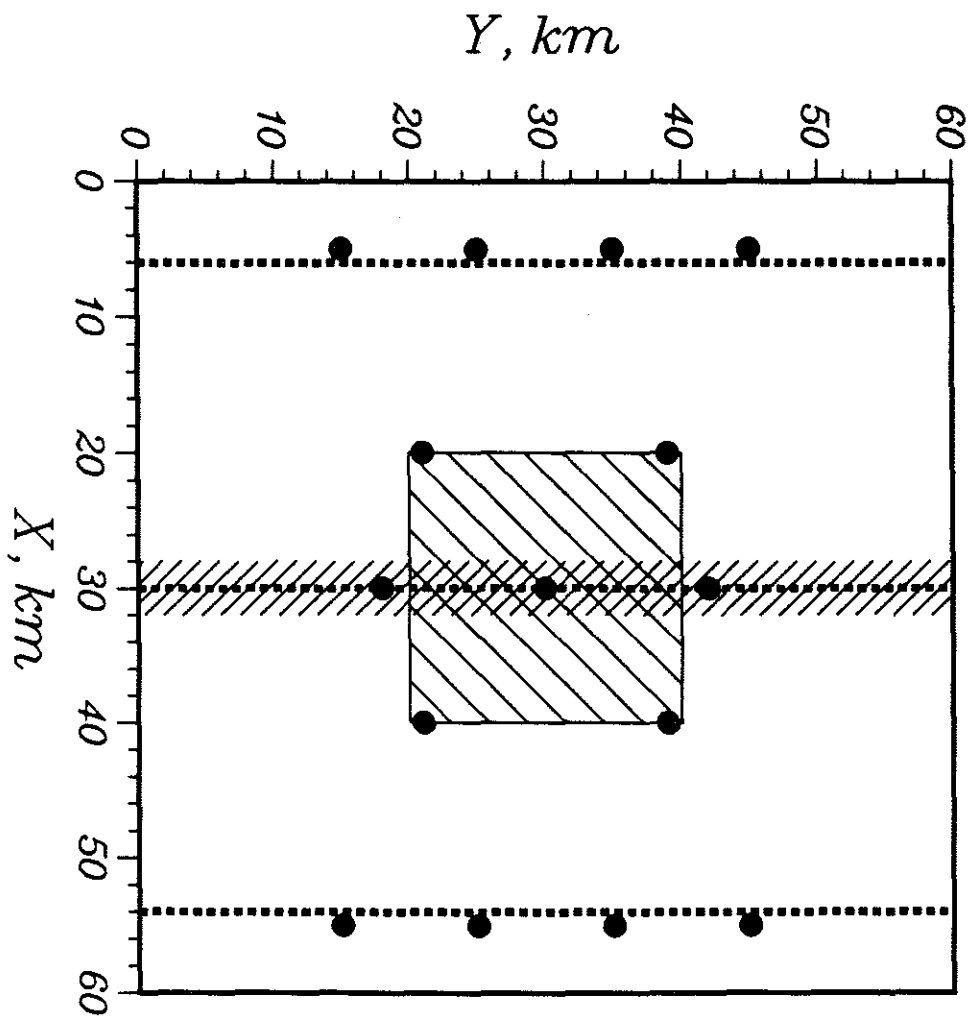

Figure 6

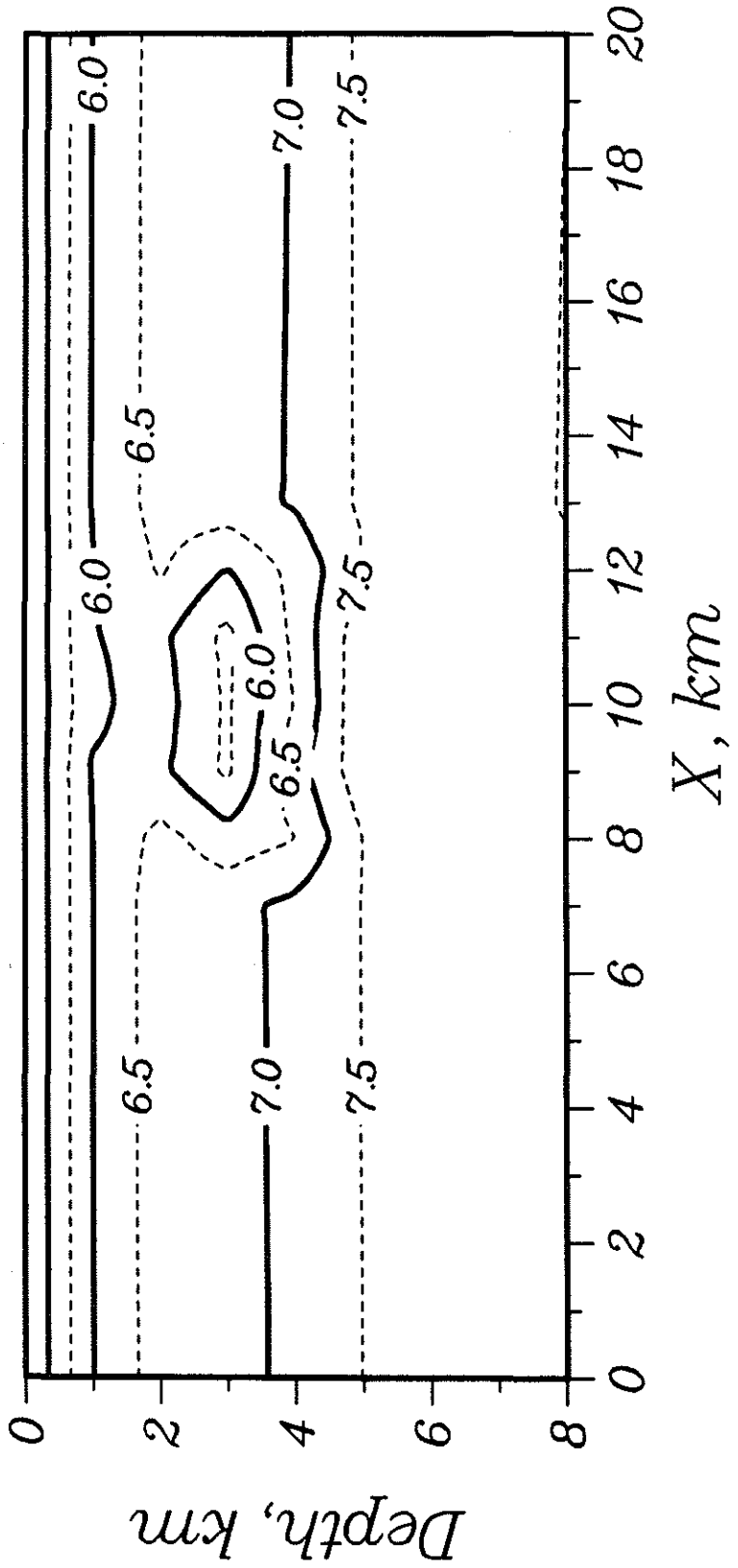

Figure 7a

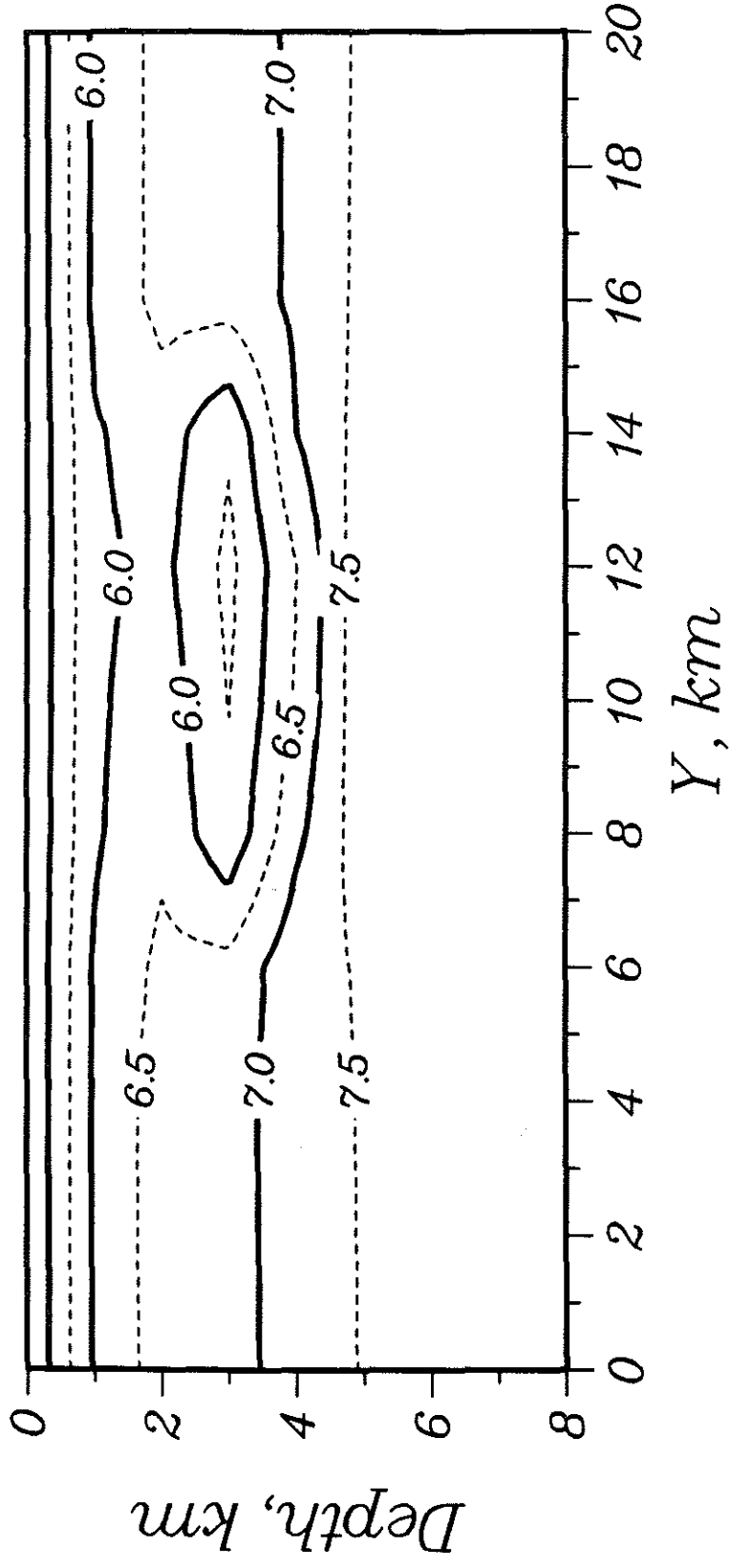
Depth, km
Y, km
0
2
4
6
8
0
2
4
6
8
10
12
14
16
18
20
6.0
6.0
6.0
6.5
6.5
7.0
7.0
7.5
7.5

Figure 7b

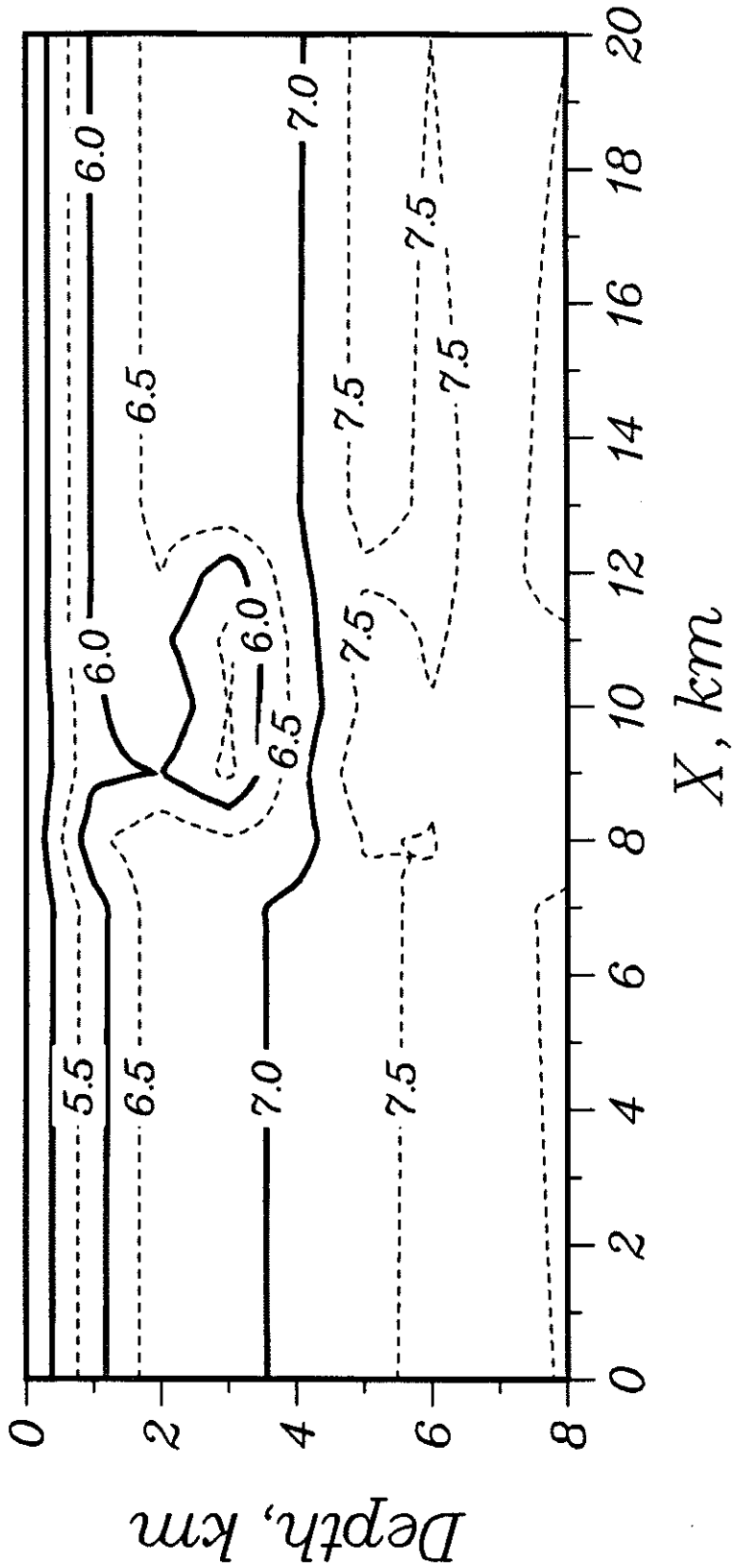

Figure 8a

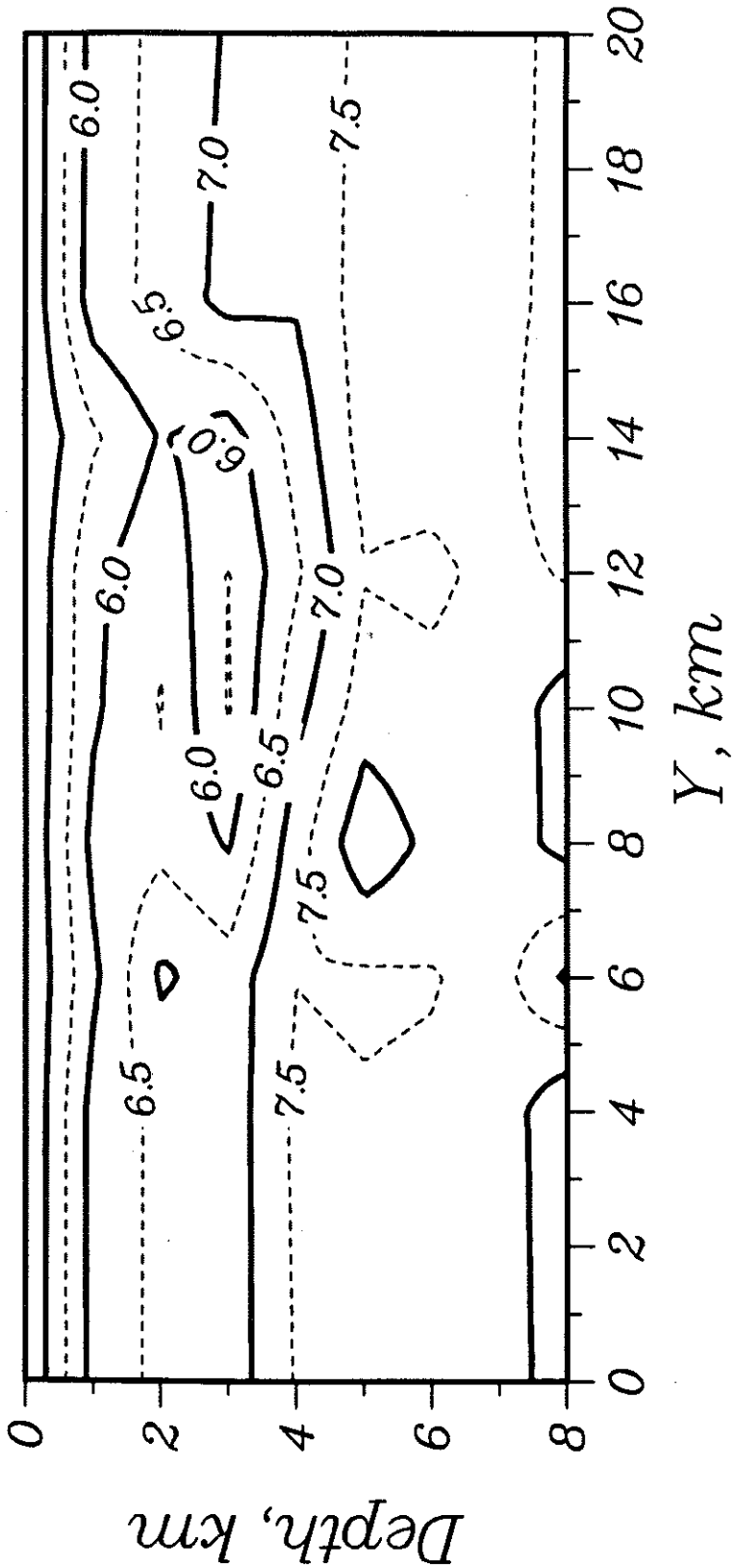

Figure 8b

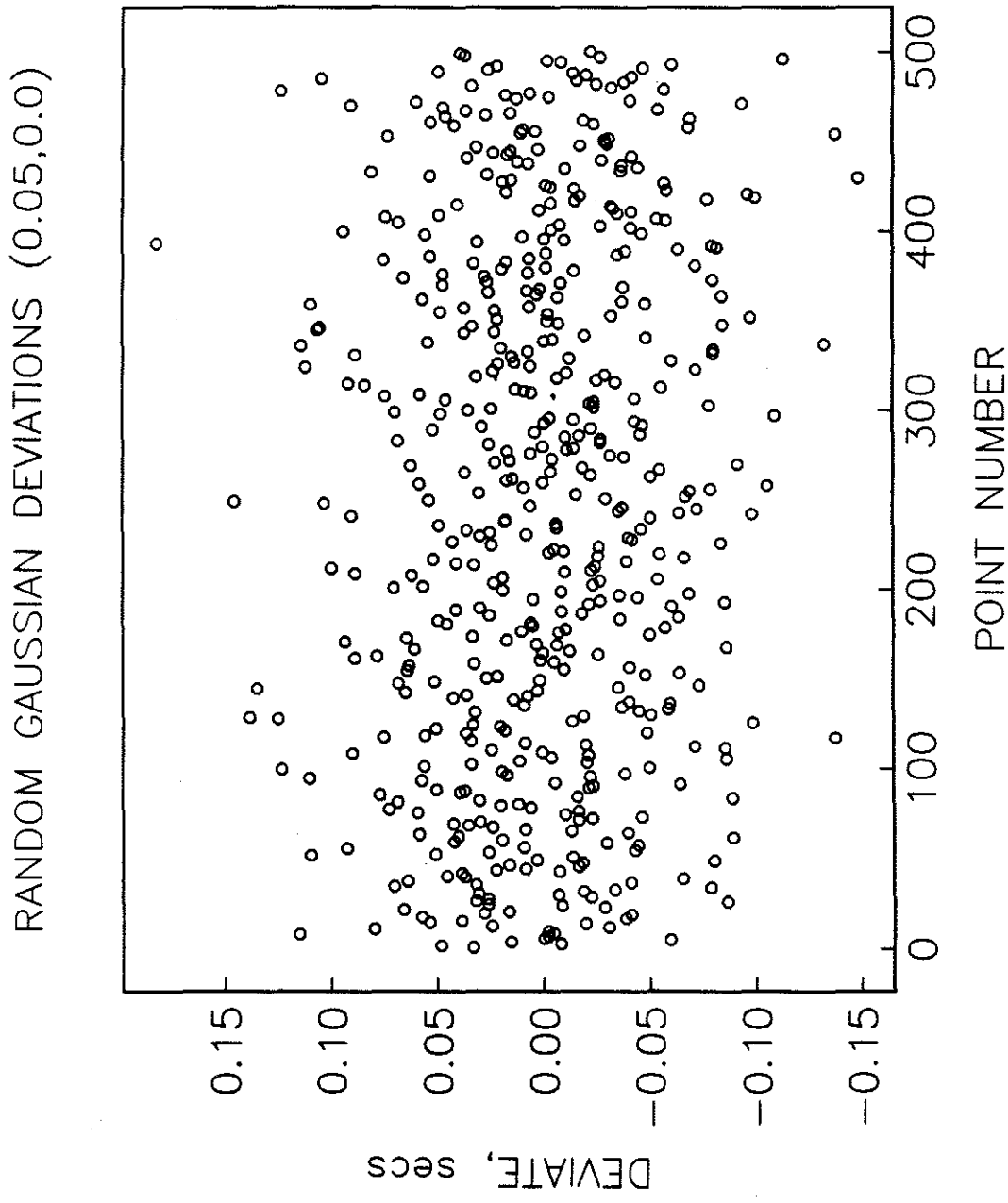
RANDOM GAUSSIAN DEVIATIONS (0.05,0.0)
DEVIATE, secs
0.15
0.10
0.05
0.00
−0.05
−0.10
−0.15
0
100
200
300
400
500
POINT NUMBER

Figure 8c

CHAPTER 3

MICROEARTHQUAKES BENEATH THE MEDIAN VALLEY OF THE MID-ATLANTIC RIDGE NEAR 23°N: HYPOCENTERS AND FOCAL MECHANISMS

JOURNAL OF GEOPHYSICAL RESEARCH, VOL. 90, NO. B7, PAGES 5443–5458, JUNE 10, 1985

Microearthquakes Beneath the Median Valley of the Mid-Atlantic Ridge Near 23°N: Hypocenters and Focal Mechanisms

DOUGLAS R. TOOMEY,[1,2] SEAN C. SOLOMON,[3] G. M. PURDY,[4] AND MARK H. MURRAY[1,2]

We report hypocenters and focal mechanisms of microearthquakes located by an ocean bottom seismic network deployed in the median valley of the Mid-Atlantic Ridge near 23°N during a 3 week period in early 1982. The network consisted of seven ocean-bottom hydrophones and three three-component ocean bottom seismometers. The instrument coordinates were acoustically determined to within 25 m at the 1 standard deviation level of confidence. The hypocentral parameters of the 26 largest microearthquakes are reported; 18 of these events have epicenters and focal depths which are resolvable to within ±1 km formal error at the 95% confidence level. Microearthquakes occur beneath the inner floor of the median valley and have focal depths generally between 5 and 8 km beneath the seafloor. Composite fault plane solutions for two spatially related groups of microearthquakes beneath the inner floor indicate normal faulting along fault planes that dip at angles of 30° or more; these solutions are similar to the mechanisms of nearby large earthquakes. Microearthquakes also occur beneath the steep eastern inner rift mountains. The rift mountain earthquakes have nominal focal depths of 5–7 km and epicenters as distant as 10–15 km from the center of the median valley, but these hypocenters have larger uncertainties because of the possible effects of large topographic relief and associated lateral heterogeneity in velocity structure. We interpret the depth distribution and source mechanisms of these microearthquakes to indicate that this segment of ridge axis is undergoing brittle failure under extension to a depth of at least 7–8 km. We infer that the entire crustal column has been cooled to temperatures within the brittle field of behavior and that significant time has elapsed since the most recent episode of volcanic or shallow magmatic activity along this ridge segment.

INTRODUCTION

The processes of generation and evolution of new oceanic lithosphere are currently the subjects of vigorous inquiry. This has been stimulated in large part by recent observations of ridge axis geology made with manned submersibles, towed camera systems, and SEABEAM surveys and by related programs in seafloor seismic and thermal structure and ocean crustal geochemistry [e.g., *Macdonald*, 1982; *Francheteau and Ballard*, 1983]. Among the most important of these processes are the evolution of axial magma chambers, hydrothermal circulation, and near-axis faulting. The first process is held responsible by many for the generation of much of the oceanic crust and uppermost mantle [e.g., *Cann*, 1974; *Bryan and Moore*, 1977]; the second probably dominates heat transfer in at least the shallow portions of young oceanic crust [e.g., *Lister*, 1977]; and the third process produces most of the topographic relief for many ridge systems [e.g., *Macdonald and Luyendyk*, 1977]. The distribution and character of earthquakes at mid-ocean ridges contribute important information on all three of these first-order processes. The depth extent of earthquakes at and near ridge axes is a signature of the local thermal and mechanical structure, both controlled by the competing effects of shallow magmatic intrusion and upward heat transfer. The source characteristics of earthquakes (e.g., individual mechanisms, swarm versus mainshock-aftershock sequence, spatial migration of hypocenters) can be important indicators of whether volcanic or tectonic processes are locally dominant. The distribution and mechanisms of earthquakes versus distance from the ridge axis can constrain the role of seismogenic faulting in the evolution of seafloor topography. With the goal of addressing these relationships we report in this paper on the determination of hypocentral locations and source characteristics of microearthquakes recorded by a network of ocean bottom seismic instruments deployed in the median valley of the Mid-Atlantic Ridge near 23°N.

A number of microearthquake surveys have been conducted on the Mid-Atlantic Ridge and other slow-spreading ridges using either sonobuoys or ocean bottom seismometers. These surveys include several at 45°N [*Francis and Porter*, 1973; *Lilwall et al.*, 1977, 1978], several in the FAMOUS region at 37°N [*Reid and Macdonald*, 1973; *Spindel et al.*, 1974; *Francis et al.*, 1977], one near 59°N [*Lilwall et al.*, 1980], surveys near ridge intersections with the Oceanographer [*Rowlett*, 1981; *Cessaro et al.*, 1982], Vema [*Rowlett and Forsyth*, 1984], and St. Paul's fracture zones [*Francis et al.*, 1978], and several experiments near the Gorda Ridge and Blanco Fracture Zone [*Johnson and Jones*, 1978; *Jones and Johnson*, 1978; *Sverdrup et al.*, 1977; *Johnson et al.*, 1978; *Solano and Bibee*, 1980].

Most of the cited experiments, however, were conducted with at most a few simultaneously operating instruments, so that epicentral location and focal depth could not be simultaneously well resolved [*Duschenes et al.*, 1983]. Further, the few reported microearthquake experiments on the Mid-Atlantic Ridge that were conducted with a number of ocean bottom sensors sufficient to produce robust earthquake locations were devoted to major transform faults or their intersections with adjacent ridge axes [*Francis et al.*, 1978; *Rowlett and Forsyth*, 1984; *Cessaro et al.*, 1982]. For those ridge axis earthquakes observed in such surveys the generality of their locations and source characteristics for spreading center segments well removed from large transforms is unknown.

We were thus motivated to carry out a microearthquake experiment in an axial valley of a slow-spreading ridge well removed from major transform faults. During February and March 1982 a network of seven ocean bottom hydrophones (OBH's) and three ocean bottom seismometers (OBS's) was deployed from the R/V Knorr for a 3-week period in the

[1] MIT/WHOI Joint Program in Oceanography, Woods Hole Oceanographic Institution, Massachusetts.
[2] Also at Department of Earth, Atmospheric and Planetary Sciences, Massachusetts Institute of Technology, Cambridge.
[3] Department of Earth, Atmospheric, and Planetary Sciences, Massachusetts Institute of Technology, Cambridge.
[4] Department of Geology and Geophysics, Woods Hole Oceanographic Institution, Massachusetts.

Paper number 4B5211.
0148-0227/85/004B-5211$05.00

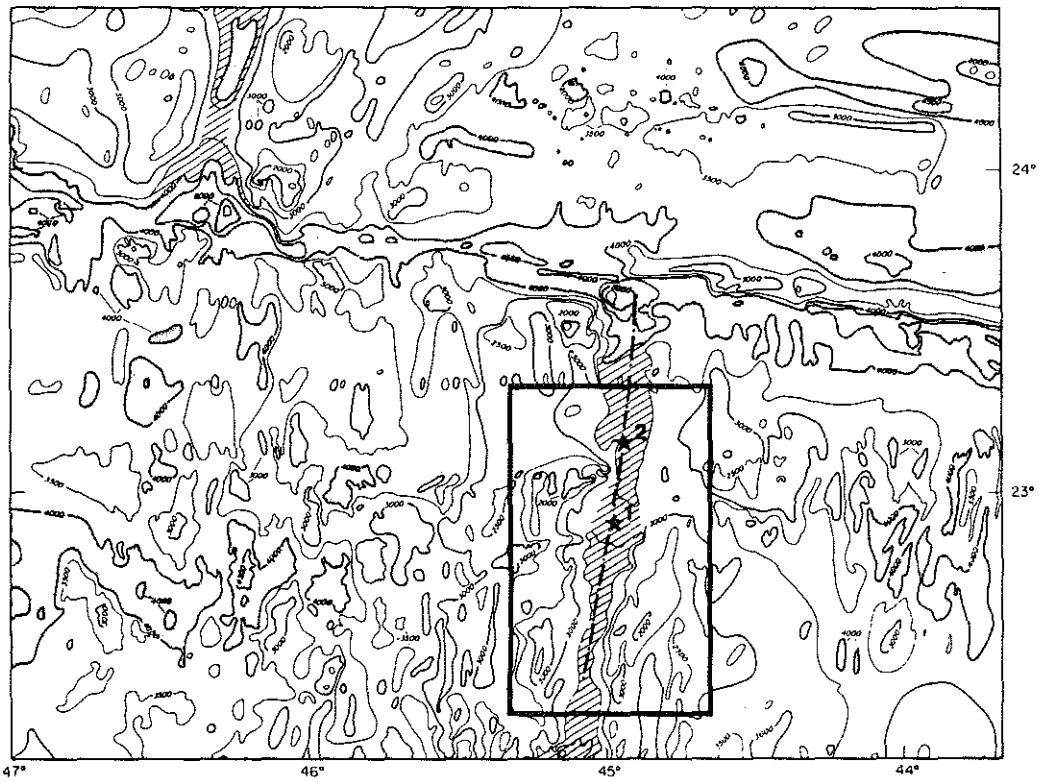

Fig. 1. Bathymetry of the Mid-Atlantic Ridge and Kane Fracture Zone (500-m contour interval), from *Detrick and Purdy* [1980]. The median valley is delineated by diagonal lines and is offset 150 km left laterally by the Kane Fracture Zone. Depths greater than 4000 m are shaded. The bold rectangle on the southern median valley defines the area of the 1982 microearthquake survey that is shown in detail in Figure 2. The dashed line down the center of the southern median valley shows the location of the refraction line used to determine local crustal structure [*Purdy et al.*, 1982]; the stars denote the locations of OBH's 1 and 2 for the refraction experiment.

median valley of the Mid-Atlantic Ridge near latitude 23°N (Figure 1). Ten stations are sufficient in number to allow the focal depth and epicentral coordinates of earthquakes observed near by to be independently well resolved [*Duschenes et al.*, 1983]. Because the experiment site is distant from any major transform fault, the earthquake characteristics should reflect the tectonic expression of the spreading process along this ridge axis segment.

In this paper we report the hypocentral locations of 26 of the largest microearthquakes recorded during the experiment and the focal mechanisms for events located within and immediately adjacent to the network. The principal conclusions of this work are that microearthquake activity is concentrated at depths of 5–8 km below the central median valley floor and that these earthquakes occur predominantly by slip on normal faults dipping at angles of at least 30°.

EXPERIMENT SITE

The site for the microearthquake experiment was in the median valley of the Mid-Atlantic Ridge approximately 90 km south of the Kane Fracture Zone (Figure 1). This ridge section has been the subject of several general surveys [*van Andel and Bowin*, 1968; *Purdy et al.*, 1978]. The local full spreading rate is about 27 mm/yr [*Minster and Jordan*, 1978], but spreading in the last few million years has been asymmetric, with rates of 17 and 11 mm/yr to the west and east, respectively [*Purdy et al.*, 1978]. The experiment site was selected because it is well removed from the influence of major transform faults; the topographic relief of the flanking rift mountains is approximately symmetric about a well-developed median valley; and finally, during the past two decades the area has been the site of several large (m_b = 5.5–6) earthquakes with normal faulting mechanisms.

A refraction survey was carried out along the median valley (Figure 1) over the site of this microearthquake study [*Purdy et al.*, 1982]. The compressional wave velocity structure obtained from travel time analysis and waveform modeling [*Purdy et al.*, 1982] was used in the earthquake location calculations. In addition, this local seismic structure provides independent information on the tectonic state of this portion of the ridge axis.

A bathymetric map of the region surrounding the microearthquake experiment site is shown in Figure 2. The median valley, approximately centered on longitude 45°W, deepens from a depth of 3800 m in the north to over 4200 m in the south. Coincident with this deepening, the rift valley narrows toward the south (particularly south of 22°40'N). South of 22°35'N the rift mountains develop a marked asymmetry, becoming extremely steep to the east but nearly absent on the opposing western side. This topographic asymmetry may be related to the local asymmetry in spreading rates. Such along-axis changes in median valley topography support the existence of widely varying dynamic conditions along the strike of a slow-spreading ridge axis.

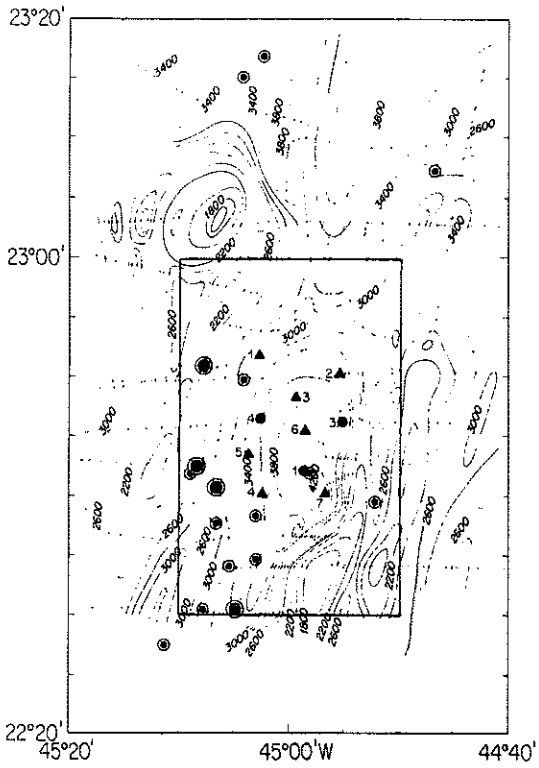

Fig. 2. Bathymetry, historical seismicity, and network configuration for the microearthquake experiment. Solid symbols denote seismic instruments: Triangles are WHOI OBH's, and circles are MIT OBS's. Epicenters of teleseismically located earthquakes for the period 1962–1982, obtained from catalogs of the ISC and NEIS, are shown as partially solid circles; larger symbols denote events with $m_b \gtrsim 5.5$. Bathymetric contours (in meters) were drawn by S. R. Bratt and C. Schramm from data collected aboard the R/V *Knorr* during the 1982 cruise; ship tracks are shown as dotted lines. The median valley is centered approximately on longitude 45°00'W. The bold rectangle defines the map area depicted in Figures 5, 7, 9, and 12.

The experiment site is the locus of several large earthquakes that have been teleseismically located. The epicentral locations of earthquakes reported in the International Seismological Centre (ISC) and National Earthquake Information Service (NEIS) bulletins for the period 1962–1982 are shown in Figure 2. A swarm of five earthquakes ($m_b = 4.6$–5.9) occurred on June 28, 1977, near the southern portion of our network. Two other large ($m_b \simeq 5.5$) earthquakes occurred near by in 1962 and 1964. The relationship of the source parameters of these large earthquakes to those of the microearthquakes in this study is discussed further below.

THE SEISMIC NETWORK

The microearthquake network shown in Figure 2 consisted of seven OBH's from the Woods Hole Oceanographic Institution (WHOI) and three OBS's from the Massachusetts Institute of Technology (MIT). The southernmost extension of the array was constrained by the difficulties of deploying instruments in an extremely narrow and steep median valley. The network covers a region of approximately 20 km in the north-south direction and about 12 km in the east-west direction; the maximum separation between adjacent instruments is about 5 km. All instruments were recovered successfully, and all but one (MIT OBS 4) returned data of good quality.

The WHOI ocean bottom hydrophones [*Koelsch and Purdy*, 1979] and the MIT ocean bottom seismometers [*Mattaboni and Solomon*, 1977; *Duschenes et al.*, 1981] complement one another in several important ways. The WHOI OBH is designed to float approximately 3 m above the seafloor and thus can be safely deployed in the roughest topography. The single hydrophone sensor records clear impulsive *P* wave arrivals but helps little in identifying the important shear phases. The MIT instrument, in contrast, is fitted with three orthogonal seismometers, essential for unambiguous identification of the shear wave arrivals [*Tréhu and Solomon*, 1983]. A deployed geophone package on the MIT OBS [*Duschenes et al.*, 1981] considerably reduces the problems caused by the cross-coupling of vertical and horizontal components, eliminates mechanical noise from the tape recorder, and attenuates current-generated instrument noise. The WHOI OBH yields continuous analog records and thus preserves the smallest to the largest events and provides a complete view of seismic activity. Recording time is limited to 10 days, however, and large events can overload the recording system, which has a dynamic range of only 60 dB. The MIT OBS records digitally, has a total dynamic range of 108 dB, and thus provides accurate waveforms from even the largest shocks. The OBS operates in an event trigger mode and preserves only those records with seismic signals larger than a preset multiple of the background noise. In this mode the MIT OBS can record on the seafloor for 1 month.

An overall view of the number of earthquakes recorded during the experiment may be gained from the histograms shown in Figure 3. The OBH instruments recorded an average of about 15 events per day, but many of these events are of very low magnitude and were not recorded sufficiently well by enough instruments to permit accurate location. At 10 Hz the OBH noise level rarely exceeded ~ 0.5 μbar (0.05 Pa) except for the case of passing ships or the vocalizations of finback whales. The latter were omnipresent on the OBH tapes but fortunately transmitted insufficient energy into ground motion to trigger the OBS instruments.

Examples of seismograms are shown in Figure 4. Clear, impulsive *P* wave arrivals are recorded on all but the most distant receivers. Both *P* and *S* waves are observable on the OBS records. Because of an electronic failure, one horizontal channel on MIT OBS 3 did not record data. The OBS seismograms following the *S* wave arrivals display an oscillatory character that differs between the two OBS instruments. Whether these signals and their variations reflect imperfect coupling to the seafloor [*Sutton et al.*, 1981; *Tréhu and Solomon*, 1981] or real ground motion is an important issue we defer to later analysis.

INSTRUMENT LOCATION

Uncertainties in the ship location at the time of deployment and the nonvertical trajectory of a free-falling package can give rise to errors in instrument position which often exceed 1 km. Errors of this magnitude are equivalent to travel time errors of several tenths of a second for typical *P* wave velocities in oceanic crust and to even larger travel time errors for *S* waves. The most pronounced effect of inaccurate instrument positions is to introduce errors in estimates of focal depth. Since a fundamental goal of this microearthquake experiment is the determination of the depth dependence of earthquake faulting, accurate instrument locations are essential.

Creager and Dorman [1982] have described a parameter estimation method by which accurate instrument positions

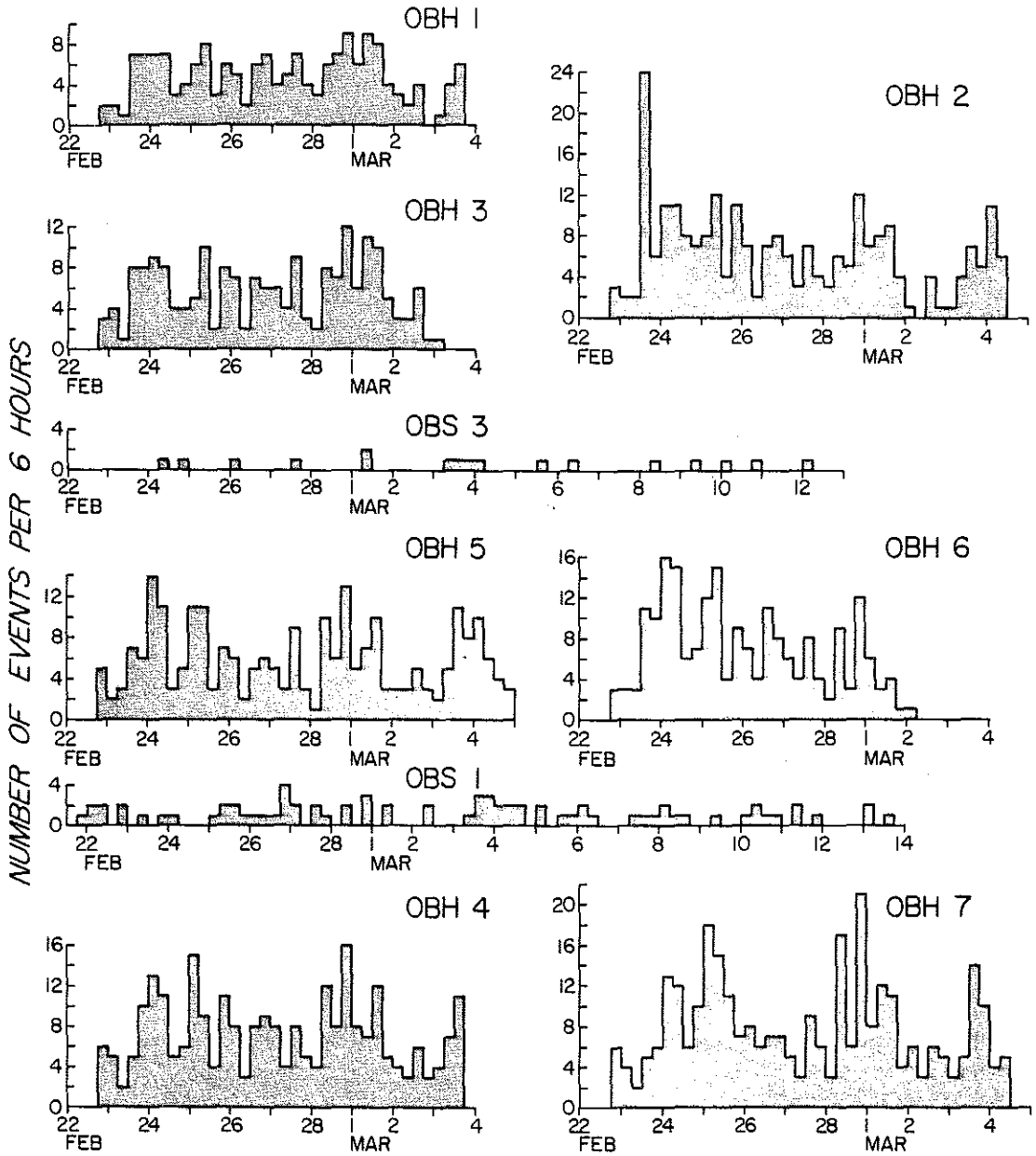

Fig. 3. Histograms of number of seismic events per 6-hour period on each OBH and OBS in the array. For instrument locations, see Figure 2.

may be determined. The technique utilizes acoustic ranging to link a set of fixes of ship position to a stationary array of receivers. The method simultaneously calculates the instrument coordinates and the ship position at the time of acoustic ranging.

Using the arrival times of water waves from 14 shots, we have employed the Creager-Dorman procedure to invert for positions of all instruments. Figure 5 shows a plot of the initial locations of the 14 shots and the initial instrument locations based on ship position fixes prior to instrument launches and dead reckoning. Since few marine microearthquake experiments have utilized instrument relocation procedures such as that of *Creager and Dorman* [1982], a full discussion of our assumptions and error analysis is given in the appendix.

The final relocated positions of all instruments and shots, together with their respective errors, are given in Table 1 and Figure 5. For some instruments the difference between the initial estimate and the relocated position is over 1 km. The a posteriori error ellipses for shot positions have semimajor axes at 1 standard deviation of 20–30 m; the rms error in water wave travel time with the final shot and receiver locations is 13 ms. The errors in latitude and longitude for each instrument shown in Table 1 are calculated from the 1 standard

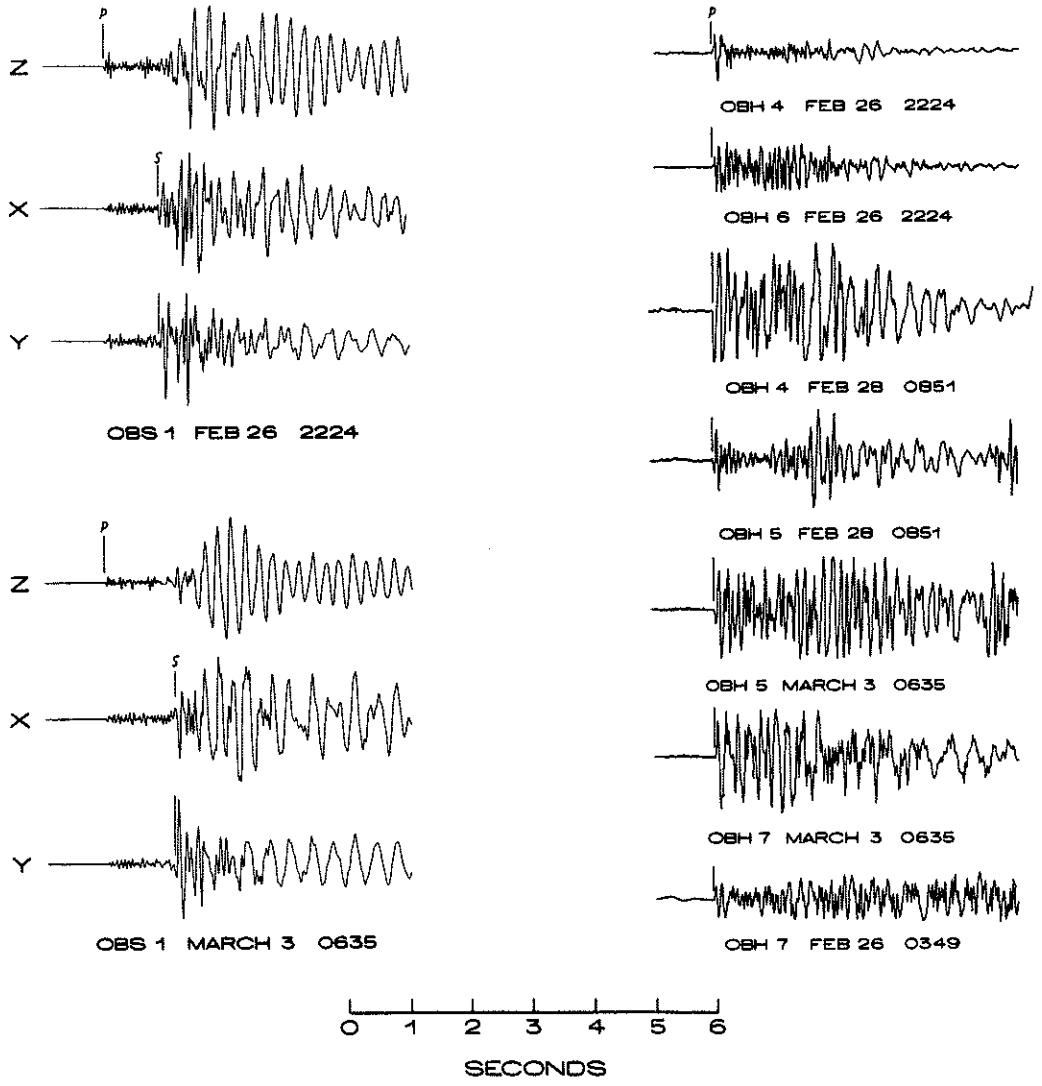

Fig. 4. Examples of microearthquake seismograms recorded by OBS and OBH instruments. All traces are aligned by the *P* wave arrival. The time scale for all records is shown at bottom. The arrival times of *P* and *S* waves on the OBS seismograms and of *P* waves only on the OBH seismograms are noted by vertical lines. The harmonic character of the OBS records after the *S* arrival may arise from imperfect instrument coupling with the seafloor.

deviation ellipsoid; the horizontal projections of the error ellipsoids have semimajor axes of 15–25 m. The calculated OBH depths and positions agree well with the bathymetric map; the errors in depth at 1 standard deviation range from 20 to 40 m. Because of the probable bias in measuring water wave arrival times at the OBS's, as mentioned in the appendix, the depths of the OBS's given in Table 1 are estimated from the bathymetric map and are accurate to about 75 m. Precise knowledge of receiver depths is not critical in the hypocentral location procedure because station delays are calculated before the final determination of all earthquake locations.

For a given velocity model the mean rms travel time residual for hypocentral location decreases by approximately 1 order of magnitude when the relocated instrument positions are used instead of the initial positions. The result of a decreased rms residual is an increase in the statistical precision of the estimated hypocenter parameters, in addition to the presumably improved accuracy of the final locations.

HYPOCENTER LOCATION METHOD

The hypocentral coordinates (latitude, longitude, depth, and origin time) were determined using the computer program HYPOINVERSE [*Klein*, 1978]. This program is based on a one-dimensional velocity model composed of homogeneous layers separated by first-order velocity discontinuities. Because the determination of hypocentral parameters is a nonlinear problem, a linear approximation is solved iteratively until convergence criteria are satisfied. The matrix of travel time derivatives which links parameter adjustments and travel time residuals is decomposed by singular-value decomposition and is inverted by calculating the generalized inverse (see, for example, *Aki and Richards* [1980]). The generalized inverse ap-

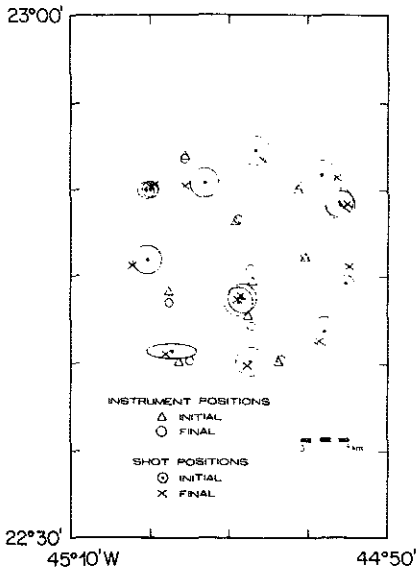

Fig. 5. Determination of instrument positions by acoustic ranging from shots, using the procedure of *Creager and Dorman* [1982]. Initial positions of the nine instruments and 14 shots (including 1 standard deviation errors) are obtained from satellite fixes and dead reckoning; a description of the a priori errors in these positions is given in the appendix. The errors in final shot and instrument coordinates are given in Table 1; if plotted on the figure, the error regions would be smaller than the symbols used to denote final positions.

proach is advantageous because it permits direct determination of the resolution, data importance, and covariance matrices in addition to the hypocentral parameters. Step-length damping is also implemented to prevent the solution from moving along weakly constrained regions of parameter space.

The formal error of a particular hypocenter solution relies, in part, upon the covariance matrix of the arrival time observations. When the data are assumed to be statistically independent and share the same arrival time variance, the elements of the parameter covariance matrix are scaled by the data variance. The square root of the data variance, or "picking error," incorporates the uncertainties of reading and correcting arrival times from the seismograms as well as the errors induced by station mislocation and the assumed layered velocity model. The adopted value of the picking error is discussed further below.

Because the clarity of the observed *P* and *S* wave arrivals may vary, the arrival times may be weighted in the HYPOINVERSE program to ensure that the most reliable observations have the most control on hypocentral solutions [*Klein*, 1978]. The a priori weights assigned in this study were based upon the uncertainty in arrival time for each phase. Subsequent to each iteration in HYPOINVERSE the magnitudes of the residuals are determined, and arrivals with residuals greater than 0.16 s are further downweighted to assure rapid convergence. This procedure is useful primarily for discovering errors in arrival times caused by clock correction errors or by phase misidentification.

ARRIVAL TIME DATA

The results of previous microearthquake studies have provided criteria for the estimation of accurate hypocentral locations in marine experiments. Among these criteria are the inclusion of arrival times from clearly identified *S* waves and the inclusion of sufficient travel time arrivals to provide redundant information on hypocentral parameters [*Duschenes et al.*, 1983]. Following these criteria, we restrict our attention in this paper to only those events for which five or more arrival time readings were available, including at least one *S* wave arrival time. Because three-component data are necessary for a reliable determination of *S* wave arrival times [*Tréhu and Solomon*, 1983], only the MIT OBS's were used to identify shear arrivals in this study. As noted above, only one horizontal channel was recorded by OBS 3. Fortunately, most events occur closer to OBS 1, which recorded high-quality data on all three channels. Only two events of the 26 reported here were located using an *S* arrival from only OBS 3.

P wave arrival times on both the OBH's and the OBS's can be picked with a precision of about 0.01 s (Figure 4), except for emergent arrivals. *S* wave arrival times on the MIT instrument can be identified from the three-component data with a precision of about 0.05 s. In the determination of hypocentral locations, arrival times of *S* waves are weighted by a factor of 0.75 times the weight for impulsive *P* wave arrivals; this factor is a compromise between the greater uncertainty in reading *S* arrivals and the greater importance of *S* wave readings toward the location solution [*Tréhu and Solomon*, 1983]. Arrival times of emergent phases, typically from the most distant stations, are also downweighted according to the approximate reading error; weights of 0.75, 0.5, and 0.25 are assigned to arrivals with reading errors of 0.02–0.05 s, 0.05–0.1 s, and 0.1-0.25 s, respectively.

All arrival times are corrected for the drift of instrument and master clocks relative to WWV. A linear drift rate is

TABLE 1. Relocated Instrument Positions

Instrument	Latitude, N	Longitude, W	Depth, m	*P* Wave Station Delay, s
OBS 1	22.7031° ± 20 m	44.9775° ± 19 m	4085 ± 75	−0.01
OBS 3	22.7706° ± 14 m	44.9204° ± 13 m	3825 ± 75	0.03
OBH 1	22.8625° ± 21 m	45.0462° ± 13 m	3709 ± 44	0.08
OBH 2	22.8368° ± 16 m	44.9249° ± 12 m	3608 ± 29	0.08
OBH 3	22.8045° ± 14 m	44.9906° ± 11 m	3743 ± 32	−0.03
OBH 4	22.6700° ± 17 m	45.0412° ± 14 m	3711 ± 35	0.07
OBH 5	22.7255° ± 13 m	45.0623° ± 14 m	3318 ± 37	−0.01
OBH 6	22.7576° ± 15 m	44.9772° ± 13 m	3908 ± 25	−0.02
OBH 7	22.6713° ± 16 m	44.9458° ± 14 m	4365 ± 23	−0.09

All uncertainties are 1 standard deviation estimates. Depths and errors for the OBS's are estimated from the horizontal coordinates and the bathymetric map (see text).

assumed in making these corrections. The maximum correction for instrument clock drift does not exceed 0.15 s over the duration of the experiment. The clock drift corrections have an uncertainty which does not exceed a few hundredths of a second.

All instruments are initially referenced to a common datum (3900 m depth) by introducing station delay times. The corrections are calculated from $\Delta h/v$, where Δh is the difference between the instrument depth (Table 1) and 3900 m, and v is the assumed correction velocity. An average P wave crustal velocity of 6.5 km/s and a V_p/V_s ratio of 1.75 were used to calculate the corrections. Our choice of datum is guided by the desire to introduce the smallest possible corrections for each instrument and should result in accurate focal depths for events beneath the nearly flat floor of the inner valley. However, the accuracy of the focal depth estimates for earthquakes beneath the rift mountains is difficult to determine, a point discussed further below.

The calculation of station delay times introduces a potentially large source of error which arises from the assumption of an average crustal velocity as well as from errors in instrument depth. To reduce this potential source of bias, station delays were recalculated iteratively from the mean travel time residuals remaining after location of 10 well-recorded earthquakes each having an epicenter less than 8 km from a recording station. The final station delays are shown in Table 1.

The cumulative effects of the errors introduced when reading arrival times, correcting for clock drift, adjusting instruments to a common isobath, and determining local station delays, as well as errors in instrument locations and the assumed velocity model, are incorporated in the estimate of the "picking error" [*Klein*, 1978]. This error is assumed to be 0.04 s for both P and S waves, a value justified a posteriori because the mean rms travel time residual based on final hypocentral locations is also 0.04 s.

Velocity Model

The accuracy of hypocentral estimates depends upon knowledge of compressional and shear wave velocity structure. A refraction experiment conducted within the region of the microearthquake network [*Purdy et al.*, 1982] permits a direct determination of the compressional wave velocity structure beneath the inner median valley. Figure 1 shows the location of the shooting profile and of the seafloor receivers. Figure 6 shows the velocity depth function derived from travel time and amplitude data along the section of the profile within the microearthquake network. For the earthquake location algorithm, this structure has been approximated by a model with 11 homogeneous layers; the layered model is also shown in Figure 6.

A V_p/V_s ratio of 1.75, equivalent to a Poisson's ratio of $\nu = 0.26$, is assumed for determining the S wave structure from the P wave model. This ratio for V_p/V_s is within the range of average values for oceanic crust and upper mantle determined elsewhere in similar tectonic settings [*Lilwall et al.*, 1977; *Francis et al.*, 1978; *Tréhu and Solomon*, 1983]. Available two-station S and P arrival time data [*Francis et al.*, 1977] from the microearthquakes of this experiment are consistent with this velocity ratio but do not constrain it well. The actual V_p/V_s ratio is likely to vary somewhat with depth in the oceanic crust [e.g., *Hyndman*, 1979], but we do not have sufficient data from our experiment to describe such a variation. The effect of adopting different average values for V_p/V_s on hypocentral locations is discussed below.

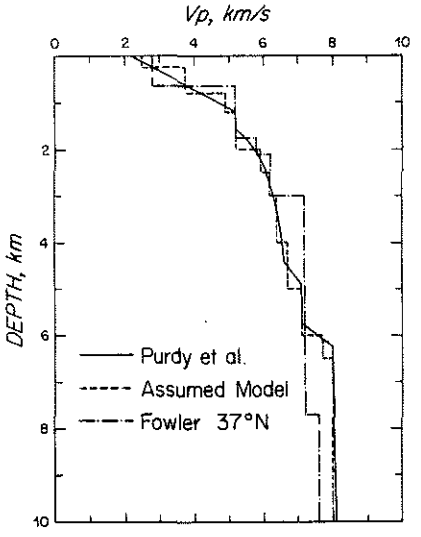

Fig. 6. Velocity-depth models. The solid line shows the preliminary velocity-depth function obtained from refraction data along the profile shown in Figure 1 [*Purdy et al.*, 1982]. The dashed line shows the plane-layered structure assumed for calculating microearthquake locations. The velocity structure determined by *Fowler* [1976] for the median valley of the Mid-Atlantic Ridge near 37°N is also shown. See text for a discussion of the effects of varying the assumed velocity model on hypocenter determinations.

Hypocenter Locations

A total of 26 earthquakes satisfied the criteria of five or more arrival time readings and one or more S wave arrival times. The hypocentral parameters of these events are given in Table 2. Eighteen of the 26 events have epicentral and focal depth estimates which may be independently estimated. The remaining eight events are located 10 km or more from the nearest receiving station and have poorly resolved depths. Epicentral coordinates for these eight events were calculated with the focal depth fixed at 5 km.

In deriving the locations given in Table 2 an initial epicentral position near the station recording the earliest arrival was assumed. The initial origin time was assumed to be 2 s before the earliest arrival time. In an attempt to avoid erroneous hypocentral estimates corresponding to local minima in solution space, the 18 microearthquakes with good depth control were located with the initial depth set to both 5 and 10 km. Within the estimated uncertainty, the locations for all but one event converged to the same solution. For the single exception (March 4) the two solutions did not differ significantly in focal depth, but the epicenters differed by about 5 km; the solution with the smaller rms travel time residual was assumed to be the correct location.

The statistical uncertainty in the estimated hypocentral parameters is calculated from the singular-value decomposition of the partial derivative matrix. The horizontal and vertical errors listed in Table 2 are formal errors at the 95% confidence level, derived from the hypocenter error ellipsoid. The vertical error is given by the largest value of the vertical components of the semiprincipal axes of the error ellipsoid. The horizontal error is the semimajor axis of the projection of the error ellipsoid onto a horizontal plane. The formal errors in Table 1 depend upon several assumptions (e.g., correctness of the velocity model, linearity of the location problem) and are

TABLE 2. Hypocentral Parameters of Microearthquakes Beneath the Mid-Atlantic Ridge Near 23°N

Origin Time						nor						
Date	Time, UT	Region	Latitude, N	Longitude, W	Depth, km	P	S	mag, deg	dcs, km	rms, s	erh, km	erz, km
Feb. 22	2322:39.41	2	22°38.4′	45°01.4′	0.9	6	1	265	3.9	0.04	0.6	0.7
Feb. 22	2324:27.50	2	22°38.6′	45°01.0′	6.9	4	1	255	4.0	0.02	1.2	1.4
Feb. 23	1126:59.84	2	22°38.1′	45°01.2′	7.5	4	1	271	4.5	0.02	0.9	1.3
Feb. 23	2225:35.81	4	22°34.4′	44°59.9′	5.0	4	1	312	11.7	0.06	0.8	pdc
Feb. 24	2151:42.06	3	22°39.2′	44°52.3′	4.5	8	1	292	7.9	0.04	1.8	0.5
Feb. 25	2012:20.20	4	22°32.1′	45°03.8′	5.0	5	1	322	15.2	0.11	1.3	pdc
Feb. 26	0349:49.29	3	22°39.2′	44°54.7′	4.6	9	2	283	4.2	0.05	0.8	0.3
Feb. 26	1729:33.23	2	22°38.2′	45°01.1′	7.0	6	1	268	4.5	0.03	0.9	1.1
Feb. 26	2224:28.42	1	22°42.5′	44°59.0′	6.5	8	1	115	0.8	0.04	0.5	0.4
Feb. 27	0506:00.07	4	22°35.0′	45°00.6′	5.0	5	1	309	10.2	0.17	1.0	pdc
Feb. 27	1612:29.75	4	22°58.1′	44°58.7′	5.0	4	1	308	13.7	0.07	0.8	pdc
Feb. 27	1634:24.67	4	22°32.9′	45°02.8′	5.0	4	1	319	13.6	0.10	1.2	pdc
Feb. 27	2144:27.96	4	22°31.9′	45°01.4′	5.0	4	1	324	15.6	0.08	1.4	pdc
Feb. 28	0849:33.15	2	22°37.4′	45°01.8′	5.7	6	1	286	5.3	0.03	0.8	0.8
Feb. 28	0851:26.09	2	22°37.4′	45°01.8′	5.3	5	1	286	5.3	0.05	1.1	0.8
Feb. 28	2333:44.44	1	22°42.2′	44°59.1′	7.0	5	1	108	0.7	0.03	0.9	0.7
March 1	1119:39.16	4	22°33.1′	44°59.1′	5.0	7	2	321	13.9	0.08	2.0	pdc
March 1	1142:05.34	4	22°35.4′	44°59.4′	5.0	6	1	304	10.1	0.07	0.8	pdc
March 2	0825:51.83	3	22°42.0′	44°56.6′	4.7	6	1	206	3.3	0.02	0.6	0.5
March 2	1023:06.17	3	22°38.7′	44°56.9′	4.8	4	1	283	3.0	0.02	1.2	1.5
March 3	0635:46.84	3	22°39.0′	44°58.3′	7.8	6	2	240	3.5	0.04	0.6	0.6
March 3	1435:56.56	1	22°43.6′	44°58.2′	6.2	4	1	248	2.8	0.01	1.8	0.6
March 3	1611:26.69	3	22°37.3′	44°54.2′	4.7	8	2	297	7.1	0.07	0.9	0.5
March 3	1715:12.04	3	22°37.3′	44°55.1′	4.4	5	1	315	6.2	0.01	1.3	0.8
March 3	2036:09.39	1	22°42.5′	44°59.2′	7.9	4	1	194	1.2	0.03	1.4	0.7
March 4	0447:46.14	3	22°39.6′	44°54.5′	5.3	6	2	293	4.2	0.02	1.2	0.4

Definitions are as follows: nor, number of readings; mag, maximum azimuthal gap; dcs, distance to the closest station; rms, root mean squared travel time residual; erh, horizontal error at 95% confidence (from projection of error ellipse onto horizontal plane); erz, error in depth at 95% confidence; pdc, poor depth control.

likely to be underestimates, perhaps by as much as a factor of 2, of the actual uncertainties in hypocentral parameters.

To assess the influence of the assumed velocity structure on the derived hypocenters, the events in Table 2 were relocated using several variants of the structure adopted above. For the 18 events with good depth control, hypocenters were redetermined with the P wave structure adopted above but with several different assumed values of the average V_p/V_s ratio. For a V_p/V_s ratio between 1.72 and 1.85, reasonable limits for oceanic crust [*Hyndman*, 1979], the precise ratio has little effect on final hypocentral locations.

The effects of the assumed shear wave velocity structure were further tested by omitting all shear wave arrival times and then determining the hypocenters of the 13 events with five or more P arrival times and good depth control. For 10 of these 13 events the 95% confidence ellipsoids determined using P arrivals alone enclose the corresponding hypocenters in Table 2. For the remaining three events the difference in locations involves principally a 3- to 5-km shift in the epicenter. The effect of including the S wave arrival times for the solutions in Table 2 is primarily to reduce the uncertainty in derived focal depth.

The locations of the 18 events with good depth control were also estimated using the crustal structure proposed by *Fowler* [1976] for the median valley of the Mid-Atlantic Ridge near 37°N. This P wave velocity structure, shown in Figure 6, differs significantly from the model used above, including somewhat higher velocities through much of the crust but a lower-velocity upper mantle. A V_p/V_s ratio of 1.75 was assumed to obtain the corresponding S wave velocity structure. Except for six events outside the instrument network, the estimated hypocenters obtained using the Fowler structure lie within the 95% confidence ellipsoids of the solutions in Table 2. Of the six exceptions a shallow event just south of the network (February 22, 2322 UT) is located 2.3 km deeper with the Fowler structure, and five events more distant from and southeast of the network are located 0.7–2.8 km shallower.

On the basis of these alternative hypocentral determinations we conclude that the microearthquake locations presented in this paper, including particularly their focal depths and their relationship to large-scale bathymetry, are not sensitive to uncertainties in the average P or S wave velocity structure.

The epicenters of all microearthquakes listed in Table 2 are displayed in Figure 7. Almost all microearthquakes detected by this network lie within or near the southern limits of our monitoring region. The southern portion of the network is near the epicenters of some of the largest earthquakes ($m_b \gtrsim 5.5$) that have been teleseismically located in the area within the last 20 years (Figure 2). Figure 7 also shows that the microearthquakes tend to occur beneath either the inner median valley or the eastern rift mountains, at least during the period of this experiment.

On the basis of the distribution of epicenters and focal depths, the earthquakes shown in Figure 7 can be divided into four distinct groups. The first two groups (here termed regions 1 and 2) consist of microearthquakes which occur beneath the inner floor of the median valley (Figure 7). Region 1 events occur within the network, while region 2 events occur immediately outside the network (less than 6 km from the nearest station). A third set of events encompasses hypocenters which occur very near or beneath the inner rift mountains. The depths and epicentral coordinates determined by HYPOINVERSE for events in these three groups are independently well resolved. The remaining events lie 10–15 km outside the

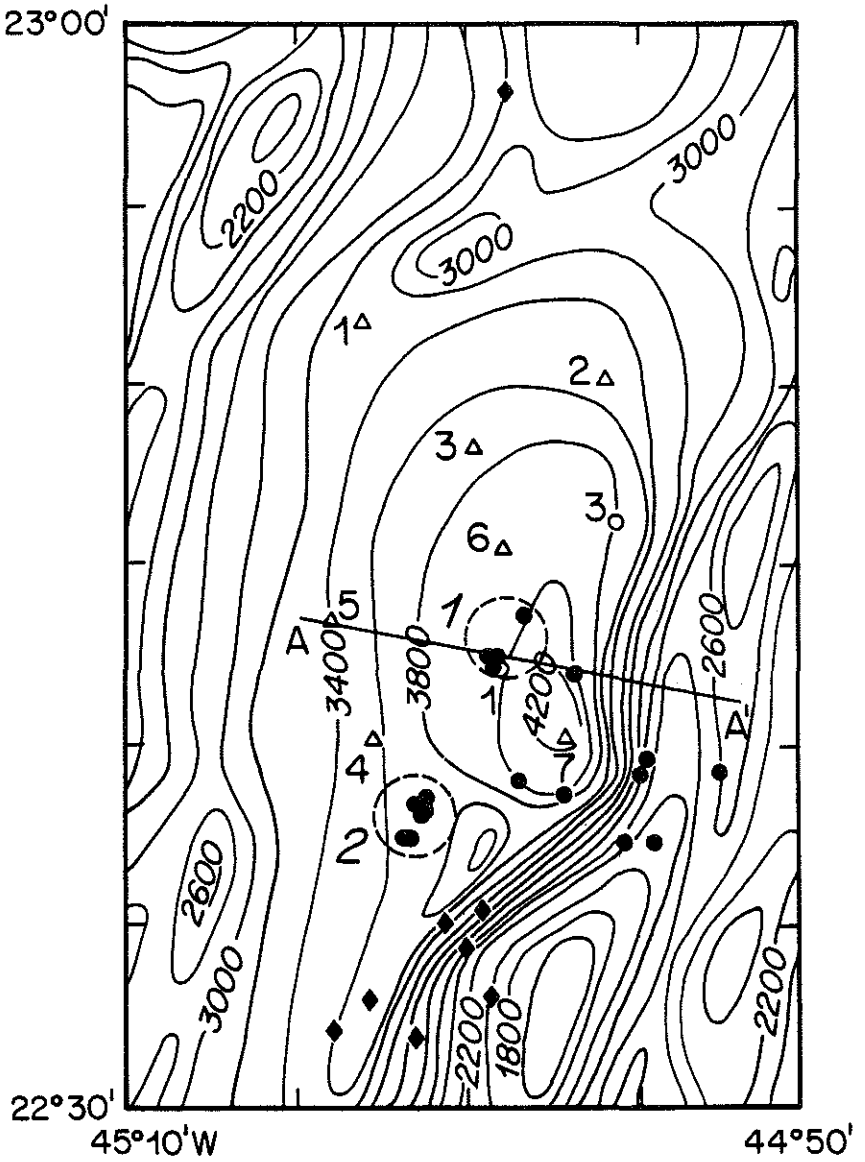

Fig. 7. Epicenters of microearthquakes located in this experiment (from Table 2). Solid circles indicate solutions with good depth resolution; regions 1 and 2 are encircled by dashed boundaries. Solid diamonds indicate solutions with no depth control. Stations are shown as open symbols. The line *A–A'* shows the location of the cross-section in Figure 8. Bathymetric contours are from Figure 2.

monitoring network (region 4) and have poor resolution of focal depth.

Seismicity of the Median Valley Inner Floor

The four events in region 1 (Figure 7) have epicenters less than 3 ± 1 km from OBS 1 and, as noted above, locations which are robust with respect to uncertainties in the *P* and *S* wave velocity structures. A projection of the hypocenters of these events onto a nearly east-west vertical plane (Figure 8) shows that the microearthquakes also cluster near a common depth of 6–8 km below the seafloor. This depth corresponds to the Moho transition zone and the uppermost mantle. Within region 1, no observed events occurred above 5 km depth. The locations of three additional events (not shown in Figure 7 or 8) with only four arrival times but with *S-P* times similar to one or more larger events provide further support for these generalizations.

The six epicenters in region 2 lie within a cluster about 10 km to the S-SW of region 1 (Figure 7). A line joining the activity of regions 1 and 2 would strike approximately N25°E, more easterly than the regional trend of the median valley (N10°E) but subparallel to the local topographic strike of the eastern crestal mountains. A single event in region 2 (February 22, 2322 UT) occurs within the uppermost kilometer below the seafloor datum, though as noted above, the focal depth for this particular event depends somewhat on the assumed velocity structure. The remaining events in region 2 cluster between 5 and 8 km depth (Figure 8). An apparent gap in seismic

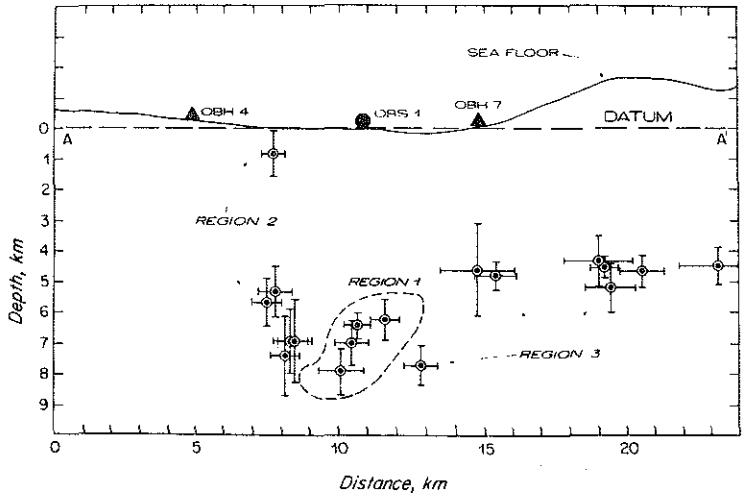

Fig. 8. Focal depths of microearthquakes beneath the median valley. Hypocenters have been projected onto the vertical plane through profile *A–A'* (Figure 7). Error bars show 95% confidence limits for focal depth and horizontal location in the plane of the figure. All depths are relative to the datum indicated by the dashed line. There is no vertical exaggeration of the bathymetry.

activity exists from 2 to 5 km depth, but this gap may be the result of the limited number of events.

The observed seismicity in regions 1 and 2 includes only microearthquakes which clearly lie within the comparatively flat-floored inner median valley. The effect of bathymetric relief on the location of these events is negligible.

Seismicity of the Inner Rift Mountains

Microearthquakes which occur within or near the rift mountains are included in region 3. The separation between median valley and rift mountain activity is somewhat arbitrary and based upon the epicentral locations relative to the bathymetry.

The eight epicenters within region 3 are dispersed throughout the eastern rift mountains (Figure 7). Some of the epicenters are as distant as 10–15 km from the center of the median valley floor. Localized areas of seismic activity similar to those observed in the median valley are not apparent beneath the rift mountains. The accuracy of the hypocenter estimates for events in region 3 is difficult to assess, however, because of the large bathymetric relief. Since the rift mountains rise 1.5 km above the datum used in HYPOINVERSE, the velocity model beneath the crestal mountains is likely to be incorrect. Without the use of a location algorithm capable of handling topography and laterally variable seismic velocity the hypocentral resolution for events in region 3 should be suspect.

The depth estimates of microearthquakes in region 3 consistently exceed 4 km below the datum (Figure 8). For the events near the median valley which do not occur beneath significant relief the depth estimates are probably correct. The depth of the westernmost event in region 3, for instance, is similar to that of events which occur clearly beneath the inner floor of the median valley. The focal depths of 4–7 km below the seafloor indicated for the remaining events in region 3 have larger uncertainties.

BODY WAVE PARTICLE MOTION

An important concern for the accurate estimation of source parameters is lateral heterogeneity in seismic velocity structure. As demonstrated from a microearthquake experiment in the Orozco transform fault [*Tréhu and Solomon*, 1983], lateral inhomogeneities can significantly affect estimates of hypocentral parameters and focal mechanisms. In that experiment, lateral variations were manifested by marked anomalies in the apparent incidence angle and approach azimuth of observed *P* and *S* waves [*Tréhu*, 1984]. In order to test for the presence of significant lateral variability within the region of our experiment, we have analyzed the particle motions of body waves recorded by OBS 1 following the procedure of *Tréhu* [1984].

The orientations of the horizontal seismometers on OBS 1 were determined from the particle motions of water wave arrivals from 11 of the 14 shots (three shots with low water wave amplitude were not included). On the basis of a least squared misfit between apparent and true azimuth for the first cycle of the water wave on the horizontal components, the *X* component (Figure 4) is oriented approximately N25° ± 10°E.

In Figure 9 the measured azimuths of approach and apparent incidence angles are shown for eight earthquakes and two shots with good signal-to-noise ratio on the horizontal channels for the first *P* arrival. The observed *P* waves for the remaining shots and earthquakes did not have a sufficient amount of energy on the horizontal components for particle motion analysis. Except for a single earthquake (March 3, 0635 UT) the measured azimuths of approach do not differ significantly from the expected values. The single anomalous azimuth may be due to event mislocation or to lateral heterogeneity along the path between this particular source-receiver pair. The observed azimuths of approach for *P* waves recorded at OBS 1 support the view that the assumed plane-layered velocity structure is a suitable first approximation to the structure in the region of this experiment.

In contrast, the observed incidence angles of the *P* waves at OBS 1 (Figure 9) display a systematic departure from predicted values. The difference between the observed incidence angles and those expected from the nominal ray parameter and the *P* wave velocity at the top of the crust is plotted as a function of azimuth in Figure 10. The departure of the incidence angle from the expected value appears to vary approximately sinusoidally with azimuth with an amplitude of about 20°. Station mislocation, a tilt of the gimballed horizontal

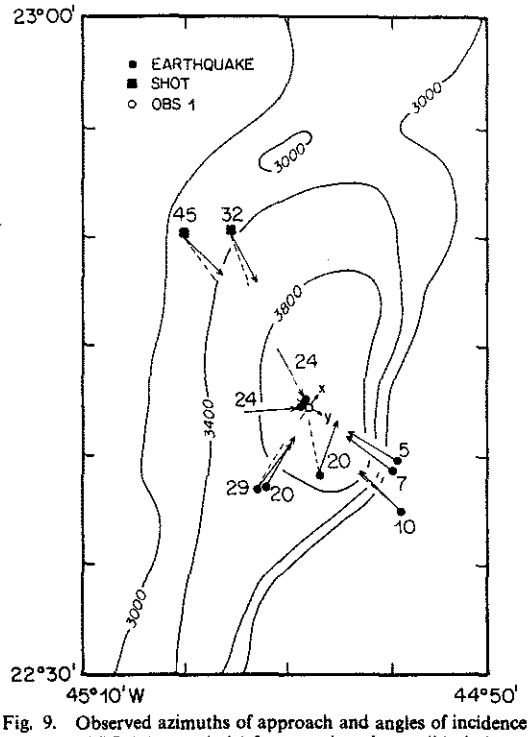

Fig. 9. Observed azimuths of approach and angles of incidence of *P* waves at OBS 1 (open circle) from earthquakes (solid circles) and shots (solid squares); only *P* waves with a good signal-to-noise ratio on the horizontal components are included. The orientation of the horizontal seismometers in OBS 1, derived from particle motion analysis of water waves from shots [*Tréhu*, 1984], is shown by the arrows marked *x* and *y*. The dashed line extending from the locus of each seismic event indicates the expected azimuth of approach, while the solid arrow shows the observed azimuth of approach as seen at the OBS. The observed angle of incidence in degrees is indicated by the number beside the corresponding epicenter or shot location. Selected bathymetric contours are from Figure 2.

geophones, and a systematic amplification of one horizontal geophone in relation to the other can probably be rejected as explanations of this variation because these effects should produce signatures at least as strong on the apparent azimuth of approach [*Tréhu*, 1984]. More likely explanations include a sloping interface beneath the OBS, poor coupling of the vertical channel, and lateral heterogeneity of crustal structure. We discount the last explanation on the basis of the general similarity of observed azimuths of approach to values expected for a plane-layered structure. A seafloor that slopes at about 25° to the E-SE can account for the anomalies in measured incidence angles for all of the data in Figures 9 and 10 except for the earthquakes located nearly beneath the OBS. An E-SE downslope direction is also in agreement with the large-scale bathymetry at the OBS 1 site (e.g., Figure 7). We thus have no strong reason to suspect that travel times or wave paths differ significantly from those predicted by the plane-layered structure of Figure 6.

FOCAL MECHANISMS

First-motion polarities from the OBH and OBS records have been used to determine composite focal mechanisms for selected groups of microearthquakes. Records of *P* waves and water waves from the 14 shots served to validate the polarities of the hydrophones and vertical seismometers. The azimuth to the station and the angle of emergence at the source follow from the calculated hypocenter and the assumed plane-layered velocity model. Equal-area projections of the lower focal hemisphere are used to plot all first-motion data; for waves leaving the source through the upper hemisphere, first motions are shown at the equivalent lower hemisphere position.

A composite fault plane solution for three earthquakes within region 1 is shown in Figure 11a. The three events (February 26, 2224 UT, February 28, 2333 UT, and March 3, 1435 UT) have epicenters within 3 km of OBS 1 (Figure 7) and focal depths between 6 and 7 km. Note that because the three-component OBS lies almost directly above the hyopcenters of region 1 earthquakes, the first-motion polarities recorded by this instrument provide unusually strong constraints on the focal mechanisms. Even including only clear and impulsive first motions, a good azimuthal distribution of stations for the composite fault plane solution (Figure 11*a*) is obtained. A normal-faulting mechanism is required by the composite first motions. The orthogonal nodal planes shown in Figure 11*a* do not fit the data perfectly, but the small misfit could easily be

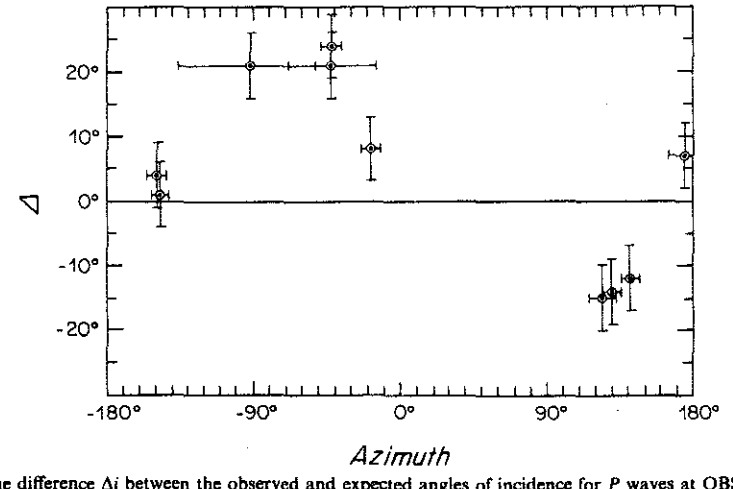

Fig. 10. The difference Δi between the observed and expected angles of incidence for *P* waves at OBS 1 as a function of path azimuth at the receiver. Azimuth is measured clockwise from north. The indicated errors in Δi are assumed to be $\pm 5°$ for all data. The indicated errors in azimuth are calculated from the errors in epicenter or shot position together with the range.

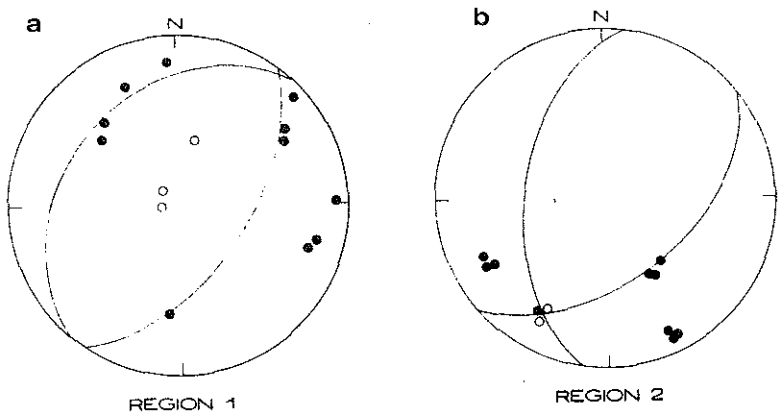

Fig. 11. Composite fault plane solutions of spatially grouped events within (*a*) region 1 and (*b*) region 2. Compressional arrivals are shown as solid circles; open circles are dilatations. Equal-area projections of the lower focal hemisphere. Fault planes shown have strike and dip (N36°E, 56°SE) and (N225°E, 35°NW) for Figure 11*a* and (N50°E, 50°SE) and (N190°E, 48°W) for Figure 11*b*.

the result of small errors in the focal depths or in the assumed velocity model. The nodal planes in the composite solution dip at about 35° and 55°; while these angles have individual uncertainties of 10° or more, the pattern of compressional first motions does not support a dip angle significantly less than 30° for either plane. The strike of both nodal planes is about N40°E, a direction oblique to the regional trend of the Mid-Atlantic Ridge (about N10°E) but closer to the local strike of the segment of inner rift mountains to the S-SE (Figure 7).

The region 1 earthquake of March 3, 2036 UT, was not included in the composite fault plane solution of Figure 11*a*. This event occurred at 7.9 ± 0.7 km depth, 1–2 km below the other earthquakes in region 1, and is the deepest event in Table 2. All first motions for that event are compressional, including the first motion at OBS 1 sited nearly above the focus. While a normal faulting mechanism can therefore be excluded, it is difficult to specify further the nature of this source from the analysis of first motions alone. A thrust-faulting mechanism would be consistent with the first motions, but we regard such a mechanism as extremely unlikely for an event within the median valley located within 1 km of a zone of normal faulting. Intrusion of magma into a crack or dike would also produce compressional first motions at all stations [*Aki et al.*, 1977; *Chouet*, 1981].

Figure 11*b* shows the composite fault plane solution determined from three earthquakes within region 2 (February 22, 2324 UT, February 23, 1127 UT, and February 26, 1729 UT). These events have very similar epicenters, and focal depths are all near 7 km. The composite first motions are compatible with normal faulting, but the mechanism is not well constrained because of the poor azimuthal distribution of receiving stations. The remaining three events within region 2 are either considerably more shallow (February 22, 2322 UT) or are located somewhat S-SW of the first group (February 28, 0849 and 0851 UT). These three events have first motions that are consistent with normal faulting, but their mechanisms differ from the composite mechanism in Figure 11*b*.

The composite fault plane solutions are shown in relation to the local bathymetry in Figure 12. Also shown are the epicenters and focal mechanisms of three large ($m_b \geq 5.3$) earthquakes that occurred in the same region. The source parameters of these events have been determined from the inversion of the long-period *P* and *SH* waveforms [*Solomon et al.*, 1983; *Huang et al.*, 1984]. A 1962 earthquake with a normal-faulting mechanism ($M = 5.7$, $M_0 = 6 \times 10^{24}$ dyn cm) has a centroid depth of 1.5 km below the seafloor. It is also possible to determine the water depth above the epicenter from the differences in arrival times of waves multiply reflected off the sea surface; the estimated water depth is about 3.5 km for this event. Two 1977 events ($m_b = 5.3$, $M_s = 5.6$, $M_0 = 3.0 \times 10^{24}$ dyn cm; and $m_b = 5.9$, $M_s = 6.0$, $M_0 = 1.1 \times 10^{25}$ dyn cm) have centroid depths of 2.5 and 1.6 km below the seafloor and estimated water depths of 4.0 and 3.5 km, respectively. These two earthquakes are part of a swarm of at least five events on the same day. Relative event relocation of this sequence shows that the event with the 4-km water depth lies to the east of the others by about the right amount for the entire sequence to have occurred beneath the inner floor of the median valley in the vicinity of the microearthquake epicenters.

Both the microearthquakes and the teleseismically recorded earthquakes display roughly similar mechanisms (Figure 12). While the focal depths for the large and small earthquakes appear to differ, the large events surely have a finite depth extent of slip. The centroid depth is generally regarded as a good estimate of the mean depth of seismic faulting, at least for nearly rectangular or circular faults with approximately uniform slip. The zone of major slip for these large earthquakes therefore extended to at least 3–5 km depth, and some limited region of slip to depths of 7–8 km is not precluded.

DISCUSSION

The hypocentral parameters for many of the earthquakes reported in this study are unusually well resolved compared to most marine microearthquake surveys described in the literature [e.g., *Duschenes et al.*, 1983]. For the 18 better located microearthquakes, epicentral coordinates and focal depths were resolved to about ±1 km formal error at 95% confidence. The robustness and precision of the estimated locations can be attributed to several factors in our experiment. A comparatively large recording network (10 instruments), with nearest instrument separation about 5 km, was employed. Instrument positions were relocated by acoustic ranging. Crustal structure was reasonably well known on the basis of a seismic refraction profile carried out within the area of the network. That plausible composite fault plane solutions of spatially related microearthquakes can be constructed is due in large part

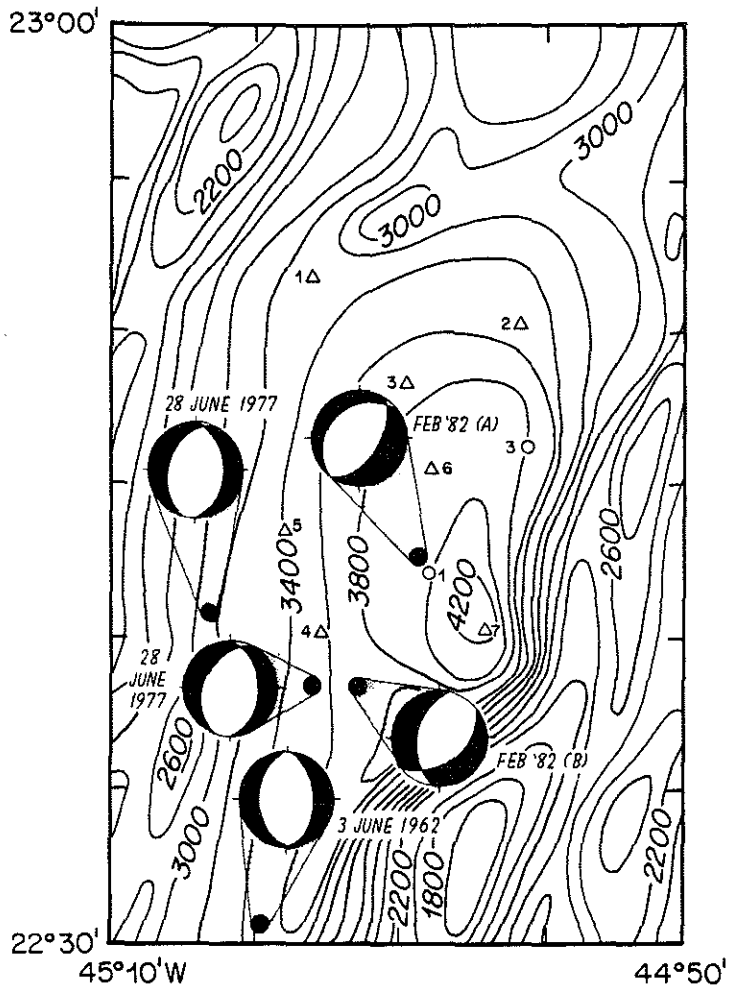

Fig. 12. Epicenters and fault plane solutions for the earthquake of June 3, 1962 ($M = 5.7$, $M_0 = 6 \times 10^{24}$ dyn cm), and two earthquakes in the swarm on June 28, 1977 ($m_b = 5.3$, $M_0 = 3 \times 10^{24}$ dyn cm; and $m_b = 5.9$, $M_0 = 1 \times 10^{25}$ dyn cm) [*Huang et al.*, 1984], compared with the composite fault plane solutions from Figure 11. Epicenters of the large earthquakes are taken from the International Seismological Summary and the International Seismological Centre; the water depths indicated by *P* waveform modeling [*Huang et al.*, 1984] suggest that these epicenters are mislocated by about 5–10 km to the west. Bathymetric contours are from Figure 2.

to the accuracy of estimated hypocentral locations and wave paths.

The focal depths of microearthquakes located beneath the inner floor of the median valley during our experiment ranged from 1 to 8 km beneath the seafloor; most events occurred at depths between 5 and 8 km (Figure 13). With one exception noted earlier all of these microearthquakes appear to have focal mechanisms characterized by normal faulting. These results indicate that brittle failure under extension is occurring to 7–8 km depth beneath the median valley inner floor along the segment of Mid-Atlantic Ridge sampled by our experiment.

The distribution of microearthquake focal depths displayed in Figure 13 may be compared with available data from other published studies for slow-spreading ridge systems. *Lilwall et al.* [1978] reported that microearthquake focal depths extended to at least 8 km beneath the Mid-Atlantic Ridge median valley floor at 45°N. Their hypocentral solutions were obtained with only three OBS's located to the west of all earthquake activity [cf. *Lilwall et al.*, 1977], however, and no errors were given for individual solutions. *Francis et al.* [1978] recorded microearthquakes near the eastern intersection of the St. Paul's Fracture Zone and the Mid-Atlantic Ridge with a four-OBS network; they reported activity to at least 7 km depth, but they did not present errors for individual solutions. The applicability of their findings to ridge axis regions well removed from the effects of large-offset transform faults was also not addressed. *Klein et al.* [1977] located 2500 hypocenters of earthquakes during a 1972 swarm on the Reykjanes Peninsula, a landward extension of the Mid-Atlantic Ridge onto Iceland. Using a 23-station network, they obtained well-constrained focal depths between 1 and 7 km; most focal depths fell between 2 and 5 km. The extent to which the Reykjanes Peninsula can serve as a tectonic model for standard mid-ocean ridges is, however, not known. These results from other studies, while limited to an unknown degree by either resolution or applicability, are broadly consistent with the distribution of microearthquake focal depths determined in our experiment.

The inference that brittle behavior extends to 7–8 km depth

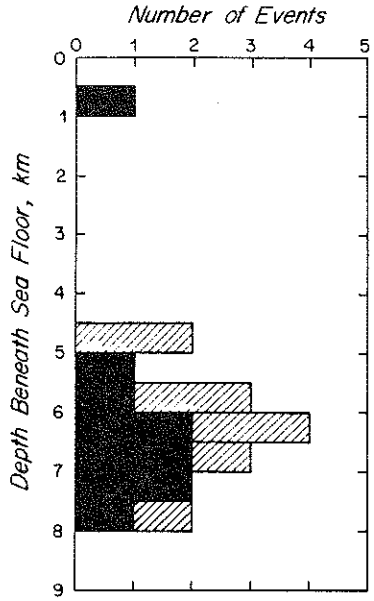

Fig. 13. Histogram of focal depths, in 0.5-km intervals, for the 18 microearthquakes with well-resolved hypocentral locations. Focal depths are relative to the seafloor at the epicenter. Solid bars denote events from regions 1 and 2; diagonally lined bars denote events from region 3.

beneath the inner floor of the median valley at the site of our experiment deserves further comment. Such a conclusion requires that the entire column of crust, perhaps including the uppermost mantle, has been cooled since emplacement to temperatures within the brittle field. Such extensive cooling, presumably caused by active hydrothermal circulation [*Lister*, 1977], suggests that significant time has elapsed since the most recent episode of crustal magma injection and volcanic activity along this segment of ridge axis.

The velocity structure determined from the refraction survey [*Purdy et al.*, 1982] conducted in the region of our microearthquake experiment provides independent support for the conclusion that the crust along this segment of ridge has been significantly cooled. The velocity distribution (Figure 6) and total crustal thickness are similar to those of normal young oceanic crust. Further, records from all shots within a 50-km range to the south and a 30-km range to the north of the OBH at 22°55'N (Figure 1) display travel time and amplitude characteristics that are typical of record sections from normal oceanic crust [*Purdy et al.*, 1982]. In particular, a clear Moho triplication is observed along the shooting line extending south of the OBH into the region of the microearthquake network and suggests a normal Moho transition zone.

The spreading process at mid-ocean ridges is likely to be episodic, so that different ridge segments are currently likely to be at different stages of volcanic and tectonic activity [e.g., *Francheteau and Ballard*, 1983]. On the basis of both earthquake hypocenters and crustal velocity structure this particular section of Mid-Atlantic Ridge median valley floor is apparently at a stage of advanced cooling. Establishing the relationship of earthquake activity to the various stages in the spreading process will require further experiments of the type reported here in axial regions of differing volcanic and tectonic characteristics.

Another feature of the distribution of focal depths in our study that may have significance is the paucity of hypocenters shallower than about 4 to 5 km depth (Figure 8). A similar observaion was made for microearthquakes at the eastern end of the St. Paul's transform by *Francis et al.* [1978], who suggested that the depth interval lacking seismic activity coincides with a layer of highly fractured, permeable material incapable of supporting stress.

As noted earlier, the composite fault plane solutions for microearthquakes within the median valley (Figure 11) are characterized by a large component of normal faulting and are similar to mechanisms obtained from an inversion of long-period *P* and *SH* waveforms from several large ridge-axis earthquakes which occurred in the same area [*Huang et al.*, 1984]. The fault planes in the composite solutions dip at angles greater than about 30° and strike parallel or subparallel to the local trend of the median valley. Because the choice of which nodal plane in each composite solution is the true fault plane cannot be made from available data, whether the fault planes dip inward toward or outward from the median valley cannot be ascertained. The similar mechanisms of large and small earthquakes together with the distribution of their focal depths suggests that this segment of Mid-Atlantic Ridge median valley is undergoing active rifting and seismogenic extension throughout the uppermost 7–8 km of oceanic lithosphere.

On the basis of first motions, relative amplitudes, and pulse durations on hydrophone records from three OBS's of microearthquakes beneath the median valley floor of the Mid-Atlantic Ridge at 45°N, *Lilwall* [1980] concluded that the focal mechanisms for those events are characterized by slip on nearly horizontal fault planes. The first motions of the microearthquakes observed in our study are not compatible with such a mechanism.

CONCLUSIONS

In this paper we have reported the locations and source mechanisms of the largest microearthquakes observed during a 3-week period in early 1982 within the median valley of the Mid-Atlantic Ridge near 23°N, approximately 90 km south of its intersection with the Kane Fracture Zone. Because of our large station network (seven OBH's and three OBS's), precise relocation of instruments by acoustic ranging, and a local crustal velocity structure known from seismic refraction analysis the best located microearthquakes have epicentral coordinates and focal depths resolved to within 1 km formal error at the 95% confidence level. Particle motion analysis lends further confidence to the locations and to the probability of minimal bias introduced by lateral heterogeneity in crustal velocity structure for events with epicenters within or immediately adjacent to the network.

Both the inner floor of the median valley and the eastern rift mountains were seismically active during the period of our experiment. Microearthquakes beneath the inner floor had focal depths generally in the range 5–8 km. Microearthquakes beneath the inner rift mountains had focal depths of 4–7 km and epicenters as much as 10–15 km from the center of the median valley, but these hypocenters have larger uncertainties because of unmodeled effects of topographic relief and potential associated complexities of velocity structure. Composite fault plane solutions for two clusters of events beneath the inner floor indicate normal faulting along planes which dip at angles greater than 30°. These solutions are similar to the mechanisms of nearby large earthquakes obtained by an inversion of long-period teleseismic *P* and *S* waveforms.

We interpret the distribution of focal depths and fault plane solutions to indicate that this segment of ridge axis is experiencing brittle failure to depths of 7–8 km. This inference requires that substantial cooling has progressed to these depths since emplacement of the crust and uppermost mantle. Additional support for a cooled crustal column in this region includes the observation of a velocity structure similar to normal young oceanic crust. The occurrence of several large earthquakes ($m_b \sim 5.5$–6) during the past 25 years may also be a signature of a brittle layer of substantial thickness. To the extent that the spreading process may be regarded as locally episodic this segment of ridge is undergoing at least limited extension but has probably not experienced recent volcanic or crustal magmatic activity.

APPENDIX: ERROR ANALYSIS FOR INSTRUMENT LOCATION

The instrument relocation algorithm of *Creager and Dorman* [1982] requires a priori estimates of shot positions, instrument depths, water-wave travel times, and the associated errors in each quantity. Instrument depths were obtained from 12-kHz echo-sounding records and an average sound velocity of 1.5137 km/s inferred from a local conductivity/temperature/depth cast. The 1 standard deviation error in instrument depth is subjectively estimated to be 150 m.

Because the satellite receiver used in this experiment did not provide estimates of the uncertainty in fix position [cf. *Matzke*, 1971], empirical estimates of the a priori uncertainty in each shot position are employed. These a priori errors depend upon the type and quality of fix and the elapsed time between a fix and acoustic ranging. For four of the shots which coincided with a satellite fix, the position errors, following *Creager and Dorman* [1982], are taken to be $\sigma_{lat} = 0.8$ km and $\sigma_{long} = 0.8/\cos\theta$ km, where θ is the elevation angle of the satellite above the horizon at the closest point of approach. For the remaining 10 shots, the 1 standard deviation location error is assumed to be described by a circle of radius 1.5 km. Because of the large number of shots used and the good geographic distribution of shot positions relative to the fixed stations the assumption of circular location errors for many of the shot positions has no significant effect on the final solution. Figure 5 shows that only four of the relocated shot positions lie outside their a priori 1 standard deviation error regions and all but one lie within their 2 standard deviation error regions.

Ocean bottom instrument positions are linked to the ship position fixes by the direct one-way acoustic travel times. Water wave arrivals on the OBH instruments are identified on a channel of filtered and rectified hydrophone data by an envelope detection procedure [*Koelsch and Purdy*, 1979]; the filter passband (0.15–2 kHz) is not sensitive to arrival of energy that has been refracted within the upper oceanic crust. Arrival times of direct water waves recorded by the OBH's may be read to within 10 ms. Water wave arrivals on the OBS instruments are identified on the normal seismometer channels, which are sensitive to frequencies within a 1- to 60-Hz band [*Mattaboni and Solomon*, 1977]. Because the water waves are often preceded by refracted waves, the uncertainty in reading water wave arrival times on the OBS's is somewhat greater than for the OBH's. In addition, identification of water wave arrivals on the OBS's may be affected by destructive interference of converted or reflected phases at the water-rock interface. That such a phenomenon may occur is suggested by a consistent overestimation of the calculated OBS depths by approximately 150 m, compared to the bathymetric map, when the Creager-Dorman relocation procedure is used simultaneously for all instruments. Because of the good azimuthal distribution of shot positions the estimated horizontal coordinates of the OBS's are probably not affected by this bias. On the basis of an a posteriori check of the statistical assumptions described below a value of 20 ms is assumed for the a priori estimate of the error in water wave travel times at 1 standard deviation for both the OBS and OBH instruments.

A total of 155 observations (118 travel times, 28 initial shot coordinates, and nine initial instrument depths) were used to estimate the 55 unknown parameters (the final positions of the 14 shot locations and the final locations, including depth, of nine instruments). A constant velocity ocean (1.5137 km/s) was assumed in calculating water wave travel times. The observed least squares residual follows a χ^2 distribution with 100 degrees of freedom. Because the *Creager and Dorman* [1982] procedure transforms data and parameter vectors into a coordinate system in which the covariance matrix of the observations is the identity matrix, the χ^2 estimate obtained from the least squares residual should approximate the number of degrees of freedom. The misfit between the least squares estimate of χ^2 and the theoretical value can be used as an a posteriori check of the statistical assumptions. Because the assumed uncertainties in instrument depths and acoustic ranging positions are comparatively well known, the a posteriori check primarily evaluates the validity of the assumed uncertainty in travel times [*Creager and Dorman*, 1982]. With the adopted uncertainties, including an a priori uncertainty in water wave travel time of 0.02 s, the estimate of χ^2 for this problem is 85. For an a priori uncertainty in travel time of 0.015 s, the estimate of χ^2 is 124. Thus the appropriate a priori error in water wave travel time lies somewhere between 0.015 and 0.02 s, and we adopt the more conservative value for the final instrument locations and errors given in Table 1 and Figure 5.

Acknowledgments. We are grateful to Don Koelsch, Carleton Grant, and Peter Roberts for their technical expertise with OBH and OBS instruments at sea, and we appreciate the considerable assistance of the captain and crew of the R/V *Knorr* in carrying out the experiment reported here. We also thank Anne Tréhu and Lee Gove for programming advice, M. D. Allison for assistance with data playback, Jan Nattier-Barbaro for help in manuscript preparation, and two anonymous reviewers for constructive comments. This research was supported by the National Science Foundation, under grants EAR-8018193 and EAR-8218611 to MIT and EAR-8018805 and EAR-8218357 to WHOI. Woods Hole Oceanographic Institution contribution 5836.

REFERENCES

Aki, K., and P. G. Richards, *Quantitative Seismology, Theory and Methods*, pp. 675–717, W. H. Freeman, San Francisco, Calif., 1980.

Aki, K., M. Fehler, and S. Das, Source mechanism of volcanic tremor: Fluid-driven crack models and their application to the 1963 Kilauea eruption, *J. Volcanol. Geotherm. Res.*, *2*, 259–287, 1977.

Bryan, W. B., and J. G. Moore, Compositional variation of young basalts in the Mid-Atlantic Ridge rift valley near 36°49'N, *Geol. Soc. Am. Bull.*, *88*, 556–570, 1977.

Cann, J. R., A model for oceanic crustal structure developed, *Geophys. J. R. Astron. Soc.*, *39*, 169–187, 1974.

Cessaro, R. K., D. M. Hussong, E. L. Ambos, and D. W. Forsyth, Transform fault seismicity in the Oceanographer Fracture Zone (abstract), *Eos Trans. AGU*, *63*, 1100, 1982.

Chouet, B., Ground motion in the near field of a fluid-driven crack and its interpretation in the study of shallow volcanic tremor, *J. Geophys. Res.*, *86*, 5985–6016, 1981.

Creager, K. C., and L. M. Dorman, Location of instruments on the seafloor by joint adjustment of instrument and ship positions, *J. Geophys. Res.*, *87*, 8379–8388, 1982.

Detrick, R. S., and G. M. Purdy, The crustal structure of the Kane Fracture Zone from seismic refraction studies, *J. Geophys. Res., 85*, 3759–3777, 1980.

Duschenes, J. D., T. W. Barash, P. J. Mattaboni, and S. C. Solomon, On the use of an externally deployed geophone package on an ocean bottom seismometer, *Mar. Geophys. Res., 4*, 437–450, 1981.

Duschenes, J. D., R. C. Lilwall, and T. J. G. Francis, The hypocentral resolution of microearthquake surveys carried out at sea, *Geophys. J. R. Astron. Soc., 72*, 435–451, 1983.

Fowler, C. M. R., Crustal structure of the Mid-Atlantic Ridge at 37°N, *Geophys. J. R. Astron. Soc., 47*, 459–491, 1976.

Francheteau, J., and R. D. Ballard, The East Pacific Rise near 21°N, 13°N, and 20°S: Inference for along-strike variability of axial processes of the mid-ocean ridge, *Earth Planet. Sci. Lett., 64*, 93–116, 1983.

Francis, T. J. G., and I. T. Porter, Median valley seismology: The Mid-Atlantic Ridge near 45°, *Geophys. J. R. Astron. Soc., 34*, 279–311, 1973.

Francis, T. J. G., I. T. Porter, and J. R. McGrath, Ocean-bottom seismograph observations on the Mid-Atlantic Ridge near lat 37°N, *Geol. Soc. Am. Bull., 88*, 664–677, 1977.

Francis, T. J. G., I. T. Porter, and R. C. Lilwall, Microearthquakes near the eastern end of St. Paul's Fracture Zone, *Geophys. J. R. Astron. Soc., 53*, 201–217, 1978.

Huang, P. Y., S. C. Solomon, E. A. Bergman, and J. L. Nabelek, Focal depths and mechanisms of Mid-Atlantic Ridge earthquakes from body waveform inversion (abstract), *Eos Trans. AGU, 65*, 273, 1984.

Hyndman, R. D., Poissons's ratio in the oceanic crust—A review, *Tectonophysics, 29*, 321–333, 1979.

Johnson, S. H., and P. R. Jones, Microearthquakes located on the Blanco Fracture Zone with sonobuoy arrays, *J. Geophys. Res., 83*, 255–261, 1978.

Johnson, S. H., H. Shimamura, K. Shibuya, K. Takano, and T. Asada, OBS study of Gorda Basin seismicity (abstract), *Eos Trans. AGU, 59*, 1199, 1978.

Jones, P. R., and S. H. Johnson, Sonobuoy array measurements of active faulting on the Gorda Ridge, *J. Geophys. Res., 83*, 3435–3440, 1978.

Klein, F. W., Hypocenter location program HYPOINVERSE, 1, User's guide to versions 1, 2, 3, 4, *U. S. Geol. Surv. Open File Rep., 78-694*, 103 pp., 1978.

Klein, F. W., P. Einarsson, and M. Wyss, The Reykjanes Peninsula, Iceland, earthquake swarm of September 1972 and its tectonic significance, *J. Geophys. Res., 82*, 865–888, 1977.

Koelsch, D. E., and G. M. Purdy, An ocean bottom hydrophone instrument for seismic refraction experiments in the deep ocean, *Mar. Geophys. Res., 4*, 115–125, 1979.

Lilwall, R. C., Fault mechanisms and sub-crustal seismic velocities on the Mid-Atlantic Ridge, *Geophys. J. R. Astron. Soc., 60*, 245-262, 1980.

Lilwall, R. C., T. J. G. Francis, and I. T. Porter, Ocean-bottom seismograph observations on the Mid-Atlantic Ridge near 45°N, *Geophys. J. R. Astron. Soc., 51*, 357–370, 1977.

Lilwall, R. C., T. J. G. Francis, and I. T. Porter, Ocean-bottom seismograph observations on the Mid-Atlantic Ridge near 45°N—Further results, *Geophys. J. R. Astron. Soc., 55*, 255–262, 1978.

Lilwall, R. C., T. J. G. Francis, and I. T. Porter, Some ocean-bottom seismograph observations on the Reykjanes Ridge at 59°N, *Geophys. J. R. Astron. Soc., 62*, 321–328, 1980.

Lister, C. R. B., Qualitative models of spreading-center processes, including hydrothermal penetration, *Tectonophysics, 37*, 203–218, 1977.

Macdonald, K. C., Mid-ocean ridges: Fine scale tectonic, volcanic and hydrothermal processes within the plate boundary zone, *Annu. Rev. Earth Planet. Sci., 10*, 155–190, 1982.

Macdonald, K. C., and B. P. Luyendyk, Deep-tow studies of the structure of the Mid-Atlantic Ridge crest near lat 37°N, *Geol. Soc. Am. Bull., 88*, 621–636, 1977.

Mattaboni, P. J., and S. C. Solomon, MITOBS: A seismometer system for ocean-bottom earthquake studies, *Mar. Geophys. Res., 3*, 87–102, 1977.

Matzke, D. E., An optimum six parameter estimation process for navigation satellite (SRN-9) data, *Mar. Technol. Soc. J., 5*, 37-42, 1971.

Minster, J. B., and T. H. Jordan, Present-day plate motions, *J. Geophys. Res., 83*, 5331-5354, 1978.

Purdy, G. M., P. D. Rabinowitz, and H. Schouten, The Mid-Atlantic Ridge at 23°N: Bathymetry and magnetics, *Initial Rep. Deep Sea Drill. Proj., 45*, 119–128, 1978.

Purdy, G. M., R. S. Detrick, and M. Cormier, Seismic constraints on the crustal structure at a ridge-fracture zone intersection (abstract), *Eos Trans. AGU, 63*, 1100, 1982.

Reid, I., and K. Macdonald, Microearthquake study of the Mid-Atlantic Ridge near 37°N, using sonobuoys, *Nature, 246*, 88–89, 1973.

Rowlett, H., Seismicity at intersections of spreading centers and transform faults, *J. Geophys. Res., 86*, 3815–3820, 1981.

Rowlett, H., and D. W. Forsyth, Recent faulting and microearthquakes at the intersection of the Vema Fracture Zone and the Mid-Atlantic Ridge, *J. Geophys. Res., 89*, 6079–6094, 1984.

Solano, A., and L. D. Bibee, Microseismic activity on the Gorda Ridge (abstract), *Eos Trans. AGU, 61*, 1048, 1980.

Solomon, S. C., E. A. Bergman, and P. Y. Huang, Earthquakes and tectonics at mid-ocean ridge axes (abstract), *Eos Trans. AGU, 64*, 759, 1983.

Spindel, R. C., S. B. Davis, K. C. Macdonald, R. P. Porter and J. D. Phillips, Microearthquake survey of median valley of the Mid-Atlantic Ridge at 36°30'N, *Nature, 248*, 577–579, 1974.

Sutton, G. H., F. K. Duennebier, and B. Iwatake, Coupling of ocean bottom seismometers to soft bottoms, *Mar. Geophys. Res., 5*, 35–52, 1981.

Sverdrup, K., K. C. Macdonald, W. A. Prothero, and I. Reid, Ocean bottom seismometer measurements of earthquakes on the Gorda Rise (abstract), *Eos Trans. AGU, 58*, 1230, 1977.

Tréhu, A. M., Lateral velocity variations in the Orozco transform fault inferred from observed incident angles and azimuths of *P* waves, *Geophys. J. R. Astron. Soc., 77*, 711–728, 1984.

Tréhu, A. M., and S. C. Solomon, Coupling parameters of the MIT OBS at two nearshore sites, *Mar. Geophys. Res., 5*, 69–78, 1981

Tréhu, A. M., and S. C. Solomon, Earthquakes in the Orozco transform zone: Seismicity, source mechanisms, and tectonics, *J. Geophys. Res., 88*, 8203–8225, 1983.

van Andel, T. H., and C. O. Bowin, Mid-Atlantic Ridge between 22° and 23° north latitude and the tectonics of mid-ocean rises, *J. Geophys. Res., 73*, 1279–1298, 1968.

M. H. Murray, MIT/WHOI Joint Program in Oceanography, Woods Hole Oceanographic Institution, Woods Hole, MA 02543.

G. M. Purdy, Department of Geology and Geophysics, Woods Hole Oceanographic Institution, Woods Hole, MA 02543.

S. C. Solomon and D. R. Toomey, Department of Earth, Atmospheric, and Planetary Sciences, Massachusetts Institute of Technology, Cambridge, MA 02139.

(Received August 1, 1984;
revised January 14, 1985;
accepted January 30, 1985.)

Chapter 4

MICROEARTHQUAKES BENEATH THE MEDIAN VALLEY OF THE MID-ATLANTIC RIDGE NEAR 23° N: TOMOGRAPHY AND TECTONICS

Introduction

The physical processes controlling crustal accretion at a mid-ocean ridge are known to display strong spatial and temporal variations. The nature and distribution of earthquakes and the lateral heterogeneity of seismic velocity structure constitute two crucial types of information on the current state of any given ridge segment. In 1982 two complementary seismic experiments were carried out to obtain such information for the segment of the median valley of the Mid-Atlantic Ridge south of its intersection with the Kane Fracture Zone (Figure 1). A seismic refraction experiment utilizing explosive charges and ocean bottom hydrophones (OBHs) was conducted along the median valley to a distance of 120 km south of the ridge-transform intersection; the analysis and interpretation of the data in terms of crustal structure and its along-axis variation have been described by *Purdy and Detrick* [1986]. A microearthquake experiment was carried out in the median valley near 22°45'N with a network of 7 OBHs and 2 ocean bottom seismometers (OBSs); the hypocenters and fault plane solutions of 26 microearthquakes located beneath the inner floor and rift mountains were reported by *Toomey et al.* [1985]. In this paper we present additional data from the microearthquake experiment on the nature of seismic faulting in the area and on the lateral variation in crustal P-wave velocity structure across the median valley; from these results and those of other

studies of the region we develop a simple model for the recent tectonic evolution of this segment of the median valley.

The segment of the Mid-Atlantic Ridge south of the Kane Fracture Zone has been the focus since 1982 of several additional geological and geophysical investigations, including a Sea Beam bathymetric survey [*Detrick et al.,* 1984], a Sea MARC I sidescan sonar imaging survey [*Mayer et al.*, 1985], an investigation of the mechanisms of several large median valley earthquakes [*Huang et al.,* 1986], discovery of a hydrothermal vent field [*Kong et al.,* 1985; *Ocean Drilling Program Leg 106 Scientific Party,* 1986], crustal drilling at two axial sites [*Leg 109 Scientific Party,* 1986], and geological exploration by submersible along several traverses of the median valley [*Karson et al.,* 1987]. Overall, these investigations document significant along-axis variability in median valley morphology, volcanic and hydrothermal activity, and styles of tectonic extension. The diverse observations of this segment of the Mid-Atlantic Ridge median valley allow us to place the results of the microearthquake and seismic velocity studies within the context of a well-documented regional description of axial processes.

We begin by augmenting the number of located microearthquakes by a factor of 2 from that considered earlier [*Toomey et al.*,1985, hereafter referred to as *Paper 1*]. The additional data help to define both seismicity patterns and possible fault geometries. We also estimate seismic moments and approximate source dimensions for the best-located earthquakes. We then employ a tomographic technique [*Thurber,* 1983] to invert the P-wave travel time residuals from microearthquakes and local shots to obtain a two-dimensional representation of

crustal structure across the median valley inner floor. We show that the travel time residual data can resolve a region of relatively low P wave velocities at 1-5 km depth beneath the central inner floor, probably the site of most recent crustal accretion. On the basis of several synthetic experiments, we demonstrate that neither this lateral heterogeneity in structure beneath the inner floor nor the velocity heterogeneity associated with the variation in topography across the transition from inner floor to rift mountains should contribute significant bias to microearthquake locations. Finally, we synthesize the microearthquake and crustal structure information with the bathymetry [*Detrick et al.*, 1984] and the record of larger earthquakes [*Huang et al.*, 1986] to suggest that this section of median valley has been undergoing continued horizontal extension and modest block rotation without crustal-level magma injection for at least the last 10^4 yr.

Microearthquake Data

In *Paper 1* consideration was limited to microearthquakes with five or more arrival time readings, including at least one S wave arrival time obtained from a three-component OBS. These criteria were satisfied by 26 microearthquakes, a small fraction of the several hundred events recorded during the experiment. An expanded microearthquake population is considered in this paper by relaxing the criteria on the number and type of arrival times to include all events with at least four arrival times. The locations of the smaller events added to the expanded data set are not, in general, as accurate as those of *Paper 1*, but similarity in waveform and relative arrival time to one of the larger and better recorded events can

nonetheless give further confidence in the locations. The additional information obtained from the enlarged data set provides an improved insight into the tectonic processes active along this segment of the median valley.

The acoustically relocated instrument positions, hypocenter location procedure, and assumed seismic velocity model are as in *Paper 1*. In a later section, we assess the effects of lateral heterogeneity of seismic velocity on hypocentral locations, and we confirm the accuracy of the locations obtained on the assumption of lateral homogeneity. Figure 2 shows the configuration of the instrument network in the context of the detailed bathymetry of the median valley [*Detrick et al.*, 1984].

Hypocenter Locations

An additional 27 microearthquakes have been located beyond those presented in *Paper 1*; their hypocentral parameters are given in Table 1. Twenty-four of the 27 new events were located with four or more P wave arrival times but no S wave arrival times, while the remaining three events were located with three P arrival times and one S time. The statistical uncertainty of these 27 locations are, in general, larger than the errors reported for hypocentral locations in *Paper 1*, a result of inadequate observations that cause the inverse problem to be ill conditioned. The smallest eigenvalue in the singular value decomposition of the partial derivative matrix [*Klein*, 1978] is usually associated with an eigenvector whose predominant component is the focal depth. When this eigenvalue is less than a cutoff value [*Klein*, 1978], we fix the focal depth and estimate epicenter and

origin time; these events are designated by the term 'poor depth control' (pdc) in Table 1. In the final inversion iteration for some of these events an additional eigenvalue associated with one of the epicentral coordinates was also less than the cutoff value; for these events an epicentral uncertainty of 5 km was arbitrarily assigned (Table 1). For the 27 events in Table 1, the overall rms travel time residual is 0.05 s; excluding two events located more than 10 km south of the array, the overall rms residual is 0.03 s. These values are consistent with our assumed 'picking error' of 0.04 s [*Paper 1*].

Of the total of 53 microearthquakes in *Paper 1* and Table 1, 22 have epicentral coordinates and focal depths which may be independently estimated. Tests conducted with various plane-layered velocity models indicate that the hypocentral parameters of these well recorded events are not sensitive to uncertainties in the average P or S wave velocity structure [*Paper 1*]. Focal depth for the remaining 31 events is poorly resolved, either because the epicenter lies more than 10 km from the nearest instrument or because the number of reliable arrival times is too small. For 16 of the events, epicentral coordinates can nonetheless be resolved when focal depth is held to a fixed value.

The epicenters of all 53 microearthquakes from *Paper 1* and Table 1 are shown in Figure 2. Microearthquake activity during the deployment period was limited to the inner floor of the median valley and to the eastern rift mountains. No earthquakes detected during the deployment period had a location in the western rift mountains, and only one event occurred north of about latitude 22°45'N. On the basis of the 26 events in *Paper 1* the microearthquake activity had been grouped

into four geographic regions. Two of these regions were located on the inner floor, including one within the monitoring array and one 5-6 km south of the array. With the additional data in this paper it is evident that the inner floor activity cannot be divided into distinct regions. We therefore divide our discussion of microearthquake activity into three categories: earthquakes beneath the inner floor, earthquakes beneath the eastern rift mountains, and events distant from the network with poorly constrained epicenters.

Seismicity of the Median Valley Inner Floor

The new data set in Table 1 includes 10 events beneath the inner floor, four with well resolved focal depths and six with epicenters estimated after fixing the depth. For the latter six microearthquakes, epicenters were estimated at a series of fixed focal depths from 1-20 km. On the basis of the rms travel-time residual as a function of assumed focal depth and the predominance of focal depths in the range 5-8 km for the better recorded inner floor microearthquakes, a fixed focal depth of 6 km was selected for the estimation of epicentral coordinates. The range in epicentral locations for other values of depth in the range 5-8 km suggest that the formal errors listed in Table 1 for these six epicenters should be increased by factors of 2 to 4.

Combining the new locations with those previously reported [*Paper 1*] yields a total of 23 microearthquakes beneath the inner floor of the median valley during the 10 day deployment period of the full network; for 17 of these events epicenters and focal depths may be independently resolved. The formal errors in hypocentral coordinates of the better located microearthquakes beneath the inner floor are

approximately ±1 km at the 95% confidence level [*Paper 1*]. Twenty of the 23 epicenters within the inner floor occur within approximately 1 km of a line which strikes N25°E (Figure 2). During the deployment period, seismic activity was observed along this line over a distance of about 17 km. For comparison, the regional trend of the median valley between latitudes 22°30' and 23°N is about N10-15°E, and the azimuth of a great circle between the deployment site and the spreading pole between the North American and African plates is N 10°E [*Minster and Jordan,* 1978]. The hypocenters of the 17 events with well resolved focal depths are projected onto a vertical plane that is perpendicular to the N25°E trend of seismicity in Figure 3. As documented in *Paper 1*, most microearthquakes beneath the inner floor have focal depths between 5 and 8 km. For comparison, *Purdy and Detrick* [1986] estimated that the crust-mantle transition beneath the inner floor at this site occurs at approximately 6-7 km depth.

Seismicity of the Inner Rift Mountains

The newly located microearthquakes in Table 1 include 13 events beneath the eastern rift mountains. None of these 13 microearthquakes were sufficiently well recorded to constrain focal depth. For two of the events the epicenters were determined with focal depth held fixed. For the remaining 11, the epicenters are not well constrained by travel time analysis alone, but a comparison of seismic waveforms with those from events with well determined hypocenters helps to estimate epicentral coordinates. Figure 4 shows the seismograms recorded by OBH 7 (Figure 2) from these 13 events, as well as the seismogram from the larger event of February 24, 2151 UT [*Paper 1*]. All but the first event in Figure 4 occurred

during a single 24-hour period. Seismograms from the first 11 events in Figure 4 display a remarkable degree of similarity. The correlation coefficient between the records of events 1 and 2 is 0.84; similar values are obtained for different combinations of the first 11 waveforms. The repeatability of short-period waveforms from these events implies that their source locations and mechanisms are nearly identical. There is also a strong similarity between the group of waveforms of the first 11 events in Figure 4 and those from the next three, for which epicentral locations have been determined with more confidence. Probably all of these earthquakes occurred near the hypocenter of the earthquake of February 24, 2151 UT, the best-located event in the sequence (Table 2, *Paper 1*).

For the first 14 waveforms in Figure 4, there is a prominent phase arriving about 0.7 s after the initial P wave. This phase cannot be a direct S wave (converted at the seafloor), which should arrive 1.2 s after P. An examination of other hydrophone and seismometer records from these and other events has also led us to rule out the likelihood that this arrival corresponds to a multiple generated beneath the receiving station, a reflection from a near-source discontinuity, an arrival from a later travel-time branch, or a complexity to the source time function. The phase was most prominent on OBH 7 and OBS 3, the two instruments nearest the steep scarps of the eastern rift mountains (Figure 2). The arrival time is consistent with that of a P wave that exited the seafloor along the inner wall, about 1 km to the east of the instruments, and traveled the final distance through the water. An S-to-P conversion at some interface along the path between the source and receiver is another possibility. We do not have sufficient information to test

these suggestions further.

Including the events reported in *Paper 1*, 18 microearthquakes can be located beneath the eastern rift mountains. The hypocenters of five rift mountain earthquakes with well resolved focal depths, all from *Paper 1*, are depicted on the vertical cross-section in Figure 3. In *Paper 1* it was noted that uncertainty in these rift mountain hypocentral locations have an unknown contribution from the likely failure of the assumption of laterally homogeneous velocity structure used in hypocentral location. We address this question at length in a later section.

Focal Mechanisms

First motion polarities from the additional microearthquake data of this paper provide stronger constraints on composite focal mechanisms of the type presented in *Paper 1.* Composite fault plane solutions from 12 inner floor events with independently resolved hypocentral parameters are depicted in Figure 5. First motions from an additional three well-located inner floor events were examined but were not included because of unusual hypocentral locations or apparently different source mechanisms. Figure 5a shows a composite focal mechanism for seven events with epicenters within the network. A normal faulting mechanism is clearly indicated by the composite first motions. The two nodal planes dip at angles of about 45° and both strike at approximately N15°E. Slip on a subhorizontal fault [cf. *Lilwall,* 1980] can be excluded for these events.

In Figure 5b first motion data from five additional inner floor microearthquakes with epicenters 4-5 km south of the network are combined with the data of Figure

5a. The source mechanism that is shown satisfies most, but not all, of the first motion data. Focal mechanisms of individual microearthquakes, of course, may vary somewhat along the inner floor, which would contribute to the misfit for such a composite solution. The mechanisms of these inner floor microearthquakes nonetheless appear to be well characterized by normal faulting on planes with dip angles in excess of 30°.

A composite fault plane solution of seven rift mountain earthquakes with well resolved hypocenters is shown in Figure 5c. Only weak constraints are possible on the fault plane solution because of the comparatively poor coverage of the focal sphere. About all we may conclude is that these data are compatible with normal faulting.

Seismic Moments and Source Dimensions

Displacement spectra of P and S waveforms on OBS records and pressure spectra of P waveforms on OBH records were determined to estimate seismic moment and source dimensions of selected earthquakes. For an OBS, displacement spectra provide a valid measure of source properties only for a seismometer package that is well coupled to the seafloor [e.g., *Sutton el al.,* 1981; *Trehu and Solomon,* 1981, 1983]. In our experiment, spectra on OBS 3 (Figure 2) appear uncontaminated by coupling resonance, but seismograms recorded on OBS 1 show an apparent resonance at 4-5 Hz in the waveform following the S arrival (Figure 4 in *Paper 1*). Inspection of displacement spectra from OBS 1 confirm that P and S waveforms were complicated by coupling resonances. From

P wave particle motions and incident angles, we suggested in *Paper 1* that the OBS 1 seismometer package may have been resting on a slope inclined at 25°; such a steep slope may have contributed to the poorer coupling characteristics. Only spectra from OBS 3 were used to estimate seismic moment and corner frequency. Displacement spectra were determined from P and S waveforms recorded on the vertical component; corrections for instrument response and for attenuation followed *Trehu and Solomon* [1983].

We determined the pressure spectra from P waves recorded on OBH 7, an instrument which yielded clear records of all but 2 of the events located beneath the inner floor and the eastern rift mountains. Spectra were corrected for instrument response [*Koelsch and Purdy*, 1979] and were converted to equivalent displacement spectra by dividing by $\rho c \omega$, where ω is the angular frequency and ρ and c are the density and sound speed of seawater, respectively. This correction is equivalent to the assumption that the P waves are incident as plane waves [*Urick,* 1975]. P wave spectra from the OBH were corrected for attenuation in the same manner as for the OBS. Examples of waveforms and displacement spectra from OBS 3 and OBH 7 are shown in Figure 6.

The seismic moment was estimated from the displacement spectral amplitude Ω_o at low frequency using the formula of *Brune* [1970]

$$M_o = \frac{4\pi \rho_o \times V^3 \Omega_o}{KR} \qquad (1)$$

where ρ and V are the density and seismic velocity, respectively, at the source, x is the path length, R is a radiation pattern factor, and K is a correction factor for the interaction of seismic waves with the seafloor. The above formula holds for both P and S waves [*Hanks and Wyss,* 1972], provided that V, Ω_0, K and R take on appropriate values for either P or S waves. For events beneath the rift mountains, the focal mechanisms are poorly constrained and R was taken equal to 1 for both P and S waveforms. For events beneath the inner floor, R for P and SV waves was calculated from the composite fault plane solution shown in Figure 5a. The values used for ρ, V_p, and V_s were 2.9 g/cm^3, 6.5 km/s, and 3.7 km/s, respectively.

The correction factor K depends on the type of receiver (OBS or OBH), the material properties of the ocean and the uppermost crust, the angle of incidence of the upcoming wave, and the wave type (P or SV). We calculated values of K from plane wave theory; the P and S velocity and density of the uppermost crust were taken to be 3.5 km/s, 2.0 km/s, and 2.9 g/cm^3, respectively, and the P velocity and density of water were taken to be 1.5 km/s and 1.0 g/cm^3, respectively. For the earthquakes under consideration the incidence angles of P and SV waves are 20 to 30°. For P waves K is approximately 1.5 and slowly varying at these angles of incidence. For SV waves K varies from 0.6 to 0.8 at these incidence angles and was taken to be 0.7.

Seismic moments and corner frequencies obtained for five events from OBS 3

waveforms and moments estimated for 39 events from OBH 7 records are listed in Table 2. Seismic moments calculated from P waveforms recorded on the OBS agree well with those obtained from S waveforms. Moments obtained from OBS and OBH records agree to within about a factor of 2. The largest recorded event, located beneath the rift mountains, had a seismic moment of about 10^{20} dyn cm. The smallest recorded earthquakes, located generally within the network and beneath the inner floor, had seismic moments of about 10^{17} dyn cm.

The distribution of earthquakes by seismic moment is often cast in the form

$$\log N(M_o) = A - B\, M_o \qquad (2)$$

where $N(M_o)$ is the number of events with moment greater than M_o for a given region and time interval. The data from OBH 7 records given in Table 2 are displayed in this form in Figure 7. A group of 19 events located within about 1 km of the trend of inner floor seismic activity (Figure 2) is treated separately from 20 other events with epicenters east of the first group. For the eastern group of 20 earthquakes, located primarily beneath the rift mountains, linear regression yields a B value of 0.5 ± 0.1. For inner floor microearthquakes, a plot of M_o versus slant range from OBH 7 suggests that the recorded events with $M_o < 10^{18}$ dyn cm sample a smaller volume than do events with $M_o > 10^{18}$ dyn cm. Including only the group of larger events yields $B = 0.8 \pm 0.2$ (Figure 7).

The S wave corner frequencies f_c in Table 2 can be related to the radius r of the equivalent circular source by the relation [e.g., *Brune,* 1970; *Madariaga,* 1976; *Brune et al.,* 1979]

$$r = C V_s / f_c \qquad (3)$$

where V_s is the S wave velocity at the source and C is a factor that depends on the azimuth to the source and a model of the rupture process. Values of C generally range from 0.2 to 0.4, giving values of source radius of about 100 to 200 m for the five rift mountain events recorded on OBS 3. The implied values for average fault slip and average stress drop for these earthquakes [*Brune,* 1970] are in the range 0.3 - 10 mm and 1 - 70 bar, respectively.

Tomographic Analysis of Travel Time Data

The distribution of seismic sources and receivers in this experiment is sufficient to conduct a tomographic inversion of travel time data to determine the two-dimensional structure of the P wave velocity across the inner floor of the median valley. One indication in *Paper 1* that lateral heterogeneity in crustal velocity structure might be present in the region of the microearthquake experiment was the distribution of P wave station delay times. These delays, introduced in *Paper 1* to account approximately for the effects of differing elevation and shallow velocity structure beneath the network stations, were obtained from the mean travel time residuals observed at each station for a group of 10 well-recorded microearthquakes. While the delays at most stations displayed the expected negative correlation with elevation, the delays at OBH 3 and OBH 5, both on the western side of the median valley, were significantly more negative than expected from local water depth (Figure 8). In this section we begin with a brief outline of the tomographic method and the data set, and we follow with a discussion of the

sensitivity of the resulting models to the assumptions. We conclude that the available P wave travel time residuals indicate a region of relatively lower velocities at 1-5 km depth confined to the central portion of the median valley inner floor.

Description of the Method

The tomographic method used to invert P wave travel times is a variation of the technique developed by *Thurber* [1981, 1983] for simultaneous inversion for earthquake location and velocity structure. Thurber's method incorporates two features that make its use advantageous. First, travel times of first arriving body waves are estimated by a computationally efficient, three-dimensional, approximate ray tracing routine [*Thurber,* 1983]. Second, the model parameterization is flexible and permits an arbitrarily and continuously varying velocity field. The velocity field is represented as a continuous function which depends on the linear average of velocity values at nearby nodes; the locations of nodal points that parameterize the velocity field may be irregularly spaced. Given that the nodes adequately sample the volume to be imaged, velocity models of arbitrary geometry can be constructed more readily than with 'block' model velocity parameterizations [e.g., *Aki and Lee,* 1976]. Velocity model perturbations are estimated iteratively by solving a linearized set of equations by the Levenburg-Marquardt method of damped least squares. An F test on the ratio of mean squared travel time residuals from two successive iterations is the basis for terminating the iterative solution; individual squared residuals are weighted in the manner described in *Paper 1.* Iteration ceases when the ratio of successive travel

time residual variances falls below a critical value defined by the 5% level of significance.

The variation of Thurber's method employed here optimizes the velocity structure while holding all four hypocentral parameters to values specified by the starting model. The fixed hypocentral parameter restriction was imposed because of the limited size of the travel time data set. For reasons given below, only six stations were included in the tomographic network, so at most six P wave arrival times were included for each earthquake. Since parameter separation would remove four of the possible six arrival time observations for hypocenter relocation [*Pavlis and Booker,* 1980], leaving at most only two observations per earthquake to constrain crustal structure variations, we opted to fix all hypocentral parameters. This approach is based on the assumption that travel time anomalies caused by small perturbations in the hypocentral parameters are independent of those due to small perturbations in the velocity model [*Pavlis and Booker*, 1980]. The fixed-hypocentral-parameter restriction could, of course, introduce erroneous results if the assumed hypocentral parameters are not 'close' to their true values. In a later section we quantify the effects of velocity heterogeneity on the hypocenter location method, we define what is meant by 'close,' and we conclude that fixing hypocentral parameters to values determined by our location procedure is a reasonable approximation.

Even with all hypocentral parameters fixed, the size of the travel time residual data set is insufficient to conduct an inversion for three-dimensional structure. We therefore chose to conduct a two-dimensional inversion for the variation in P wave

velocity within a cross section perpendicular to the median valley axis.

Summary of Data

The data set to be inverted consists of travel times from 37 earthquakes and nine shots to six stations (Figure 9). The six instruments are located at the southern end of the network and recorded clear P arrivals for most earthquakes. The two northernmost ocean bottom hydrophones (OBH 1 and OBH 2) and the northernmost ocean bottom seismometer (OBS 3) were not included in the tomography analysis because few P arrivals were well recorded at these stations. The 37 microearthquakes exclude all events with poorly constrained epicenters, events with less than four clear P arrivals at the six stations, and the February 22, 2322 UT, inner floor earthquake with a focal depth that is strongly dependent on the assumed source structure [*Paper 1*]. Focal depths of 21 of these 37 earthquakes were independently resolved. Of the remaining hypocenters determined for fixed depths, three were located beneath the inner floor and 13 beneath the rift mountains. The microearthquake travel time data as utilized in the tomography analysis are not corrected for station delays. Station elevations must therefore be explicitly included in the definition of station locations.

Nine of the 14 shots used for network station location [*Paper 1*] were included as sources in the tomography analysis (Figure 9). For each shot, travel times and source coordinates were adjusted to the seafloor by applying simple water path corrections [*Purdy*, 1982]. Ray entry points at the seafloor for each shot-receiver pair were determined from the range, an estimate of phase velocity derived from the refraction data of *Purdy and Detrick* [1986], and the assumption that the P wave

propagated in the sagittal plane. The water depth at the ray entry point was assumed to be equal to the water depth beneath the shot point, taken from the Sea Beam bathymetric map of *Detrick et al.* [1984]. Travel times of shots were corrected for the water segment of the path assuming a uniform velocity of 1.5137 km/s [*Paper 1*]. Origin times and locations of shots, so adjusted, remained fixed throughout the tomographic inversion. The five shots not included in the inversion were located above the rough topography of the eastern rift mountains; the simple water path corrections for some source-receiver paths for these shots were subject to errors of as much as 0.1 s because of incorrect water depth. Trial inversions that included travel times from these shots yielded rms travel time residuals for these 5 shots approximately 0.03 s larger than for the other nine.

The inclusion in the tomography analysis of travel time data from the shots, whose positions are known to within 20-30 m at one standard deviation [*Paper 1*], helps to constrain the inversion results in two different and important ways. First, the shot data improve the sampling of layer 2 and uppermost layer 3. Second, the shot data are not biased by the velocity structure assumed in the estimation of hypocentral parameters. In the next section we demonstrate that inversions including shot data can be used to discriminate among source structures assumed for hypocentral locations.

The total travel time data set prior to inversion has an rms residual of 0.13 s; the travel times of P waves from the 37 earthquakes to the 6 stations have an rms residual of 0.11 s; the travel times for P waves from the 9 shots to the same 6 stations have an rms residual of 0.19 s. These values exceed the likely uncertainty,

about 0.04 s [*Paper 1*], due to errors in reading arrival times, locating sources and receivers, correcting for clock drift, and correcting wave paths from shots to the seafloor. We attribute a significant portion of the excess residual to heterogeneous velocity structure.

Description of Starting Models: Tests of Robustness

The two-dimensional P wave velocity model to be estimated by tomographic inversion is defined parametrically by the values of velocity at each of 12 nodes. The nodes are arranged in three vertical columns spaced 6 km apart; the columns are aligned in a plane oriented perpendicular (N100°E) to the regional trend of the median valley. Each column contains a node at 0, 1, 3 and 5 km depth. The closely spaced shallow nodes were found to be necesary in order to model the steep velocity gradient in the uppermost crust. Several different placements of the nodes with respect to sources and receivers have been considered (Figure 9). Velocity is estimated between nodes by linear interpolation [*Thurber*, 1983]. For all inversions, the initial velocity model is laterally homogeneous.

Non-linear inverse problems require an assessment of the dependence of the final solution upon the assumed initial values of model parameters. We conducted several tests of the influence on the final solutions of the initial velocity model and the assumed source population and hypocentral parameters (Table 3). Two velocity models were considered for both the initial velocity model and the source structure for microearthquake location. These were the median valley structure of *Purdy and Detrick* [1986] obtained from refraction data collected near the site of the microearthquake survey (Figures 1 and 9) and the velocity model obtained by

Detrick and Purdy [1980] from a refraction experiment on 7 m.y.-old oceanic crust. Hypocentral parameters of the 21 microearthquakes with independently resolved focal depths were calculated for both velocity models. Model-dependent station delays were included in the location procedure. Values of focal depth and origin time calculated with the 7 m.y.-old crustal structure were systematically shallower and later by about 0.4 km and 0.09 s, respectively, than values estimated for the inner floor crustal structure. These systematic biases produce travel times for the 7 m.y.-old crustal structure that are less, on average, by as much as 0.10 s.

Tomographic inversions of travel times from the 21 microearthquakes with well-resolved focal depths were conducted for each initial velocity structure in order to assess the influence of hypocentral parameters on the tomography results. Inversions numbered 1 and 3 of Table 3 summarize the results for hypocentral parameters based on the 7 m.y.-old and inner floor source structures, respectively. The final rms travel time residual and percent variance reduction are similar for both inversions, indicating that the two inversion solutions model the travel time data equally well. Inspection of the final velocity models, however, indicates that while the relative velocity variations are similar between the two models, the values of velocity at a given node differ by as much as 1 km/s. These results suggest either that travel time data from earthquakes alone do not constrain strongly the absolute values of velocity or that at least one of the sets of hypocentral parameters yields travel time data that are biased by the assumed source structure.

The ambiguous character of these results can be resolved by inclusion of the travel time data from shots. The input to inversions 2 and 4 (Table 3) is identical to

that for inversions 1 and 3, respectively, except for the addition of shot data. The relatively small variance reduction and large value of final rms residual for inversion 2 (Table 3) suggests that the travel time data from shots are inconsistent with the earthquake travel time data determined with the 7 m.y.-old source structure. In contrast, the larger variance reduction and smaller final residual for inversion 4 (Table 3) indicates that the travel time data from shots and earthquakes are more nearly consistent when the inner floor structure is assumed for hypocentral locations. For inversions 2 and 4, the values of velocity at well resolved nodes at 0 and 1 km depth agree to within 0.2 km/s, underscoring the important control of shallow structure by the shot data. At depths of 3 - 5 km, however, values of velocity differ by as much as 1 km/s between inversions 2 and 4. Also, nodal velocity values differ between inversions 1 and 2 by as much as 1.3 km/s, while velocities obtained from inversions 3 and 4 agree, on average, to within 0.3 km/s at well resolved nodal locations. We conclude from these results that inclusion of travel time data from shots is capable of resolving the ambiguity in velocity models obtained from microearthquake travel time data alone. In particular, the microearthquake hypocentral parameters calculated with the 7 m.y.-old source structure are less compatible with the travel time data from shots than are those calculated with the inner floor structure.

It is important to note that these results do not prove that the hypocentral parameters obtained with the one-dimensional inner floor velocity model are unbiased. The possibility remains that our location method is not adequate for locating events in a laterally heterogeneous structure. We address this point in a

later section and we conclude that the errors introduced by our location procedure are acceptably small.

In addition to the above tests of the inversion procedure, we also varied the initial velocity model from that assumed in calculating hypocenters, and we varied the subset of microearthquake sources included in the set of travel time data. Inversion 5 (Table 3) is identical to inversion 4 except for the initial velocity structure. The final rms travel time residual and variance reduction for inversions 4 and 5 are nearly identical. Values of nodal velocity agree at all but two poorly resolved seafloor nodes to within 0.2 km/s for the solutions from the two inversions. This degree of agreement suggests that the final velocity model is independent of the assumed initial structure. Inversion 6 is similar to inversion 4 except that travel times from all 37 microearthquakes with well-resolved epicenters are included in the data set. The effect of including more events is principally to increase ray-path sampling. Nodal values of velocity in the final solution of inversion 6 agree to within 0.2 km/s of the values for the solution from inversion 4 at all but one node. Inversion 7 is similar to inversions 4 and 6 except that the microearthquake travel time data set is limited to the 19 inner floor events. Nodal velocity values agree to within 0.2 km/s with those from inversion 4. These tests demonstrate that the final velocity models are robust with respect to the subset of microearthquake travel time data that is utilized in the inversion.

Results of Tomographic Inversions

Representative solutions to the tomographic inverse problem are depicted in Figures 10 and 11. Figure 10 gives the values of P-wave velocity and associated

error and resolution at each of the 12 parametric nodes for inversions 3 and 6 (Table 3). The linearly interpolated two-dimensional velocity structure resulting from inversion 6 is shown in Figure 11. The error is the standard deviation in the percent difference between the final nodal velocity and the initial value. Parameter resolution values, obtained from the diagonal elements of the resolution matrix [*Wiggins,* 1972; *Jackson*, 1972], provide approximate estimates of the ability of the data to resolve the parameter in question. A resolution value of 1 indicates that a parameter was independently resolved, while a value of 0 indicates that a parameter is either unconstrained by the data or completely dependent on the values of other parameters. A threshold for an acceptable resolution value depends on the application. For the present problem we somewhat arbitrarily choose a value of 0.4 for the threshold, a value above which indicating that the travel time data constrain the given nodal velocity. Naturally, the higher the value of the resolution the more confident we are that the available data constrain the velocity.

The two-dimensional velocity models resulting from tomographic inversion indicate that P-wave velocities at 1-5 km depth beneath the central median valley inner floor are significantly lower than in surrounding regions (Figures 10 and 11). The velocity contrast is most pronounced between the central and western inner floor. For inversions 4 through 7, the velocity contrast is largest (0.4 - 1.0 km/s) at 0 - 2 km depth, indicating that upper crustal P wave velocities are 10 to 20% higher beneath the western inner floor than along the center. The average velocity contrast over this depth range is not dependent on the initial velocity model. For

these same inversions, the velocity below about 2 km depth is 0.2 - 0.8 km/s, or about 5%, higher beneath the western inner floor than along the center. Velocity contrast between the eastern and central inner floor at shallow depth (0 - 2 km) is poorly resolved by the available data (Figure 10). Resolution improves at 3 - 5 km depth, with velocities higher by several percent beneath the eastern inner floor than in the center. An inversion identical to inversion 6 but with each column of nodes shifted westward by 2 km (Figure 9) yielded a velocity solution nearly indistinguishable from that in Figures 10 and 11.

It should be noted that, because of the coarse horizontal spacing between adjacent nodes in the velocity parameterization, the inversion solutions are laterally smoothed representations of the crustal structure. While the tomographic results demonstrate that P wave velocities are systematically lower within the narrow volume of crust beneath the central inner floor, the detailed form of the velocity structure on a lateral scale less than the nodal separation cannot be specified. Improved resolution of lateral heterogeneity of velocity structure beneath the Mid-Atlantic Ridge median valley must await experiments that provide a denser sampling of the crustal volume to be imaged.

Effects of Velocity Heterogeneity on Hypocenter Locations

The hypocentral parameters of microearthquakes reported in *Paper 1* and in Table 1 were calculated under the assumption of a laterally homogeneous velocity model [*Purdy and Detrick,* 1986]. Both the rugged topography of the rift mountains and the laterally heterogeneous velocity structure of the median valley inner floor

obtained by tomographic inversion call this assumption into question. We have consequently evaluated the effects of velocity heterogeneity on hypocentral locations by means of three-dimensional ray tracing. As we demonstrate below, a comparison of travel time calculations for heterogeneous and homogeneous models indicates that the hypocentral parameters calculated for the homogeneous structure are generally reliable. Two separate models of lateral heterogeneity have been examined. First, a model representing the velocity heterogeneity associated with topographic relief was tested to assess the accuracy of earthquake locations beneath the eastern rift mountains. Second, the two-dimensional model obtained from tomographic analysis was tested to determine the effects of heterogeneity on the locations of microearthquakes beneath the inner floor.

We adopted the following procedure for constructing these velocity models. A three-dimensional grid of P or S wave velocity values was used to define a set of cubic splines, from which values of velocity and its first and second spatial partial derivatives were obtained within the model. The method employed the tensor product of splines under tension [*Cline* , 1974], which incorporates a norm that minimizes the curvature of the functional representation, thus effectively limiting the magnitude of unwanted oscillations of the spline fit. The values of velocity and its spatial partial derivatives as calculated from the spline representation were inspected to assure smoothness and accuracy.

Rift Mountain Model

For the model of rift mountain topography, we assume that surfaces of constant velocity are simple downward translations of seafloor topography; i.e., the velocity

is a uniform function of the depth beneath the seafloor. One justification for this simple model is the demonstration by *Purdy and Detrick* [1986] that the crustal structure beneath the inner floor is similar to normal oceanic crust, so that thermal and lithologic contributions to lateral velocity variations associated with crustal aging are likely to be less important than those associated with topographic relief. Since a major contributor to the relief is normal faulting [e.g., *Macdonald and Luyendyk,* 1977] and since the results of this study suggest that active normal faults extend to the base of the crust, simple translation of crustal velocity structure across major faults is a reasonable working hypothesis. For simplicity, we do not include the seismic velocity heterogeneity of the inner floor as documented by the tomographic analysis in this first model.

A two-dimensional P wave velocity model consistent with these assumptions is shown in Figure 12. The model includes a flat inner floor and represents the inner rift mountains by a steep rise of 1.8 km over a horizontal distance of 5 km. A sine function was used to describe the topographic relief across this rise. The P wave velocity as a function of depth beneath the seafloor was taken to be the piecewise exponential structure used by *Purdy and Detrick* [1986] to model the travel times along the inner floor (Figure 12a).

Seismic rays were traced through the model of Figure 12 using two complementary methods. First, a 'shooting' routine [*Lee and Stewart,* 1981] was employed to explore the general effects of topography upon ray paths. The shooting method is an efficient initial value formulation which does not incorporate control over the final end point of the ray. We examined hundreds of P wave ray

paths for different source positions beneath the rift mountain portion of the model. Results of these calculations allow us to conclude that ray paths of P waves from sources with shallow depths (within 1-2 km of the seafloor) deviate from a vertical plane because of upper crustal lateral heterogeneity. In contrast, paths from sources deeper than about 2 km beneath the seafloor to positions within the inner floor lie within or very close to a vertical plane. P wave ray paths from these deeper sources are not noticeably perturbed by the laterally variable structure associated with topographic relief.

Second, an approximate ray tracing routine [*Thurber,* 1983], which does not attempt to solve the ray equations, was used to estimate the P and S ray paths between a specified source and receiver. These estimates served as initial ray paths to the 'bending' routine of *Pereyra et al.* [1980]. The bending method is a boundary value formulation in which the endpoints of a ray and an initial estimate of a stationary ray path are specified. The results of ray bending calculations are summarized in Figure 13. This figure shows the P and S wave travel time differences between the laterally homogeneous (Figure 12a) and laterally heterogeneous (Figures 12b and 12c) velocity models for six stations; the S velocity structures are determined from the P wave structures of Figure 12 assuming $V_p/V_s = 1.75$. The six fixed receiver positions (Figure 12b) approximate those of actual stations which routinely recorded arrivals from rift mountain earthquakes.

Results from the ray bending calculations indicate that travel times (Figure 13) and ray paths of P and S arrivals from sources deeper than about 2 km below the

seafloor are similar for both the laterally homogeneous and heterogeneous velocity models. The average travel time difference for sources deeper than 2 km is about 0.03 s (Figure 13), a figure less than our estimated travel time picking error [*Paper 1*] of 0.04 s.

As a final check, we inverted the synthetic travel times generated from the ray bending calculations and the laterally heterogeneous P and S velocity models with the same laterally homogeneous velocity structure and hypocentral location procedure used for our microearthquake data; station delays were recalculated for the new synthetic travel time residual data set in accordance with our procedure in *Paper 1*. In agreement with our results above, estimated focal depth and epicentral coordinates of rift mountain earthquakes deeper than 3 km beneath the seafloor are within 0.3 km of their correct values. These results indicate that the formal errors given by the location procedure give reasonable estimates of the uncertainty in hypocentral parameters. In contrast, locations of sources less than 3 km beneath the seafloor were poorly resolved and the convergence rate of the iterative location procedure was unusually slow. On the basis of these travel time calculations and source relocations we conclude that the hypocenters of the seven well recorded rift mountain earthquakes reported in *Paper 1* are accurately estimated despite the large topographic relief and associated lateral heterogeneity in velocity structure.

Inner Floor Model

For the P velocity model of the inner floor, the solution to the tomographic inversion was merged with the refraction results [*Purdy and Detrick*, 1986]. Within the central region of the two-dimensional model (Figure 14), P wave velocity versus

depth follows Figure 12a. To either side of the central region, velocity increases smoothly with distance by a depth dependent amount that agrees with the results of tomographic inversion. The functional form of this increase is taken to be a sine function with a full wavelength of 10 km. As discussed earlier, the precise width of the low-velocity region of the central inner floor crust and the detailed shape of the velocity contours are not well resolved by the tomographic analysis. The S wave velocity structure was obtained from the P wave structure assuming $V_p/V_s = 1.75$.

For inner floor microearthquakes, most paths between sources and receivers are nearly straight lines. Because of this simple geometry, the effects of lateral heterogeneity will be confined principally to travel times. Extensive ray shooting calculations to explore for anomalous travel path effects were therefore not performed with this structure. The ray bending method was used to compare travel times for the laterally homogeneous and heterogeneous velocity models for a source beneath the inner floor and receiver locations as depicted in Figure 14. The fixed receiver locations in Figure 14 mimic those of the experiment and are identical to those of Figure 12b. Travel time differences between the two structures are shown in Figure 15. While travel times to stations within the central inner floor are largely unaffected by the laterally heterogeneous velocity, significant travel time differences are apparent for all source depths at stations outward of the axial low velocity region (compare stations OBH 5 and OBH 4, and to a lesser degree, OBH 7 in Figures 15 and 14b).

The effect of these travel time differences on hypocenter locations was evaluated by using the travel times calculated for the heterogeneous model as

input to the location procedure employed for the microearthquake data. In order to be consistent with our location procedure [*Paper 1*], station delays were recalculated for the new travel time data set. The range in station delays (0.10 s) is comparable to the range in travel time residuals (0.12 s) in Figure 15, though the delays and residuals at individual stations differ. Epicentral coordinates and focal depths calculated for the synthetic travel time data were, on average, within 0.3 km and 0.5 km, respectively, of their correct values. In comparison with the known locations, calculated focal depths were systematically underestimated. Estimated origin times were within 0.01 s of their correct values. These calculations indicate that hypocentral parameters presented in Table 1 and *Paper 1* for inner floor microearthquakes are robust with respect to the effects of laterally heterogeneous structure.

From the above results we can estimate the contribution from source mislocation to travel time anomalies and evaluate our assumption, utilized in the tomography analysis, that observed travel time residuals are due principally to path effects. For the average error quoted above for hypocentral parameters the travel time anomaly due to mislocation of a source whose focal depth is about 6 km is expected to be less than 0.07 s. This value is significantly less than the rms travel time residual prior to tomographic inversion and comparable to the final rms travel time residual (Table 3). The attribution of a major component of the initial residuals to path effects is therefore reasonable.

Tectonic Synthesis

In this section we attempt to place the results of the microearthquake observations and tomographic inversion within the context of Sea Beam bathymetry [*Detrick et al.*, 1984], the source mechanisms of large median valley earthquakes [*Huang et al.*, 1986], and the along-axis variation in inner floor crustal structure indicated by seismic refraction measurements [*Purdy and Detrick*, 1986]. We then present a simple kinematic model of the recent tectonic evolution of the median valley inner floor near the site of the microearthquake experiment.

Related Studies

The Sea Beam bathymetric map [*Detrick et al.*, 1984] provides substantially better resolution of the morphology of the median valley near 23°N than was previously available from single, wide-beam echo sounding data. As may be discerned from Figure 2, south of the along-axis high in the median valley near 22°55'N, there is an elongate axial depression that exceeds 4400 m in depth and abuts the steep scarp of the eastern rift mountains near 22°40'N. The overall length and trend of the depression, on the basis of the 4200-m depth contour, are about 12 km and N10°E, respectively. The topography of both the inner floor and the rift mountains is asymmetric across the median valley. The rift mountain inner wall is much steeper on the eastern side than on the west. As may be seen in the bathymetric profile displayed in Figure 16, the inner floor in the region of the microearthquake network dips eastward at about 5°. At its deepest point the axial depression is 300 to 400 m deeper than other portions of the inner floor at this latitude (Figure 2).

During the period 1962-1986 the median valley near the 22°40'N axial

depression has been the site of several large ($m_b > 5$) earthquakes. Focal mechanisms of three of the largest of these earthquakes determined by an inversion of long-period teleseismic P and S waveforms [*Huang et al.,* 1986] are similar to the normal faulting mechanisms of inner floor microearthquakes at this site (Figure 5) [*Paper 1*]. Epicentral locations of these earthquakes are constrained by the local bathymetry and estimates of the water depth above the epicenter from water-column reverberations in the P wavetrains [*Huang et al.,* 1986]. For example, a water depth of 4000 m above the epicenter of the initial event (m_b = 5.3) of an earthquake swarm on June 28, 1977 [*Huang et al.,* 1986], constrains the epicentral location to be near or within the 22°40'N axial depression. The maximum depth of slip beneath the seafloor and the along-axis extent of rupture for the three large earthquakes are constrained by the centroid depth and the duration of the source time function to be approximately 3-5 km and 10-15 km, respectively [*Huang et al.,* 1986]. In general, the strike and area of the seafloor projection of the fault surfaces for these large earthquakes are similar to the azimuthal trend and areal extent of the 22°40'N axial depression. These results are consistent with the simple hypothesis that a single large fault plane, with a down-dip length of 5-7 km and an along-strike extent of 10-15 km, undercuts the 22°40'N axial deep and has been the site of the several large earthquakes observed teleseismically in this region during the last 25 years. This hypothesis is depicted schematically in Figure 16; though the earthquake mechanisms are consistent with either a westward- or eastward-dipping fault plane, because of the asymmetric seafloor topography we prefer a westward dipping fault plane that cuts the seafloor at the base of the

eastern rift mountains. With this geometry, the inner floor microearthquakes cluster about the lower portions of this fault plane (Figure 16).

The P wave velocity structure of the inner floor crust near the axial depression is well constrained along strike by the seismic refraction line of *Purdy and Detrick*, [1986] and across strike by the tomography analysis presented above. *Purdy and Detrick* [1986] have demonstrated that the crustal thickness and P-wave velocity structure beneath the central inner floor, except for the lower velocities in layer 3, are similar to those of nearby 7 m.y.-old crust [*Detrick and Purdy,* 1980]. In particular, the layer 2-layer 3 and crust-mantle transition zones are well developed, and the uppermost mantle has a nearly normal P-wave velocity (7.9 km/s) and a positive gradient of velocity with depth. This crustal structure, in addition to the depth distribution of microearthquakes, constitutes strong evidence against recent magmatic activity beneath the inner floor of this segment of the median valley [*Paper 1*; *Purdy and Detrick*, 1986].

A Tectonic Model of Crustal Extension

A simple kinematic model of block faulting can satisfy these observations of bathymetry, earthquake source parameters, and seismic structure. In the model, the westward dipping fault of Figure 16 separates the eastern rift mountain and inner floor tectonic provinces. This boundary fault extends down-dip at an angle of about 45° from the seafloor at the foot of the crestal mountains to a depth of 5-8 km beneath the inner floor and extends along axis for a distance of at least 10 km. Repeated seismic slip on the boundary fault accommodates inner floor extension and rift mountain uplift and gives rise to progressive rotation of the inner floor fault

block. The combination of a eastward dipping inner floor with the exposed footwall scarp forms an asymmetric axial depression on the seafloor above the boundary fault (Figure 16).

The westward-dipping boundary fault is associated in this kinematic model with the rupture plane of at least some of the large earthquakes that have occurred in this region in the last 25 years. The dimensions and orientation of the boundary fault are consistent with the rupture dimensions and epicentral characteristics indicated by waveform inversion [*Huang et al.,* 1986]. By inference, the microearthquakes observed beneath the inner floor are also associated with the westward dipping boundary fault, either on the main fault itself or on nearby secondary faults. That the focal depths of the microearthquakes (5-8 km) coincide with the maximum depth of slip for the large earthquakes (approximately 5 km) [*Huang et al.,* 1986] lends support to this inference. Further support is provided by the similarity between the focal mechanisms of the smallest ($M_o = 10^{17}$-10^{19} dyn cm, Table 2) and largest ($M_o = 10^{24}$-10^{25} dyn cm [*Huang et al.,* 1986]) earthquakes observed [*Paper 1*] and the agreement between the along-axis extent and strike of the fault planes of the large earthquake [*Huang et al.,* 1986] and the observed distribution of inner floor microearthquakes (Figure 2).

The kinematic block faulting model permits order of magnitude estimates to be made of the time required to form the axial depression as well as the number and frequency of large earthquakes necessary to create the 300 to 400 m of associated relief. We assume, for simplicity, that the full spreading rate is currently being accommodated across the westward-dipping boundary fault, i.e., that neither

magmatic injection nor faulting on the western boundary of the median valley contribute significantly at present to plate spreading. By this assumption the vertical component of relative motion between the inner floor and the eastern rift mountains is equal to the full spreading rate of 27 mm/yr [*Minster and Jordan*, 1978]. If this geometry of faulting persisted unmodified for a finite duration, then the minimum time required to form the axial depression is approximately 10^4 yr. By this line of reasoning, we can also estimate the number of large earthquakes which would have occurred along the boundary fault of the axial depression within the past 10^4 yr. Assuming that the events studied by *Huang et al.* [1986] are representative of large earthquakes along the Mid-Atlantic Ridge median valley, we may infer that the average fault slip during large earthquakes is about 0.5 m. Thus, if the axial depression is principally the result of seismogenic slip associated with large earthquakes, about 10^3 large events are necessary to yield 300-400 m of relief. This number is equivalent to a recurrence period of about 10 yr. This compares with 4 earthquakes with $m_b \geq 5.5$ in the general vicinity of the axial depression near 22°40'N in the last 25 years. These simple calculations support the view that both the ongoing extension of the young oceanic lithosphere and the generation of the axial depression near 22°40'N are the result of repeated normal-faulting earthquakes during the past 10^4 yr.

Discussion

The seismicity, earthquake source properties, and seismic velocity structure observed during this experiment characterize this segment of the Mid-Atlantic Ridge as one that is currently undergoing active tectonic extension in the absence of crustal magmatic activity. The simple kinematic model of crustal extension and block faulting presented above suggests that this state has persisted for at least the last 10^4 yr. Several aspects of these results are deserving of further discussion. These include possible explanations for the low values of P wave velocity beneath the central inner floor, the fate of the boundary fault at depth, and the implications of our findings for the along-axis variability of spreading center processes, particularly along the portion of the Mid-Atlantic Ridge south of the Kane Fracture Zone.

The tomographic inversion of travel time data and the refraction analysis of *Purdy and Detrick* [1986] indicate relatively low P-wave velocities at 1-5 km depth within a narrow volume (less than 10 km wide) beneath the central inner floor. Lateral variation in crustal temperature structure can contribute to some, but not all, of the observed velocity heterogeneity. The temperature derivative of P wave velocity in oceanic gabbro is about -6×10^{-4} km/s/K [*Christensen,* 1979]; a lateral temperature contrast of 400 K at 3-5 km depth would account for a horizontal variation in velocity of about 0.25 km/s, or only about one third of the variation indicated in the tomographic inversion solutions (Figure 10). Such a temperature contrast is about the maximum that could be sustained without placing the lower crust beneath the central inner floor outside of the brittle field of behavior for gabbroic material [*Caristan,* 1982].

Purdy and Detrick [1986] attributed the low velocities to the presence of unfilled cracks and voids remaining after rapid cooling of the most recently injected crustal magma body. They further suggested that the evolution to the higher and more normal P-wave velocities that they observed beneath 7 m.y.-old crust occurs as a result of sealing of the cracks and pores by deposition of hydrothermal minerals. By this reasoning, the narrow volume of low velocities beneath the central inner floor (Figure 11) marks the locus of most recent magmatic emplacement, and the evolution of oceanic crustal structure is inferred to be essentially complete within a few hundred thousand years after crustal emplacement. This interpretation attributes the lateral differences in velocity in Figure 11 to a variation with crustal age.

An alternative interpretation of the low P-wave velocities beneath the central inner floor attributes significance to the coincidence of the zone of reduced velocities and the lower reaches of the inferred boundary fault (Figure 16). It is plausible that a major active fault extending to 5-8 km depth provides a ready route for seawater to penetrate the lower crust. Such penetration may have led to significant hydrothermal alteration and consequent reduction of the P-wave velocity [e.g., *Christensen,* 1966] in the overlying crustal column. By this scenario, the horizontal velocity variations in Figure 11 are not functions of crustal age. To the contrary, the block of lower velocities presently beneath the median valley inner floor will, by implication, be transported laterally by seafloor spreading processes without a significant increase in P-wave velocity and will remain a region of anomalously low velocity even at greater crustal ages.

Under these two interpretations of the velocity structure in Figure 11, somewhat different variations of P-wave and S-wave velocity across the median valley would be predicted , but the tomographic inversion does not have the spatial resolution necessary to resolve the differences in P-wave structure and insufficient S-wave arrivals were recorded during this experiment to address the S-wave velocity structure. The along-axis variation in structure is another potential discriminant between the two interpretations. *Purdy and Detrick* [1986] inferred that the crustal structure along this portion of the median valley inner floor is similar for an along-strike distance of 50-60 km, except for a 10- to 15-km-length zone of significantly lower velocity beneath the along-axis high at 22°55'N (Figure 1). Since such a distance considerably exceeds the length of the axial depression within which the microearthquake experiment was conducted (Figure 2), their observation favors the view that the variation in P-wave structure seen in Figure 11 is primarily a function of seafloor age.

The rotation of the inner floor crustal block in the kinematic model of Figure 16 raises the question of the nature of faulting at or below the depth of the deepest earthquakes. Finite rotation requires either that the bounding fault display a listric geometry or that the fault truncate at depth at a ductile shear zone [*Jackson and McKenzie,* 1983; *Brun and Choukroune,* 1983]. Such a zone of ductile shear has been suggested to occur at mid to lower crustal levels on the basis of field observations in ophiolites [*Casey et al.,* 1981]. The focal depths and mechanisms of large earthquakes [*Huang et al.,* 1986] and microearthquakes (Figure 5) at this site constrain the principal fault or faults to be planar or nearly planar to at least 5

km depth (Figure 16); modest lessening of the fault dip angle with greater depth is neither required nor precluded by the locations of microearthquake hypocenters and their associated errors (Figure 3). The nature of the deformation accommodating extension below about 8 km depth is not constrained by available data.

The 100 km of Mid-Atlantic Ridge median valley south of the Kane Fracture Zone can be divided into several distinct spreading center segments or cells [*Schouten and Klitgord,* 1982; *Schouten et al.,* 1985] variously dominated by recent tectonic extension or volcanic and hydrothermal activity [*Karson et al.,* 1987]. The microearthquake network (Figure 2) was located south of a prominent along-axis topographic high near 23°55'N (Figure 1). In the spreading cell hypothesis, along-axis highs correspond to sites of enhanced rates of crustal magma injection and generally higher crustal temperatures [*Whitehead et al.,* 1984; *Crane,* 1985; *Schouten et al.,* 1985]. *Purdy and Detrick* [1986] found that the P-wave velocities in the lower crust beneath the axial high near 22°55'N are even lower than elsewhere beneath the median valley inner floor, consistent with this high being a center of recent magmatic injection. During the period of the microearthquake experiment of this paper, only one earthquake was located in the vicinity of the along-axis high (Figure 2); had additional earthquakes of comparable size occurred during the deployment, the network configuration was such that they would have been readily detected and located. While a period of a few weeks is too short to characterize rates of seismic activity, the low seismicity we observed for the along-axis high is at least consistent with that region being in a state of higher

crustal temperatures and less well developed fault systems than in the region of the axial depression to the south.

In the spreading cell hypothesis, boundaries between adjacent cells are generally along-axis bathymetric lows [*Schouten et al.,* 1985; *Crane,* 1985]. These along-axis lows are often held to correspond principally to intersections with transform faults, small offsets of the ridge axis, or changes in the strike of the axial neovolcanic zone [*Macdonald et al.,* 1984; *Langmuir et al.,* 1986]. The axial depression at 22°45'N, however, appears to be simply a zone of prolonged crustal cooling and extension, rather than an obvious discontinuity in the position or trend of the accretion axis. This result suggests that boundaries to spreading cells along slow-spreading ridges can be manifested by regions in which prolonged periods of extension without magmatic injection occur without disruptions of the trend of the median valley inner floor. Whether this portion of the ridge axis serves as a boundary between spreading cells over time scales longer than 10^4 years remains to be demonstrated. Further microearthquake studies along axial lows and highs will be required to explore further the relationship between zones of active extension and possible configurations of spreading cells.

Conclusions

In this paper we report on the microearthquake source parameters and laterally heterogeneous seismic velocity structure of the Mid-Atlantic Ridge median valley near 23°N. In a data set expanded over that in an earlier report [*Paper 1*], a total of 53 microearthquakes were located over a 10-day period; all events

occurred beneath the median valley inner floor and eastern rift mountains. Twenty of 23 well-located inner floor epicenters define a line of activity 17 km long having a strike of N25°E. Linear trends were not resolved by the distribution of epicenters in the eastern rift mountains, although the earthquakes in that region displayed considerable temporal and spatial clustering. Earthquakes with well-resolved hypocenters, with the exception of a single shallow event beneath the inner floor, had focal depths of 4-8 km beneath the seafloor; the formal uncertainty in hypocentral coordinates for the better-located events is ±1 km at the 95% confidence level. Composite fault plane solutions determined from 12 inner floor events along the linear seismicity trend indicate normal faulting on planes dipping at angles near 45°. Normal faulting mechanisms, although poorly constrained, are also indicated for the rift mountain microearthquakes. The seismic moments of the recorded microearthquakes are in the range 10^{17}-10^{20} dyn cm; the moment-frequency distribution can be described by a B value of 0.8 ± 0.2 for the inner floor and 0.5 ± 0.1 for the rift mountains. Fault dimensions and stress drops for the largest microearthquakes are 200-400 m and 1-70 bar, respectively.

The inner floor seismicity is concentrated near an along-axis deep some 300-400 m deeper than immediately surrounding areas. Sea Beam bathymetry [*Detrick et al.,* 1984] indicates that the floor of the deep tilts eastward at about a 5° angle until it abuts the steeply dipping inner wall of the eastern rift mountains. The region of the along-axis deep has also been the site of several large earthquakes during the last 25 years [*Huang et al.,* 1986]. The along-axis length of the deep, the length of the inner floor seismicity trend, and the fault lengths of the large

earthquakes are all about 15 km. These results provide the motivation for a simple kinematic model of the local tectonics of the inner floor. According to the model, a major fault bounds the eastern limit of the inner floor within the deep; the fault is about 15 km long, dips westward at about 45°, and extends to 5-8 km in depth. Repeated slip on the fault during major earthquakes, at a rate of about one per 10 years, has led to the formation of the along-axis deep and to the eastward tilt of the seafloor. At the current rate of plate divergence, the observed relief could have been achieved in 10^4 years of extension without accompanying magmatic injection.

A tomographic inversion of P-wave travel time residuals from micro-earthquakes and local shots yielded an image of the lateral heterogeneity in crustal velocity structure across the median valley inner floor. P-wave velocities at 1-5 km depth within a narrow zone (less than 10 km wide) beneath the central inner floor are lower by several percent than in surrounding regions. The velocity anomaly is too large to be due to likely lateral variations in crustal temperature. One possible explanation for the low velocities [*Purdy and Detrick,* 1986] is that the region is the site of most recent magmatic injection and remains pervasively fractured as a result of rapid hydrothermal quenching of the newly emplaced crustal column. An alternative explanation is that the region is one of anomalously extensive alteration of the mid to lower crust enabled by deep penetration of seawater along the active normal fault bounding the along-axis deep. The along-axis extent of the region of lower velocities indicated by refraction data [*Purdy and Detrick,* 1986] favors the first explanation. By this interpretation, the seismic velocity structure at the ridge

axis evolves to that of normal oceanic crust within the first few hundred thousand years of crustal emplacement.

References

Aki, K. and W. H. K. Lee, Determination of three-dimensional velocity anomalies under a seismic array using first P arrival times from local earthquakes, 1, A homogeneous initial model, *J. Geophys. Res., 81,* 4381-4399, 1976.

Brun, J.-P., and P. Choukroune, Normal faulting, block tilting, and decollement in a stretched crust, *Tectonics, 2,* 345-356, 1983.

Brune, J. N., Tectonic stress and the spectra of seismic shear waves from earthquakes, *J. Geophys. Res., 75,* 4997-5009, 1970. (Correction, *J. Geophys. Res., 76,* 5002, 1971.)

Brune, J. N., R. J. Archuleta, and S. Hartzell, Far-field S wave spectra, corner frequencies and pulse shapes, *J. Geophys. Res., 84,* 2262-2272, 1979.

Caristan, Y., The transition from high temperature creep to fracture in Maryland diabase, *J. Geophys. Res., 87,* 6781-6790, 1982.

Casey, J.F., J.F. Dewey, P.J. Fox, J.A. Karson, and E. Rosencrantz, Heterogeneous nature of oceanic crust and upper mantle: A perspective from the Bay of Islands Ophiolite complex, in *The Sea,* vol. 7, *The Oceanic Lithosphere,* edited by C. Emiliani, pp. 305-338, John Wiley, New York, 1981.

Christensen, N.I., Elasticity of ultrabasic rocks, *J. Geophys. Res., 71,* 5921-5931, 1966.

Christensen, N.I., Compressional wave velocities in rocks at high temperatures and pressures, critical thermal gradients, and crustal low-velocity zones, *J. Geophys. Res., 84,* 6849-6857, 1979.

Cline, A. K., Scalar- and planar-valued curve fitting using splines under tension,

Numer. Math., 17, 218-220, 1974.

Crane, K., The spacing of rift axis highs: Dependence upon diapiric processes in the underlying asthenosphere?, *Earth Planet. Sci. Lett., 72,* 405-414, 1985.

Detrick, R. S., and G. M. Purdy, The crustal structure of the Kane Fracture Zone from seismic refraction studies, *J. Geophys. Res., 85,* 3759-3777, 1980.

Detrick, R. S., P. J. Fox, K. Kastens, W. B. F. Ryan, L. Mayer, and J. A. Karson, A Sea Beam survey of the Kane Fracture Zone and the adjacent Mid-Atlantic Ridge rift valley (abstract), *Eos Trans. AGU, 65,* 1006, 1984.

Hanks, T. C., and M. Wyss, The use of body-wave spectra in the determination of seismic-source parameters, *Bull. Seis. Soc. Am., 62,* 561-589, 1972.

Huang, P. Y., S. C. Solomon, E. A. Bergman, and J. L. Nabelek, Focal depths and mechanisms of Mid-Atlantic Ridge earthquakes from body waveform inversion, *J. Geophys. Res., 91,* 579-598, 1986.

Jackson, D. D., Interpretation of inaccurate, insufficient and inconsistent data, *Geophys J. R. Astron. Soc., 28,* 97-110, 1972.

Jackson, J., and D. McKenzie, The geometrical evolution of normal fault systems, *J. Struct. Geol., 5,* 471-482, 1983.

Karson, J. A., G. Thompson, S. E. Humphris, J. M. Edmond, W. B. Bryan, J. R. Brown, A. T. Winters, R. A. Pockalny, J. F. Casey, A. C. Campbell, G. Klinkhammer, M. R. Palmer, R. J. Kinzler, and M. M. Sulanowska, Along-axis variations in seafloor spreading in the MARK area, *Nature*, in press, 1987.

Klein, F. W., Hypocenter location program HYPOINVERSE, 1, User's guide to versions 1, 2, 3, 4, *U.S.Geological Survey Open File Rep., 78-694,* 103 pp.,

1978.

Koelsch, D. E., and G. M. Purdy, An ocean bottom hydrophone instrument for seismic refraction experiments in the deep ocean, *Mar. Geophys. Res., 4*, 115-125, 1979.

Kong, L., W. B. F. Ryan, L. A. Mayer, R. S. Detrick, P. J. Fox, and K. Manchester, Bare-rock drill sites, O. D. P. Legs 106 and 109: Evidence for hydrothermal activity at 23°N on the Mid-Atlantic Ridge (abstract), *Eos Trans. AGU, 66*, 936, 1985.

Lee, W. H. K., and S. W. Stewart, *Principles and Applications of Microearthquake Networks*, Academic Press, N.Y., 293 pp., 1981.

Leg 109 Scientific Party, Coring the crust and mantle, *Nature, 323*, 482-483, 1986.

Lilwall, R. C., Fault mechanisms and sub-crustal seismic velocities on the Mid-Atlantic Ridge, *Geophys. J. Roy. Astron. Soc., 60*, 245-262, 1980.

Macdonald, K. C., and B. P. Luyendyk, Deep-tow studies of the structure of the Mid-Atlantic Ridge crest near lat 37°N, *Geol. Soc. Amer. Bull., 88,* 621-636, 1977.

Macdonald, K.C., and J.C. Sempere, East Pacific rise from Siqueiros to Orozco Fracture Zones: Along-strike continuity of axial neovolcanic zone and structure and evolution of overlapping spreading centers, *J. Geophys. Res., 89,* 6049-6069, 1984.

Madariaga, R., Dynamics of an expanding circular fault, *Bull. Seismol. Soc. Am., 66*, 639-666, 1976.

Mayer, L. A., W. B. F. Ryan, L. Kong, and K. Manchester, Structure and tectonics of

the Mid-Atlantic Ridge South of the Kane Fracture Zone based on Sea Marc I and Sea Beam site surveys (abstract), *Eos Trans. AGU, 66,* 1092, 1985.

Minster, J. B., and T. H. Jordan, Present-day plate motions, *J. Geophys. Res., 83,* 5331-5354, 1978.

Ocean Drilling Program Leg 106 Scientific Party, Drilling the Snake Pit hydrothermal sulfide deposit on the Mid-Atlantic Ridge, lat 23°22'N, *Geology, 14,* 1004-1007, 1986.

Pavlis, G. L., and J. R. Booker, The mixed discrete-continuous inverse problem: Application to the simultaneous determination of earthquake hypocenters and velocity structure, *J. Geophys. Res., 85,* 4801-4810, 1980.

Pereyra, V., W. H. K. Lee, and H. B. Keller, Solving two-point seismic-ray tracing problems in a heterogeneous medium, Part 1. A general adaptive finite difference method, *Bull. Seismol. Soc. Amer., 70,* 79-99, 1980.

Purdy, G. M., The correction for the travel time effects of seafloor topography in the interpretation of marine seismic data, *J. Geophys. Res., 87,* 8389-8396, 1982.

Purdy, G. M., and R. S. Detrick, The crustal structure of the Mid-Atlantic Ridge at 23°N from seismic refraction studies, *J. Geophys. Res., 91,* 3739-3762, 1986.

Schouten, H., and K.D. Klitgord, The memory of the accreting plate boundary and the continuity of fracture zones, *Earth Planet. Sci. Lett., 59,* 255-266,1982.

Schouten, H., K.D. Klitgord, and J.A. Whitehead, Segmentation of mid-ocean ridges, *Nature, 317,* 225-229,1985.

Sutton, G. H., F. K. Duennebier, and B. Iwatake, Coupling of ocean bottom seismometers to soft bottoms, *Mar. Geophys. Res., 5,* 35-51, 1981.

Thomson, D. J., Spectrum estimation techniques for characterization and development of WT4 waveguide - 1, *Bell System Tech. J., 56,* 1769-1815, 1977.

Thurber, C. H., Earth structure and earthquake locations in the Coyote Lake area, central Califormia, Ph.D. Thesis, Mass. Inst. of Technol., Cambridge, 332 pp., 1981.

Thurber, C. H., Earthquake locations and three-dimensional crustal structure in the Coyote Lake area, central California, *J. Geophys. Res., 88,* 8226-8236, 1983.

Toomey, D. R., S. C. Solomon, G. M. Purdy, and M. H. Murray, Microearthquakes beneath the median valley of the Mid-Atlantic ridge near 23°N: Hypocenters and focal mechanisms, *J. Geophys. Res., 90,* 5443-5458, 1985.

Trehu, A. M., and S. C. Solomon, Coupling parameters of the MIT OBS at two nearshore sites, *Mar. Geophys. Res., 5*, 69-78, 1981.

Trehu, A. M., and S. C. Solomon, Earthquakes in the Orozco transform zone: Seismicity, source mechanisms, and tectonics, *J. Geophys. Res., 88,* 8203-8225, 1983.

Urick, R. J., *Principles of Underwater Sound*, 2nd ed., McGraw-Hill, New York, 384 pp., 1975.

Whitehead, J.A., H.J.B. Dick, and H. Schouten, A mechanism for magmatic accretion under spreading centres, *Nature, 312,* 146-148, 1984.

Wiggins, R. A., The general linear inverse problem: Implication of surface waves and free oscillations for earth structure, *Rev. Geophys. Space Phys., 10,* 251-285, 1972.

Table 1. New Hypocentral Parameters of Microearthquakes Beneath the Mid-Atlantic Ridge Near 23°N.

Origin Time		Latitude,	Longitude,	Depth,	nor		mag,	dcs,	rms,	erh,	erz,
Date	Time, UT	N	W	km	P	S	deg	km	s	km	km
Feb. 22	2246:22.11	22°35.2'	45°03.0'	6	4	0	308	9.4	0.12	5	pdc
Feb. 24	0107:53.05	22°44.3'	44°58.1'	6	4	0	183	2.3	0.02	0.7	pdc
Feb. 24	0401:18.93	22°35.7'	44°59.2'	5	4	0	301	9.4	0.06	5	pdc
Feb. 24	0734:00.91	22°40.8'	45°00.0'	6	4	0	158	4.3	0.07	0.7	pdc
Feb. 24	0757:18.75	22°43.7'	44°59.1'	5.7	5	0	132	3.4	0.02	0.6	1.6
Feb. 24	0907:46.11	22°39.6'	44°53.0'	5	5	0	309	6.7	0.03	5	pdc
Feb. 24	1055:24.15	22°40.1'	44°53.6'	5	4	0	305	5.3	0.02	5	pdc
Feb. 24	2154:50.66	22°39.7'	44°53.3'	5	5	0	307	6.1	0.02	5	pdc
Feb. 24	2223:45.32	22°39.9'	44°53.8'	5	4	0	305	5.2	0.03	5	pdc
Feb. 25	0205:38.24	22°39.2'	44°52.3'	5	5	0	313	7.9	0.03	4.6	pdc
Feb. 25	0206:16.93	22°39.6'	44°53.2'	5	5	0	308	6.2	0.03	5	pdc
Feb. 25	0323:36.10	22°39.4'	44°52.9'	5	4	0	310	6.8	0.02	5	pdc
Feb. 25	0533:49.74	22°39.4'	44°52.7'	5	5	0	310	7.1	0.03	5	pdc
Feb. 25	0621:56.93	22°45.6'	44°57.9'	4.5	4	0	247	1.4	0.00	2.4	1.1
Feb. 25	0806:18.83	22°39.6'	44°53.3'	5	4	0	308	6.0	0.01	5	pdc
Feb. 25	0808:36.77	22°39.6'	44°53.4'	5	5	0	307	5.9	0.01	5	pdc
Feb. 25	0812:27.81	22°39.6'	44°53.1'	5	5	0	307	6.3	0.03	5	pdc
Feb. 25	0823:56.60	22°38.8'	44°52.0'	5	4	0	315	8.7	0.01	4.6	pdc
Feb. 25	2106:44.19	22°42.8'	44°59.2'	6.3	5	0	128	5.1	0.03	0.6	1.9
Feb. 26	0014:07.00	22°39.8'	44°53.5'	5	4	0	308	5.7	0.02	5	pdc
Feb. 26	0049:49.63	22°30.9'	45°02.8'	6	5	0	326	17.2	0.16	5	pdc
Feb. 26	1825:49.73	22°44.9'	44°56.9'	4.5	5	0	212	3.0	0.01	1.0	1.0
Feb. 26	2041:53.42	22°35.4'	44°59.0'	5	4	0	304	9.8	0.04	5	pdc
March 1	1103:34.05	22°43.3'	44°59.3'	6	4	0	124	4.1	0.01	0.6	pdc
March 3	2127:18.13	22°41.4'	44°60.0'	6	3	1	191	2.7	0.03	1.5	pdc
March 4	0636:19.46	22°42.5'	44°59.5'	6	3	1	183	1.5	0.04	2.7	pdc
March 4	1015:35.75	22°40.2'	44°59.3'	6	3	1	223	3.9	0.03	1.2	pdc

Definitions are as follows: nor, number of readings; mag, maximum azimuthal gap; dcs, distance to the closest station; rms, root mean squared travel time residual; erh, horizontal error at 95% confidence (from projection of error ellipse onto horizontal plane); erz, error in depth at 95% confidence; pdc, poor depth control. Values of depth and erh given only to one significant figure are fixed estimates; see text.

Table 2. Moments and Corner Frequencies for Selected Earthquakes

Event		OBH 7	OBS 3		
Date	Time, UT	M_o (P), dyn cm	M_o (P), dyn cm	M_o (S), dyn cm	f_c, Hz
Feb. 22	2322	4×10^{19}			
Feb. 22	2324	7×10^{18}			
Feb. 23	1127	6×10^{18}			
Feb. 24	107	1×10^{18}			
Feb. 24	734	2×10^{17}			
Feb. 24	757	4×10^{17}			
Feb. 24	907	1×10^{19}			
Feb. 24	1055	4×10^{18}			
Feb. 24	2151	4×10^{19}	2×10^{19}	3×10^{19}	7
Feb. 24	2223	2×10^{18}			
Feb. 25	205	8×10^{18}			
Feb. 25	206	1×10^{19}			
Feb. 25	323	2×10^{18}			
Feb. 25	533	8×10^{18}			
Feb. 25	621	3×10^{17}			
Feb. 25	806	3×10^{18}			
Feb. 25	808	4×10^{18}			
Feb. 25	812	8×10^{18}			
Feb. 25	824	2×10^{18}			
Feb. 25	2106	9×10^{17}			
Feb. 26	14	2×10^{18}			
Feb. 26	349	3×10^{19}	1×10^{19}	1×10^{19}	9
Feb. 26	1729	4×10^{18}			
Feb. 26	1825	2×10^{18}			
Feb. 26	2224	8×10^{18}			
Feb. 28	849	3×10^{18}			
Feb. 28	851	2×10^{19}			
Feb. 28	2333	5×10^{18}			
March 1	1103	6×10^{17}			
March 2	825	4×10^{18}			
March 2	1023	5×10^{18}			
March 3	635	4×10^{19}	2×10^{19}	1×10^{19}	9
March 3	1435	7×10^{18}			
March 3	1611	5×10^{19}	1×10^{20}	1×10^{20}	9
March 3	1715	1×10^{19}			
March 3	2127	8×10^{17}			
March 4	447	4×10^{19}	6×10^{19}	4×10^{19}	9
March 4	636	3×10^{17}			
March 4	1015	3×10^{18}			

Table 3. Summary of Tomographic Inversions

Inversion Number	Source Structure	Initial Structure	Data	r_i, s	r_f, s	s^2, %
1	7 m.y.	7 m.y.	B	0.13	0.07	76
2	7 m.y.	7 m.y.	A,B	0.15	0.12	37
3	0 m.y.	0 m.y.	B	0.11	0.07	67
4	0 m.y.	0 m.y.	A,B	0.14	0.09	57
5	0 m.y.	7 m.y.	A,B	0.14	0.09	56
6	0 m.y.	0 m.y.	A,C	0.13	0.08	60
7	0 m.y.	0 m.y.	A,D	0.14	0.10	54

Inversions are numbered for reference; see text. The source structure and initial structure are the laterally homogeneous models used to determine hypocentral location and as the initial velocity model for tomographic inversion, respectively; the models are designated by approximate seafloor age as 7 m.y. [*Detrick and Purdy,* 1980] or 0 m.y. [*Purdy and Detrick,* 1986]. The code for the subset of sources of travel time data used in the tomographic inversion is as follows: A, 9 shots; B, 21 microearthquakes with independently resolved focal depths; C, 37 microearthquakes with well-resolved epicenters; D, 21 inner floor events. The quantities r_i, r_f, and s^2 are the initial and final rms travel time residual and the variance reduction, respectively.

Figure Captions

Figure 1. Bathymetry of the Mid-Atlantic Ridge median valley to the south of the Kane Fracture Zone (0.5-km contour interval), from *Detrick et al.* [1984]. The rectangle in the southern portion of the figure defines the area of the 1982 microearthquake survey that is shown in detail in Figure 2. The dashed line shows the location of the refraction line used to determine the crustal structure along the axis of the median valley [*Purdy and Detrick* 1986].

Figure 2. Configuration and setting of the microearthquake experiment. Open symbols denote seismic instruments: circles are WHOI OBH's, triangles are MIT OBS's. Filled symbols indicate microearthquake epicenters: circles denote epicenters with independently resolved focal depth, diamonds denote epicenters determined for a fixed focal depth. Bathymetric contours, at 100m intervals, are from the Sea Beam survey of *Detrick et al.* [1984]; closed highs and lows are indicated by H and L, respectively. Contours are dashed in regions between Sea Beam swaths. The solid line AA' marks the location of the vertical cross section depicted in Figure 3. The dashed line through the epicenters in the inner floor strikes at N25°E.

Figure 3. Well resolved focal depths of microearthquakes beneath the median valley. Hypocenters have been projected onto the vertical plane through profile AA' (Figure 2). Error bars show 95% confidence limits for focal depth and horizontal location in the plane of the figure. All depths are relative to the datum indicated by the dashed line. There is no vertical exaggeration of the bathymetry.

Figure 4. Seismograms of 14 rift mountain earthquakes recorded by OBH 7. The first 11 events have epicentral coordinates and focal depth poorly resolved by travel times, the next 2 events have well resolved epicenters if the focal depth is held fixed, and the last event has epicenter and focal depth well resolved. Seismograms are aligned at the P wave onset and are scaled to have identical maximum amplitudes.

Figure 5. Composite fault plane solutions of selected microearthquakes. (a) Composite for seven inner floor events with epicenters within the network (February 24, 0757 UT, February 25, 0621 UT, February 25, 2106 UT, February 26, 1825 UT, February 26, 2224 UT, February 28, 2333 UT, and March 3, 1435 UT). (b) Composite for five additional inner floor events located about 5 km south of OBH 4 (February 22, 2324 UT, February 23, 1126 UT, February 26, 1729 UT, and February 28, 0849 UT and 0851 UT) as well as the events from (a). (c) Composite for seven rift mountain events (February 24, 2151 UT, February 26, 0349 UT, March 2, 0825 UT, March 2, 1023 UT, March 3, 1611 UT, March 3, 1715 UT, and March 4, 0447 UT). Compressional arrivals are shown as solid circles, dilatations as open circles. Equal-area projections of the lower focal hemisphere. Fault planes shown have strike and dip angles of (N15°E, 45°E) and (N15°E, 45°W).

Figure 6. Examples of P (solid line) and S (dashed line) displacement spectral amplitude from an OBS 3 vertical channel record and equivalent P displacement spectral amplitude from an OBH 7 record. The time

windows used for the calculation of spectra are bracketed by vertical lines; the S-wave window begins immediately prior to the S arrival as indicated on horizontal component seismograms. Data were premultiplied by a pi-prolate window [*Thomson*, 1977]. The Nyquist frequency is 60 Hz for the OBS and 50 Hz for the OBH.

Figure 7. The number $N(M_o)$ of earthquakes with moment in excess of M_o for microearthquakes beneath the inner floor (solid squares) and rift mountains (solid circles). The straight lines are least squares fits to the indicated data.

Figure 8. P wave stations delay versus instrument depth for the OBH-OBS network (Figure 2). See *Paper 1* for a discussion of station delay determination.

Figure 9. Positions of microearthquakes (solid circles), ranging shots (solid squares), ocean bottom instruments (open circles - OBH; open triangle - OBS) included in the tomography analysis. The Sea Beam bathymetry is from *Detrick et al.* [1984]. The dashed line indicates the location of the refraction line of *Purdy and Detrick* [1986]. The solid line marked by arrows is the surface projection of the vertical plane containing parametric velocity nodes (diamonds); solid and open symbols denote two distinct parameterizations (see text).

Figure 10. Nodal values of P wave velocity, associated error, and resolution for inversions 3 and 6 (Table 3). Columns labeled west, central, and east denote the relative locations of nodal columns across the inner floor.

The depth z of each node relative to the 3900-m isobath is indicated in km. The error in percent velocity deviation is given at the one-standard-deviation level of confidence for nodes with non-zero resolution. See text for a discussion of resolution.

Figure 11. Two-dimensional model of P wave velocity beneath the median valley inner floor resulting from tomographic inversion of travel times (inversion 6, Table 3). Velocity values are obtained by two-dimensional linear interpolation from the nodal velocity values in Figure 10; the contour interval is 0.5 km/s. The surface trace of the cross section is shown in Figure 9 (nodes at open diamonds).

Figure 12. Two-dimensional velocity model adopted to approximate the effect of rift mountain topography on crustal structure. Velocity contours follow topography. (a) P wave velocity versus depth beneath the seafloor, from *Purdy and Detrick*, [1986]. (b) Representative ray paths in plan view for a source beneath the rift mountains (solid square). The cross-ruled region represents the rift mountains. (c) Cross section of model and representative ray paths from a rift mountain earthquake (solid square) at a depth of 3 km below the zero datum. Lines marked A and B correspond to the inflection points of the velocity model in (a) at the top of layer 3 and the top of the Moho transition zone, respectively.

Figure 13. Differences in travel times for P and S waves from a rift mountain microearthquake between the two-dimensional and laterally homogeneous velocity models of Figure 12. Travel time differences

are for the station and epicenter positions shown in Figure 12b for various depths of focus below the zero datum in Figure 12c. The 'picking error' of 0.04 s [*Paper 1*] is indicated by the dashed line.

Figure 14. Two-dimensional velocity model used to evaluate the effects of lateral heterogeneity on hypocentral locations beneath the inner floor. (a) Cross section through the model. Contours of P wave velocity are in km/s. (b) Plan view of the model. Selected ray paths are shown for a source (solid square) at 6 km depth. Receiver symbols are the same as in Figure 13. The cross ruled area indicates the region of anomalously low velocities in the mid to lower crust.

Figure 15. Differences in travel times for P and S waves from an inner floor microearthquake between the laterally heterogeneous velocity model of Figure 13 and the laterally homogeneous model of *Purdy and Detrick* [1986]. Travel time differences are for the station and epicenter positions shown in Figure 14b for various depths of focus below the seafloor. Symbols for stations are as in Figure 13. The 'picking error' of 0.04 s [*Paper 1*] is indicated by the dashed line.

Figure 16. Schematic cross section of the Mid-Atlantic Ridge median valley at about 22°40'N. Bathymetry and locations of inner floor microearthquakes (circles) are from Figure 3. Contours of P wave velocity (dashed), in km/s, are from Figure 11. The location of the fault plane for recent large ($m_b > 5$) earthquakes is conjectural, but the dip angle and down-dip extent are constrained by body waveform inversion [*Huang et al.*, 1986].

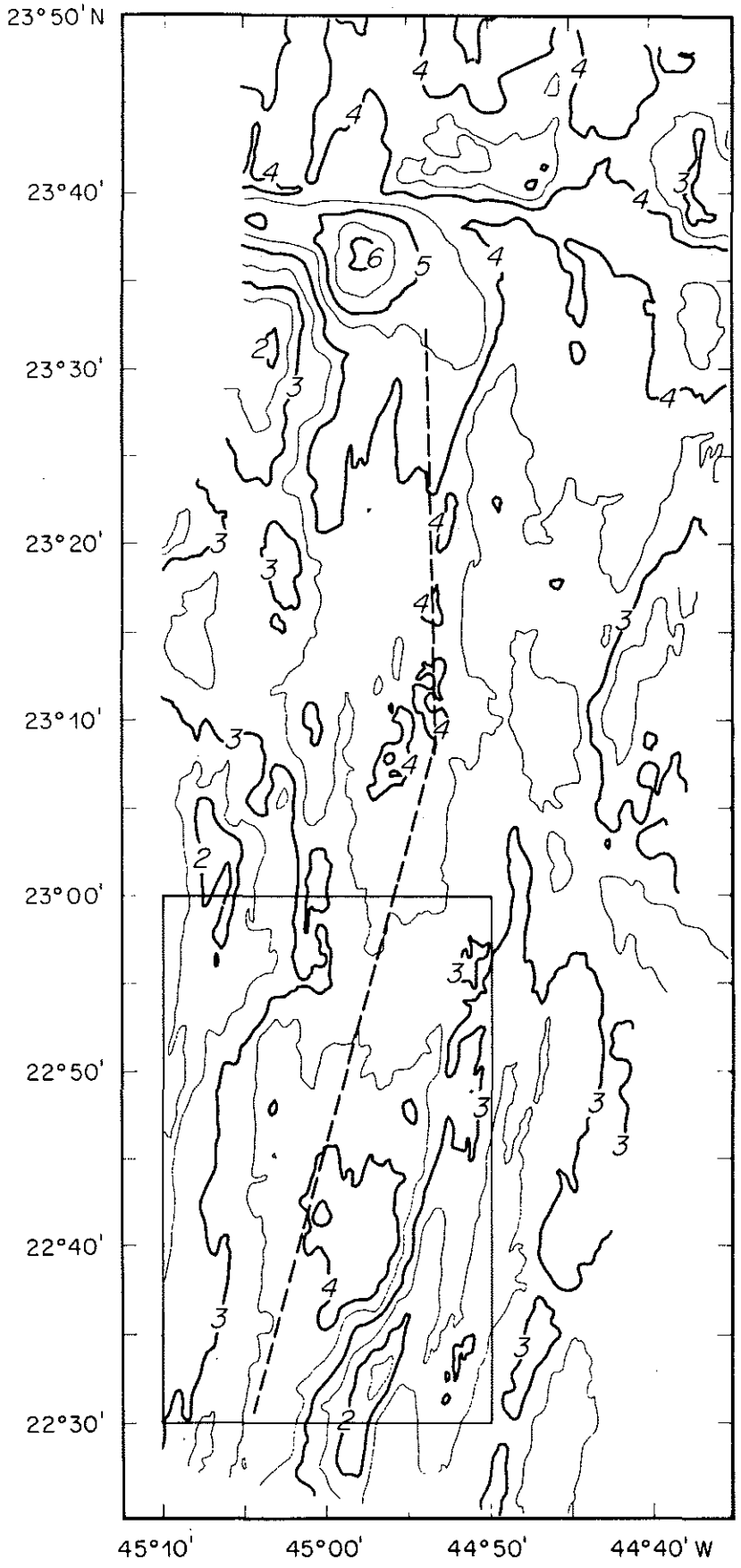
23°50' N
23°40'
23°30'
23°20'
23°10'
23°00'
22°50'
22°40'
22°30'
45°10'
45°00'
44°50'
44°40' W

Figure 1

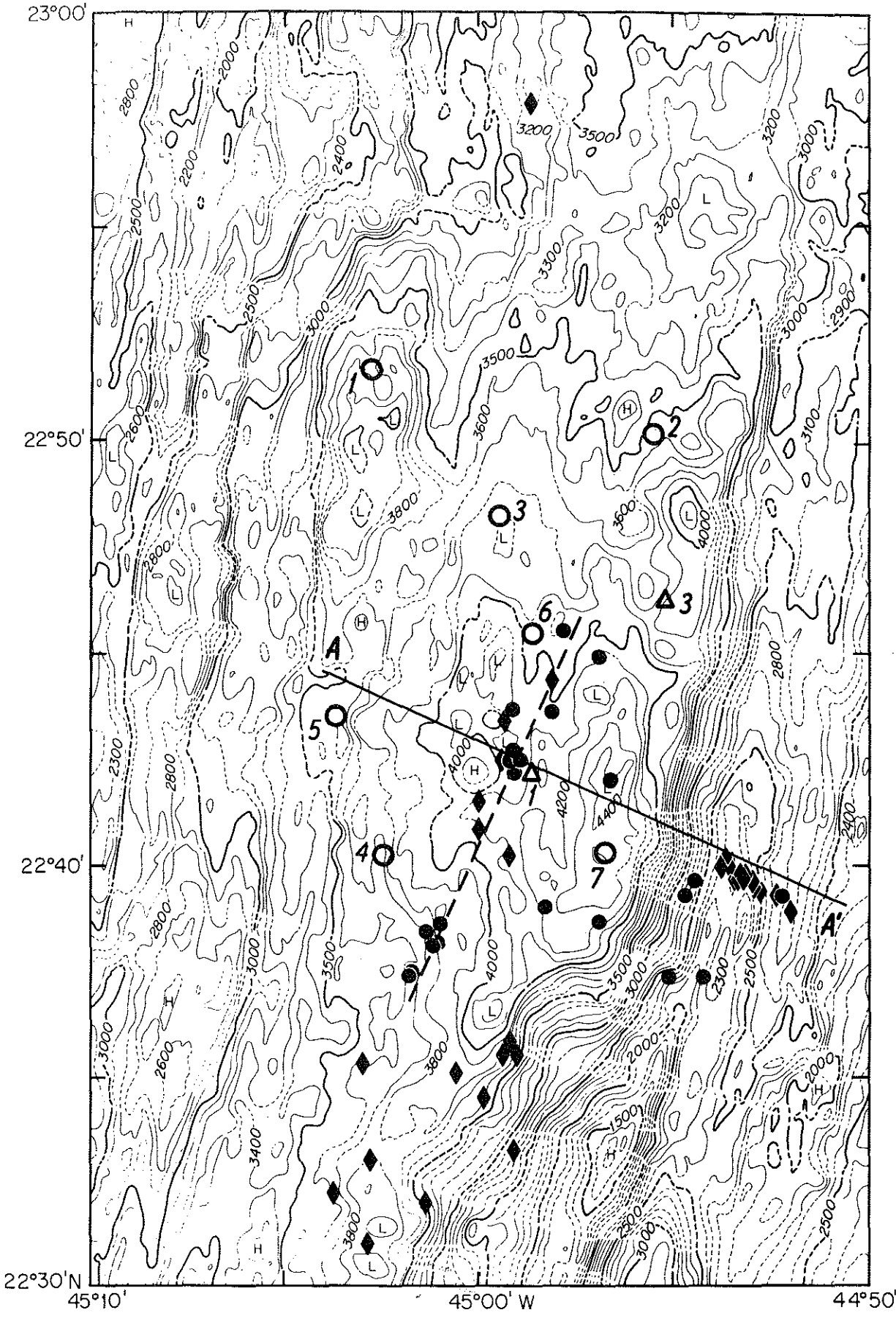

Figure 2

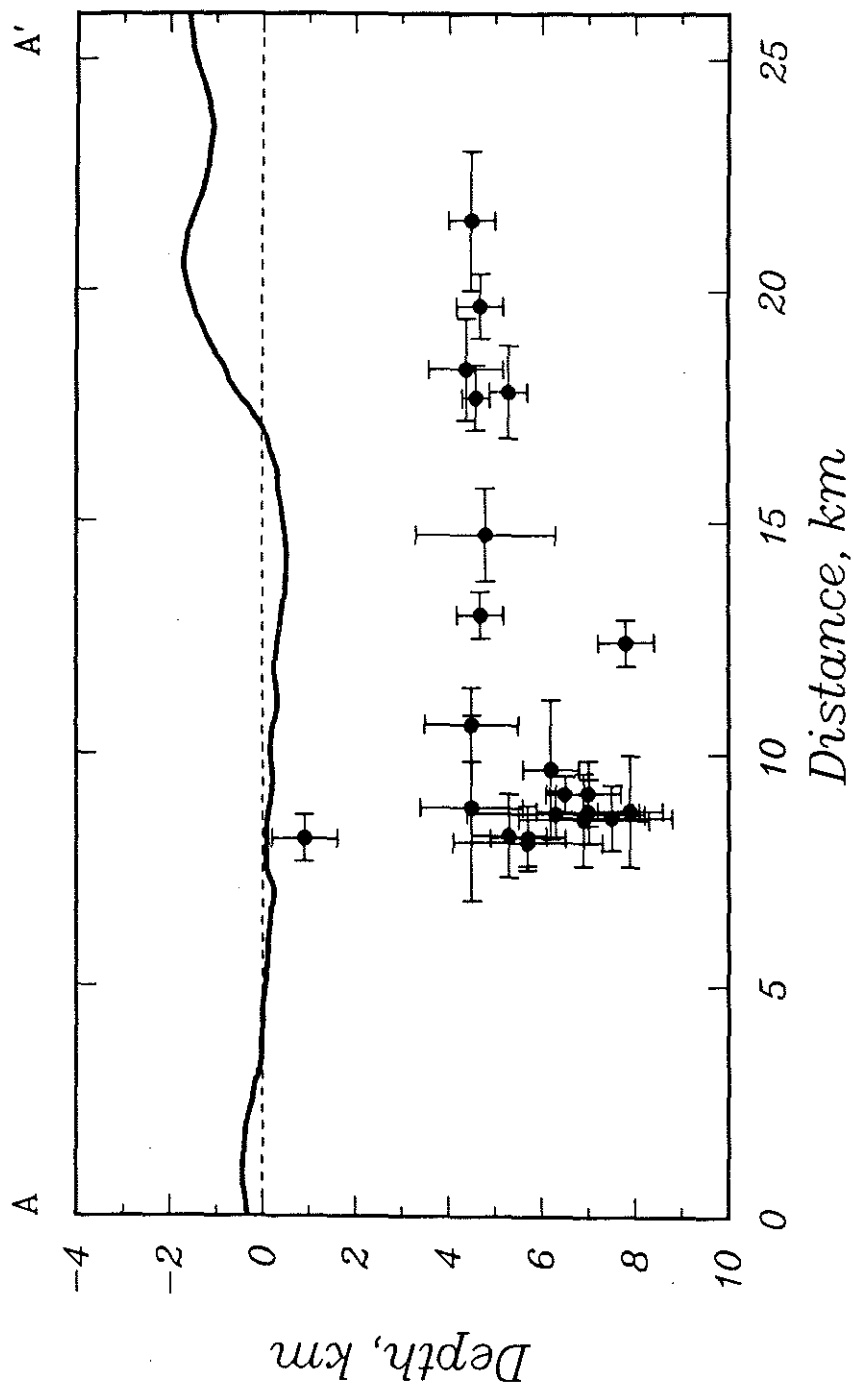

Figure 3

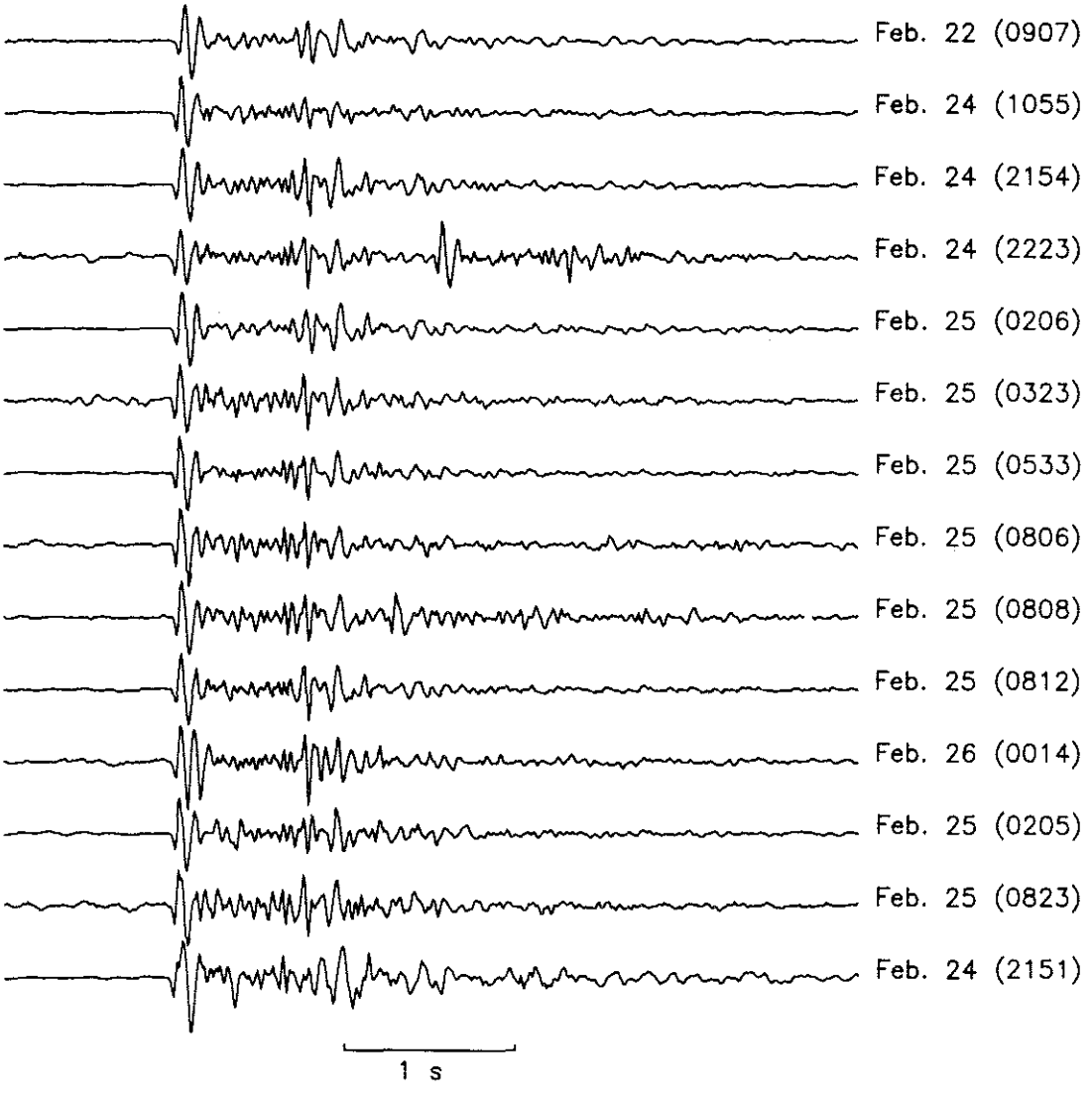
Feb. 22 (0907)
Feb. 24 (1055)
Feb. 24 (2154)
Feb. 24 (2223)
Feb. 25 (0206)
Feb. 25 (0323)
Feb. 25 (0533)
Feb. 25 (0806)
Feb. 25 (0808)
Feb. 25 (0812)
Feb. 26 (0014)
Feb. 25 (0205)
Feb. 25 (0823)
Feb. 24 (2151)
1 s

Figure 4

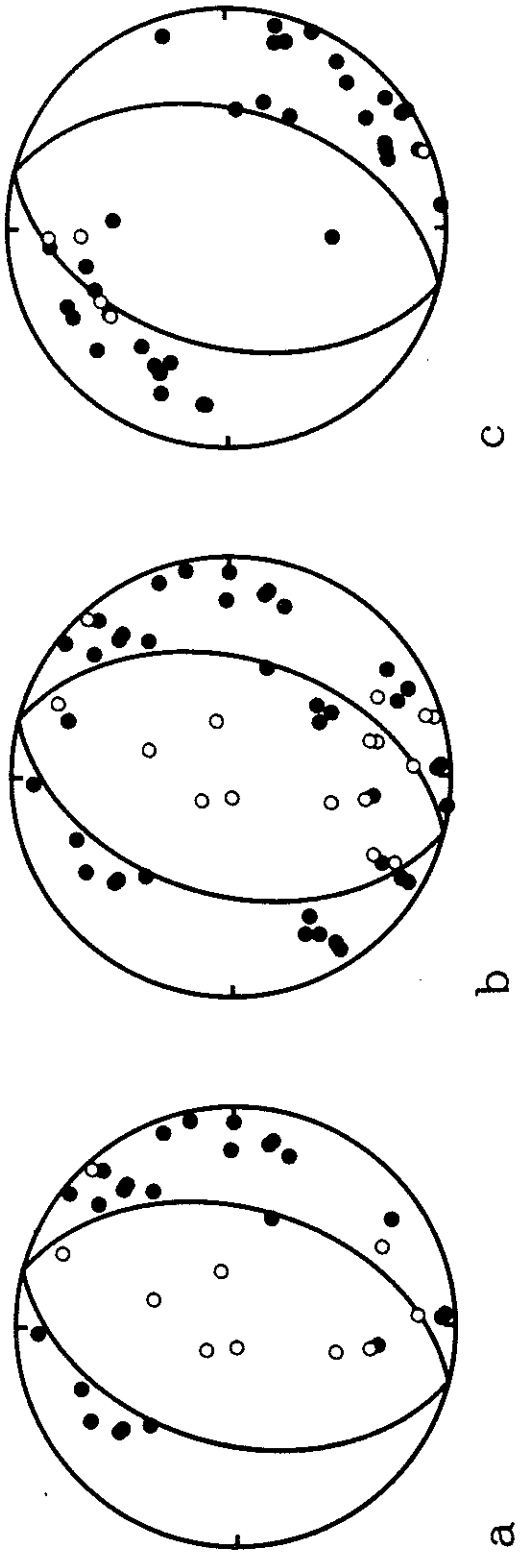

Figure 5

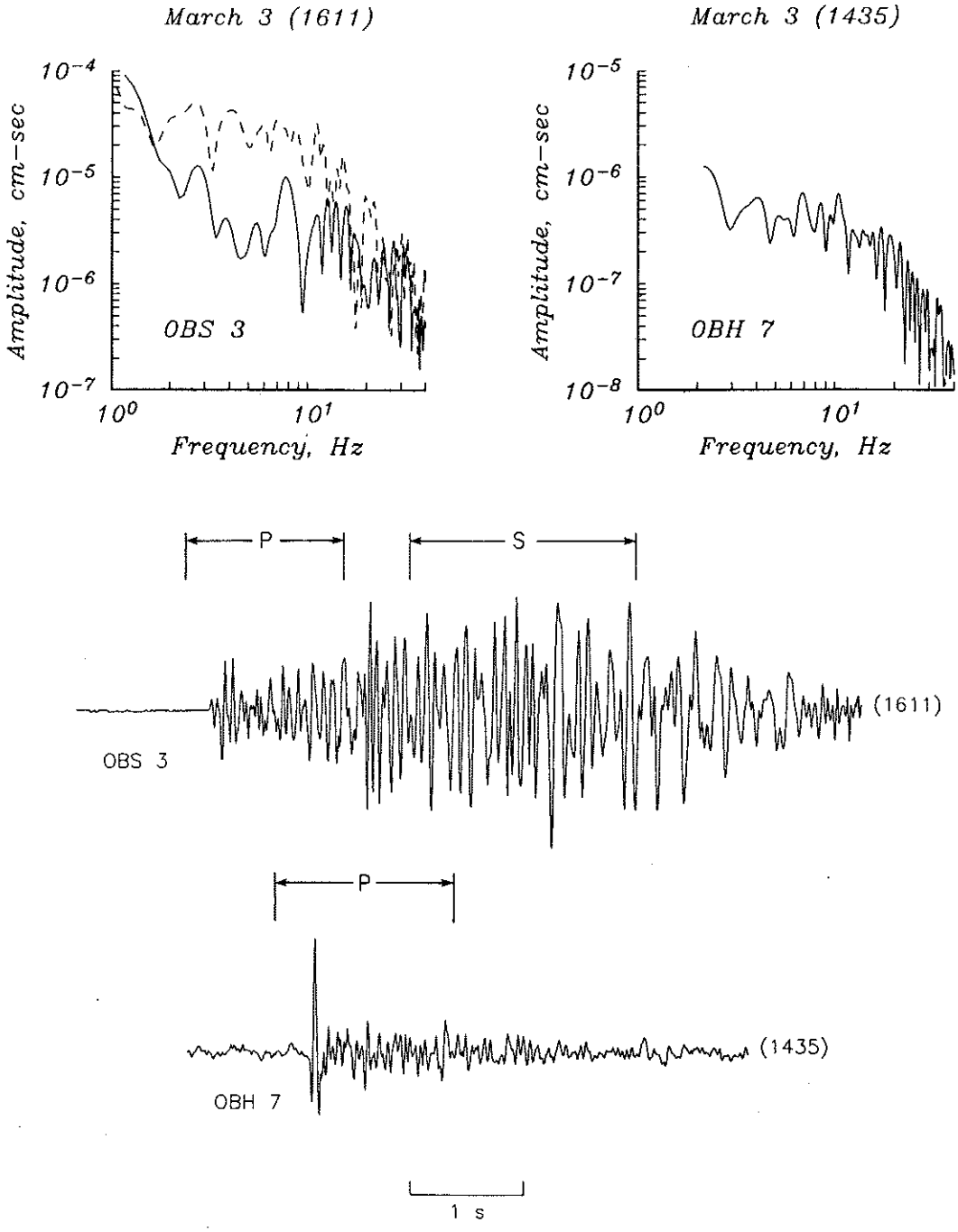
March 3 (1611)
March 3 (1435)
Amplitude, cm-sec
10^{-4}
10^{-5}
10^{-6}
10^{-7}
10^{-8}
OBS 3
OBH 7
10^{0}
10^{1}
Frequency, Hz
P
S
OBS 3
(1611)
P
OBH 7
(1435)
1 s

Figure 6

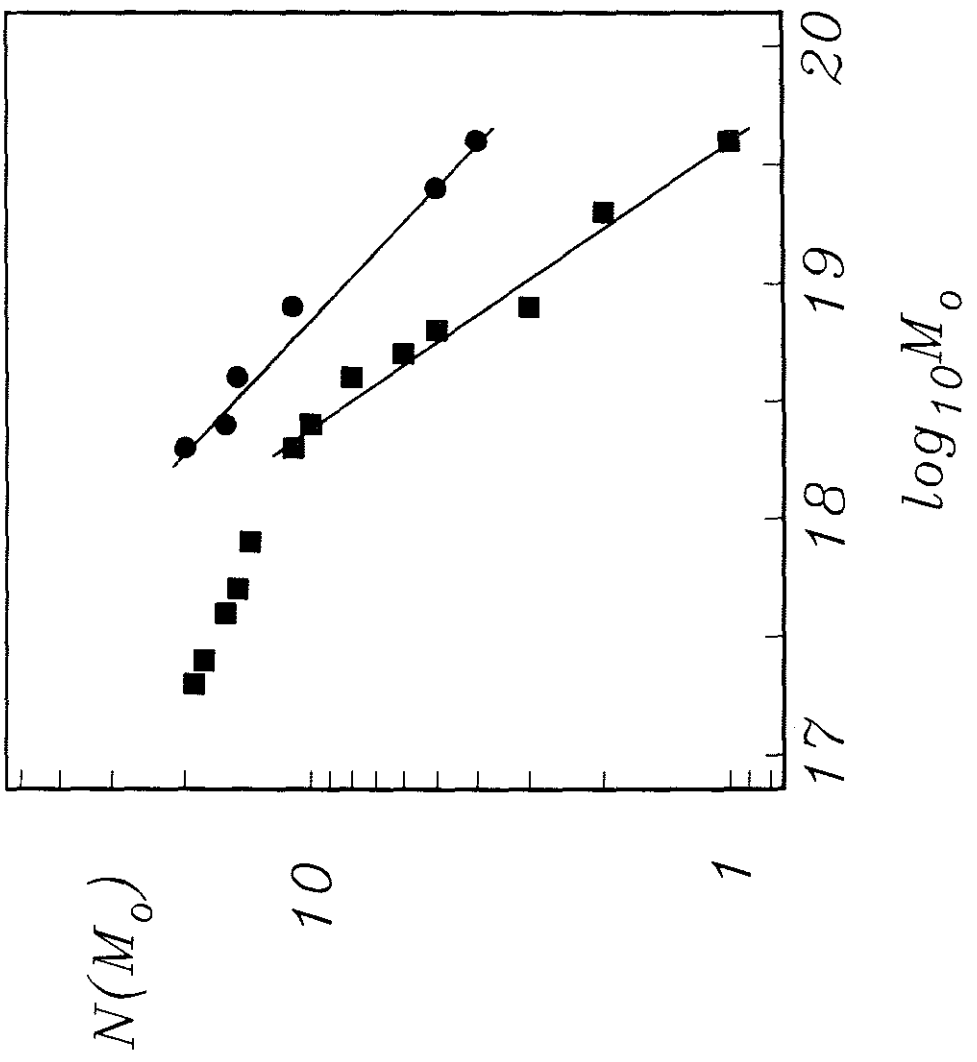

Figure 7

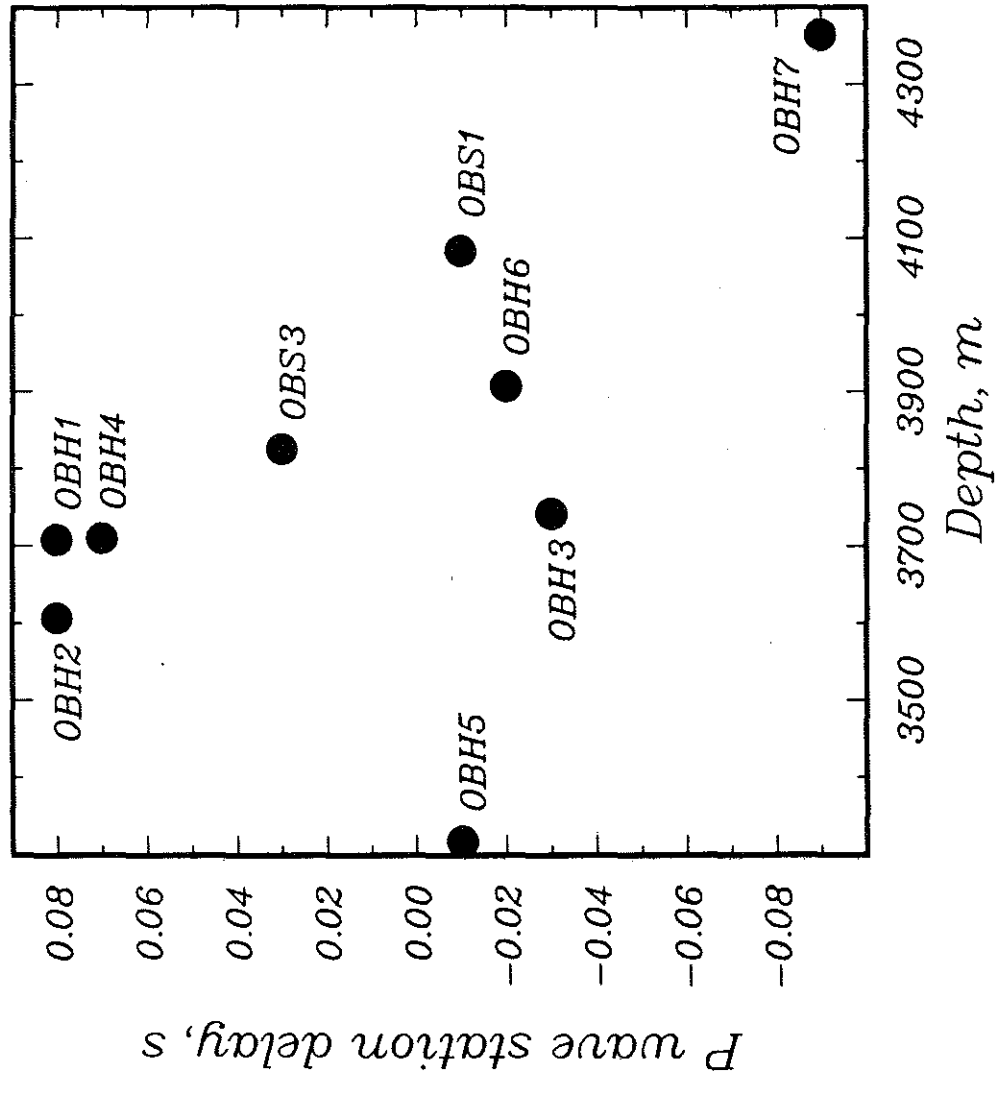
OBH2
OBH1
OBH4
OBS3
OBH5
OBS1
OBH6
OBH3
OBH7
0.08
0.06
0.04
0.02
0.00
−0.02
−0.04
−0.06
−0.08
3500
3700
3900
4100
4300
Depth, m
P wave station delay, s

Figure 8

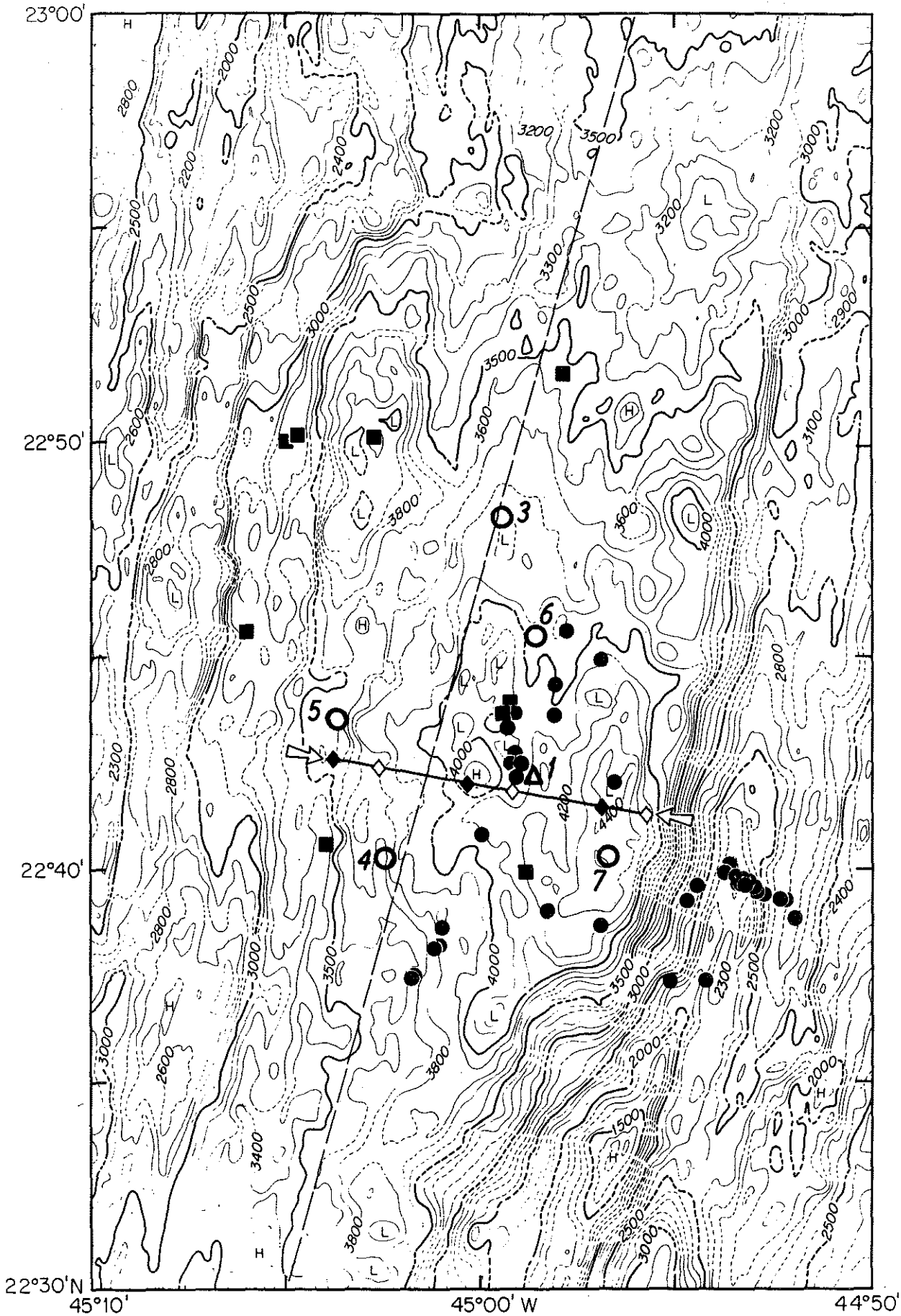

Figure 9

	Inversion 3				Inversion 6		
	West	*Central*	*East*		*West*	*Central*	*East*
Velocity, km/s *Percent deviation* *Resolution*	3.6 20±1 0.2	3.0 1±1 0.1	3.0 --- 0	z=0	3.5 17±3 0.6	3.2 5±3 0.3	2.8 -7±1 0
	4.8 8±1 0.3	4.4 -3±2 0.4	4.5 --- 0	z=1	5.0 11±2 0.7	4.0 -11±2 0.7	4.2 -8±2 0.4
	7.0 9±1 0.3	6.0 -6±2 0.5	6.0 -6±2 0.6	z=3	6.5 1±2 0.7	6.3 -2±2 0.7	6.4 0±2 0.6
	7.9 11±2 0.6	7.1 0±2 0.8	7.4 5±1 0.9	z=5	7.9 12±3 0.7	7.2 1±2 0.9	7.6 7±1 1.0

Figure 10

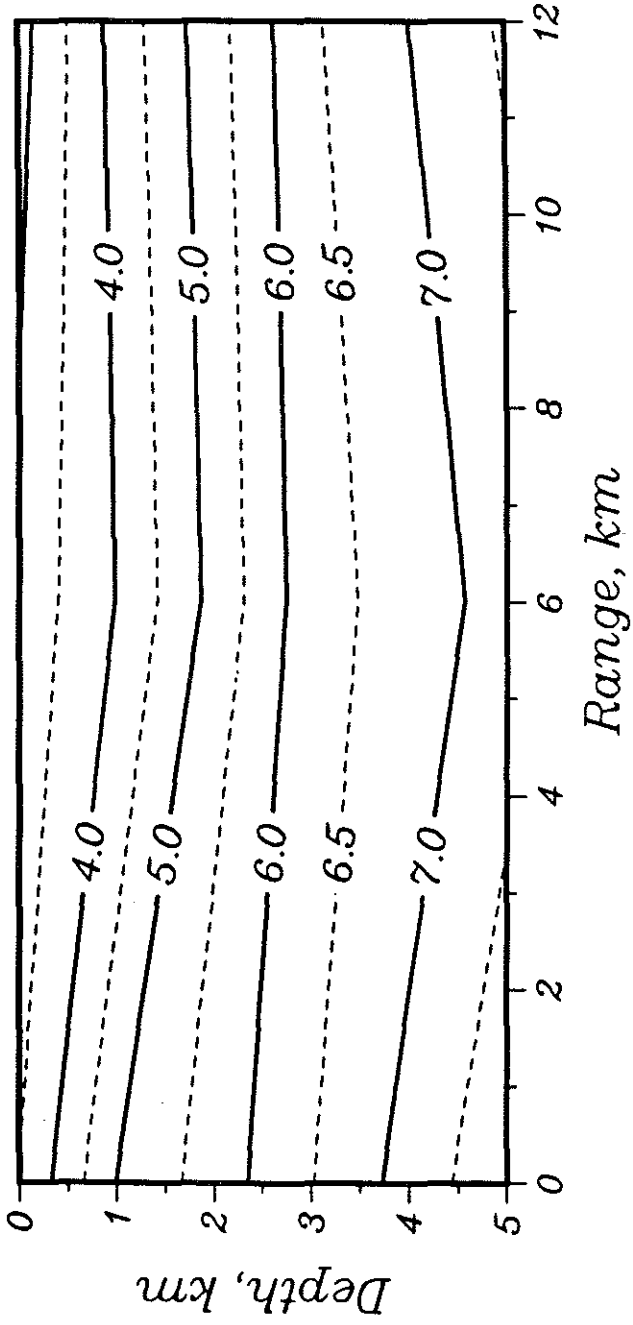

Figure 11

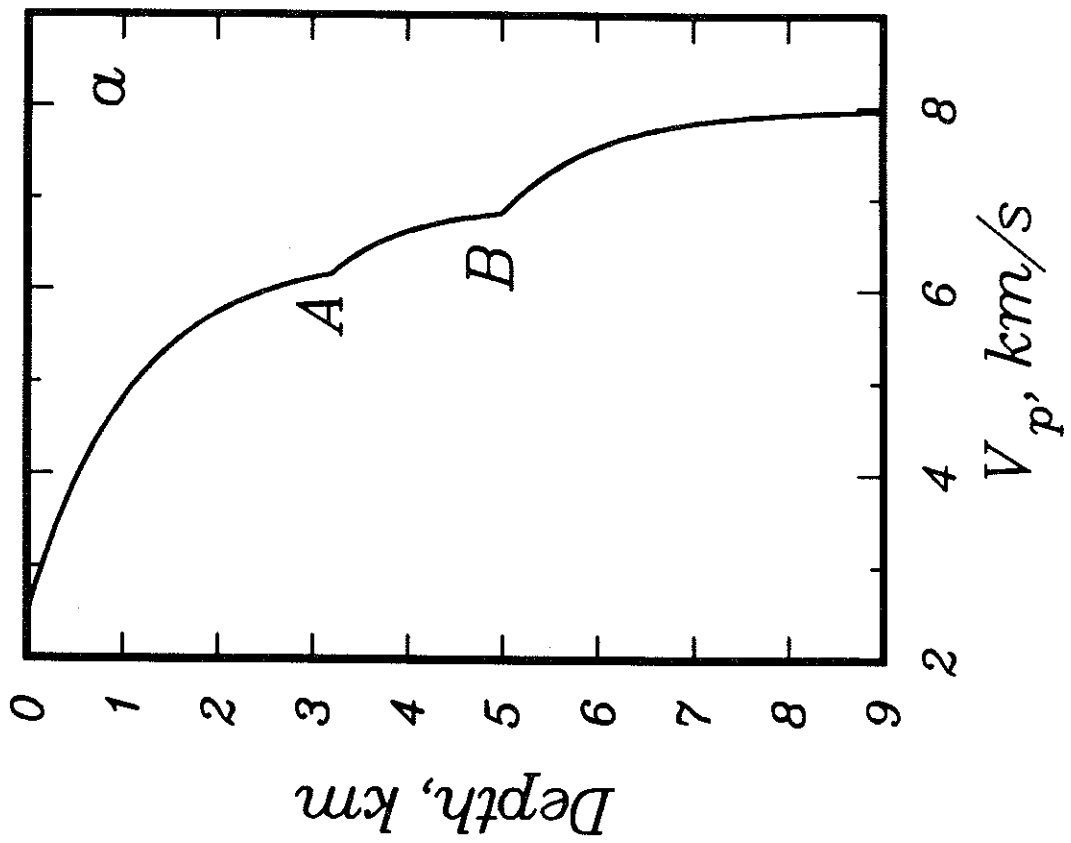

Figure 12a

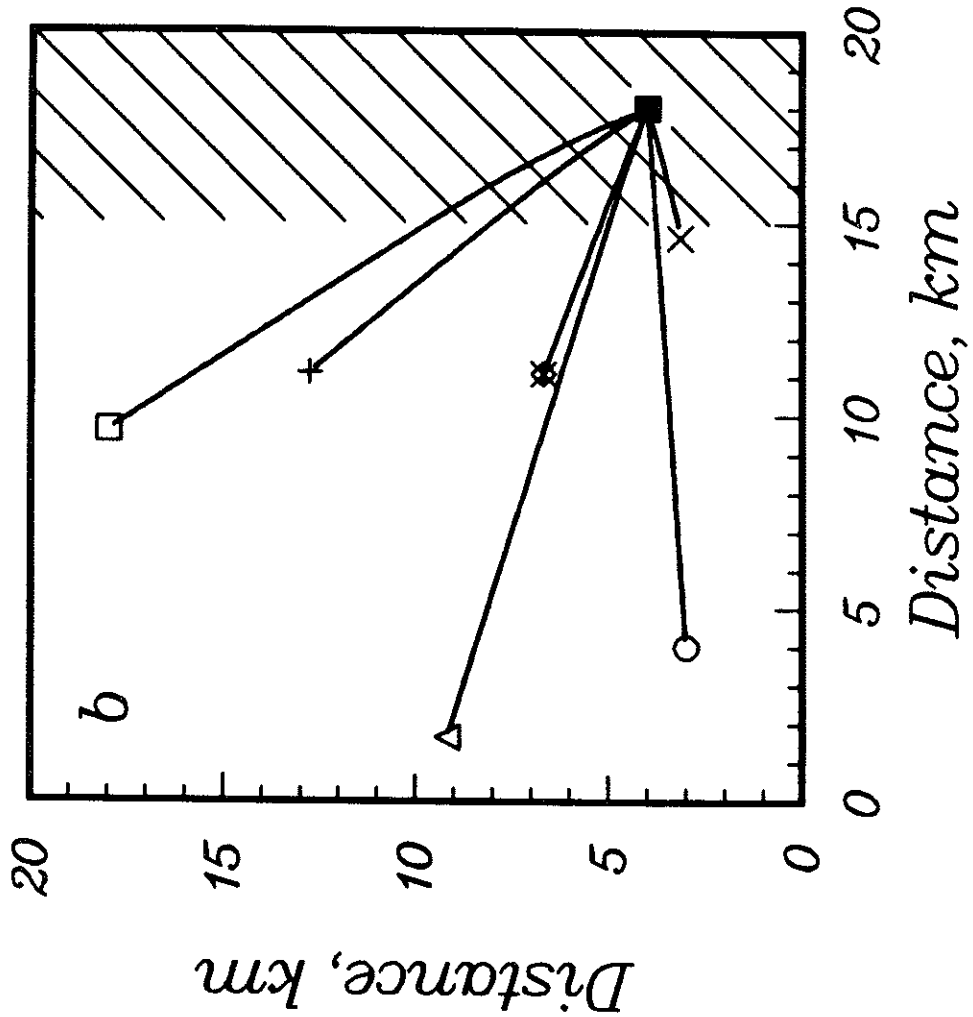

Figure 12b

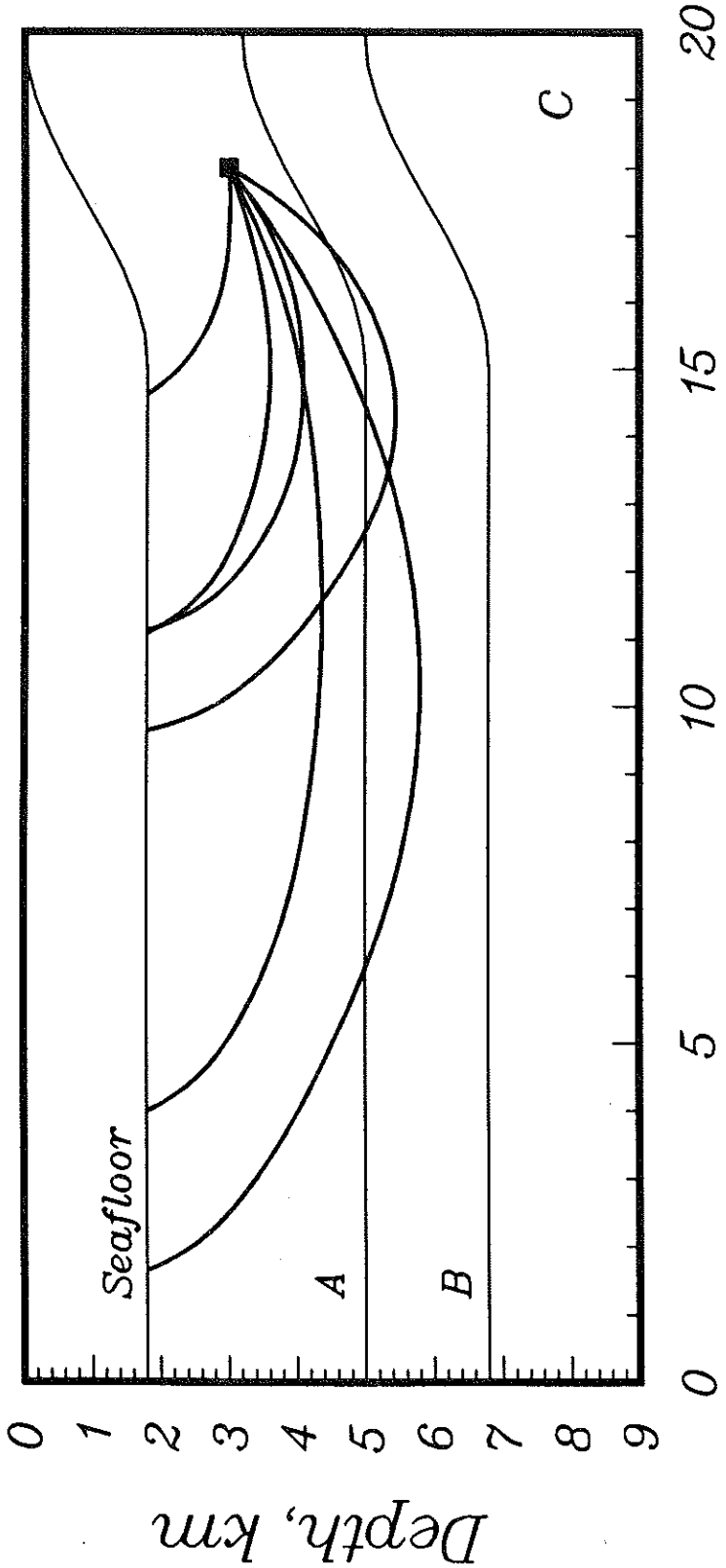

Figure 12c

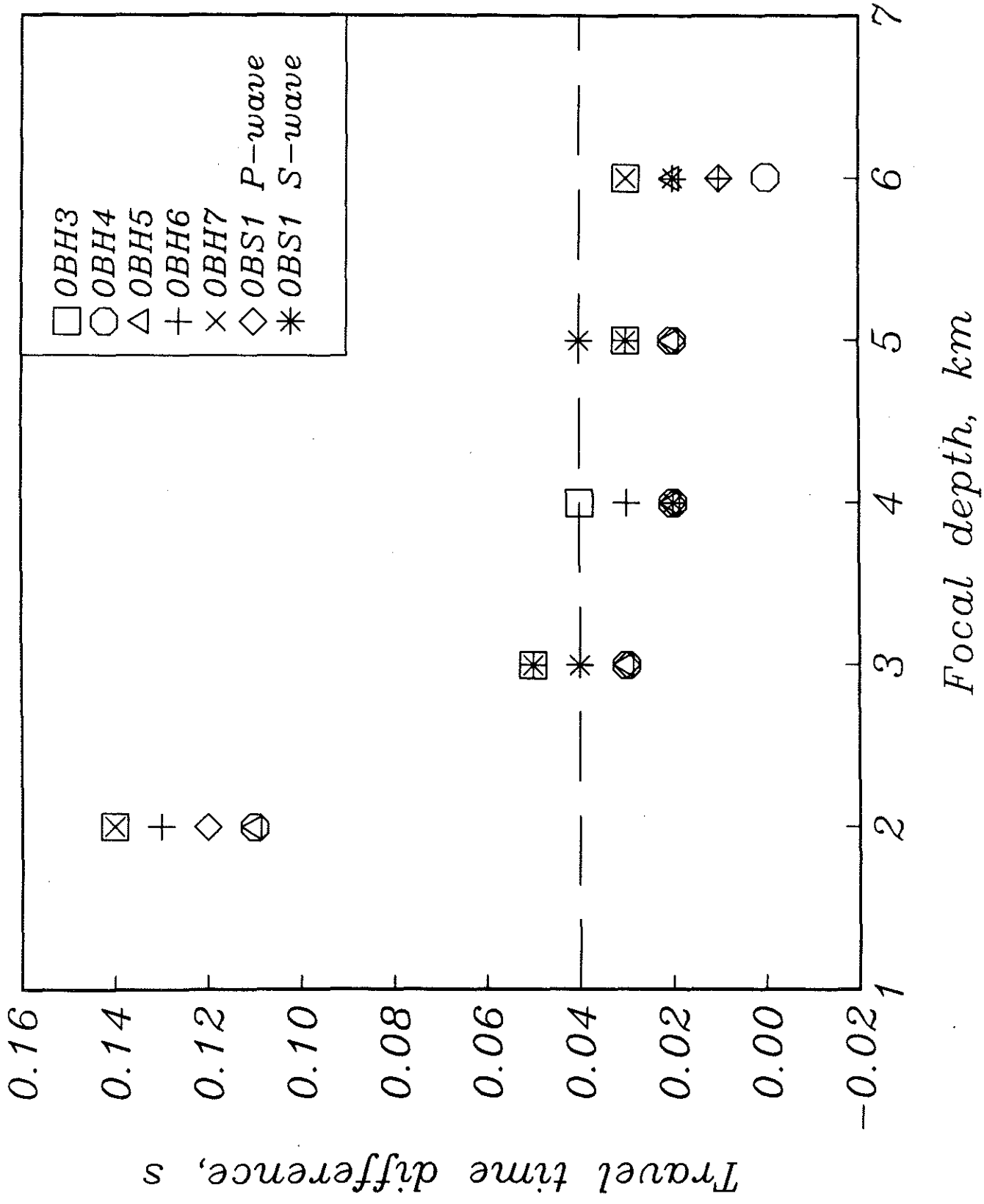
OBH3
OBH4
OBH5
OBH6
OBH7
OBS1 P-wave
OBS1 S-wave
0.16
0.14
0.12
0.10
0.08
0.06
0.04
0.02
0.00
-0.02
1
2
3
4
5
6
7
Travel time difference, s
Focal depth, km

Figure 13

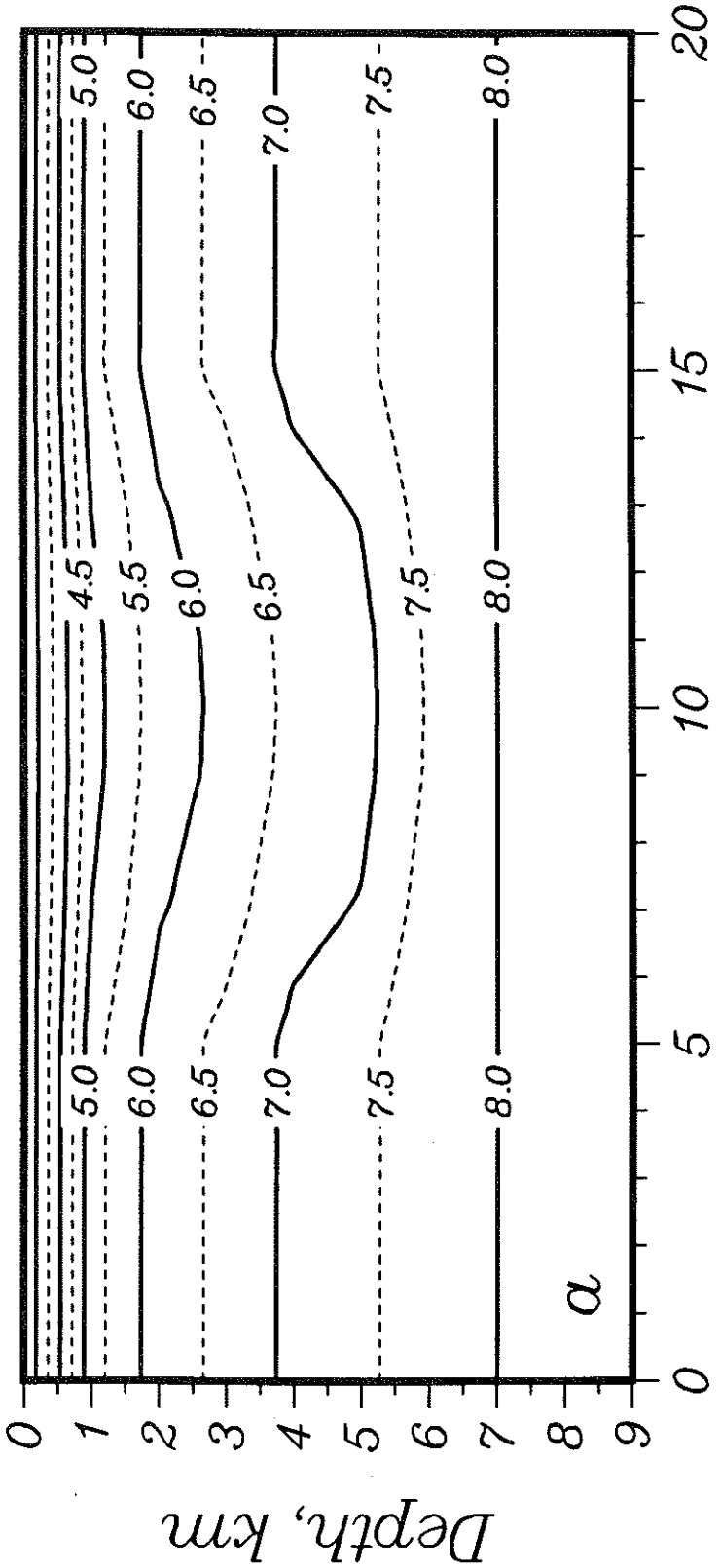

Figure 14a

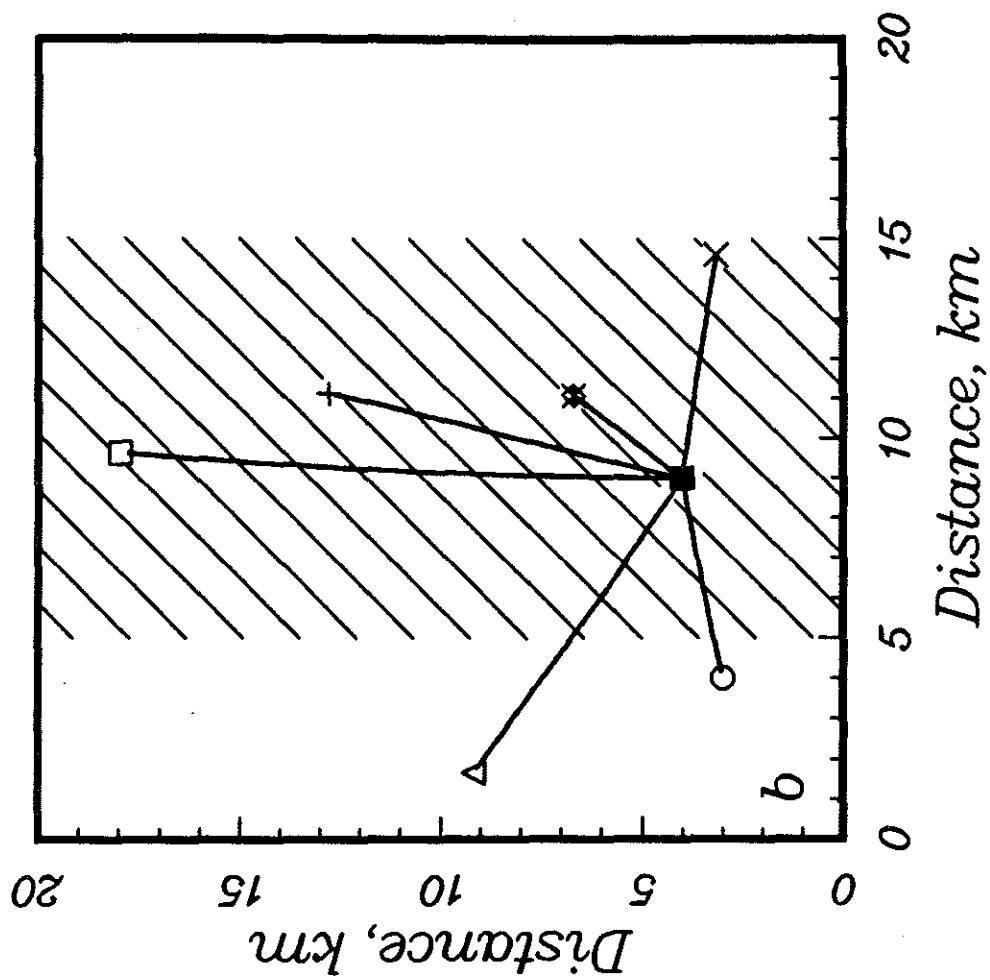

Figure 14b

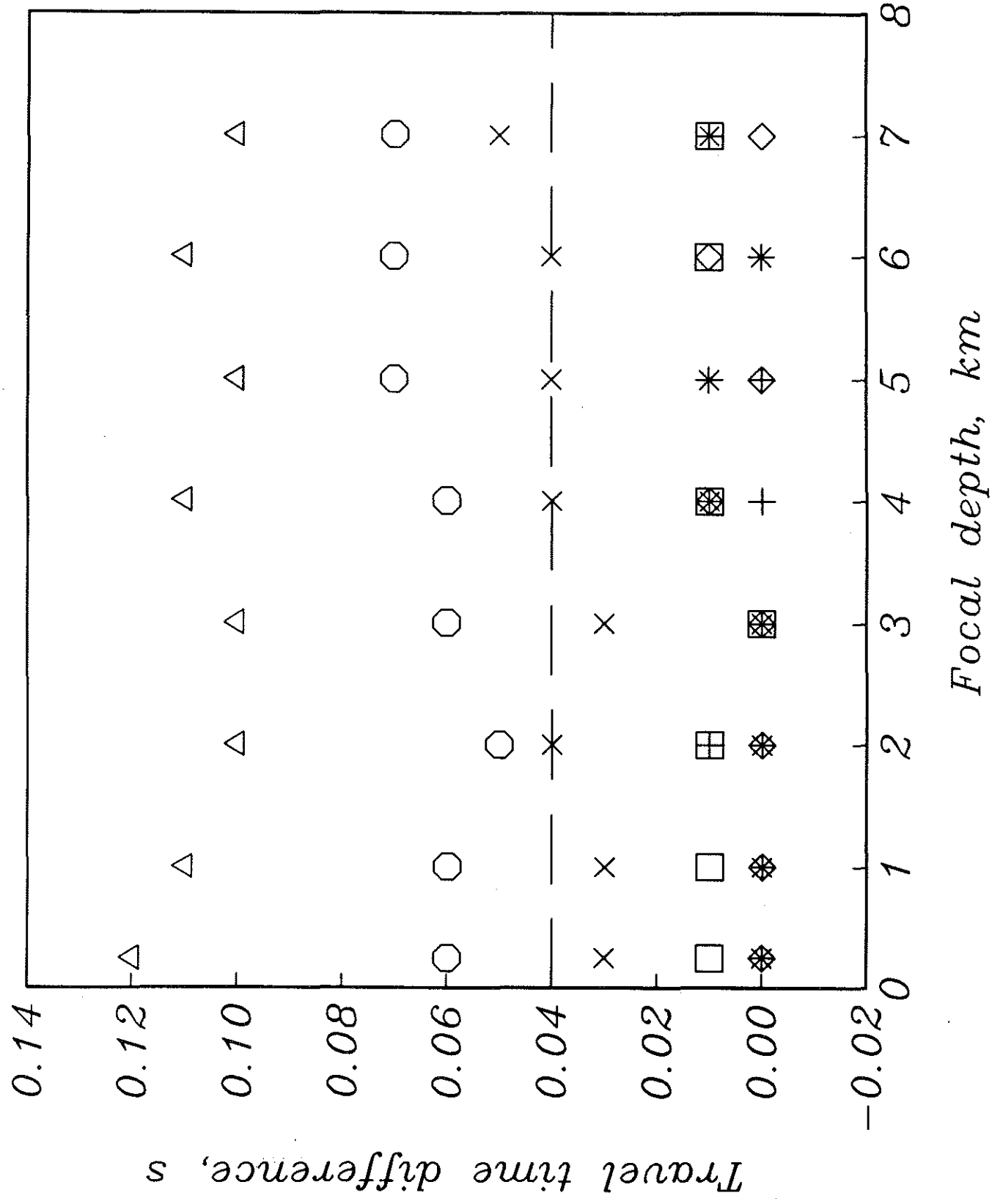
Travel time difference, s
0.14
0.12
0.10
0.08
0.06
0.04
0.02
0.00
−0.02
Focal depth, km
0
1
2
3
4
5
6
7
8

Figure 15

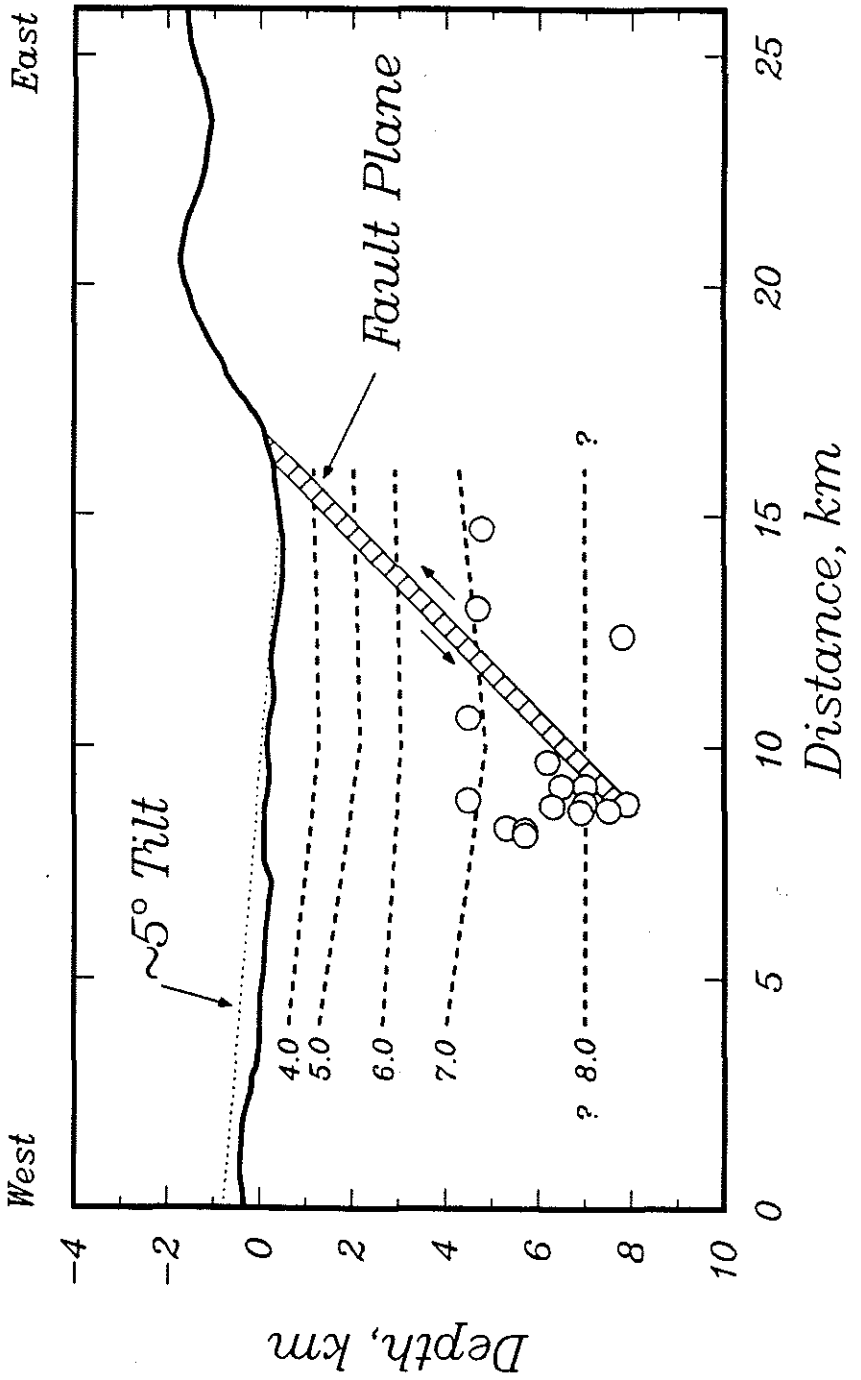
East
West
Fault Plane
~5° Tilt
4.0
5.0
6.0
7.0
? 8.0
?
Depth, km
Distance, km
-4
-2
0
2
4
6
8
10
0
5
10
15
20
25

Figure 16

CHAPTER 5

A TOMOGRAPHIC INVERSION OF LOCAL EARTHQUAKE DATA: HENGILL-GRENSDALUR CENTRAL VOLCANO, ICELAND

INTRODUCTION

Seismic tomography is a powerful tool for imaging three-dimensional earth structure over a variety of length scales. For studies of local crustal structure, seismic tomography and hypocentral location have been incorporated into a single problem, known as simultaneous inversion [e.g, Aki and Lee, 1976; Pavlis and Booker, 1980; Spencer and Gubbins, 1980; Thurber, 1983]. Simultaneous inversion has been used successfully to image crustal heterogeneity associated with fault zones [Aki and Lee, 1976; Thurber, 1983], volcanic and geothermal systems within intraplate and transform plate-boundary regions [Thurber, 1984; Benz and Smith, 1984; Eberhart-Phillips, 1987], and subduction zones [e.g., Roecker, 1982; Hasemi et al., 1984]. Simultaneous inversion has proven to be a powerful method for imaging subsurface velocity anomalies that, in many cases, correlate spatially with surface geology. In this paper, we apply the simultaneous inversion method to a data set collected near the Hengill central volcano and geothermal field in southwestern Iceland [Foulger, 1984, 1987].

The emphasis in this paper is on the careful use of the simultaneous inversion method to image the internal structure of the Hengill central volcano complex and the results of inversion. A companion paper [Foulger and Toomey, 1986, in preparation] presents an interpretation of these results in the context of local geology and tectonics. We begin by briefly summarizing

the experiment site and our selection of arrival time data. We then review the simultaneous inversion method, due to Thurber [1981, 1983], and examine factors that define an optimum model parameterization; an important part of this section is the introduction of a quantitative measure of resolution. We follow with a detailed account of our application of simultaneous inversion to the Hengill data set. For this data set, a comprehensive analysis of resolution indicates that bodies of anomalous velocity are resolved at ± 2 and ± 1 km in the horizontal and vertical directions, respectively. The results show that well-defined images of bodies of anomalously high velocity correlate spatially with prominent geologic features such as centers of past volcanic eruptions and an active high-temperature geothermal field.

EXPERIMENT SITE

The Hengill volcano and geothermal field is located at the junction of three seismically active regions in southwestern Iceland (Figure 1): the Reykjanes Peninsula, the Western Volcanic Zone, and the South Iceland Seismic Zone [Einarsson, 1979; Einarsson and Bjornsson, 1979; Foulger and Einarsson, 1980; Einarsson et al., 1981]. The Hengill volcano, of Pleistocene to Recent age, sits astride an 80-km-long fissure swarm trending N65^{o}E, one of five en echelon fissure swarms located on the Reykjanes Peninsula [Klein et al., 1973, 1977; Jakobsson et al., 1978]. The high temperature (>300^{o}C) geothermal field, 70 km^{2} in area, is one of Iceland's principal supplies of harnessed geothermal energy [Bjornsson and Hersir, 1981]. The locations of the Hengill volcano, volcanic eruptive fissures, and hot springs and fumeroles associated with the geothermal field are shown in Figure 2.

During the period 1978-1981, seismological surveys were carried out in the region surrounding the Hengill fissure swarm to explore the geothermal

potential and tectonic structure of the area [Einnarsson et al., 1981; Foulger and Einnarsson, 1980; Foulger, 1984, 1987]. One component of these investigations was a 4-month experiment during June-September 1981 to monitor the abundant microseismicity within the approximate 500 km^2 area encompassing the Hengill central volcano, the geothermal field, and a segment of the fissure swarm [Foulger, 1984, 1987]. The locations of the temporary seismic stations deployed for this study are shown in Figure 2. In this paper, we make use of the P wave arrival time data gathered during the experiment to solve simultaneously for the microearthquake hypocentral parameters and the three-dimensional velocity structure.

ARRIVAL TIME DATA

The highest quality P wave arrival times, as determined by the criteria outlined below, were selected from a data set that includes observations of 1,918 microearthquakes and five explosive sources [Foulger, 1984, 1987]. Microearthquake hypocenters were located using P wave arrival times recorded by a telemetered network of 23 vertical-component seismometers at the sites shown in Figure 2. Arrival times of impulsive P waves could be read to an estimated precision of 0.01 s; because of instrument corrections and variability of the telemetered timing signal, however, the overall uncertainty of the travel times is conservatively estimated to be $\pm$0.03 s at the one standard deviation level of confidence [Foulger, 1987]. Earthquake locations were determined by Foulger [1984, 1987] under the assumption of a laterally homogeneous velocity structure [Palmason, 1971] using the computer algorithm HYPOINVERSE [Klein, 1978]. Further details regarding network operation and data reduction are presented by Foulger [1984, 1987].

The large size of this data set and the variable accuracy of estimated hypocentral parameters allows winnowing of the travel time data on the basis of hypocentral resolution. Criteria applied for this winnowing are the following: (1) Epicentral locations were restricted to a 14 x 15 km^2 area encompassed by the seismic network and shown by the rectangle in Figure 2. The crustal volume to be imaged underlies this area. (2) At least 12 reliable arrival times were necessary for each event. (3) Uncertainties in epicentral position and focal depth were required to be less that 1.0 and 2.0 km, respectively. (4) The total rms travel-time misfit for each event was required to be less than 0.10 s. (5) The maximum gap in source-to-receiver azimuth [Klein, 1978] was required to be less than 180^o. (6) The epicentral distance of the station nearest the event was required to be less than twice the focal depth. With these criteria, the 1,918 microearthquakes were winnowed to obtain the 303 events with the best resolved hypocenters.

The hypocenters of the 303 well-located and -recorded events selected by this winnowing process were not uniformly distributed throughout the volume to be imaged. To improve the sampling of the crustal volume, these 303 hypocenters were further sorted to remove redundant events within regions of dense activity, and 4 earthquakes were added in areas of sparce seismicity. These 4 additional events fullfilled the six constraints given above except for that on the minimum number of impulsive P wave arrivals; for these four events at least nine arrival times were available. This sorting process reduced the total number of distinct earthquake sources to 158. The epicenters of these sources are shown in Figure 3a; a projection of the hypocenters onto a vertical plane is shown in Figure 3b. Of the 5 explosions recorded by the network, travel times from only two of these shots (Figure 3a) were included in the data to be inverted. The shot points of the 3 remaining

explosions were located well outside of the volume to be imaged. Twenty of the 23 available stations were used for arrival times (Figure 3a); the three remaining stations were also located well outside the crustal volume to be imaged (Figure 2). In all, a total of 2,409 P-wave arrival times constitute the data set for tomographic inversion. The hypocentral parameters of the final set of 158 earthquakes, obtained with the laterally homogeneous velocity model, serve as the initial source locations prior to inversion; the two shot positions are held fixed throughout the inversion.

SIMULTANEOUS INVERSION METHOD, OPTIMUM PARAMETERIZATION, AND RESOLUTION

In this section we discuss the simultaneous inversion method used to invert the Hengill P wave arrival time data. Several tomographic techniques are presently available to analyze body wave arrival time data from local experiments with a network dimension on the order of 10 km; a recent review of the different approaches is presented by Thurber and Aki [1987]. A principal distinction among tomographic methods is the choice of velocity model parameterization. Model parameterization affects both the underlying form and the resolution of imaged heterogeneous velocity structure. After a brief overview of the simultaneous inversion method to be followed, we examine some of the factors that influence parameterization.

The tomographic inversion method utilized in this paper is that developed by Thurber [1981, 1983]. Source location parameters and velocity model perturbations are simultaneously estimated from travel times of P waves from local earthquakes or controlled sources. The technique incorporates three noteworthy components. First, parameter separation [Pavlis and Booker, 1980; Spencer and Gubbins, 1980] is used to decouple hypocenter locations and velocity model perturbations into theoretically equivalent subsets of

equations that are computationally manageable. Second, an approximate ray tracing algorithm that requires little computational time is used to estimate minimum travel time paths between specified end points [Thurber and Ellsworth, 1980; Thurber, 1981, 1983]. The utilization of an efficient ray tracing algorithm permits an iterative solution to the simultaneous inversion problem. Iteration ceases when the ratio of successive travel time residual variances falls below a critical value, as defined by an F test for the 5% level of significance. Third, a velocity model parameterization is used that is capable of rendering a realistic and continous velocity structure. Of these three components-- parameter separation, approximate ray tracing, and velocity model parameterization-- only the last requires extensive testing and evaluation for individual data sets in order to achieve optimum results.

Heterogeneous earth structure has been parameterized by constant velocity layers [Crosson, 1976], constant velocity blocks [Aki and Lee, 1976], plane layers constructed of laterally varying blocks with vertically constant velocity [Benz and Smith, 1984], analytical functions specified by a small number of parameters [Spencer and Gubbins, 1980], arbitrarily shaped averaging volumes [Chou and Booker, 1979], continous functions with a priori probabilty density distributions [Tarantola and Nercessian, 1984], and interpolatary functions defined by values specified at nodal points within a 3-dimensional grid [Thurber, 1983]. For the case of the Hengill data set we prefer the interpolatary method of Thurber, for several reasons. A working computer algoritm for simultaneous inversion that incorporates the representation was available to us. The velocity function is capable of reproducing anomalous bodies with characteristic dimensions on the order of a few kilometers or more. The representation is general and does not assume a specific geometry of structural heterogeneity [e.g., Spencer and Gubbins, 1980]. Finally, the

parameterized model yields a continous velocity field, in contrast to discrete block structures with velocity discontinuities across block boundaries.

The interpolation method of Thurber [1981, 1983] describes a continous velocity field by linearly interpolating between velocity values defined at a three-dimensional matrix of parametric nodes. Nodal locations are fixed prior to an inversion, and the spatial distribution of nodes throughout the volume may be irregular. Inversions for heterogeneous structure systematically perturb the values of velocity at the nodal locations. A velocity perturbation depends, in part, on the partial derivative of travel time with respect to a model parameter. Thurber [1981] defines two different forms of these velocity medium partial derivatives, referred to as 'block' and 'linear' partial derivatives; the latter, which are derived directly from the interpolation method, are used in this paper. In practice, an important aspect of this parameterization is the placement and spatial density of nodes within the volume to be imaged.

An optimum configuration of nodes takes into consideration both the inverse method and the spatial distribution of seismic ray paths. Seismic tomography is often formulated as a non-linear, least-squares optimization problem. In principle, a set of travel-time residual data is related linearly, to first order, to a finite number of velocity model perturbations plus a term describing the contributions of random and non-random error. Sources of random error include, for example, uncertainties in picking the P-wave arrival time and clock corrections; these errors can be treated by statistical analysis [e.g., Wiggins, 1972; Jackson, 1972]. An important source of non-random error is the potential inability of a finite set of parameters to reproduce significant variations of a continous field [Jackson, 1979]. The undesirable effects of non-random error on the final solution

cannot be predicted. Non-random errors are avoided by choosing suitable basis functions and a large number of parameters that acceptably describe expected variations [Jackson, 1979].

A practical upper-limit on the total number of model parameters, however, may be imposed by the distribution of seismic ray paths. The simultaneous inversion method, due to Thurber [1983], employs the damped least squares operator to solve the inverse problem. In the case of a damped least squares inversion, poorly sampled parameters are unperturbed. An overly dense distribution of nodal locations will give rise to localized volumes that are poorly sampled, thus resulting in unresolved and possibly misleading patches of unperturbed velocity. This can be avoided by choosing a nodal configuration with a minimum of poorly sampled nodes.

C.H. Thurber [personal communication, 1986] defines a useful measure of the sampling of nodal locations which he calls the derivative weight sum (DWS). The DWS provides an average relative measure of the density of seismic rays near a given velocity node. The DWS of the n^{th} velocity parameter α_n is defined as

$$DWS(\alpha_n) = \sum_i \sum_j \int_{P_{ij}} w_n \, ds \qquad (1)$$

where i and j are the event and station indices, w is the weight used in the linear interpolation and depends on coordinate position [Thurber, 1981], and P_{ij} is the ray path between i and j. The magnitude of the DWS depends on the step size of the incremental arc length ds utilized in the numerical evaluation of equation (1); smaller step lengths yield larger DWS values. Poorly sampled nodes are marked by relatively small values for the DWS. In practice, it is useful to monitor changes in the distribution of the DWS while testing for an optimum nodal configuration. An optimum parameterization, in

general, maximizes the number of parameteric nodes within a volume and, for a damped least squares inversion, minimizes the number of poorly sampled nodes.

It is worth noting that a non-linear stochastic inversion [Tarantola and Valette [1982] or smoothing constraints [Parker, 1975; Sabatier, 1977] would likely relax the upper-limit on the density of nodes imposed by a damped least squares inversion. For the Hengill data set, however, the distribution of data allows a close spacing of nodal locations that is acceptable for reproducing expected velocity heterogeneity while simultaneously minimizing the number of poorly sampled nodes.

In practice, the number of parameters required to describe spatial variations of a seismic velocity field will greatly exceed the number of linearly independent observations, giving rise to non-uniqueness of the final model. This is a well-known problem in geophysical inverse theory [e.g., Backus and Gilbert, 1970; Wiggins, 1972; Jackson, 1972, 1979]. The standard approach to solving a non-unique problem is to define averages of model parameters that are well-constrained by a combination of data and a priori assumptions [e.g., Jackson, 1979]. The damped least squares operator is effective for non-unique and ill-conditioned problems since it preferentially fits well-resolved weighted averages of model parameters, as opposed to the non-unique value of distinct parameters [e.g., Wiggins, 1972; Jackson, 1972, 1979; Menke, 1984]. The weights utilized in this averaging process are defined by the resolution matrix [Wiggins, 1972; Jackson, 1972, 1979]; the resolution matrix linearly relates actual values of model parameters, in the absence of error, to the estimated values. Each row of the resolution matrix is an averaging vector for a single model parameter [e.g., Wiggins, 1972; Jackson, 1972, 1979; Menke, 1984], and, as such, the row describes the dependence of an estimated parameter value on the values of all other model

parameters; further properties of the model resolution matrix are discussed by Wiggins [1972] and Jackson [1972, 1979] and reviewed by Menke [1984, Chap. 4, 6]. Utilizing a large number of parameters in a simultaneous inversion, so as to avoid non-random errors [Jackson, 1979], makes it necessary to examine the averaging vector of each model parameter in order to assess the quality of a solution.

The averaging vector of a model parameter can be pictorially or quantitatively examined, as described below. The model parameters in a tomographic inversion have an obvious spatial ordering within the volume to be imaged. An instructive way of examining the resolution matrix is to plot the elements of the averaging vector for a single model parameter in the three-space of the study volume [e.g., Menke, 1984]. A qualitative definition of good resolution for a model parameter would be that the weights of the averaging vector were non-zero only in the vicinity of the parameter of interest. Such an averaging vector would be considered compact [Wiggins, 1972]. Plots of the averaging vector are presented later in this paper, and they indicate clearly that estimated values of selected model parameters are weighted averages over localized volumes. For a simultaneous inversion with hundreds of nodes, it is impractical to pictorially examine the averaging vector of each node. The definition of a spread function [Backus and Gilbert, 1967, 1968; Menke, 1984] provides a synoptic view of resolution. For the present problem, we define the spread function for a single averaging vector, following Menke [1984], as

$$S(\underline{r}_p) = (\|\underline{r}_p\|)^{-1} \sum_{q=1}^{m} \Omega(p,q)\, R_{pq}^2 \qquad (2)$$

where $\underline{r}_p$ is the averaging vector of the p^{th} parameter, R_{pq} is an element of the resolution matrix, $\Omega(p,q)$ is a weighting function defined as the

distance between the p^{th} and q^{th} nodes, and m is the number of parameters. For a compact averaging vector, the spread function is small. In a later section, we utilize both pictorial representations of selected averaging vectors and the spread function of all averaging vectors to assess the resolving power of the Hengill data set.

APPLICATION OF SIMULTANEOUS INVERSION

The application of the simultaneous inversion method to the Hengill data set will be presented in three parts. First, we discuss our choice of initial values for hypocentral and velocity model parameters, and we present an optimal configuration of nodal locations. Second, given this configuration of nodes and the available data, we evaluate the resolving power of the arrival time data through an analysis of the averaging vector of each model parameter. Third, the results of simultaneous inversion are presented.

Initial Values and Nodal Placement

The final three-dimensional velocity structure determined by the simultaneous inversion method depends on arrival time uncertainty, ray coverage, a priori values for hypocenter and velocity model parameters, and the representation of the velocity field (in this case, the number and placement of nodal points). For the Hengill study, travel time data quality is good, one standard deviation arrival time errors are less than 0.03 s, and the distribution of sources and stations provides extensive ray coverage (Figure 3a).

Initial estimates of hypocentral and velocity model parameters, of course, should not be too different from the final values in order to reduce the effects of non-linearity. A natural choice of hypocentral parameters are those calculated by HYPOINVERSE for the assumed laterally homogeneous velocity

model. The combination of excellent station distribution in the Hengill area and the expected degree of velocity heterogeneity (see below) suggests that the hypocentral parameters determined by Foulger [1987] are good starting values for the simultaneous inversion.

Refraction profiles collected near the Hengill area [Palmason, 1971] provide good constraints on the laterally averaged P-wave velocity structure (Figure 4). Steep velocity gradients (1 s^{-1}) are present at shallow depths (0-3 km), low velocity gradients (0.1-0.2 s^{-1}) occur from 3 to 10 km depth, and a halfspace velocity of 7.0 km/s at 10 km depth is assumed, based on the work of Angenheister et al. [1980]. This velocity structure was used by Foulger [1984] in the calculation of the microearthquake hypocentral parameters. Also shown in Figure 4 is a second velocity-depth function that is similar in form to that of Palmason [1971] but with velocities that at all depths are higher, by 0.2 to 0.5 km/s. This model is a lateral average of several trial inversions conducted to explore nodal configuration. The higher velocities are consistent with the observations of Palmason [1971] and Flovenz [1980] that suggest higher than average velocities near Icelandic central volcanos. Both velocity depths structures were tested as starting models for the simultaneous inversion.

The choice of a starting model for inversion for three-dimensional structure depends upon the degree of crustal velocity heterogeneity. In extremely heterogeneous areas it is often beneficial to step progressively from one-, to two-, to three-dimensional models [e.g., Thurber, 1983]. Such an approach minimizes the chance of poor convergence caused by a starting model that is not sufficiently close to the structure of the actual earth. Foulger [1984] examined travel time delays from teleseismic events and regional explosions and found that the anomalies were consistent with lateral

velocity variations of less than 5-10%. The magnitude of the expected heterogeneity of velocity within the Hengill area suggests that determination of an intermediate two-dimensional model is unnecessary. The rapid covergence and consistency of all attempted simultaneous inversions supports this claim.

Several nodal configurations were tested for the velocity parameterization to determine the optimal configuration. In a series of test inversions, the horizontal and vertical separation of nodes was varied from 2 to 4 km and 1 to 2 km, respectively. The results of simultaneous inversion for all nodal configurations were in general agreement, in that regions of anomalously high or low velocities were observed at similar locations. However, whereas coarser nodal spacing (4 km) led to solutions displaying broad regions of anomalous velocity, a finer nodal spacing (2 km) permitted the definition of distinct bodies of anomalous velocity. Compared with the coarser nodal configuration, the final rms travel time residual for the finer spacing was significantly smaller by 0.01 s, a difference significant at 95% confidence as determined by an F test. The total number of iterations of the linear equations for the coarse and fine nodal spacings was two and three, respectively.

The nodal distribution used for the final inversion results includes nodes spaced every 2 km in the horizontal direction, except for a 3 km spacing between rows at y=0 and y=3 km. Nodes in the vertical direction were spaced at 1 km intervals from 0 km (sea level) to 6 km depth. A total of 448 nodes sample the 14 x 15 x 6 km^3 volume. Plan-view contour plots of the DWS are shown in Figure 5 at depths of 0, 3, and 5 km. The contour plots indicate, in a relative sense, that nodes at the intermediate depth of 3 km are evenly and well sampled by ray paths. The distribution of the DWS at 0 km depth shows marked lateral variability relative to the plot for 3 km depth, reflecting to

the distribution of receiving stations (Figure 3a), i.e., large values directly beneath stations and small values in regions were no stations are located. At a nodal depth of 5 km the DWS decreases due to the fall off of seismicity with depth (Figure 3b). Overall, inspection of the DWS contour plots for all nodal depths between 0 and 6 km indicates that away from the edges of the 14 x 15 km^2 area and between the depths of 1 and 5 km the distribution of seismic ray paths is in general adequate to resolve structural variations at the spatial scales defined by nodal distances.

Resolution of Model Parameters

Given a nodal configuration and an estimate of ray path distribution, we can evaluate the resolution matrix and the spread function of each averaging vector. For the following analysis of resolution, we used our inversion results, presented further on, to calculate the seismic ray paths.

The spread function $S(\underline{r}_p)$, defined by equation (2), was evaluated for the averaging vector of each model parameter. Figure 6 shows a plot of the DWS versus the spread of the averaging vector for each of the 448 model parameters. As expected, well-sampled nodes (large DWS) generally correspond to smaller values of $S(\underline{r}_p)$. Since an averaging vector depends on the geometry of rays near a node, and not just the total number or density of rays, there is scatter about the general trend shown in Figure 6. The sensitivity of parameter resolution on ray geometry is well-known [e.g., Aki et al., 1977].

A subjective choice of the range of acceptable values of the spread function can be made by examining the individual averaging vectors. An acceptable averaging vector, or spread function value, should indicate localized averaging of velocity. Figures 7 and 8 show three-dimensional perspective plots of two averaging vectors in the three-space of the study

volume; the values of the elements of each averaging vector are plotted at the nodal location corresponding to that element. The averaging vector in Figure 7 is for a node in the center of the volume (x=8, y=7, and z=3 km); the spread of the averaging vector for this node is 0.3. This averaging vector is clearly 'compact', indicating localized averaging of velocity. Figure 8 displays an averaging vector for a node at x=2, y=3, and z=2 km; the spread of the averaging vector for this node is 1.9. The averaging vector in Figure 8, while less compact than that of Figure 7, is considered to be acceptable. On the basis of pictorial examination of numerous averaging vectors, we choose a spread value of 2 as an upper limit for the range of acceptable values of $S(\underline{r}_p)$. Naturally, the smaller the value of $S(\underline{r}_p)$ the better is the resolution of the model parameter. Figure 9 shows plan-view contour plots of $S(\underline{r}_p)$ at nodal depths between 0 and 5 km depth. Areas where $S(\underline{r}_p)$ is less than 2 are well-resolved.

Results

Simultaneous inversions were conducted for both of the velocity-depth functions shown in Figure 6. For an inversion initialized with the velocity model of Palmason [1971], hereafter referred to as inversion 1, the initial rms travel time residual was 0.06 s. For inversion 2, which was initialized by the second velocity-depth function in Figure 6, the initial rms travel time residual was 0.05 s; in both cases the initial rms travel time residual was calculated after a relocation of hypocenters but before velocity model perturbation. Iteration of the complete simultaneous inversion terminated after 4 and 3 steps for inversions 1 and 2, respectively. In both cases, the final rms travel time residual was 0.04 s; the travel time residual variance reduction for inversions 1 and 2 was 46% and 37%, respectively. An F test on the ratio of the final travel time variance from the two inversions indicates

that the overall travel time misfits are indistinguishable at the 5% level of significance. With respect to the final variance of travel time residuals, it appears that the inversion results are independent of the initial velocity model.

A comparison of the final heterogeneous velocity structures provides important information on the influence of initial models. The a posteriori covariance estimates of model parameters, as defined by Thurber [1981, 1983], should give approximate limits for acceptable differences between the final models of inversions 1 and 2. For both inversions, the mean standard error of fractional perturbations, defined as the percent deviation from the starting model, was 2% [Thurber, 1981, 1983]; this average value is equivalent to an error of about 0.1 km/s in the final estimate of velocity at a node. We evaluated the difference between the final models using several comparisons. Simply subtracting the final velocity values obtained from inversion 2 from those of inversion 1, for all well-resolved nodal locations ($S(\underline{r}_p) < 2$), proved to be a poor means of comparison; the mean and the rms difference between the final velocity models was -0.1 and 0.2 km/s, respectively. The negative mean indicates that the offset of the two final models is similar to the offset of the starting models, i.e., velocities from inversion 2 were systematically greater than velocities from inversion 1. We then subtracted from each final model the respective initial model, and compared these velocity perturbations for all well-resolved nodal locations; the mean and the rms of the difference between these velocity perturbations were both 0.2 km/s. The positive mean indicates that perturbations for inversion 1 were generally greater that those of inversion 2. As a final test, we compared the final velocity models in the following way. For each inversion and for each horizontal layer of nodes, the average velocity was calculated for the final

structure; again, only well-resolved nodes were included in this averaging process. These average velocity-depth structures were then subtracted from their respective final models, yielding 'normalized' velocity perturbations. The mean and the rms difference between these two sets of normalized velocity perturbations was 0 and 0.1 km/s, respectively, showing good agreement between the two normalized models.

On the basis of these comparisons, we conclude that both the final velocity field and the magnitude of the perturbations from an initial model may be biased by the choice of the starting model. However, velocity perturbations relative to a lateral average of the final model are apparently unbiased or at most modestly biased by the initial model. This important result suggests that tomographic inversions utilizing predominantly earthquake sources are, within the limits of acceptable initial models, insensitive to absolute values of velocity. In a tomographic study of the Mid-Atlantic Ridge median valley, it was shown that a combination of travel times from both controlled and natural sources can resolve the ambiguity in the absolute value of the final velocity model [Toomey et al., 1987].

The results of inversion 2 are shown in Figure 9. In this figure we depict plan-view contour plots of normalized velocity perturbations at nodal depths between 0 and 5 km; structure below a depth of 5 km was unresolvable. The contour interval for the plots, 0.2 km/s, exceeds the estimate of the standard error of the velocity perturbations. Shown alongside each contour plot of normalized velocity perturbation is the contour plot of the spread $S(\underline{r}_p)$ for the associated horizon of nodes. As stated previously, only regions where $S(\underline{r}_p) < 2$ are well-resolved. Together, the two types of plots summarize the distribution of well-resolved velocity anomalies. For example, inspection of Figure 9a at a depth of 0 km shows that two near-surface

velocity anomalies are clearly within areas in which $S(\underline{r}_p) < 2$. However, in some regions the lateral extent of these bodies (at sea level) is poorly resolved since the zero contour of velocity perturbation occurs where $S(\underline{r}_p) > 2$. For the horizon of nodes at 3 km depth (Figure 9b), the plots of normalized velocity perturbations exhibit pronounced lateral variability of crustal structure. The contour plots of $S(\underline{r}_p)$ at this depth show that most of these velocity anomalies lie within regions with $S(\underline{r}_p) \leq 1$, indicating good resolution.

The final model of velocity heterogeneity is characterized by several distinct bodies of anomalously high velocity. At shallow (0-2 km) crustal depths, Figure 9a shows two prominent velocity highs centered at approximately x=3, y=13 km and x=8, y=7 km, respectively. Both of these anomalies are horizontally removed from the Hengill volcano and the trace of the fissure swarm. Within the center of these anomalies, velocities are greater than the average structure by approximately 10% . At shallow depths, a single low velocity anomaly was observed at x=12, y=13 km; the maximum deviation from the average model is about -10%. The most pronounced velocity anomalies occur at a depth of 3 km (Figure 9b). At this depth, the anomaly centered near x=3, y=13 km is still present, but the anomaly at x=8, y=7 km is not apparent. A prominent high velocity anomaly at a depth of 3 km is centered on x=6, y=9 km. Within this structure velocities are higher than the average model by more than 15%. This anomalous volume clearly continues to a depth of 4 km. The two high velocity bodies at a depth of 3 km are separated by a narrow zone of relatively low velocities at x=7, y=11 km.

The spatial separation of distinct velocity anomalies and the vertical coherence of anomalous bodies is best shown in the perspective view in Figure 10; the normalized velocity perturbations are expressed as percent deviations

in these views. Also plotted on the surface planes of Figure 10 are the locations of the extinct Grensdalur volcano, the Hengill volcano, and the trend of the fissure swarm which marks the most recent locus of crustal extension. The three distinct bodies of anomalously high velocities are clearly present in the figures; the two high velocity volumes extending from the surface to approximately 3 km depth are associated with past volcanic eruptions. The third high velocity body at a depth of 3-5 km lies beneath the center of the geothermal field (Figure 2), located midway between the recently active Hengill volcano and the extinct Grensdalur volcano. A full geologic interpretation of these results is presented elsewhere [Foulger and Toomey, 1986].

CONCLUSIONS

The simultaneous inversion method of Thurber [1981, 1983] has been applied to travel time data from earthquakes in the Hengill volcano and geothermal field in southwestern Iceland. Consideration of the model parameterization and inversion method suggests that an optimum parameterization, as expected, maximizes the spatial density of model parameters but minimizes the number of poorly sampled nodes. For an extensive distribution of seismic ray paths such an optimum parameterization gives rise to a non-uniqueness of the final model. Drawing from the results of geophysical inverse theory for parameterized systems [e.g., Wiggins, 1972; Jackson, 1972, 1979; Menke, 1984], we have discussed a general means for analyzing the resolution matrix of model parameters. In particular, we have shown that the averaging vector of individual model parameters is summarized by its spread function [Backus and Gilbert, 1967, 1968; Menke, 1984]. The synoptic view of model resolution permitted by the analysis of spread functions is invaluable for interpreting

the significance of imaged velocity heterogeneity. When applied to the Hengill data set, the analysis of resolution has shown that tomographic images are the results of weighted averages of velocity over localized volumes.

Simultaneous inversion results in images of distinct bodies of anomalous velocity that correlate spatially with such prominent geologic features as sites of past volcanic eruptions and an active high-temperature geothermal field. Two distinct anomalies extend from near the surface to a depth of about 3-4 km, and both underlie past eruptive sites. A third subsurface anomaly is centered between the depths of about 3-4 km, and it underlies an active geothermal field. All of these anomalies are limited in their horizontal extent to dimensions of 3-5 km. An interpretation of these anomalies in the context of local geology and tectonics is presented by Foulger and Toomey [1986, in preparation].

References

Aki, K., and W.H.K. Lee, Determination of three-dimensional velocity anomalies under a seismic array using first P arrival times from local earthquakes, 1, A homogeneous initial model, J. Geophys. Res., 81, 4381-4399 1976.

Aki, K., A. Christofferson, and E.S. Husebye, Determination of the three-dimensional seismic structure of the lithosphere, J. Geophys. Res., 82, 277-296, 1977.

Angenheister, G., Sv. Bjornsson, P. Einarsson, H. Gebrande, P. Goldflam, W.R. Jacoby, I.V. Litvinenko, B. Loncarevic, H. Miller, G. Palmason, N.I. Pavelnkova, S. Richard, S.C. Solomon, W. Weigel, and S.M. Zverev, Reykjanes Ridge Seismic Experiment (RRISP 77), J. Geophys., 47, 228-238, 1980.

Backus, G. E., and J. F. Gilbert, Numerical application of a formalism for geophysical inverse problems, Geophys. J. R. Astron. Soc., 13, 247-276 1967.

Backus, G. E., and F. Gilbert, The resolving power of gross earth data, Geophys. J. R. Astron. Soc., 16, 169-205, 1968.

Backus, G. E., and F. Gilbert, Uniqueness in the inversion of inaccurate gross earth data, Philos. Trans. R. Soc. London, 266, 123-192, 1970.

Benz, H.M., and R.B. Smith, Simultaneous inversion for lateral velocity variations and hypocenters in the Yellowstone region using earthquake and refraction data, J. Geophys. Res., 89, 1208-1220, 1984.

Bjornsson, A., and G.P. Hersir, Geophysical reconnaissance study of the Hengill high-temperature geothermal area, SW-Iceland, Geothermal Resources Council, Trans., 5, 55-58, 1981

Chou, C.W., and J.R. Booker, A Backus-Gilbert approach to inversion of travel-time data for three-dimensional velocity structure, Geophys. J.R. Astron. Soc., 59, 325-344, 1979.

Crosson, R.D., Crustal structure modeling of earthquake data, 1, Simultaneous least squares estmation of hypocenter and velocity parameters, J. Geophys. Res., 81, 3036-3046, 1976.

Eberhart-Phillips, D., Three-dimensional velocity structure in northern California Coast Ranges from inversion of local earthquake arrival times, J. Geophys. Res., submitted, 1987.

Einarsson, P., Seismicity and earthquake focal mechanisms along the mid-Atlantic plate boundary between Iceland and the Azores, Tectonophysics, 55, 127-153, 1979.

Einarsson, P., and S. Bjornsson, Earthquakes in Iceland, Jokul, 29, 37-43, 1979.

Einarsson, P., S. Bjornsson, G. Foulger, R. Stefansson, and T. Skaftadottir, Seismicity pattern in the South Iceland Seismic Zone, in D.W. Simpson and P.G. Richards eds., Earthquake prediction--An International Review, Maurice Ewing Series 4, Amer. Geophys. Un., Washington, D.C., pp 141-151, 1980.

Eiriksson, J., Stratigraphy of the western part of the South Iceland lowland (in Icelandic), B.S. Thesis, University of Iceland, 98 pp., 1973.

Flovenz, O.G., Seismic structure of the Icelandic crust above layer three and the relation between body wave velocity and alteration of the basaltic crust, J. Geophys., 47, 211-220, 1980.

Foulger, G.R., Seismological Studies at the Hengill geothermal area, SW Iceland, Ph.D. Thesis, Univ. of Durham, England, 313 pp., 1984.

Foulger, G.R., Seismological studies at the Hengill geothermal area, S.W. Iceland, submitted, J. Geophys. Res., 1987.

Foulger, G.R., and P. Einarsson, Recent earthquakes in the Hengill-Hellisheidi area in SW-Iceland, J. Geophys., 47, 171-175, 1980.

Foulger, G.R. and D.R. Toomey, 3-D crustal structure of the Hengill-Grensdalur central volcano complex, Iceland, from seismic tomography, (abstract), EOS, 67, 1110, 1986.

Hasemi, A.H., H. Ishii, and A. Takagi, Fine structure beneath the Tohoku district, northeastern Japan arc, as derived by an inversion of P-wave arrival times from local earthquakes, Tectonophysics, 101, 245-265, 1984.

Jackson, D.D., Interpretation of inaccurate, insufficient and inconsistent data, Geophys. J. R. Astron. Soc., 28, 97-110, 1972.

Jackson, D.D., The use of a priori data to resolve non-uniqueness in linear inversion, Geophys. J. R. Astron. Soc., 57, 137-157, 1979.

Jakobsson, S.P., J. Jonsson, and F. Shido, Petrology of the western Reykjanes Peninsula, Iceland, J. Petrol., 19, 669-705, 1978.

Klein, F.W., Hypocenter location program HYPOINVERSE, 1, User's guide to versions 1,2,3,4, U.S. Geological Survey Open File Rep., 78-694, 103 pp., 1978.

Klein, F.W., P. Einarsson, and M. Wyss, Microearthquakes on the mid-Atlantic plate boundary on the Reykjanes Peninsula in Iceland, J. Geophys. Res., 78, 5084-5099, 1973.

Klein, F.W., P. Einarsson, and M. Wyss, The Reykjanes Peninsula, Iceland, earthquake swarm of September 1972 and its tectonic significance, J. Geophys. Res., 82, 865-888, 1977.

Menke, W., Geophysical data analysis: discrete inverse theory, New York: Academic Press, 260 pp., 1984.

Palmason, G., Crustal structure of Iceland from explosion seismology, Soc. Sci. Islandica Rit., 40, 187 pp, 1971.

Parker, R.L., The theory of ideal bodies for gravity interpretation, Geophys. J. R. Astron. Soc., 42, 315-334, 1975.

Pavlis, G.L., and J.R. Booker, The mixed discrete-continuous inverse problem: Application to the simultaneous determination of earthquake hypocenters and velocity structure, J. Geophys. Res., 85, 4801-4810, 1980.

Roecker, S.W., The velocity structure of the Pamir-Hindu Kush region: possible evidence of subducted crust, J. Geophys. Res., 87, 945-959, 1982.

Sabatier, P.C., On geophysical inverse problems and constraints, J. Geophys., 43, 115-137, 1977.

Saemundsson K., Vulkanismus und tektonik des Hengill-Gebietes in Südwest-Island, Acta Nat. Islandia, 11, 7, 105 pp., 1967.

Spencer, C., and D. Gubbins, Travel time inversion for simultaneous earthquake location and velocity structure determination in laterally varying media, Geophys. J.R. Astron. Soc., 63, 95-116, 1980.

Tarantola, A., and A. Nercessian, Three-dimensional inversion without blocks, Geophys. J. R. Astron. Soc., 76, 299-306, 1984.

Tarantola, A., and B. Valette, Inverse problems = quest for information, J. Geophys., 50, 159-170, 1982.

Thurber, C.H., Earth structure and earthquake locations in the Coyote Lake area, central California, Ph.D. Thesis, Mass. Inst. of Technol., Cambridge, 332 pp., 1981.

Thurber, C.H., Earthquake locations and three-dimensional crustal structure in the Coyote Lake area, central California, J. Geophys. Res., 88, 8226-8236 1983.

Thurber, C.H., Seismic detection of the summit magma complex of Kilauea volcano, Hawaii, Science, 223, 165-167, 1984.

Thurber, C.H. and K. Aki, Three-dimensional seismic imaging, Ann. Rev. Earth Plant. Sci., 15, 115-139, 1987.

Thurber, C.H., and W.L. Ellsworth, Rapid solution of ray tracing problems in heterogeneous media, Bull. Seismol. Soc. Am., 70, 1137-1148, 1980.

Toomey, D.R., S.C. Solomon, and G.M. Purdy, Microearthquakes beneath the median valley of the Mid-Atlantic Ridge near 23°N: Tomography and tectonics, J. Geophys. Res., submitted, 1987.

Wiggins, R.A., The general linear inverse problem: Implication of surface waves and free oscillations for earth structure, Rev. Geophys. Space Phys., 10, 251-285, 1972.

Figure 1. Map of principal tectonic features in southwestern Iceland, after Einarsson and Bjornsson [1979]. The extent of the South Iceland Seismic Zone is shown schematically. Zones of fissure swarms are outlined by parallel saw-toothed lines. The bold rectangle defines the area of the 1981 Hengill microearthquake survey that is shown in Figure 2.

Figure 2. Principal geologic features near the Hengill central volcano and the network configuration for the microearthquake experiment. Topography greater than 600 m is hachured and shows the location of Hengill volcano; dashed lines denote volcanic eruptive fissures [Saemundsson, 1967; Eiriksson, 1973]; open squares are locations of hot springs and fumeroles [Saemundsson, 1967]; closed circles denote seismic instruments; stippled areas represent lakes and rivers. The rectangle in the center of the map encloses the surface area of the volume imaged by tomographic inversion.

Figure 3. (a) Epicenters, seismic stations, and shot locations used in the tomographic analysis. Closed circles represent seismic stations; open circles denote microearthquake epicenters; open triangles show shot locations. The origin of the coordinate system used in simultaneous inversion is the southernmost corner of the rectangle in the center of the map; the x- and y-axes are 14 and 15 km in length, respectively, and the z-axis is positive downwards with 0 km depth at sea level.

(b) Projection of microearthquake hypocenters onto a vertical plane parallel to the x-axis of Figure 3a.

Figure 4. P wave velocity depth models used to initialize simultaneous inversions. The solid line is taken from the refraction results of Palmason [1971]. The dashed line is a lateral average of several test inversions (see text).

Figure 5. Plan-view contour maps of the derivative weight sum (DWS) at selected depths of 0, 3, and 5 km. The contour interval is 50.

Figure 6. A plot of the DWS versus the spread function of the averaging vector for each of the 448 model parameters. The dashed line is the upper limit for acceptable values of the spread function (see text).

Figure 7. A three-dimensional perspective plot of the averaging vector for the node located at x=8, y=7, and z=3 km. The values of the elements of the averaging vector are plotted at the nodal location corresponding to that element; six perspective plots are shown for a single averaging vector, one for each nodal depth between 0 and 5 km. Within a single perspective plot the vertices of a box correspond to one of the 64 nodal locations within a horizontal plane. The vertical scale is identical in Figures 7 and 8.

Figure 8. A three-dimensional perspective plot of the averaging vector for the node located at x=2, y=3, and z=2 km. See Figure 7 for further explanation.

Figure 9. (a) Plan-view contour plots of spread and normalized velocity perturbations at nodal depths of 0, 1, and 2 km. The contour interval for the plots of spread $S(\underline{r}_p)$ is 1; regions where $S(\underline{r}_p)$ is less than 2 are well-resolved. The contour interval for normalized velocity perturbations is 0.2 km/s.

(b) Plan-view contour plots of spread $S(\underline{r}_p)$ and normalized velocity perturbations at nodal depths of 3, 4, and 5 km; nodes at 6 km depths were poorly resolved, i.e., $S(\underline{r}_p)$ was greater than 2.

Figure 10. Three-dimensional image of the solution to the tomographic inversion. The grey shading denotes percentage difference in velocity from the normalized structure. For display purposes, the model is represented by constant-velocity cubic blocks of dimension 0.25 km; the actual inversion solution, as described in the text, is a continous function of each spatial coordinate. Two separate views of the solution are shown in (a) and (b). The vertical coordinate increases upward in these figures; z = 5 km corresponds to sea level.

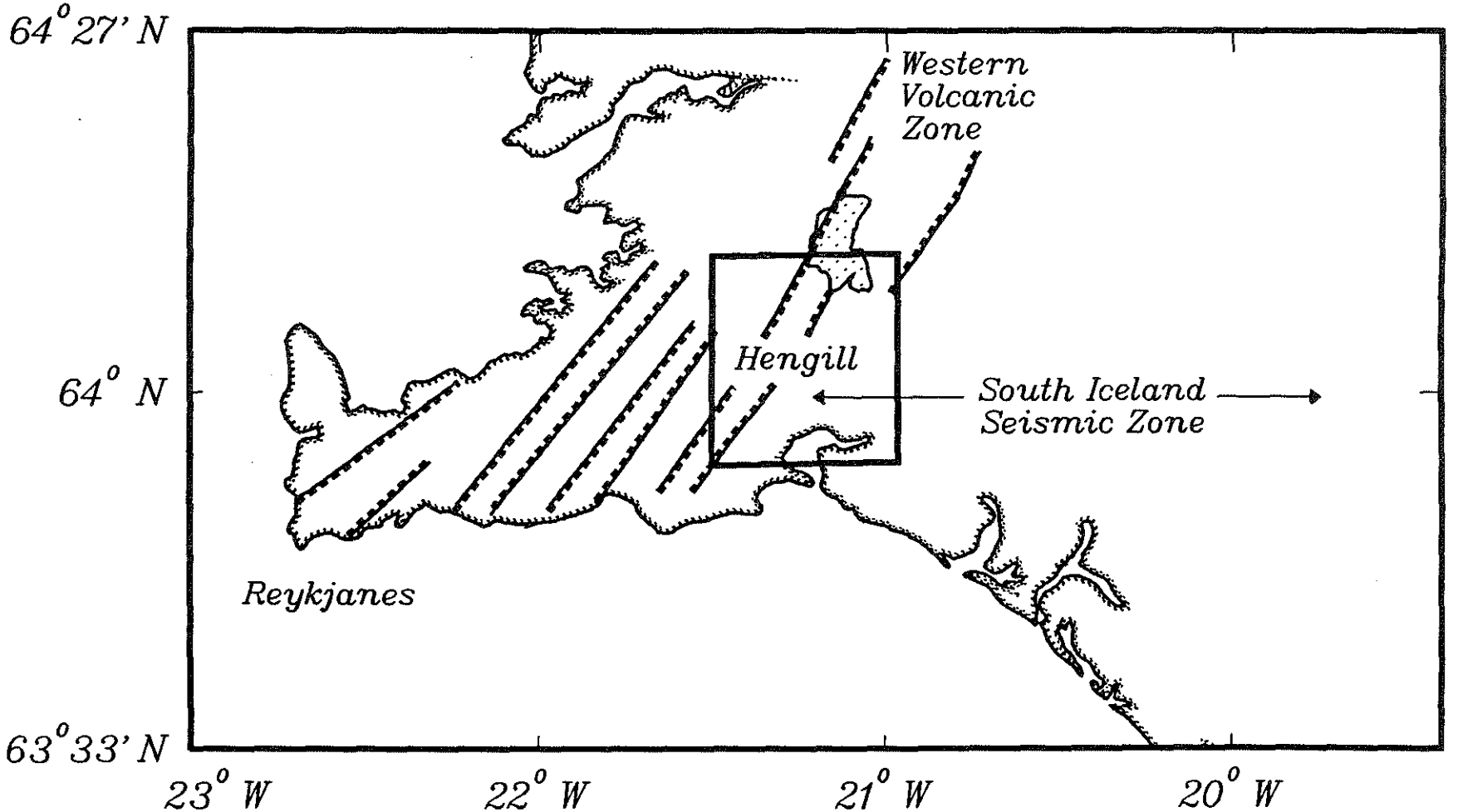
64° 27' N
64° N
63° 33' N
23° W
22° W
21° W
20° W
Western
Volcanic
Zone
Hengill
South Iceland
Seismic Zone
Reykjanes

Figure 1

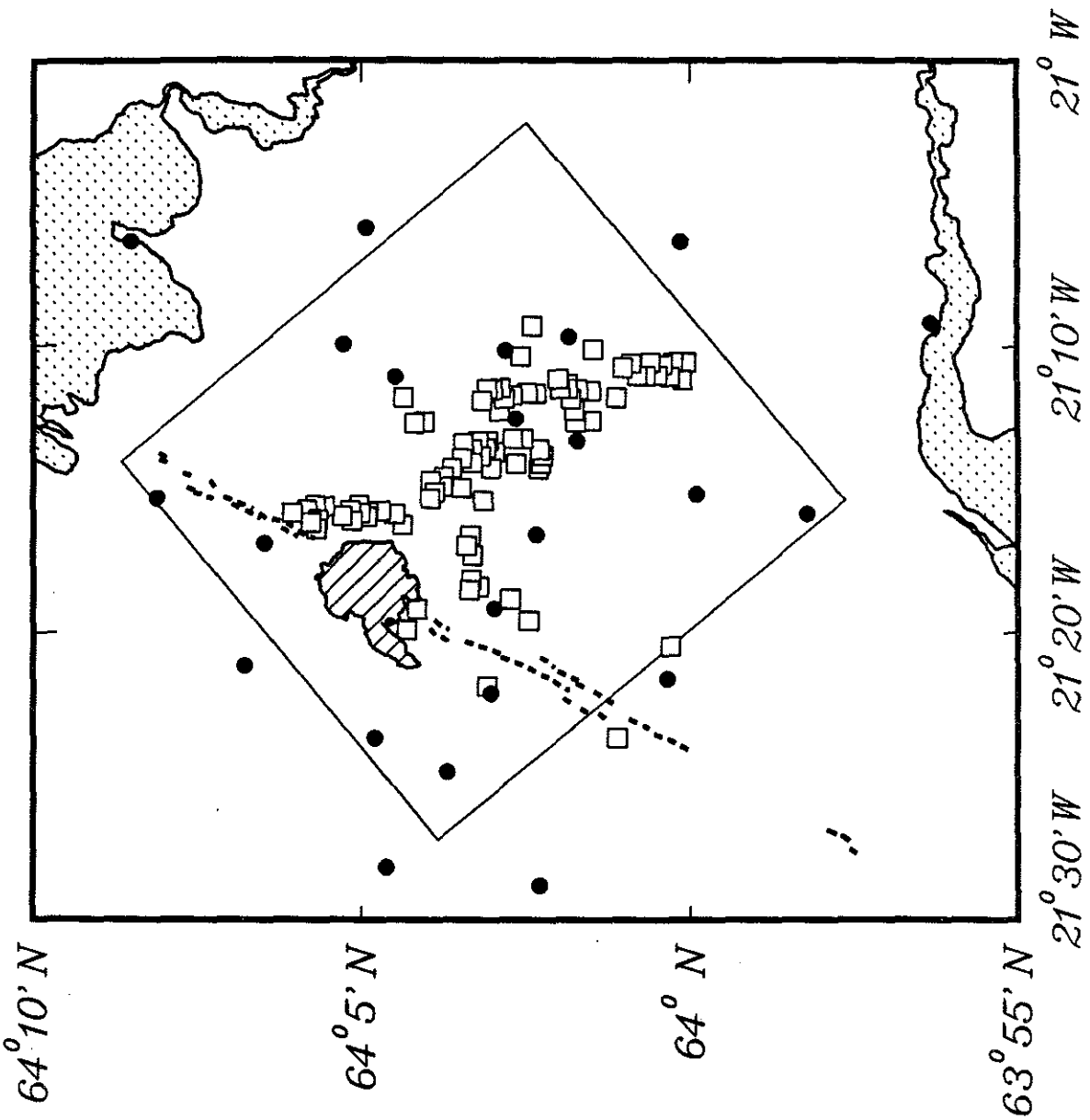

Figure 2

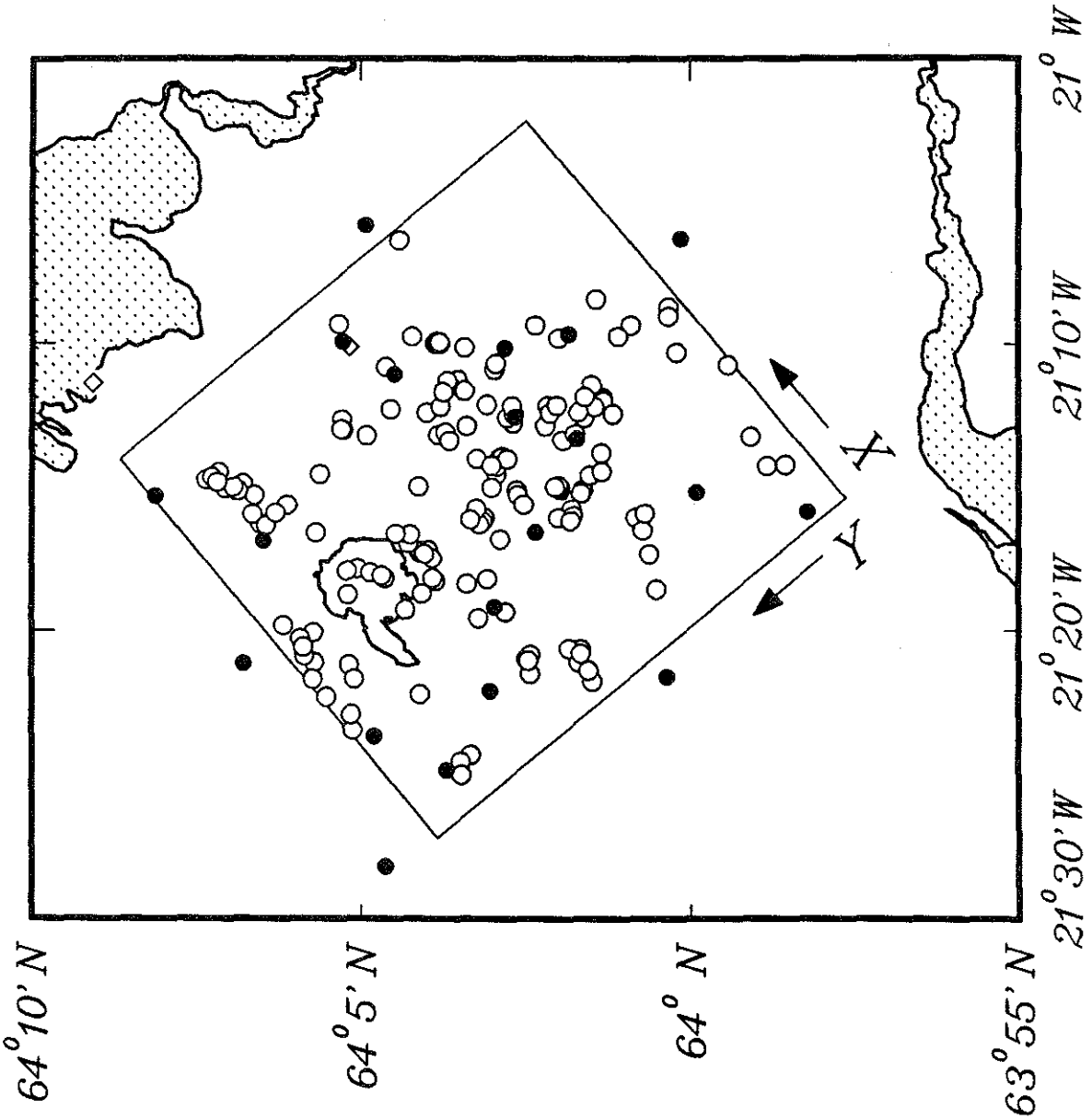

Figure 3a

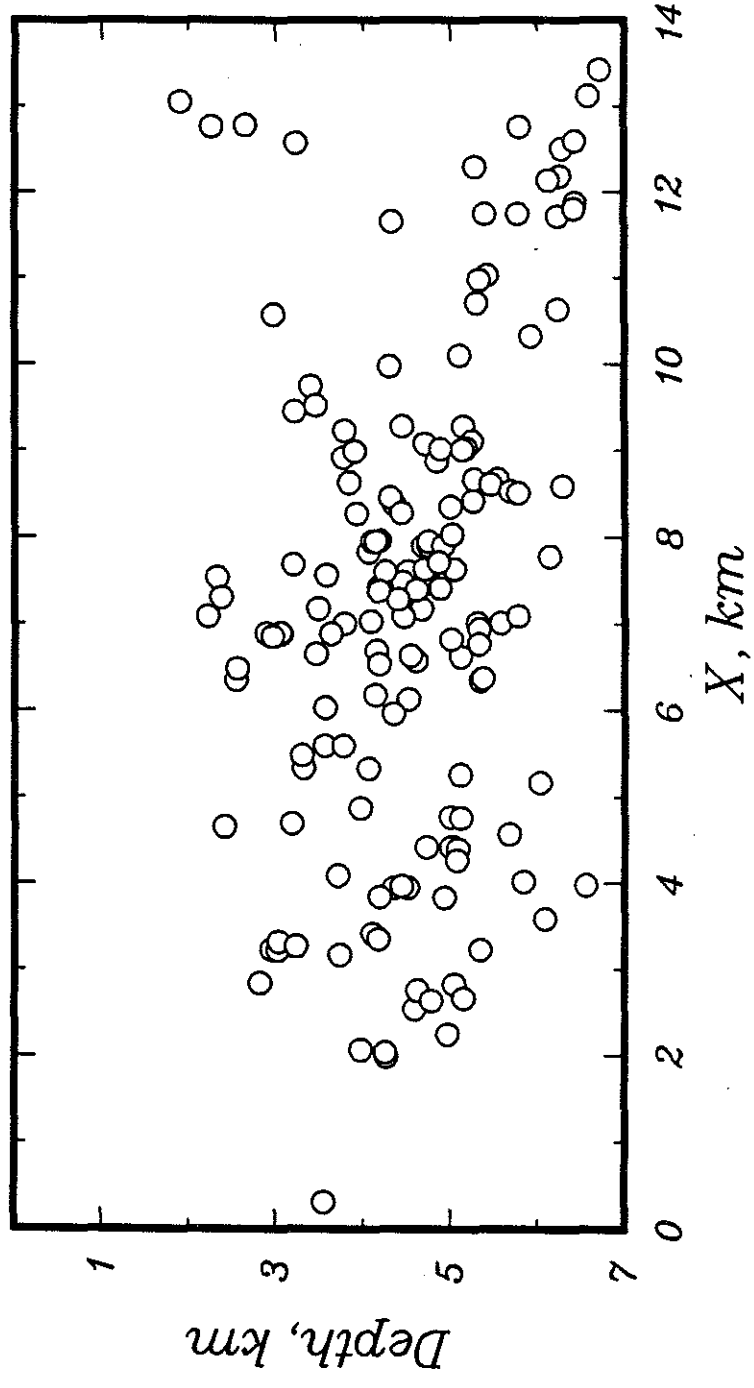

Figure 3b

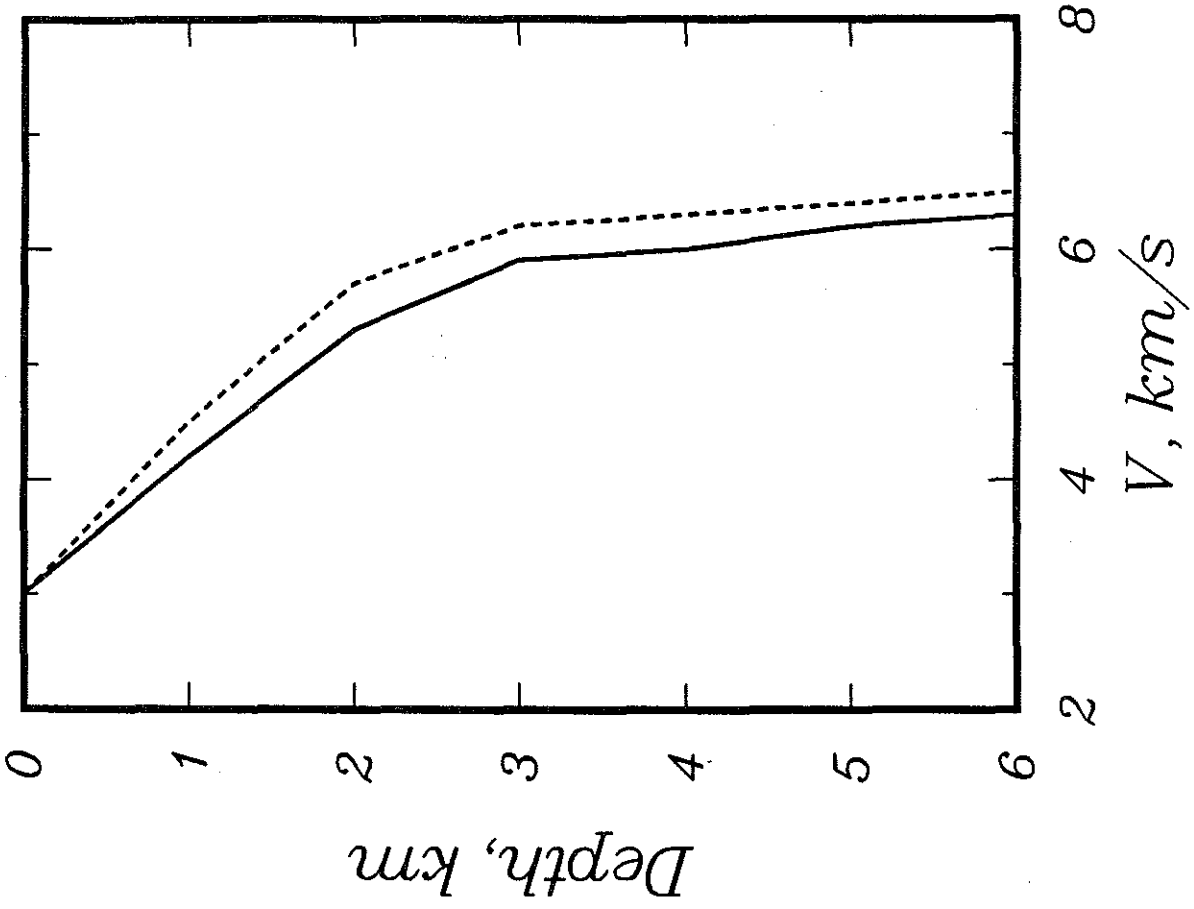

Figure 4

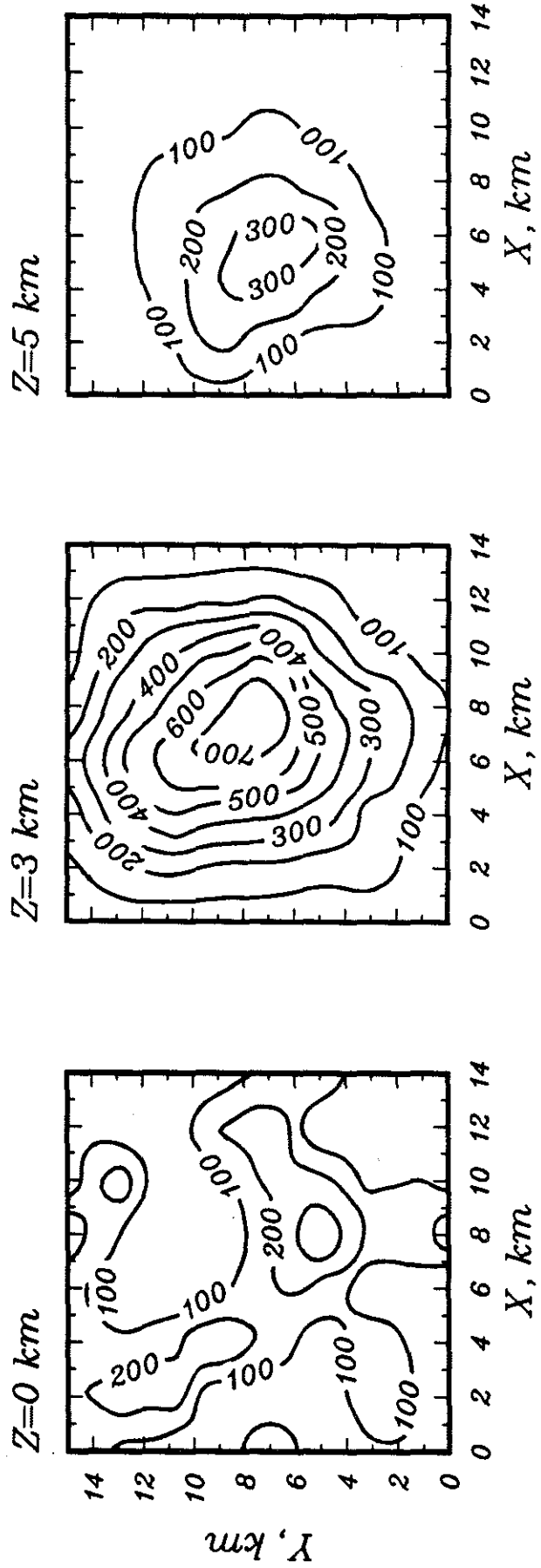
Z=0 km
Z=3 km
Z=5 km
X, km
Y, km
0 2 4 6 8 10 12 14
100
200
300
400
500
600
700

Figure 5

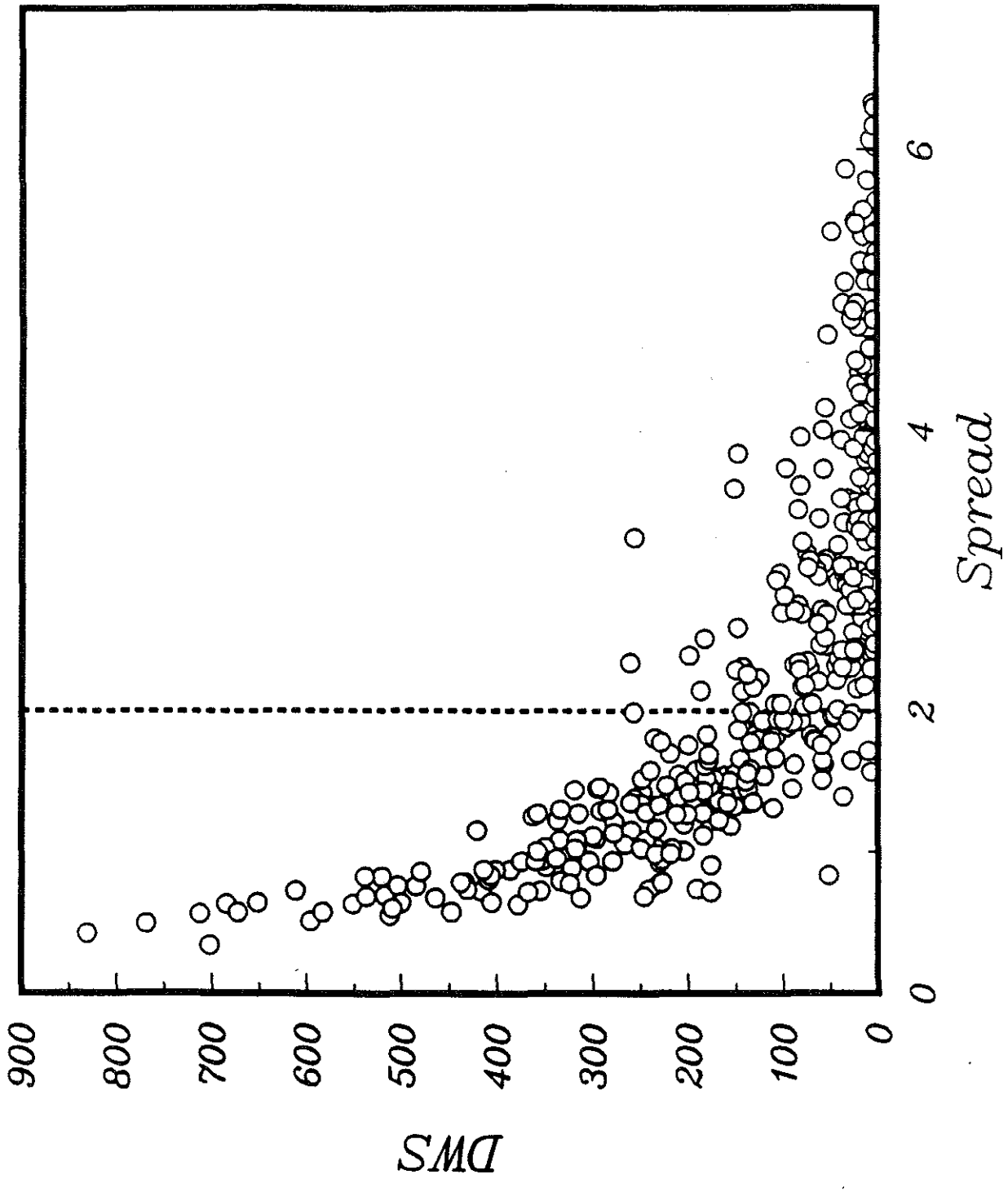

Figure 6

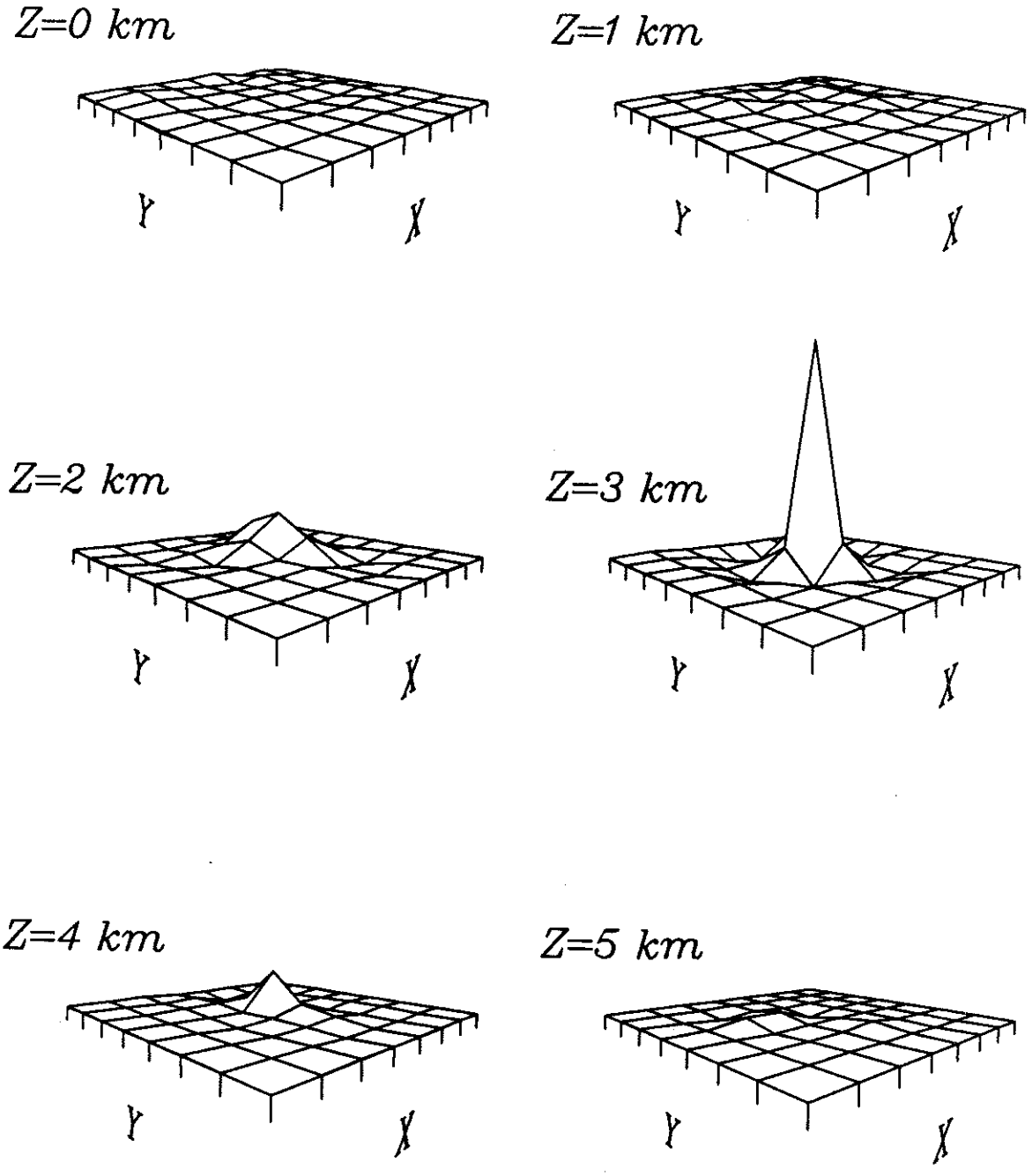

Figure 7

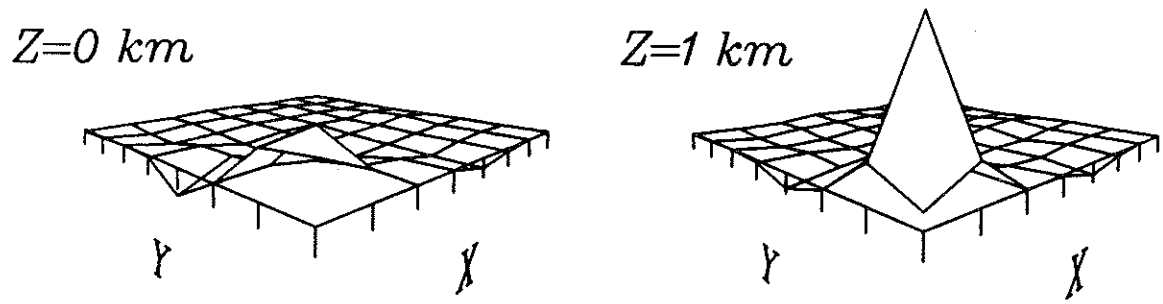

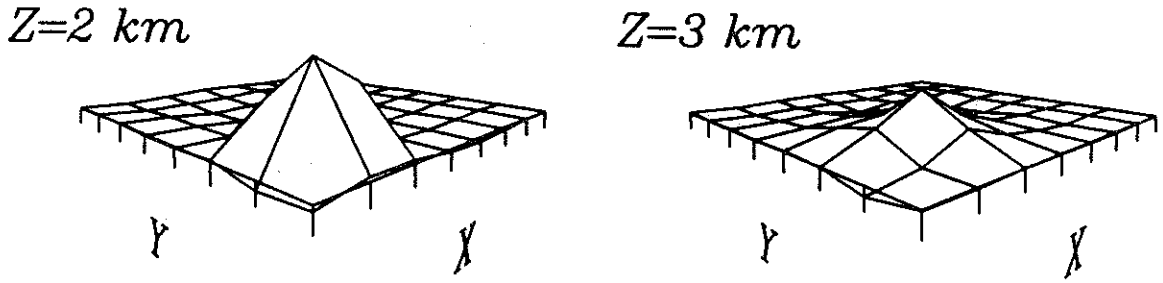

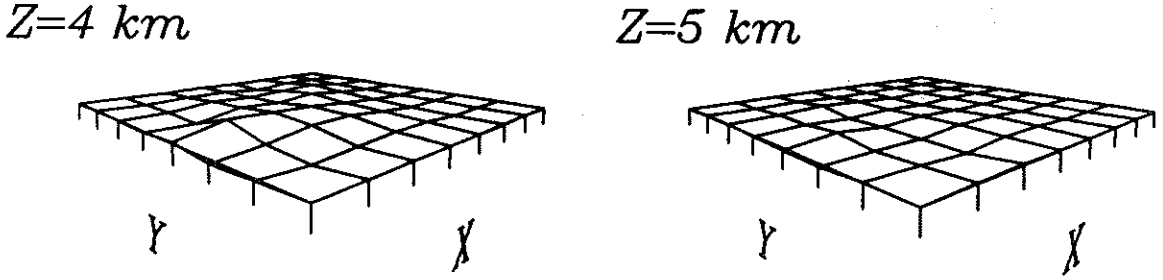

Figure 8

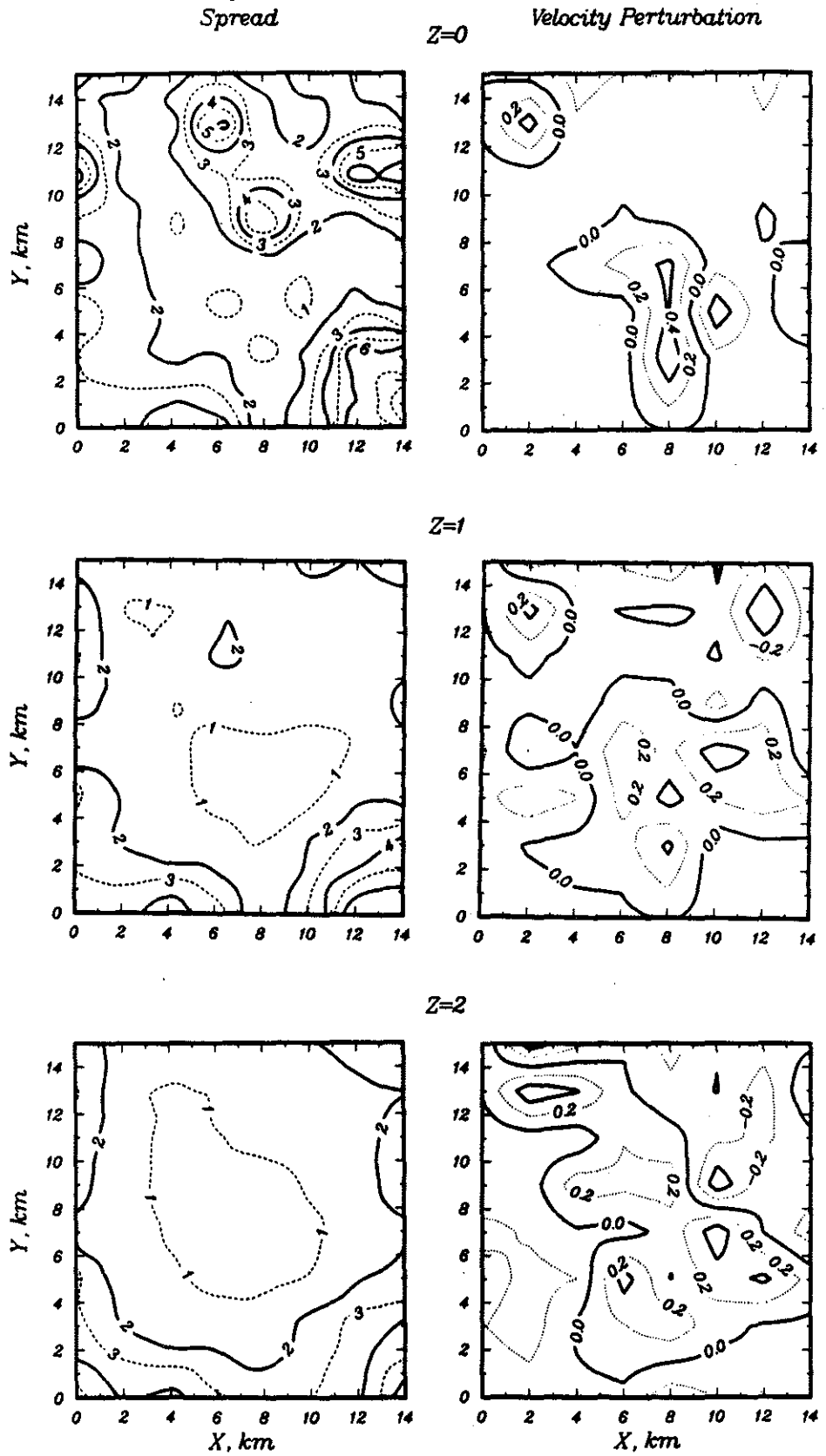

Figure 9a

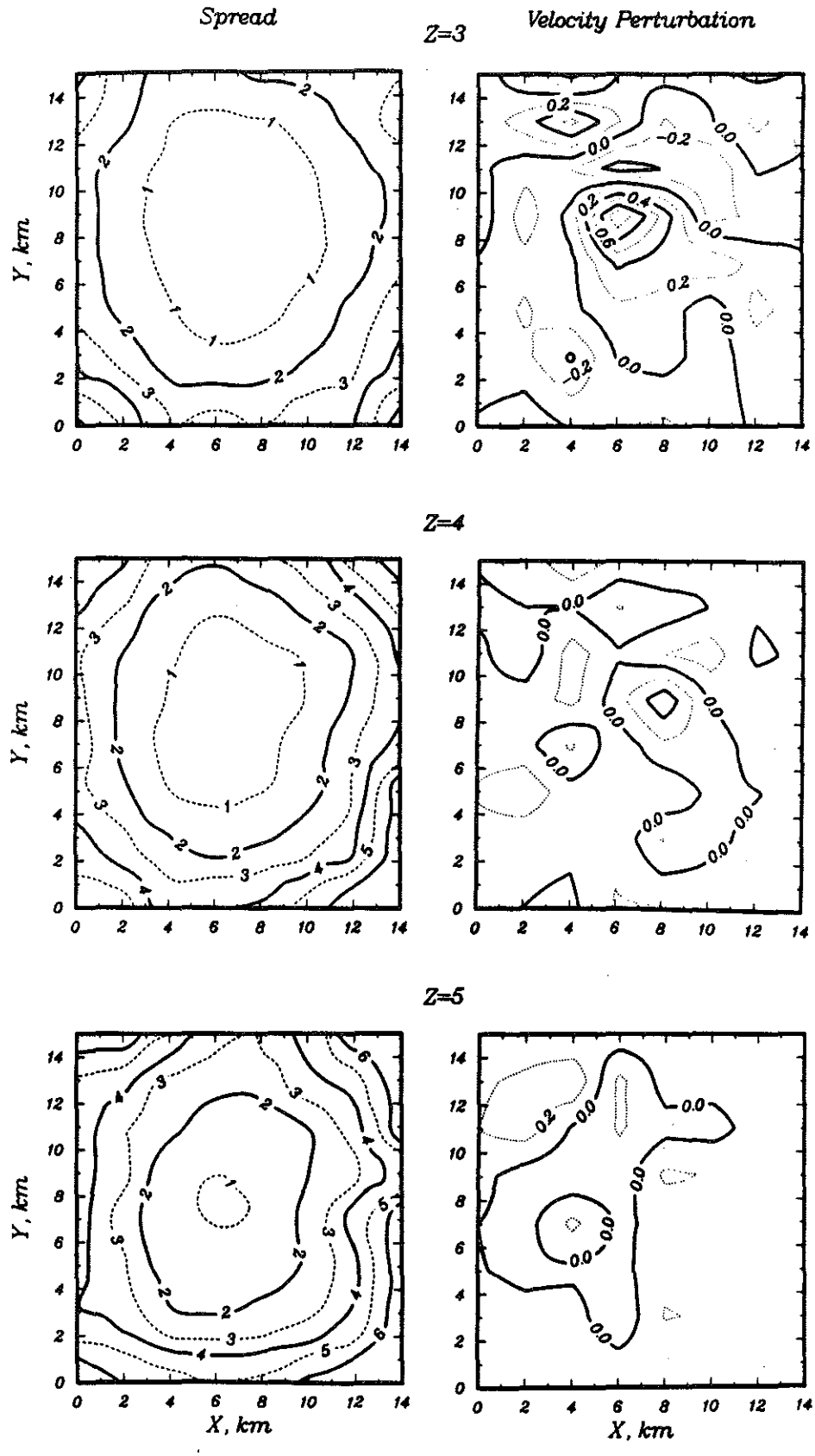

Figure 9b

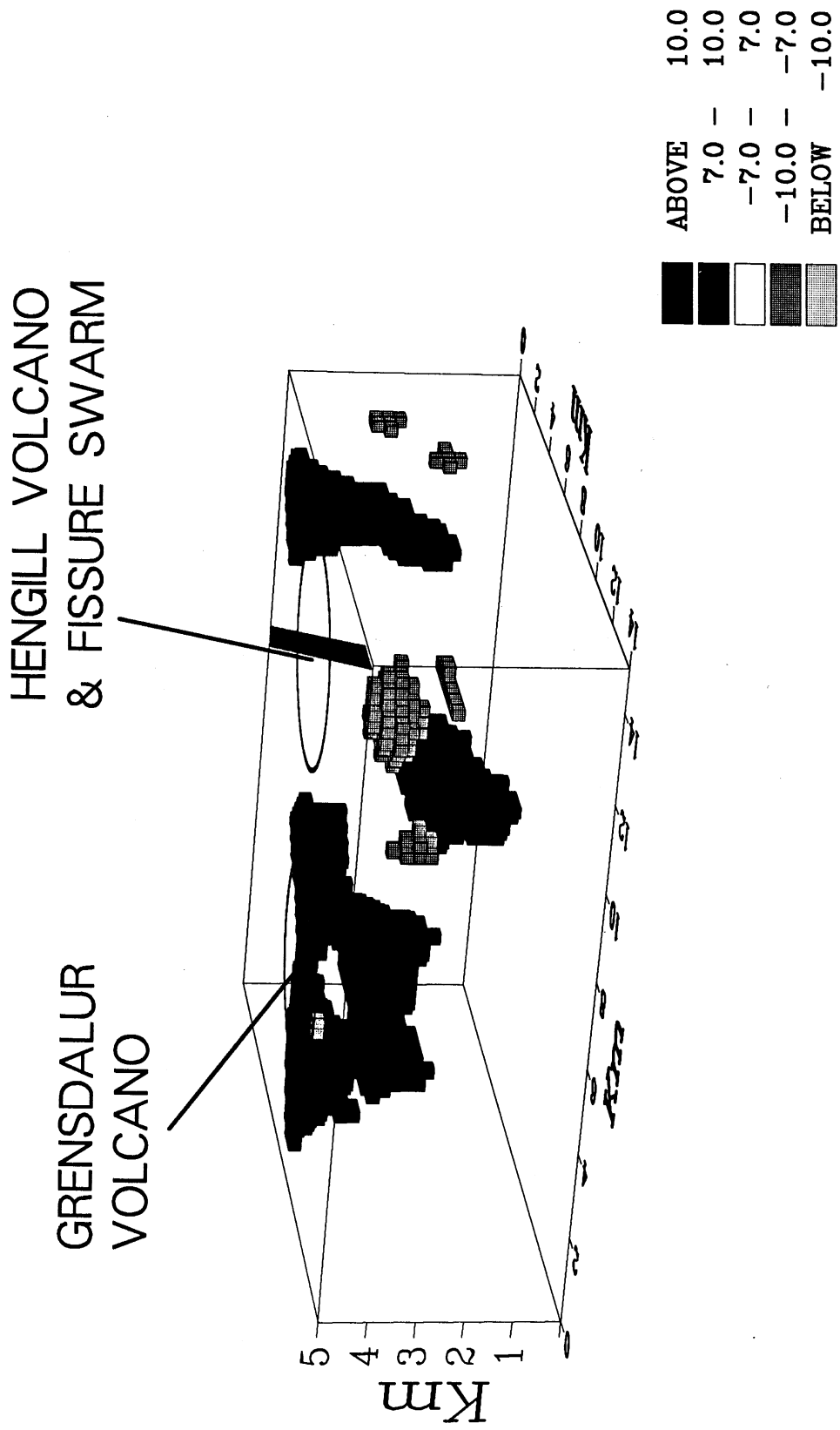
HENGILL VOLCANO
& FISSURE SWARM
GRENSDALUR
VOLCANO
Km
5
4
3
2
1
0
ABOVE 10.0
7.0 — 10.0
−7.0 — 7.0
−10.0 — −7.0
BELOW −10.0

Figure 10a

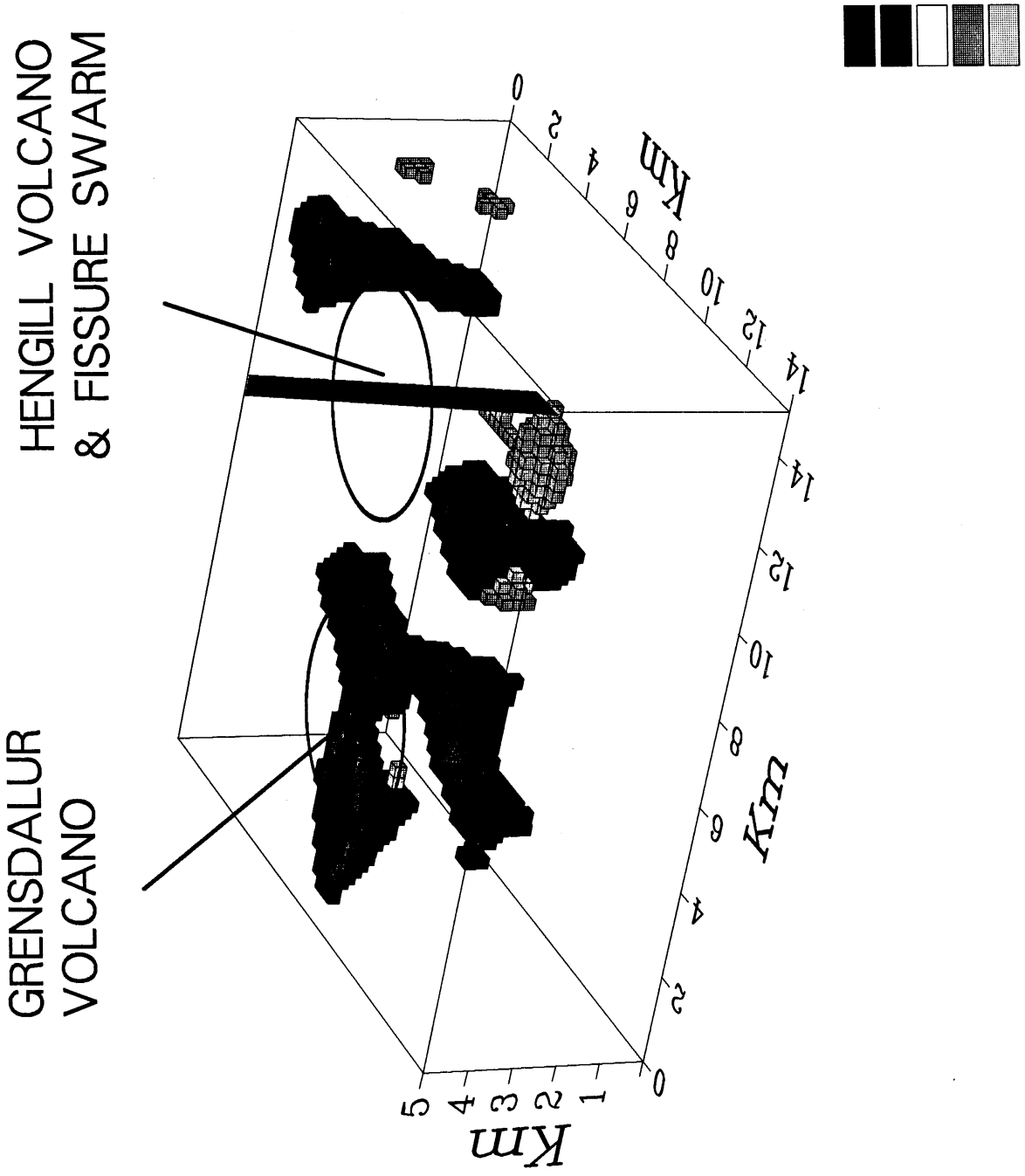
HENGILL VOLCANO
& FISSURE SWARM
GRENSDALUR
VOLCANO
ABOVE 10.0
7.0 – 10.0
-7.0 – 7.0
-10.0 – -7.0
BELOW -10.0
Km
Km
Km

Figure 10b